Design Synthesis and Optimization of Permanent Magnet Synchronous Machines Based on Computationally-Efficient Finite Element Analysis

Gennadi Sizov
Marquette University

DESIGN SYNTHESIS AND OPTIMIZATION OF PERMANENT MAGNET SYNCHRONOUS MACHINES BASED ON COMPUTATIONALLY - EFFICIENT FINITE ELEMENT ANALYSIS

by

Gennadi Y. Sizov, B.S., M.S.

A Dissertation Submitted to the Faculty of the Graduate School,
Marquette University,
in Partial Fulfillment of the Requirements for
the Degree of Doctor of Philosphy

Milwaukee, Wisconsin

December, 2013

ABSTRACT

DESIGN SYNTHESIS AND OPTIMIZATION OF PERMANENT MAGNET SYNCHRONOUS MACHINES BASED ON COMPUTATIONALLY - EFFICIENT FINITE ELEMENT ANALYSIS

Gennadi Y. Sizov, B.S., M.S.

Marquette University, 2013

In this dissertation, a model-based multi-objective optimal design of permanent magnet ac machines, supplied by sine-wave current regulated drives, is developed and implemented. The design procedure uses an efficient electromagnetic finite element-based solver to accurately model nonlinear material properties and complex geometric shapes associated with magnetic circuit design. Application of an electromagnetic finite element-based solver allows for accurate computation of intricate performance parameters and characteristics.

The first contribution of this dissertation is the development of a rapid computational method that allows accurate and efficient exploration of large multi-dimensional design spaces in search of optimum design(s). The computationally efficient finite element-based approach developed in this work provides a framework of tools that allow rapid analysis of synchronous electric machines operating under steady-state conditions. In the developed modeling approach, major steady-state performance parameters such as, winding flux linkages and voltages, average, cogging and ripple torques, stator core flux densities, core losses, efficiencies and saturated machine winding inductances, are calculated with minimum computational effort. In addition, the method includes means for rapid estimation of distributed stator forces and three-dimensional effects of stator and/or rotor skew on the performance of the machine.

The second contribution of this dissertation is the development of the design synthesis and optimization method based on a differential evolution algorithm. The approach relies on the developed finite element-based modeling method for electromagnetic analysis and is able to tackle large-scale multi-objective design problems using modest computational resources. Overall, computational time savings of up to two orders of magnitude are achievable, when compared to current and prevalent state-of-the-art methods. These computational savings allow one to expand the optimization problem to achieve more complex and comprehensive design objectives.

The method is used in the design process of several interior permanent magnet industrial motors. The presented case studies demonstrate that the developed finite element-based approach practically eliminates the need for using less accurate analytical and lumped parameter equivalent circuit models for electric machine design optimization. The design process and experimental validation of the case-study machines are detailed in the dissertation.

ACKNOWLEDGMENTS

Gennadi Y. Sizov, B.S., M.S.

I would like to thank my advisor, Prof. Nabeel Demerdash, for his never ending support and encouragement during my studies at Marquette University. I am deeply grateful for his efforts in sparking my interest in electric machinery and the opportunity to work under his supervision. A special thanks to my industrial advisor, Dr. Dan Ionel, for his constant encouragement, expert knowledge and patient guidance that were invaluable to the success of this project.

I would also like to thank the committee members, Prof. Michael Johnson, Prof. James Richie and Prof. Edwin Yaz of Marquette University, Dr. Russel Kerkman of Rockwell Automation, and Dr. Thomas Nehl of General Motors for their guidance, advice and support throughout this project.

I wish to acknowledge the financial and engineering support of Marathon Electric of Regal Beloit Corporation, A.O. Smith Corporation, and the US National Science Foundation under GOALI Grant ECCS - 1028348. I would also like to acknowledge the support of ANSYS Corporation for providing access to world class simulation software.

Throughout this project I was fortunate to work with and learn from industry experts: Steve Stretz and Alan Yeadon of Marathon Electric, Ronald Bartos, Brian Branecky, Matthew Critchley, Robert Heideman, Stephen Memory of A.O. Smith Corporate Technology Center, and Mark Solveson and Dr. Marius Rosu of ANSYS Corporation.

A special thanks to Dr. Ian Brown, now with Illinois Institute of Technology and formerly with A.O. Smith Corporate Technology Center, for our long and fruitful discussions. Thanks to all my colleagues and friends at Marquette University: Peng Zhang, Jiangbiao He, Alireza Fatemi, Alia Strandt, Andrew Strandt, Dr. Ahmed Sayed Ahmed, and Dr. Chiachou Yeh for sharing the long hours of exciting and hard work.

Most of all, I would like to thank my family Maria, Nikolay and Olga for filling my life with love and joy. This dissertation would not be possible without you!

TABLE OF CONTENTS

LIST OF TABLES

LIST OF FIGURES

NOMENCLATURE

λ	Instantaneous flux linkage (Weber).
i	Instantaneous current (Ampere).
v	Instantaneous voltage (Volts).
r	Resistance (Ohm).
H_c (H_{cB})	Normal permanent magnet coercive field intensity (Amperes per meter).
H_{cJ}	Intrinsic permanent magnet coercive field intensity (Amperes per meter).
BH_{max}	Maximum permanent magnet energy product (Joules per meter cubed).
B_{rem}	Permanent magnet remnant (residual) flux density (Tesla).
α	Temperature coefficient (percent per degree Celsius).
L_{kk}	Self inductance of winding (or coil), k, (Henry).
L_{kj}	Mutual inductance between two windings (or coils), k and j, (Henry).
L^{app}	Apparent inductance (Henry).
L^{inc}	Incremental (differential) inductance (Henry).
T_{em}	Developed electromagnetic torque profile (Newton meters).
T_{dq}	Developed electromagnetic torque profile computed using dq-based motor model (Newton meters).

T_{avg}	Average value of the developed electromagnetic torque (Newton meters).
$B_{r,t}$	Radial and tangential components of flux density (Tesla).
$f_{r,t}$	Radial and tangetial air-gap stresses calculated using the Maxwell stress tensor (Newton per square meter).
$F_{r,t}$	Radial and tangetial air-gap forces calculated using the Maxwell stress tensor (Newton).
F_{SR}	Resultant MMF (Ampere turns per pole).
F_S	Stator MMF (Ampere turns per pole).
F_R	Rotor MMF (Ampere turns per pole).
B_g	Resultant peak air-gap flux density (Tesla).
w_g	Air-gap energy density (Joules per cubic meter).
W_g	Air-gap energy (Joules).
W_{stored}	Stored energy (Joules).
W'_{stored}	Stored co-energy (Joules).
μ	Magnetic permeability (Henry per meter).
g	Air-gap height (along radial direction) (meters).
D	Diameter in the middle of the air-gap (meters).
l_{Fe}	Effective axial stack length of an electric machine (meters).
f_{stk}	Lamination stacking factor (per unit).
l_{stk}	Total axial stack length of an electric machine (meters).

A_c	Electric (ampere) loading or linear current density along the mid-air gap circumference (Ampere per meter).
J	Electric current density (Ampere per square meter).
J_{PM}	Equivalent electric current density used to represent a permanent magnet excitation (Ampere per square meter).
A	Magnetic vector potential (Webers per meter).
s_f	Slot fill factor (per unit).
s_{fG}	Gross slot fill factor (per unit).
N_{ph}	Number of turns per phase.
N_s	Number of stator slots.
m	Number of phases.
a	Number of parallel paths per phase.
I_{ph}	Value of rms phase current (Amperes).
τ_s	Slot pitch (meters).
P	Number of poles.
q	Number of slots per pole per phase.
k_w	Winding factor (per unit).
k_d	Distribution factor (per unit).
k_p	Pitch factor (per unit).
k_s	Skew factor (per unit).

N_{cog}	Number of cogging cycles per revolution.
N_{sp}	Number of slots per machine periodicity span.
β	Torque angle (electrical radians).
γ	Current advance angle (electrical radians).
θ	Angle (electrical radians).
θ_m	Angle (mechanical radians).
ω	Frequency (in electrical radians per second).
ω_m	Frequency (in mechanical radians per second).
P_{em}	Developed electromagnetic power (Watts).
P_{Cu}	Ohmic power losses (Watts).
P_{Fe}	Lamination eddy current and hysteresis losses (Watts).
p_h	Lamination hysteresis loss density (specific losses) (Watts per kilogram).
p_e	Lamination eddy current loss density (specific losses) (Watts per kilogram).
k_h	Lamination hysteresis loss coefficient (Watts per Hertz per square Tesla per kilogram).
k_e	Lamination eddy current loss coefficient (Watts per square Hertz per square Tesla per kilogram).
p_{Fe}	Lamination eddy current and hysteresis loss density (specific losses) (Watts per kilogram).

$\mathbf{P}_g$	Population vector containing individual population members.
$\mathbf{P}_0$	Randomly initialized initial generation.
$\mathbf{x}_{g,k}$	An individual population member.
$\mathbf{u}$	Mutated trial individual.
G_{max}	Maximum number of generations.
N_p	Number of members in a generation.
p	Number of design parameters describing an individual population member.
b_{Li}	Lower design parameter boundary.
b_{Ui}	Upper design parameter boundary.
F	Difference scale factor.
Cr	Cross-over probability.

Chapter 1

Introduction

1.1 Background

DESIGN of electric machines is a challenging task that involves multi-domain physical phenomena, a large number of design variables and a broad set of design objectives and constraints. In electric machines, electromagnetic, thermal and mechanical phenomena are tightly coupled and require careful consideration. A large number of design choices such as motor topologies, geometrical dimensions, and material properties introduce high degrees of variability in the design process making optimal design difficult. Additional complications are introduced by multiple and oftentimes conflicting specifications, objectives and constraints that have to be simultaneously achieved and satisfied. Furthermore, high performance and high efficiency electric machines have to be designed for operation with variable speed drives. In fact, in a number of emerging applications, such as electric (or hybrid-electric) vehicles, machine-drive systems are co-designed together to achieve highest performance and efficiency throughout a wide torque and speed operating range. When considered together, all of the above mentioned difficulties make the process of electric machine design a multi-disciplinary task challenging the designer's knowledge in a broad range of engineering fields.

Over the years, numerous textbooks outlining common practices used in the design of electric machines have been written, among them are [1–7]. These classical texts treat various aspects of electric motor design and provide a good starting point for electromagnetic, thermal and mechanical designs. A common theme of the design procedures outlined in these texts and frequently used in industrial settings relies heavily on the analytical (or empirical) formulations, legacy designs and experience of the design engineer. Oftentimes,

these design procedures involve building, testing and iteratively improving multiple design prototypes which may be costly and time consuming.

In the past several decades, numerical modeling tools have become widely accepted and are used to aid in the tasks of design and analysis of electric machines. Oftentimes, a motor designer will rely on lumped-parameter or finite element (FE) numerical models to predict and verify the performance of the machine. This model-based design approach has the potential of reducing the number of prototypes that need to be built and tested during the design process. Unfortunately, neither of these design approaches guarantee optimality of the final design with respect to design objectives and specifications. Furthermore, due to the significant computational burden associated with FE-based machine models, these models are typically used only in the final stages of the design process when major design variables have been fixed and most design variability (flexibility) eliminated.

In the face of all of the above mentioned difficulties, efficient automated design tools that can assist the engineer in the tedious and iterative design process are becoming a necessity. Design synthesis and optimization tools that can simultaneously manipulate a large number of design variables while accurately considering a wide range of performance parameters are the subject of this dissertation.

1.2 Literature Review

In this section, developments in the areas of model-based design synthesis and optimization are reviewed. First, various reduced effort finite element models are reviewed and compared. Second, a survey of model-based optimization methods pertaining to design of electric machines and electromagnetic actuators is presented.

1.2.1 Efficient Modeling Approaches

In this section, recent developments in the area of reduced effort FE analysis are outlined and reviewed. Minimization of the computational effort and preservation of the accuracy

of geometric and/or material properties that is inherent to FE-based solvers is a common feature of the techniques reviewed in this section. Techniques described in the literature are presented and compared in terms of assumptions and simplifications used in the analysis, execution times, and computationally obtained performance parameters that can be extracted with reasonable accuracy.

In any model-based design and analysis there are two commonly conflicting requirements on the modeling approach used to estimate the performance of the device: 1) accuracy, and 2) execution time. The latter requirement has prompted development of various analytical models and lumped parameter (magnetic equivalent circuit) models. While useful for performance analysis and initial device sizing, analytical and magnetic equivalent circuit models may leave much to be desired for accurate representation of complex geometric shapes and nonlinear material properties. On the other hand, design and analysis by means of more comprehensive FE models may be inappropriate due to the prohibitively long execution times. This limitation of FE-based models has to date prevented their application in large-scale design optimization studies, where significant number of design parameters are varied in a search for an optimum design(s). In a typical design flow, FE analysis (FEA) is used in the final steps of the design process for verification and parameter fine tuning.

In the early applications of FE-based models to electric machine analysis, there has been a considerable effort to maximize the amount of useful machine performance information that can be extracted from such FE solutions, while minimizing the computational effort. However, the development of modern FEA tools has been driven by the needs of more complex problems, such as time-stepping circuit-coupled, motion, and 3-D problems. While more comprehensive in terms of complexity of physical phenomena being modeled, these tools still pose significant computational burdens limiting their use to the final stages of the design process.

Recently, there has been significant interest in the development of design tools that can introduce and automate model-based design in the early stages of such electric machine

design processes. These techniques aim to minimize the computational effort required to obtain the maximum possible information about the performance of the device being modeled. Hence, these techniques have the potential of allowing the use of FE-based machine models at much earlier stages of the design process, thus improving the overall quality/optimality of the final design. Moreover, application of such simplified FE models preserves most of the benefits of conventional FE-based solvers, i.e. accuracy of geometric shape and material properties representations. This is especially useful in large-scale, comprehensive design optimization studies where thousands of candidate machine designs are evaluated.

Hybrid FE *abc* [8–14] and *dq* analysis [15–18]

In the early application of numerically based modeling (finite difference and finite element) to electric machinery significant effort was focused on the extraction of equivalent circuit parameters that were used to relate distributed field solution to such machine's terminal quantities. A voltage, current and flux-linkage relationship for a coil participating in the magnetic circuit of the electric machine with multiple coupled coils can be written based on Faraday's Law as follows:

$$v_k = r_k i_k + \frac{d\lambda_k}{dt} \tag{1.1}$$

where, the flux linkage of the coil, λ_k, is a result of self-induced flux produced by the current, i_k, and the mutual flux produced by other coils participating in the overall flux production and, r_k, is the resistance of the coil. In the case of a rotating electric machine, equation (1.1) is typically both time-varying and nonlinear. In the most general case, the flux linking k^{th} coil is a nonlinear function of instantaneous currents contributing to the magnetization of the stator and rotor magnetic structures and the rotor position, θ, as shown in (1.2), below:

$$\lambda_k = \lambda_k(i_1, i_2, i_3, ..., i_k, \theta) \tag{1.2}$$

and can be expanded for a machine with permanent magnet field excitation as follows:

$$\lambda_k = \lambda_k(i_1, i_2, i_3, ..., i_k, \theta) + \lambda_{PM}(H_c, i_1, i_2, i_3, ..., i_k, \theta) \tag{1.3}$$

where, λ_{PM}, is the flux linkage produced by a permanent magnet excitation, and H_c, is the permanent magnet coercive field strength. Equation (1.2), can be rearranged by recognizing that permanent magnet can be represented by an equivalent coil with excitation current related to the magnet's normal coercive field intensity, H_c, and thickness along the direction of magnetization, h_{PM}, as follows:

$$i_{PM} = H_c h_{PM} \tag{1.4}$$

$$\lambda_k = \lambda_k(i_1, i_2, i_3, i_{PM}, ..., i_k, \theta) \tag{1.5}$$

where, i_{PM}, represents an equivalent current to account for the presence of a permanent magnet field excitation. Equations (1.1) and (1.5) are sufficient to describe the time-varying and nonlinear relationships between the physical quantities of current and flux-linkage. However, in practical electric machines with nonlinear material properties, evaluation of a complex relationship between magnetic field quantities and electric circuit quantities of current and voltage requires the use of numerical models. Hence, the classical analysis always followed the path of reducing the field problem to an easily manageable equivalent circuit problem with known circuit parameters (self and mutual inductances) relating circuit quantities of electric currents to the magnetic quantities of flux linkages. In the linear case the self and mutual inductances are defined as follows:

$$L_{kk} = \frac{\lambda_{kk}(i_k)}{i_k} \tag{1.6a}$$

$$L_{kj} = \frac{\lambda_{kj}(i_j)}{i_j} \tag{1.6b}$$

where, for calculation of a self-inductance, L_{kk}, and a mutual-inductance, L_{kj}, the excitation

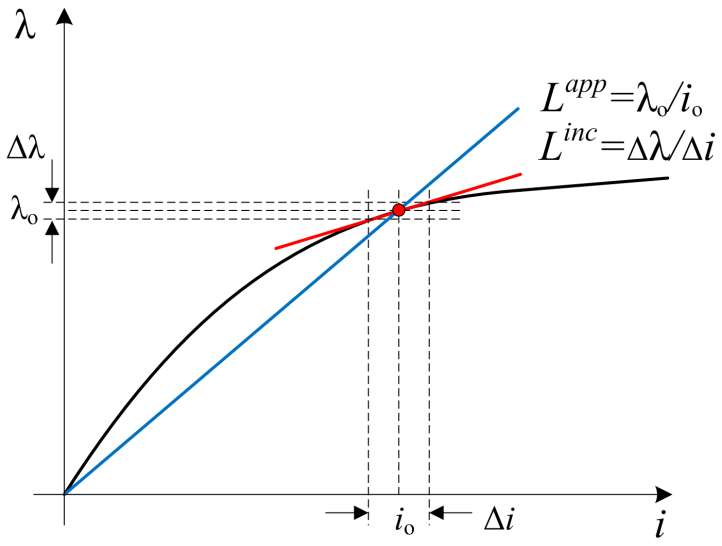

Figure 1.1: Definition of apparent and incremental inductances.

is assumed only due to current, i_k, in the case of the self-inductance and only due to current, i_j, in the case of the mutual-inductance, respectively.

In the nonlinear case where saturable ferromagnetic materials are present the definition of the proportionality between the current and flux linkage is revised to include apparent and incremental self and mutual inductances, as follows [13, 19–21]:

$$L_{kk}^{app} = \frac{\lambda_k}{i_k} \tag{1.7a}$$

$$L_{kj}^{app} = \frac{\lambda_k}{i_j} \tag{1.7b}$$

$$L_{kk}^{inc} = \frac{\partial \lambda_k}{\partial i_k} \tag{1.7c}$$

$$L_{kj}^{inc} = \frac{\partial \lambda_k}{\partial i_j} \tag{1.7d}$$

where, λ_k, is the flux linkage corresponding to the saturated magnetic circuit. Graphical definition of the apparent and incremental (differential) inductances is provided in Fig. 1.1. Considering equation (1.7) and Fig. 1.1, one should notice that: 1) in practical ferromag-

netic materials the incremental (differential) inductance is always lower in value than the apparent inductance, and 2) in the linear region the apparent and incremental inductances are equal. Apparent and incremental inductances can be calculated from numerical FEA solutions by means of the energy perturbation method described by Nehl *et al.* in [13] and Demerdash and Nehl in [20, 21], and is demonstrated graphically in Fig. 1.1. The energy perturbation method can be used to extract load and position dependent inductances that can later be utilized in the dynamic simulations that accurately capture effects of space harmonics and saturation on the terminal quantities of the machine. Both *abc* and *dq* load and position dependent incremental and apparent inductances can be extracted. This method can be used to provide time-stepping circuit coupled FE simulations [19, 22–25] or for computation of inductances that can be used off-line in system level simulations.

As a variation of the energy perturbation method several methods for efficient FE-based calculation of inductance parameters intended for use with two-axis *dq* models were developed. These *dq* methods provide the means to partially account for the effect of self and *dq* cross-axis magnetic saturation in PM ac machines operated from sine-wave current-regulated drives. Two such models were proposed by Ionel *et al.* [15] and [16]. Further work on the subject was published by Bianchi *et al.* [17] and Zarko [18]. Only a few magnetostatic FE solutions were employed for calculating the *dq* parameters. Saturated *dq* parameters are extracted by the means of the "frozen" permeability method. In this approach, the field distribution is initially solved through a single nonlinear magnetostatic FE solution with excitation from both stator currents and rotor PMs. Based on the results of the initial nonlinear simulation, elemental permeabilities are fixed (*frozen*) to the levels corresponding to the particular load condition and only the stator current excitation is considered for additional linear FE solutions. Two additional linear static simulations are performed, one with the current in the *d*-axis and one with the current in the *q*-axis. Quasi-saturated apparent inductances at a given load condition are then extracted using two additional linear magnetostatic simulations as follows:

- Holding the saturated permeabilities constant, while "disabling" the magnets $\lambda_{PM} = 0$ and applying an arbitrary value of current only along the d-axis, L_{dd} and L_{qd} can be estimated as follows:

$$L_{dd}|_{\lambda_{PM}=0, i_{qs}=0} = \frac{\lambda_{ds}}{i_{ds}} \tag{1.8}$$

$$L_{qd}|_{\lambda_{PM}=0, i_{qs}=0} = \frac{\lambda_{qs}}{i_{ds}} \tag{1.9}$$

- Holding the saturated permeabilities constant, while "disabling" the magnets $\lambda_{PM} = 0$ and applying current only along the q-axis, L_{qq} and L_{dq} can be estimated as follows:

$$L_{qq}|_{\lambda_{PM}=0, i_{ds}=0} = \frac{\lambda_{qs}}{i_{qs}} \tag{1.10}$$

$$L_{dq}|_{\lambda_{PM}=0, i_{ds}=0} = \frac{\lambda_{ds}}{i_{qs}} \tag{1.11}$$

where, the currents, i_{ds} and i_{qs}, are arbitrary due to the linearity assumed after fixing the elemental permeabilities to corresponding saturated values. It should be noted that fixing the permeabilities allows one to partially capture effects of both saturation and dq cross-saturation. A third linear magnetostatic simulation with only the rotor PM excitation enabled, and stator excitation eliminated (*disabled*), is performed to extract the flux linking the armature winding due to the PMs, λ_{md} and λ_{mq}. This method has been extended to calculation of incremental (*differential*) inductances in [26]. The overall flux-linkage model describing the machine at a single load condition in the synchronous frame of reference is then given as follows [17]:

$$\lambda_{ds} = \lambda_{md} + L_{dd} i_{ds} + L_{dq} i_{qs} \tag{1.12}$$

$$\lambda_{qs} = \lambda_{mq} + L_{qq} i_{qs} + L_{qd} i_{ds}. \tag{1.13}$$

The developed torque is then estimated based on dq conventional formulation using the

following:

$$T_{dq} = \frac{3}{4} P(\lambda_{ds} i_{qs} - \lambda_{qs} i_{ds}). \tag{1.14}$$

It should be noted that this torque expression can only be used for accurate calculation of the average torque, while the ripple and cogging torque components are mostly ignored. While useful in estimating effects of certain magnetic circuit nonlinearities on the average quantities, the method described above ignores position dependent variation of inductances and saturation patterns. In order to evaluate variation of inductances with position additional FE-evaluations are required. This allows one to include instantaneous torque ripple in the *dq*-based torque calculation by considering the variation of stored electromagnetic energy (or co-energy, W'_{em}) with position [27] as follows:

$$T_{dq} = \frac{3}{4} P(\lambda_{ds} i_{qs} - \lambda_{qs} i_{ds}) + \frac{\partial W'_{em}}{\partial \theta}. \tag{1.15}$$

The introduction of the $\frac{\partial W'_{em}}{\partial \theta}$ term effectively accounts for the variation of inductances with rotor position.

A common theme in the approaches described above involved calculation of inductance parameters. However, as observed from (1.4) in the nonlinear flux-current relationships, definition of the inductance becomes ambiguous.

The Flux-MMF Diagram [27–31]

An alternative approach relies entirely on the instantaneous, nonlinear and position dependent relationships of fluxes and currents (1.5) and avoids the need for introduction of inductance parameters. The so-called flux-mmf diagram was proposed by Staton *et al.* as a method for computing the average torque of electric motors [28]. The typical algorithm consists of magnetostatic FEA for calculating the flux linkage in the *abc* reference frame and plotting the results against the current on a per phase basis. The typical flux-mmf diagram of an ac (sine-wave) motor is substantially elliptical (Fig. 1.2) and of the brushless

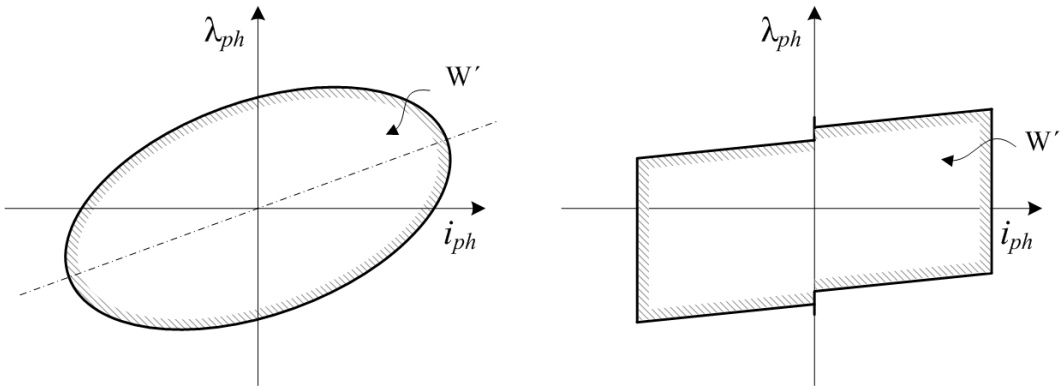

Figure 1.2: Flux-mmf diagrams of: ac (sine-wave) motor, and brushless DC (square-wave) motor.

DC (square-wave) is substantially polygonal. The area of the diagram, W', is proportional to the average value of the torque [27–31]:

$$T_{avg} = \frac{mPW'}{4\pi} \tag{1.16}$$

where, m is the number of phases and, P, is the number of poles. The method was extended by Deodhar *et al.* for the the calculation of cogging torques [29]. Ionel *et al.* showed that for brushless DC (square wave) motors the average torque can be estimated based on only two magnetostatic FE solutions [30]. The minimum number of magnetostatic solutions required for the calculation of the average torque of a PM ac (sine-wave) motor and its relationship with the flux-mmf diagram was recently discussed by Ionel and Popescu [32]. Further improvements were brought about by Miller *et al.* who implemented the method, also referred to as the i-ψ diagram, in a popular motor design software [31]. Recently, Bianchi and Alberti proposed a technique for calculating the ripple torque [27]. The flux-mmf diagram and its variations deal with flux linkages and do not include the calculation of flux density waveforms in the magnetic circuit nor provide an estimate of the core losses.

Hybrid Analytical-FE Models [33–35]

A combination of FE and analytical methods can yield, in principle, further savings of computational effort, while enabling the estimation of torque and radial force variation with time and rotor position. Such a method was developed by Schlensok *et al.* for estimating the cogging torque based on only two static FE solutions [33]. The first solution employs a model with a smooth stator to calculate the radial flux density distribution due to the permanent magnets and one with a smooth rotor, to derive a relative air-gap permeance function. The radial flux density and air-gap permeance function obtained from these static FE solutions are then used to estimate and minimize the harmonics of the cogging torque component. It is assumed that due to a large equivalent air-gap (both actual air-gap and permanent magnet), the air-gap permeance function is only modulated by the stator slotting. The method relies on the superposition principle, which assumes linearity of the magnetic circuit. As described in [33], the method is applicable to open-circuit simulations. Although the method could be extended, in principle, to load studies the practical applicability would be limited in this case as most modern motor designs are expected to run heavily saturated. Another hybrid analytical-FE method, entitled Field Reconstruction (FR), was proposed by Zhu *et al.* [34]. This method has been developed especially for the optimization of excitation currents in order to reduce torque ripples and radial forces. According to this method, a limited number of FE solutions are used to calculate the radial and tangential components of air-gap flux densities as functions of excitation currents under the assumption of a linear characteristic for the magnetic circuit. The resultant radial and tangential components of the air-gap flux density are obtained through superposition as follows:

$$B_r = B_{rPM} + B_{rS} \tag{1.17}$$

$$B_t = B_{tPM} + B_{tS} \tag{1.18}$$

where, B_{rPM}, and, B_{tPM}, are the radial and tangential components of flux density due to the PMs, and, B_{rS} and B_{tS}, are the radial and tangential flux density due to stator excitation. These flux density components are then used to calculate the Maxwell stress components in the motor air-gap. Accordingly, the radial and tangential stress distributions per unit of axial length are given as follows [34]:

$$f_r = \frac{B_r^2 - B_t^2}{2\mu_0} \tag{1.19}$$

$$f_t = \frac{B_r B_t}{\mu_0}. \tag{1.20}$$

Integration of the force densities yields the resultant radial force and shaft torque. Due to the assumption of magnetic circuit linearity the FR method is better suited for simulation of surface PM (SPM) machines that have larger equivalent air-gaps and hence reduced saturation. The method, as published in [34], is confined to the air-gap field calculation and does not include the values of the flux densities in the magnetic circuit nor the core loss estimation. In terms of the execution time, the FR approach requires a significant number of static solutions to be performed. However, once these solutions are carried out and the required relationships between air-gap fields and terminal currents are established the need for further FE evaluations is eliminated.

A coupled magnetic equivalent circuit (MEC)-FE model was proposed by Gyselnick *et al.* [35]. In principle, computational effort savings were achieved in this case by employing lumped reluctance/permeance elements in locations where the field may exhibit less variation and the accuracy of the local solution does not significantly affect the global performance, such as torque and efficiency. The proposed regions for MEC modeling were the back-iron of the stator and rotor cores. The coupled MEC-FEA model can be used both for steady-state and transient performance simulation. Unlike typical magnetostatic FEA, the MEC-FEA model will require a full (as opposed to a sparse) matrix of coefficients that may actually lead to increased computational time. Additionally, the MEC-FEA model requires

special pre-processing, which unlike automatic FE mesh generators, maybe dependent on the motor topology and design details.

1.2.2 Model-Based Optimization

In this section state-of-the-art of model-based optimization of electric machinery is reviewed. Proposed methods are classified as those relying on FEA-based solvers for objective function approximation and those relying on less accurate analytical or magnetic equivalent circuit solvers. In addition, the reviewed optimization techniques are classified in terms of the number of candidate design evaluations and optimization algorithm used.

Advantages and potential of automated model-based design were recognized in the early years of application of computers to analysis of electric machinery. Early work by Saunders [36], Veinott [37] and Chalmers [38] performed in the 1950s and 1960s concentrated on the design of induction motors and employed equivalent circuit based models. Model-based design that considered complex geometric shapes and nonlinear material properties became possible in the 1970s and 1980s with the proliferation of numerical methods such as magnetic equivalent circuits, finite differences, and finite elements in the electric machinery analysis. In the same time frame the finite element method was successfully applied [9], and established as a method of choice in the nonlinear low frequency (quasi-static) magnetic field analysis [39]. In the following decades continuous advances in both numerical methods and computing hardware opened new possibilities that allowed designers to tackle problems with ever increasing complexity.

The work of Nakata [40] was one of the early developments in the area of FE-based optimization. In [40], a permanent magnet shape is designed to match the the prescribed air-gap flux density. The design procedure is formulated as an inverse problem, two example studies are provided, one with 4 model iterations and the other with 18 model iterations. The later example considers a design of a curved magnet that can support sinusoidal air-gap flux density.

In [41], Preis presented a finite element based evolutionary optimization of the pole shape to achieve a uniform flux distribution in the air-gap. Preis considered three different evolutionary approaches and compared them to a Gauss-Sidel method. The objective function was approximated using 2-dimensional nonlinear magnetostatic finite elements with approximately 150 model iterations. In addition, 3-dimensional linear magnetostatic finite element model was used. A single evaluation of the finite element model was required to estimate the objective function (flux distribution in the air-gap). In the examples provided in [41], Preis considered up to 8 parameters in the single objective optimization.

In [42], Mohammed used an example of the transformer to present a nonlinear magnetostatic finite element based optimization method. The method utilized dynamic programming that was embedded into finite element formulation to minimize a single objective (magnetic circuit volume) while satisfying a predefined excitation current and the resulting core flux density. In a later project [43], Mohammed used a Genetic Algorithm (GA) in combination with a magnetostatic linear FE solver to design the pole face of a salient pole synchronous machine. The procedure was used to shape the pole face to produce sinusoidal air-gap flux density, a slot-less stator was assumed. A single linear FE model evaluation was used to evaluate air-gap flux distribution. A total of 720 model evaluations were used in the search for the optimum design. In later work Cingoski *et al.* [44], used 2D linear magnetostatic FE analysis and a dynamically adjustable GA to optimize the pole face of an electric machine. A total of 3000 model iterations were used.

Early applications of finite elements to optimization problems reviewed above, considered simple magnetic circuit structures and typically required a single FE evaluation to determine the objective function. However, application to comprehensive design of electric machines required additional costly model evaluations in order to determine parameters such as cogging torque and torque ripple, back emf and induced voltage, core losses and efficiency. This resulted in the significant effort to incorporate less demanding analytical based methods [45–51] and magnetic equivalent circuit (MEC) based methods [52] into the

design synthesis and optimization process. Examples of analytical methods include the work by Deng [45, 46], Zhu [47, 48] and more recently the work by Zarko [49], and Gysen [50]. These methods attempt to solve the distributed boundary value field problem by including simplified geometrical details of the stator and rotor, while assuming linear material properties. The assumption of linear material properties makes application of such methods to the detailed design of electric machinery problematic. To date application of analytical-based methods was mostly limited to surface permanent magnet machines, where their use can be justified due to a typically large equivalent air-gap that results in low operating core flux densities.

Examples of MEC-based optimization routines are provided in the work of Hameyer [53], Lovelace [54], Kim [55], and Cassimere [56, 57], [58]. While useful for basic design analysis and initial electromagnetic core sizing, application of MEC solvers to detailed design problems that include fine geometrical variation and local material nonlinearities may result in erroneous results. It is a generally accepted fact that due to their lower spatial resolution, MEC solvers compromise model fidelity over execution speed. Weaknesses of analytical methods and MEC solvers are especially evident in the analysis of machines that operate with high core flux densities and have heavy local saturation, such as for example interior (or embedded) permanent magnet motors and traction and servo motors designed for high intermittent overload conditions.

In [59], Bianchi and Bolognani described a GA-based optimization method that used both a simplified analytical machine analysis and a detailed FE-based design procedure. The method was demonstrated on the example of a surface permanent magnet (SPM) motor supplied with regulated sinusoidal current. Five design variables were used in the FE-based optimization process. The routine was executed twice for two different design scenarios. First, the objective function was to find the motor with minimum magnet mass, while satisfying the constraints related to output shaft torque, winding temperature rise and magnet demagnetization. Second, the objective function was to find the motor with

the highest torque density for a motor with fixed outside diameter and axial length. The average torque was estimated using a single nonlinear magnetostatic FE solution. During the search process a total of 1250 candidate designs requiring a single FEA solution each were evaluated. Practical issues regarding selection of GA optimizer parameters were also discussed.

In [60], Alhamadi presented an FE-based method of optimization of the rotor skew angle. Multi-sliced 2D FE analysis was used to approximate the 3D effects of skew. The objective function was to minimize the harmonic distortion of the back emf waveform. Every model was evaluated with 10 motor cross-sections to approximate the skew at 37 rotor positions each. The gradient based inverse problem method (GIPM) converged to the final solution after 8 iterations (candidate designs).

In his dissertation [61], Zarko presented two model-based design methods. The first method employed an analytical motor model [61] and was used for of an SPM motor. The later method used an FE-based model and was used to design an interior permanent magnet (IPM) motor for field weakening operation. A differential evolution (DE) optimizer was used to iteratively improve the model in the multi-objective search. The motor was designed to improve two objective functions, cogging torque and field weakening performance by maximizing the characteristic current [62]. The final Pareto-set consisted of 9 optimal designs. A total of 8750 candidate design were considered during the search. Good convergence properties and simplicity of implementation of the DE optimizer were recognized in the recent work by Beniakar [63], and Baek [58].

In [64], Arkadan *et al.* presented an FE-based optimization method of a Synchronous Reluctance motor (SynRM). Initially, a circuit-coupled FE analysis was used to establish a relationship between the design variables and the objectives (performance characteristics). The FE model was executed on a reduced set of candidate designs to establish a training set that was used to train a Fuzzy Logic (FL) model. The Fuzzy Logic model was trained to represent the continuous nonlinear relationships between the design variables and design

objectives, and was subsequently used in the later optimization search. Arkadan, proposed the use of the Particle Swarm Optimizer (PSO) to search the design space. In principle, this technique resembles the Response Surface Methodology (RSM) where the designed experiments are used to establish an analytical multi-dimensional surface model that relates design variables to a design objective (or objectives).

An example of RSM-based optimization applied to design of a spoke-type IPM is presented by Giurgea in [65]. In [65] a combination of MEC and FE-based models were used to establish a response surface. A total of 125 of the FEA evaluations are performed in the search for the optimal solution. In [66], Brown presented an RSM-based method for design of induction motors for sensorless (self-sensing) applications. The electromagnetic design of the rotor cage was modified to include spatial saliencies that could be used to resolve rotor position using a high frequency injection method for sensorless operation. Three different saliency types were investigated. The aim of the technique was to improve the sensorless performance while preserving power conversion properties. Time-stepping FE analysis was used in the investigation to accurately capture the power conversion and sensorless operation performance. Since sensorless operation relied on the high frequency injection method, a fine time-step was used in the simulation and a total of 52 candidate designs were used in the designed experiment to establish the response surfaces.

In his work [67], Pellegrino developed a multi-objective FE-based design method for IPM motors. This was accomplished using a multi-objective genetic algorithm (MOGA). The method was used to improve four design objectives, namely, average and ripple torque, field weakening performance, and rotor losses. Every candidate design was evaluated using a reduced set of FE simulations, the number of evaluations ranged from 4 for low fidelity analysis, to 7 and 15 for higher fidelity analysis that included torque ripple and rotor loss evaluations. A comprehensive multi-objective search of the design space took 110 hours using modest computational facilities.

In the recent work [68], Parasiliti *et al.* used an FE-based optimization method for

design of an IPM motor for field weakening operation. The method considered three objectives and optimized the motor for two operating conditions at rated and high speed. Three objectives were selected to: 1) maximize torque at rated speed, 2) maximize torque in the field weakening speed range, and 3) minimize motor active mass. The method was demonstrated on two example IPM motors. A mix of discrete and continuous design variables were used. A total of 13,000 and 12,000 candidate designs were investigated for each of the two optimized motors, respectively. In [68], Parasiliti also proposed a modified controlled random search (CRS) algorithm for exploring the design space.

An alternative approach that relies on advanced computing facilities was recently presented by Jiang *et al.* [69]. The proposed method relied on the computationally intensive time-stepping FEA for evaluation of motor performance that included efficiency, torque ripple, power factor and motor mass. Model evaluation was parallelized and distributed on the large high throughput computing facility that had up to 10,000 cores available. The method was demonstrated on a simple SPM motor with parametric geometry described by 6 geometrical variables. The differential evolution optimizer was used in the multi-objective search that included 4,250 candidate design evaluations. Candidate designs of every generation were distributed on up to 85 cores for parallel simulation. The total simulation time for the 4,250 candidate designs using advanced computing facilities was 25 hours. The same authors point out that using a single core the proposed method would take approximately 29 days to execute. While the computational method currently used by the authors in [69] is inefficient compared to the method proposed and used in this dissertation, the application of advanced computing facilities to electric machine optimization can be extremely beneficial. Authors point out that in their example with parallelization on 85 cores, an execution speed-up of 30 to 50 times faster than that of a single core is achievable using a dedicated high throughput computing environment.

A comprehensive review of developments in the field of model-based optimization applied to electric machinery in the last two decades was presented by Duan and Ionel in [70]. In

addition, the authors presented an FEA-based benchmark study comparing the response surface and differential evolution optimization algorithms on a sample multi-objective motor design study with 5 independent stator and rotor lamination design variables. Performance of the two optimization algorithms was compared to the results of the detailed direct-search with 16,807 candidate design evaluations. Direct-search was used to obtain a well developed Pareto-set that was used as a baseline for comparison between the RSM and DE algorithm performance. In this particular example, the DE algorithm was able to resolve the Pareto-set with the least amount of objective function evaluations (FEA simulations). Also, the advantages of the DE-based optimization in problems with increasing number of design variables were highlighted using an example with 11 independent design variables. A sensitivity analysis based RSM pre-screening of design variables was proposed by the same authors in [71]. Response surface methodology was used to establish objective function sensitivity to variations of design parameters. Then a reduced set of design variables that have a significant effect on the design objectives was used in the final DE-based optimization.

It should be pointed out that most relevant model-based optimization methods reviewed in this section are summarized in Table 1.1. The reviewed techniques are compared based on the modeling approach, optimization algorithm, number and complexity of objectives (design goals), and number of candidate design evaluations explored in the search.

Table 1.1: Comparison of proposed model-based optimization methods.

Ref.	Model	Algorithm	Variables	Objectives	Candidates
[40]	2D FEA	Inverse Problem	5	sinusoidal air-gap field	18
[41]	2D and 3D (linear) FEA	Evolutionary	8	uniform air-gap field	150
[42]	2D FEA	Dynamic Programming	8	size	n/a
[43]	2D (linear) FEA	Genetic	8	sinusoidal air-gap field	720
[17]	2D FEA	Genetic	5	PM mass and torque density	1250
[44]	2D (linear) FEA	Genetic	8	sinusoidal air-gap field	3000
[60]	Sliced 2D FEA	Gradient Based	1	sinusoidal emf	8
[61]	2D FEA	Differential Evolution	12	cogging and field weakening	8750
[65]	2D FEA and MEC	Response Surface	9	torque density	125
[67]	2D FEA	Genetic	6	average and ripple torque, field weakening, rotor losses	several thousand*
[70]	2D FEA	Response Surface and Differential Evolution	up to 11	goodness and mass	16,807
[68]	2D FEA	Controlled Random Search	up to 18	torque density and field weakening	up to 13,000
[69]	2D FEA	Differential Evolution	6	efficiency, torque ripple and density	4,250

* Number of candidate designs was not explicitly stated in the paper.

1.3 Dissertation Contribution

In this dissertation, the model-based optimal design problem of permanent magnet ac machines supplied by sine-wave current regulated drives is considered. A typical motor design problem encompasses multiple design objectives and constraints. Further complications

arise from the high degree of variability attributed to topological, geometrical and material properties requiring a search of large design spaces. In addition, the resulting large number of design variables, nonlinear material properties, and complex geometric shapes, make a definition of the analytical objective function (or functions) relating design parameters to the design objectives difficult, thus forcing the designer to use numerical models to approximate (or sample) the objective function. Application of electromagnetic FEA-based solvers allows for accurate estimation of intricate performance parameters, such as, cogging torque and torque ripple, core losses, and terminal conditions. However, to date the computational burden associated with such objective function evaluation has limited their use in large-scale comprehensive design synthesis and optimization tools.

The first contribution of this dissertation is the development of a rapid computational method that allows accurate and efficient exploration of large design spaces in search of a global optimum design(s). The developed computationally efficient finite element analysis (CE-FEA) approach provides a framework of tools that allow rapid analysis of synchronous electric machines operating under steady-state conditions. In the CE-FEA method, symmetries of electric and magnetic circuits of sine-wave current-regulated synchronous machines are fully exploited yielding substantial savings in the computational effort, while preserving the characteristic accuracy of FE-based solvers. Motor performance is evaluated through Fourier analysis and a minimum number of magnetostatic FEA solutions. In the CE-FEA approach, major steady-state performance parameters such as: terminal flux linkages and voltages, average, cogging and ripple torques, stator core flux densities, core losses and efficiencies are calculated with a minimum computational effort. In addition, the CE-FEA method includes means for rapid estimation of distributed stator forces and effects of stator and/or rotor skew on the performance of a machine.

The second contribution of this dissertation is the development of a design synthesis and optimization method that relies solely on FEA for electromagnetic analysis and is able to tackle large-scale design problems using modest computational facilities. Overall

computational time savings of up to an order of magnitude are achievable when compared to other available state-of-the-art methods. These computational savings allow one to expand the optimization problem to achieve more complex and comprehensive design objectives. The method developed in this work was successfully used in the design process of several interior permanent magnet industrial motors, details of which will be given in Chapter 4.

1.3.1 Summary of Case-Study Optimization Projects

Motor design synthesis and optimization tools developed in this project were used to assist in the design of several industrial permanent magnet motors. Provided below is the summary of case-study design optimization projects that benefited from the tools developed in this research:

- Design optimization of an existing 200-hp IPM motor used in hermetic compressor application.
- Design synthesis of a new 18-hp IPM motor used in hermetic compressor application, which will be detailed in Chapter 4.
- Design optimization of a 30-hp IPM motor used in general purpose industrial application, which will be detailed in Chapter 4.

1.3.2 List of Published Papers

To date there have been 8 refereed journal and refereed conference publications based on the work presented in this dissertation. The work published in [72–75] and listed below focused on the presentation of the FE-based computational method used to extract a comprehensive set of motor performance information:

- *G. Y. Sizov, D. M. Ionel, and N. A. O. Demerdash, "Modeling and design optimization of PM AC machines using computationally efficient-finite element analysis," IEEE Energy Conversion Congress and Exposition (ECCE 2010), pp. 578-585, September 2010.*

- *G. Y. Sizov, D. M. Ionel, and N. A. O. Demerdash, "A review of efficient FE modeling techniques with applications to PM AC machines," IEEE Power and Energy Society General Meeting 2011, pp. 1-6, July 2011.*
- *G. Y. Sizov, D. M. Ionel, and N. A. O. Demerdash, "Modeling and parametric design of permanent-magnet AC machines using computationally efficient finite-element analysis," IEEE Transactions on Industrial Electronics, vol. 59, pp. 2403-2413, June 2012.*
- *G. Y. Sizov, P. Zhang, D. M. Ionel, N. A. O. Demerdash, I. P. Brown, and M. G. Solveson, "Modeling and analysis of effects of skew on torque ripple and stator tooth forces in permanent magnet AC machines," IEEE Energy Conversion Congress and Exposition (ECCE 2012), pp. 3055-3061, September 2012.*

The work presented in [76–79] concentrated on the application of the computational method developed in this investigation to a problem of design synthesis and optimization using a differential evolution (DE) optimization algorithm:

- *G. Y. Sizov, D. M. Ionel, and N. A. O. Demerdash, "Multi-objective optimization of PM AC machines using computationally efficient - FEA and differential evolution," IEEE International Electric Machines Drives Conference (IEMDC 2011), pp. 1528-1533, May 2011.*
- *G. Y. Sizov, P. Zhang, D. M. Ionel, N. A. O. Demerdash, and M. Rosu, "Automated bi-objective design optimization of multi-MW direct-drive PM machines using CE-FEA and differential evolution," IEEE Energy Conversion Congress and Exposition (ECCE 2011), pp. 3672-3678, September 2011.*
- *G. Y. Sizov, P. Zhang, D. M. Ionel, N. A. O. Demerdash, and M. Rosu, "Automated multi-objective design optimization of PM AC machines using computationally efficient - FEA and differential evolution," IEEE Transactions on Industrial Applications, accepted for publication, 2012.*
- *I. P. Brown, G. Y. Sizov, M. W. Critchley, J. Yin, S. B. Memory, S. W. Elbel, C. D. Bowers, M. Petersen, and P. S. Hrnjak, "Design and evaluation of interior permanent magnet compressor motors for commercial transcritical CO2 (R-744) heat pump water heaters," IEEE Energy Conversion Congress and Exposition (ECCE 2012), pp. 2790-2797, September 2012.*

1.4 Dissertation Organization

Including this introductory chapter, this dissertation is organized into five chapters. In Chapter 2, the design of permanent magnet ac machines is discussed. More specifically, analytical sizing equations, material choices, differences between various motor layouts (number of slots and poles), winding design, and practical issues related to motor-drive integration are discussed. In Chapter 3, the computationally-efficient FEA (CE-FEA) method is presented and validated. In Chapter 4, an automated design method that utilizes the CE-FEA method coupled to a differential evolution (DE) optimizer is presented. The automated design method is demonstrated on four case-study design problems. Finally, in Chapter 5 conclusions and recommendations for future work are presented.

Chapter 2

Design of Permanent Magnet Machines and Drives

2.1 Introduction

In this chapter, choices related to the basic machine layout are discussed. The intent of this chapter is to establish the necessary background for the following chapters and to introduce the reader various components of the machine design process. Where appropriate, the significance and the necessity for model-based numerical design tools will be highlighted. This chapter presents analytical sizing equations, guidelines for selection of the number of poles and slots and magnetic circuit materials. Also practical issues related to winding design and machine-drive operation are discussed. The primary focus of the chapter is on permanent magnet (PM) ac motors.

2.2 Design Choices

The design of ac electric machinery is a well developed art that builds on over one hundred years of engineering experience. This section will present sizing equations, and empirically determined electrical and magnetic loading ranges which are useful in the preliminary phase of a design process. This initial step is useful in determining the initial layout and rough dimensions of the machine, such as mid air-gap diameter and axial stack/useful conductor length. This initial step is also used to identify preliminary material (electrical steel, insulation, and permanent magnet) requirements and cooling arrangement.

Using an example of an idealized radial flux rotating electric machine, depicted in Fig. 2.1, the most basic sizing equation relating electromagnetic loading and rotor volume to average torque production can be derived. Provided in Fig. 2.1 is a simplified electric

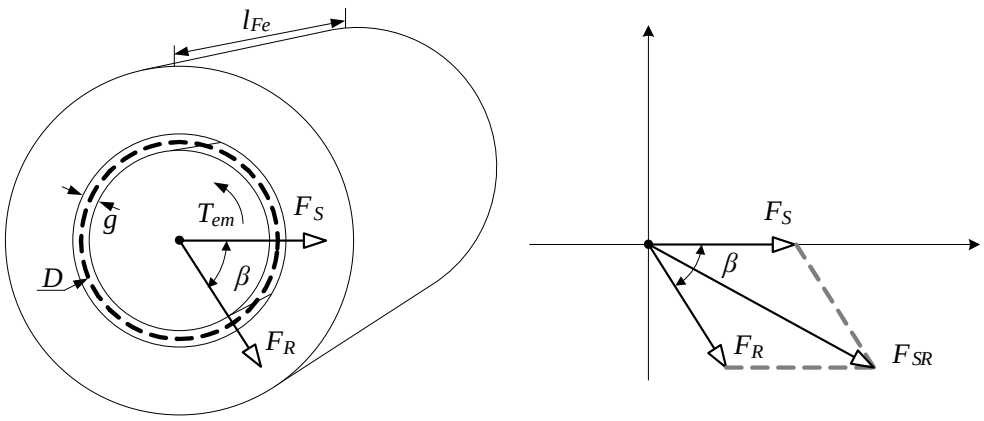

Figure 2.1: Idealized rotating electric machine.

machine with infinitely permeable smooth stator and rotor members. The stator magnetomotive force (MMF), F_S, is produced by the stator winding represented here by a sinusoidal current sheet on the inner surface of the stator facing the air-gap, while the rotor MMF, F_R, is produced by either an electromagnetic excitation as in the case of a wound field synchronous machine or the cage of an asynchronous (induction) machine, or by rotor-mounted permanent magnets as in the case of a synchronous PM motor. The resultant air-gap MMF, F_{SR}, can be derived from trigonometric principles using the torque angle between the stator and the rotor MMFs as shown in (2.1), below:

$$F_{SR} = \sqrt{F_S^2 + F_R^2 + 2F_S F_R \cos\beta} \tag{2.1}$$

where, β, is the torque angle. The resultant peak air-gap flux density can thus be expressed as follows:

$$B_g = \mu_o \left(\frac{F_{SR}}{g} \right). \tag{2.2}$$

Assuming a sinusoidal air-gap flux density distribution, the density of the stored energy in

the air-gap can be written as follows:

$$w_g = \frac{B_g \cos(\theta) H_g \cos(\theta)}{2} = \frac{(B_g \cos(\theta))^2}{2\mu_o}, \tag{2.3}$$

and the average of the stored energy is thus given as:

$$w_g = \frac{1}{\pi} \int_0^{\pi} \frac{(B_g \cos(\theta))^2}{2\mu_o} \, d\theta \; = \frac{B_g^2}{4\mu_o} \tag{2.4}$$

which, can be expressed in terms of the resultant air-gap MMF as follows:

$$w_g = \frac{\mu_o}{4} \left(\frac{F_{SR}}{g} \right)^2 . \tag{2.5}$$

Assuming smooth stator inner surface and rotor outer surface, results in an air-gap volume equal to $\pi D l_{Fe} g$, see Fig. 2.1, and a total energy stored in the air-gap that can be expressed as given in (2.6) below:

$$W_g = \frac{\mu_o}{4} \left(\frac{F_{SR}}{g} \right)^2 \pi D l_{Fe} g = \frac{\mu_o \pi D l_{Fe}}{4g} \left(F_S^2 + F_R^2 + 2 F_S F_R \cos \beta \right). \tag{2.6}$$

The developed electromagnetic torque acts to minimize the stored air-gap energy by aligning the stator and rotor mmfs. Assuming an electromagnetic excitation which is independent of the rotor position, the developed torque can be written as follows [3]:

$$T_{em} = \left. \frac{\partial W}{\partial \beta} \right|_{F_S, F_R} = - \left(\frac{\mu_o \pi D l_{Fe}}{4g} \right) \left(2 F_S F_R \sin \beta \right). \tag{2.7}$$

For a machine having more than two poles, the developed electromagnetic torque is scaled upward by the number of pole pairs, $\left(\frac{P}{2}\right)$, which yields:

$$T_{em} = - \left(\frac{P}{2} \right) \left(\frac{\mu_o \pi D l_{Fe}}{2g} \right) F_S F_R \sin \beta. \tag{2.8}$$

The above equation can be expressed in different forms that are more suitable to the analysis of a specific electric machine i.e. dc, ac synchronous or ac induction. In the context of this work, it is more appropriate to express the developed electromagnetic torque as a function of peak air-gap flux density established by the rotor excitation, B_R, and stator MMF as established by stator current sheet representing the mmf of the stator winding, F_S, as follows:

$$T_{em} = -\left(\frac{P}{2}\right)\left(\frac{\pi D l_{Fe}}{2}\right) F_S B_R \sin\beta. \tag{2.9}$$

Alternatively, (2.9) can be rewritten in terms of the electric (ampere) loading or linear current density, defined as the current density per unit length around mid air-gap periphery:

$$A_c = \frac{2mN_{ph}(I_{ph}/a)}{\pi D} = \frac{I_s}{\tau_s} \tag{2.10}$$

where, m, is the number of phases, N_{ph}, is the number of turns per phase, I_{ph}, is the rms value of the phase current, a, is the number of parallel paths per phase, I_s, is the current per stator slot, and, τ_s, is the slot pitch. Geometrical parameters used in the definition of the linear current density, A, are provided in Fig. 2.2. For a three-phase winding, the linear current density is related to the magnitude of the fundamental component of the stator MMF, $F_S = F_1$, as follows [3, 80]:

$$F_1 = \frac{3}{2}\left(\frac{4}{\pi} k_{w1} \frac{N_{ph}}{aP} \sqrt{2} I_{ph}\right) = \sqrt{2} k_{w1}\left(\frac{A_c \pi D}{P}\right) \tag{2.11}$$

where, k_{w1}, is the winding factor corresponding to the fundamental component of the stator MMF. The torque expressed in terms of both the electric and magnetic loadings, A and B_R, is thus given in (2.12), below:

$$T_{em} = -\sqrt{2} k_{w1} A_c B_R \sin\beta \left(\frac{\pi D^2 l_{Fe}}{4}\right) = -\sqrt{2} k_{w1} A_c B_R \sin\beta \,(\text{Rotor Volume}) \tag{2.12}$$

where, $\left(\frac{\pi D^2 l_{Fe}}{4}\right)$ is the rotor volume, A_c, is the value of the stator rms current loading,

and, B_R, is the peak air-gap flux density produced by the rotor excitation. The expression provided in (2.12) gives an alternative view of the torque production in the air-gap of an electric machine. Shown in Fig. 2.3 is the graphical representation of the tangential force produced by the interaction of the radial flux density and the infinitely thin current sheet established by the stator currents on the inner stator surface facing the air-gap. In the ideal case, where both stator and rotor surfaces are smooth cylinders, and are infinitely permeable, the magnitude of the tangential air-gap field intensity, H_t, on the surface of the stator is equal to $\sqrt{2}k_{w1}A_c$. Considering Fig. 2.3, one should also note that the stator currents are responsible for the tangential air-gap field component, the interaction of which with the radial field component produces a tangential air-gap sheer stress and consequently a useful torque.

Finally, the developed electromagnetic torque can be related to both the air-gap flux density and conductor current density, J. Here, the conductor current density can be defined in terms of the phase current, I_{ph}, and the basic coil dimensions as:

$$J = \frac{I_s}{\text{Copper Area}} = \frac{N_{ph}(I_{ph}/a)}{\text{Copper Area}} \tag{2.13}$$

where, with consideration of Fig. 2.2, the copper area can be defined as $(w_{Cu}h_{Cu})$. Alternatively defining the slot-fill as the ratio of total slot area to the effective area occupied by the conductor:

$$s_f = \frac{\text{Copper Area}}{\text{Slot Area}} = \frac{w_{Cu}h_{Cu}}{w_s h_s} \tag{2.14}$$

the current density can thus be defined as follows:

$$J = \frac{I_s}{s_f(\text{Slot Area})} = \frac{N_{ph}(I_{ph}/a)}{s_f(\text{Slot Area})} \tag{2.15}$$

where, considering the example of a simple slot shown in Fig. 2.2, the slot area can be defined as $w_s h_s$. Using (2.10), the conductor current density, J, can be expressed in terms

of the linear current density, A_c, as follows:

$$J = \frac{A_c \tau_s}{\text{Copper Area}} = \frac{A_c \tau_s}{s_f(\text{Slot Area})} \tag{2.16}$$

Practical ranges for the electric loading and magnetic loading are constrained by the properties of the materials that are used in the construction of electric machines. Conductor current density, and consequently electric loading, is limited by the temperature rise of the insulation system and is heavily dependent on the thermal management system of the machine (cooling means, such as fan, liquid, etc.). On the other hand, the air-gap flux density is mostly limited by the saturation characteristics of the magnetic steels used in the construction of the electromagnetic core, and to a lesser degree by the amount of induced core losses that can be removed from the machine volume.

Typical electromagnetic loading ranges are provided in Tables 2.1 and 2.2. Considering electric loading, it should be noted that typical ranges for the values provided in Table 2.1 are highly dependent on the machine dimensions and cooling system. For example, conductor current densities are expected to be higher for smaller machines, while linear current densities are normally higher for larger machines that have large air-gap diameters and rely on more sophisticated thermal management systems, such as hydrogen cooling and liquid (water or oil) cooling. In principle, to establish an envelope for the safe and reliable machine operation in terms of its thermal performance, selection of the electric loading should be accompanied by power loss and thermal analysis. Typical flux densities shown in Table 2.2 are highly dependent on operating conditions. Also provided in Table 2.2 are flux density values specific to the interior-PM rotor designs, namely, radial and tangential bridges.

The analysis presented in this section assumes infinitely permeable stator and rotor cores and a smooth air-gap. These assumptions also imply that no geometric and saturation induced saliencies exist in the magnetic circuit of the machine, which allows for the vectorial

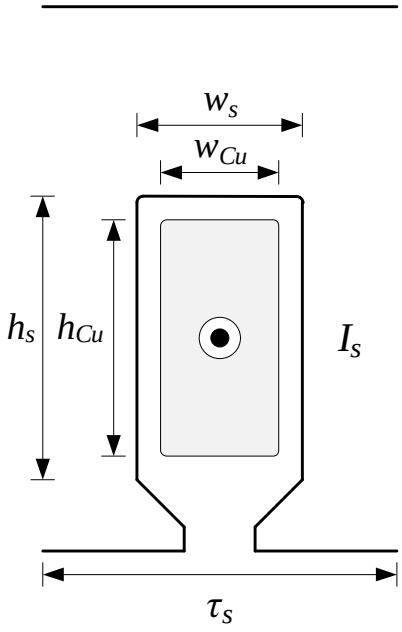

Figure 2.2: Dimensions used in the definitions of linear and surface current densities.

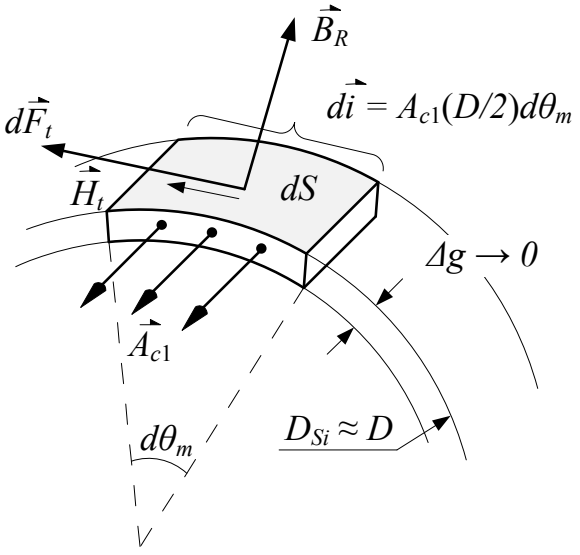

Figure 2.3: Tangential force produced in the air-gap of the electric machine.

Table 2.1: Typical rms values of electric loading for PMSM machines.

	Totally-enclosed	Air-cooled	Water-cooled
J [A_{rms}/mm^2]	2 - 5	4 - 7	6 - 30
A [A_{rms}/mm]	30 - 60	30 - 80	50 - 200

Table 2.2: Typical core flux densities in the various parts of the electric machine.

	Air-gap	Stator		Rotor		
		Tooth	Yoke	Yoke	Radial*	Tangential*
B [T]	0.5 - 1.2	1.3 - 2.0	0.5 - 1.5	0.5 - 1.5	> 2.0	1.0 - 2.0

* Radial and tangential bridges are specific to IPM rotor designs.

summation of the mmfs in (2.1). In principle, the analysis presented above can be extended to the nonuniform (salient) air-gap case, however, the general relationships between output torque and machine dimensions will be preserved. In the context of this work, due to the inherent oversimplifications assumed in (2.1) - (2.12), these expression are not implicitly used in the design procedure. In the proceeding chapters, the electromagnetic analysis is carried out using nonlinear FE-based solvers that eliminate most of the uncertainties typically present in the analytical formulations given above.

2.2.1 Selection of Poles and Slots

In this section criteria for selection of number poles and slots for sinusoidal current regulated PM AC motors will be discussed. Both integer-slot and fractional-slot combinations are commonly used in the construction of PM ac machines. This section will focus on the slot-pole combinations considered throughout the project, it should be pointed out that by no means is this an exhaustive review of a broad topic. It should be noted that when PM ac machines are considered, selection of slots and poles along with specifics of the winding design represent an active ongoing research area with continued contributions to the state-of-the-art.

Traditionally, both integer-slot and fractional-slot motors were used in the construction

of PM ac machines. The number of slots per pole per phase is defined as:

$$q = \frac{N_s}{mP} \tag{2.17}$$

where, N_s, is the number of slots, P, is the number of poles, and m, is the number of phases. The winding is referred to as an integer-slot type if q is an integer number. Otherwise, the winding is referred to as a fractional-slot type. An attractive class of fractional-slot windings with the number of slots per pole per phase less than or equal to $\frac{1}{2}$, $q \leq 0.5$, allows for single tooth wound windings. Two specific types of slot-pole combinations are investigated in the context of this work:

- integer-slot windings with $q \geq 1$,
- fractional-slot concentrated tooth wound windings with $q \leq 0.5$.

The winding factor, k_w, is defined as the product of distribution factor, k_d, pitch factor, k_p, and skew factor, k_s:

$$k_w = k_d k_p k_s \tag{2.18}$$

and is used to describe a winding which is distributed into discrete slots. Harmonic pitch (or cording) factor, k_{pn}, and skew factor, k_{sn} are defined for the n^{th} harmonic as follows:

$$k_{pn} = \sin\left(\frac{n\beta}{2}\right), \tag{2.19}$$

$$k_{sn} = \frac{\sin\left(\frac{n\rho}{2}\right)}{\frac{n\rho}{2}}, \tag{2.20}$$

where, β, is the pitch angle of the coil (coil span in electrical radians), and ρ, is the skew angle in electrical radians also. Here, these factors in equations (2.19) and (2.20) are valid for both integer-slot and fractional-slot machines. On the other hand, the calculation of the distribution factor, k_d, for both integer-slot and fractional-slot machines can best be accomplished using the winding layout and individual coil phasor diagrams. Several

methods for winding design specific to fractional-slot machines are provided in [81–84]. In addition, several software packages developed to assist in the winding design and analysis are available in [85,86]. Recent contributions to the state-of-the-art include design of multi-layer (more than two) fractional-slot windings proposed by several authors in [87–90].

Integer-slot windings, in general, offer highest values of winding factors and typically can benefit from existing and well developed induction motor winding practices and manufacturing equipment. However, the resulting long and overlapping end windings as well as the low values of attainable slot fills associated with integer-slot windings should be carefully considered. Practical fractional-slot tooth wound (concentrated windings), in general, offer reduced length non-overlapping end windings, increased slot fill and overall simplicity of the winding. These qualities are beneficial for high efficiency and high volume production machines. However, the resulting low fundamental winding factors, associated rich harmonic content of the stator mmf and potential high core losses, should be carefully considered in the selection of fraction-slot windings. Some attractive slot-pole combinations may result in mmf sub-harmonics that can lead to significant rotor losses.

Example: comparing the mmfs of three 6-pole machines, one with 36-slot single-layer integer-slot winding, one with 18-slot single-layer integer-slot winding, and one with 9-slot double-layer fractional-slot winding is provided in Figs. 2.4, 2.5, and 2.6. Comparing the mmf profiles of Figs. 2.4, 2.5, and 2.6, the increase of the harmonic content with the reduction in the value of the slots per pole per phase, q, should be noted.

A common approach is to begin the selection of the slot-pole combination based on the two parameters, namely, fundamental (synchronous) winding factor, k_{w1}, and the number of cogging periods per revolution. The number of cogging periods per revolution can be calculated from the machine slot-pole combination as follows:

$$N_{cog} = \frac{N_s P}{\gcd(N_s, P)} = \text{lcm}(N_s, P) \tag{2.21}$$

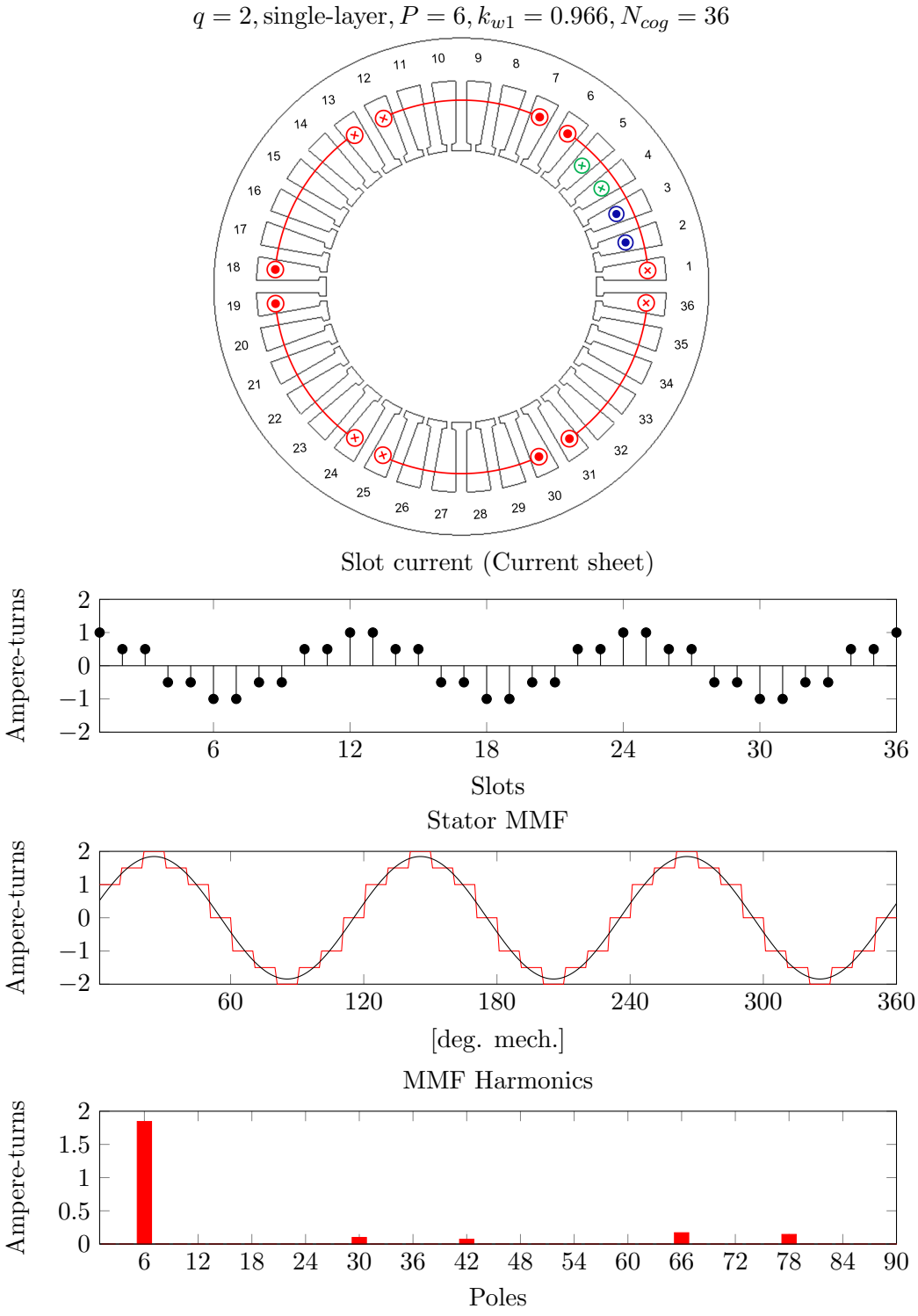

Figure 2.4: Stator MMF produced by 36-slot, 6-pole ($q = 2$) single-layer winding (waveforms are plotted for a time instant when $i_a = I_{max}$, $i_b = -\frac{1}{2}I_{max}$, $i_c = -\frac{1}{2}I_{max}$

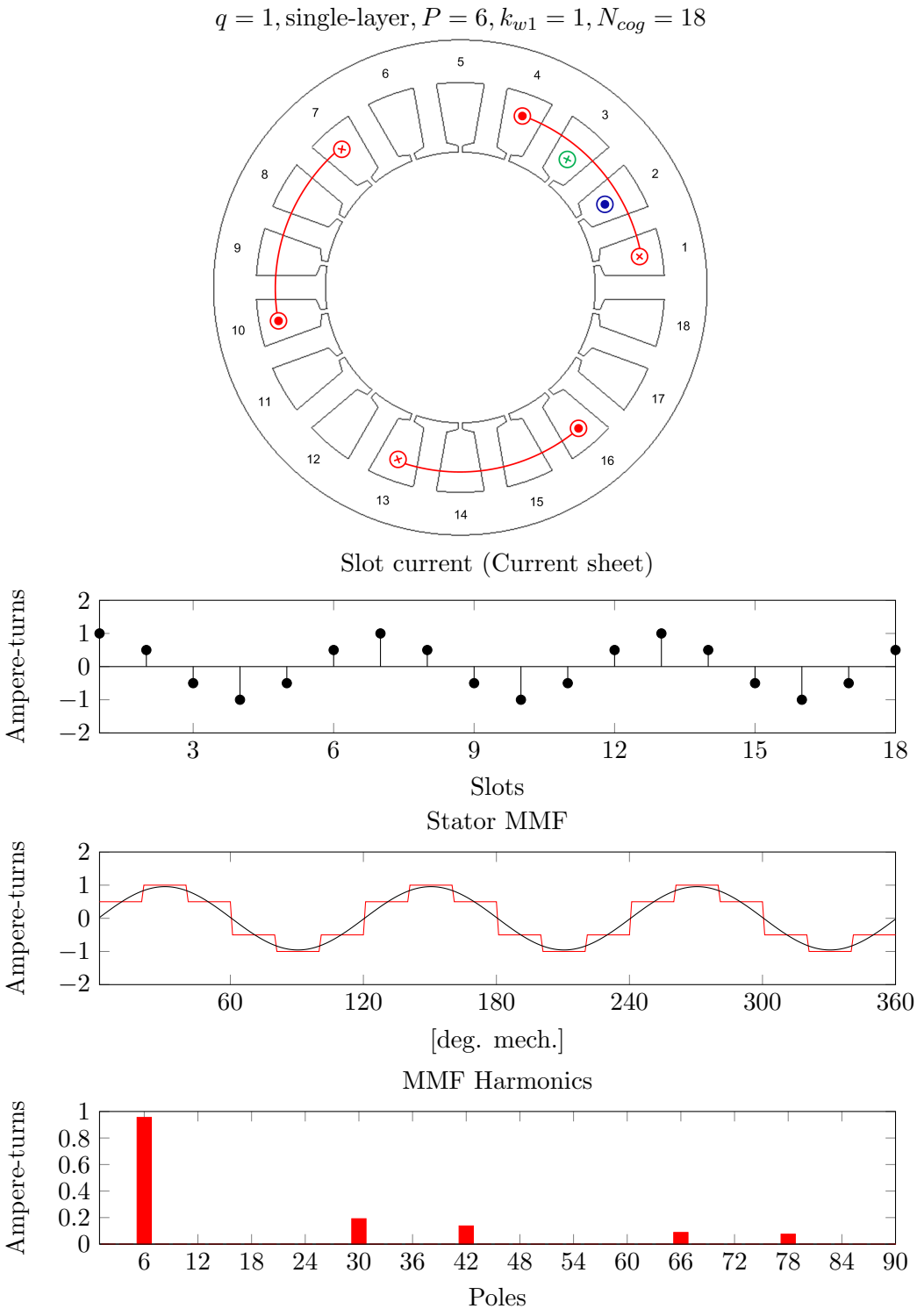

Figure 2.5: Stator MMF produced by 18-slot, 6-pole ($q = 1$) single-layer winding (waveforms are plotted for a time instant when $i_a = I_{max}$, $i_b = -\frac{1}{2}I_{max}$, $i_c = -\frac{1}{2}I_{max}$

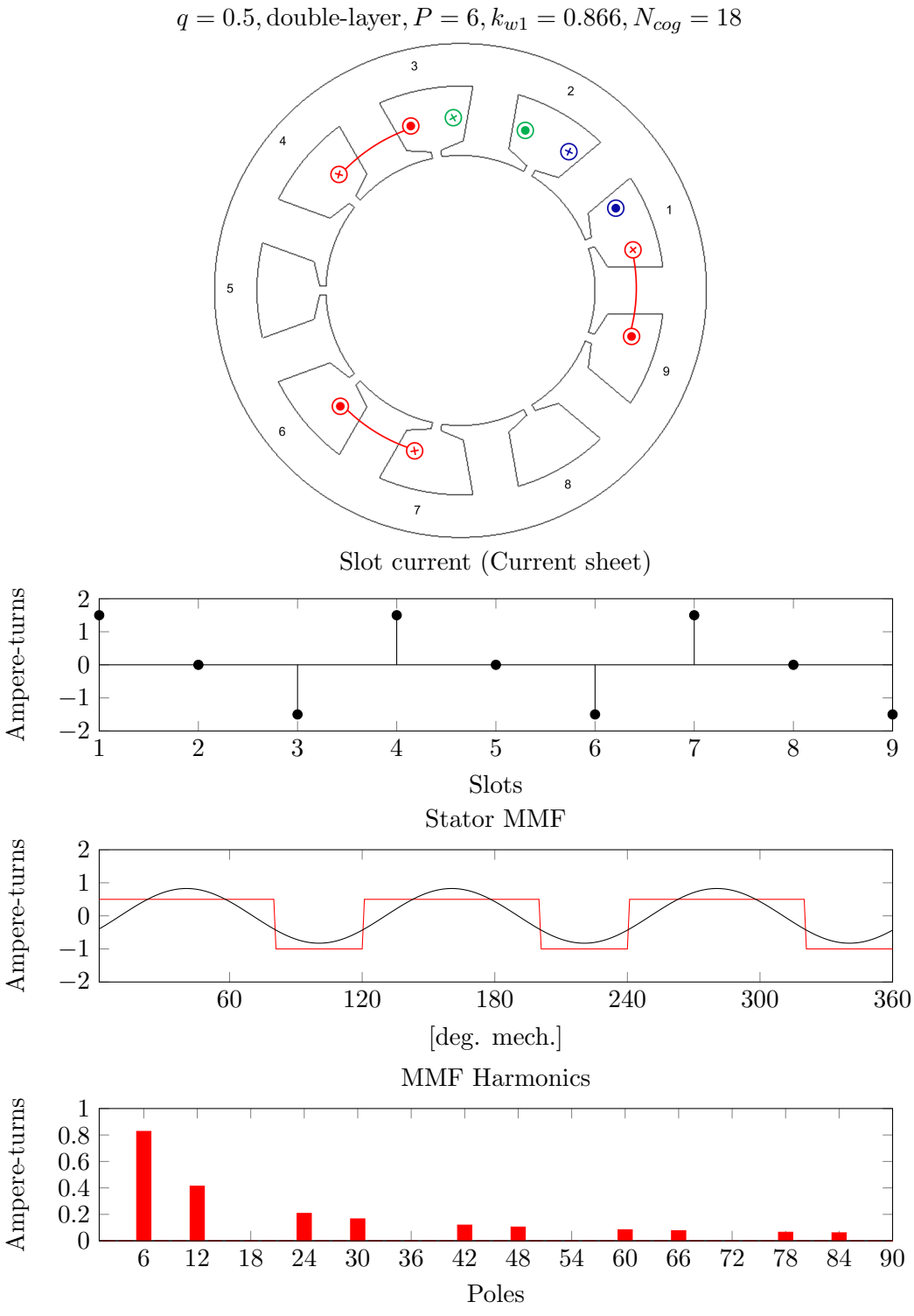

Figure 2.6: Stator MMF produced by 9-slot, 6-pole ($q = 0.5$) double-layer winding (waveforms are plotted for a time instant when $i_a = I_{max}$, $i_b = -\frac{1}{2}I_{max}$, $i_c = -\frac{1}{2}I_{max}$

The first parameter, k_{w1}, is indicative of how much of the PM flux links the stator winding, while the second parameter, N_{cog}, provides the number of cogging periods per revolution and is indicative of the torque quality. Common slot-pole combinations and their relation to these common parameters are provided in Tables 2.3 and 2.4. As mentioned earlier, when considering a specific fractional-slot tooth winding slot-pole combination, one needs to pay special attention to the secondary effects not considered in Tables 2.3 and 2.4.

For **example**, after inspection of Tables 2.3 and 2.4, a 12-slot, 10-pole motor appears to be an attractive option for low to moderate speed operation. With single-layer winding a 12/10 topology has a relatively high fundamental winding factor of 0.966. In addition, the number of cogging pulsations per revolution is 60, which indicates potentially good torque quality. However, considering the mmf waveforms produced by this type of the winding, one should notice a significant sub-harmonic corresponding to the number of poles equal to 2, as shown in Fig. 2.7. This mmf sub-harmonic will result in the 2-pole air-gap flux density component rotating at 5 times the synchronous frequency, which in turn will result in significant increase of the core and permanent magnet losses. An improvement to the 12-slot, 10-pole combination is obtained by rearranging the winding into a double-layer winding, which is shown in Fig. 2.8. Here the sub-harmonic is significantly reduced. Further improvements to the 12-slot 10-pole combination can be obtained by adopting a multi-layer winding (with more than two layers) as reported in [87–89]. Using the multi-layer winding the sub-harmonic can be completely eliminated if the number of turns of the center coil is selected to be equal to $\sqrt{3}$ of the auxiliary coils, see Fig. 2.9. However, as can be seen from Figs. 2.9 these improvements come at the cost of reducing the fundamental (torque producing) field component. Furthermore, additional slot and phase insulation required to support the multi-layer winding will inevitably lead to a reduction of the slot fill. Both, reduction of the fundamental winding factor, k_{w1}, and slot fill, s_f, will result in the reduction of the torque-density as should be observed from (2.12) and (2.17).

In the design of high performance machines, it is common to consider additional criteria

Table 2.3: Fundamental winding factors, k_{w1}, for various fractional-slot topologies. Where possible winding factors are reported for both single-layer and double-layer windings, number of slots per pole and phase is indicated as (q). Three integer-slot topologies considered in this work are included for reference.

Slots	Poles, P												
N_s	2	4	6	8	10	12	14	16	18	20	22	24	26
3	- - .866 (.5)	-	-	-	-	-	-	-	-	-	-	-	-
6	-	- - .866 (.5)	-	-	-	-	-	-	-	-	-	-	-
9	-	-	- - .866 (.5)	- - .945 (.375)*	- - .945 (.3)*	- - .866 (.25)†	-	-	-	-	-	-	-
12	-	-	-	- - .866 (.5)	.966 .933 (.4)†	-	.965 .933 (.286)†	- - .866 (.25)†	-	-	-	-	-
15	-	-	-	-	- - .866 (.5)	-	- - .951 (.357)*†	- - .951 (.313)*†	-	- .866 (.25)†	-	-	-
18	-	-	1.000 - - (1)	-	-	- - .866 (.5)	- - .902 (.429)†	- - .945 (.375)†	-	- - .945 (.3)†	- - .902 (.273)†	- - .866 (.25)†	-
21	-	-	-	-	-	-	- - .866 (.5)	-	-	-	-	-	-
24	-	.966 .933 (2)	-	-	-	-	-	- - .866 (.5)	-	.965 .933 (.4)†	.958 .949 (.363)†	-	.958 .949 (.308)†
27	-	-	-	-	-	-	-	-	- - .866 (0.5)	-	- - .915 (.409)†	- - .945 (.375)†	- - .954 (.346)†
30	-	-	-	-	-	-	-	-	-	- - .866 (0.5)	-	-	- - .936 (.385)†
36	-	-	.966 .933 (2)	-	-	-	-	-	-	-	- - .866 (0.5)	-	-

† Fractional-slot winding produces low pole count subharmonic.

* Fractional-slot winding produces unbalanced magnetic pull under normal operation.

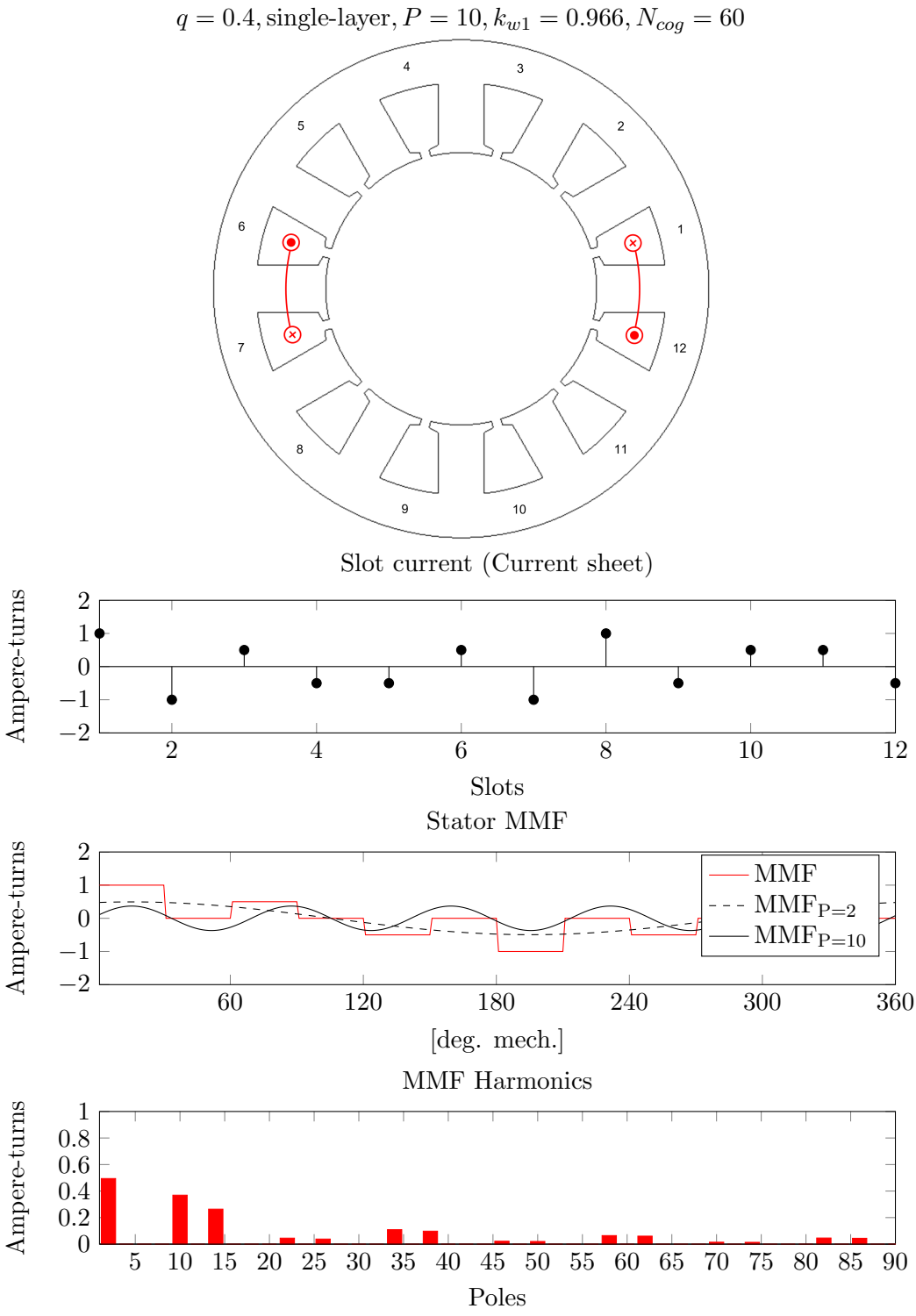

Figure 2.7: Stator MMF produced by 12-slot, 10-pole ($q = 0.4$) **single-layer** winding (waveforms are plotted for a time instant when $i_a = I_{max}$, $i_b = -\frac{1}{2}I_{max}$, $i_c = -\frac{1}{2}I_{max}$

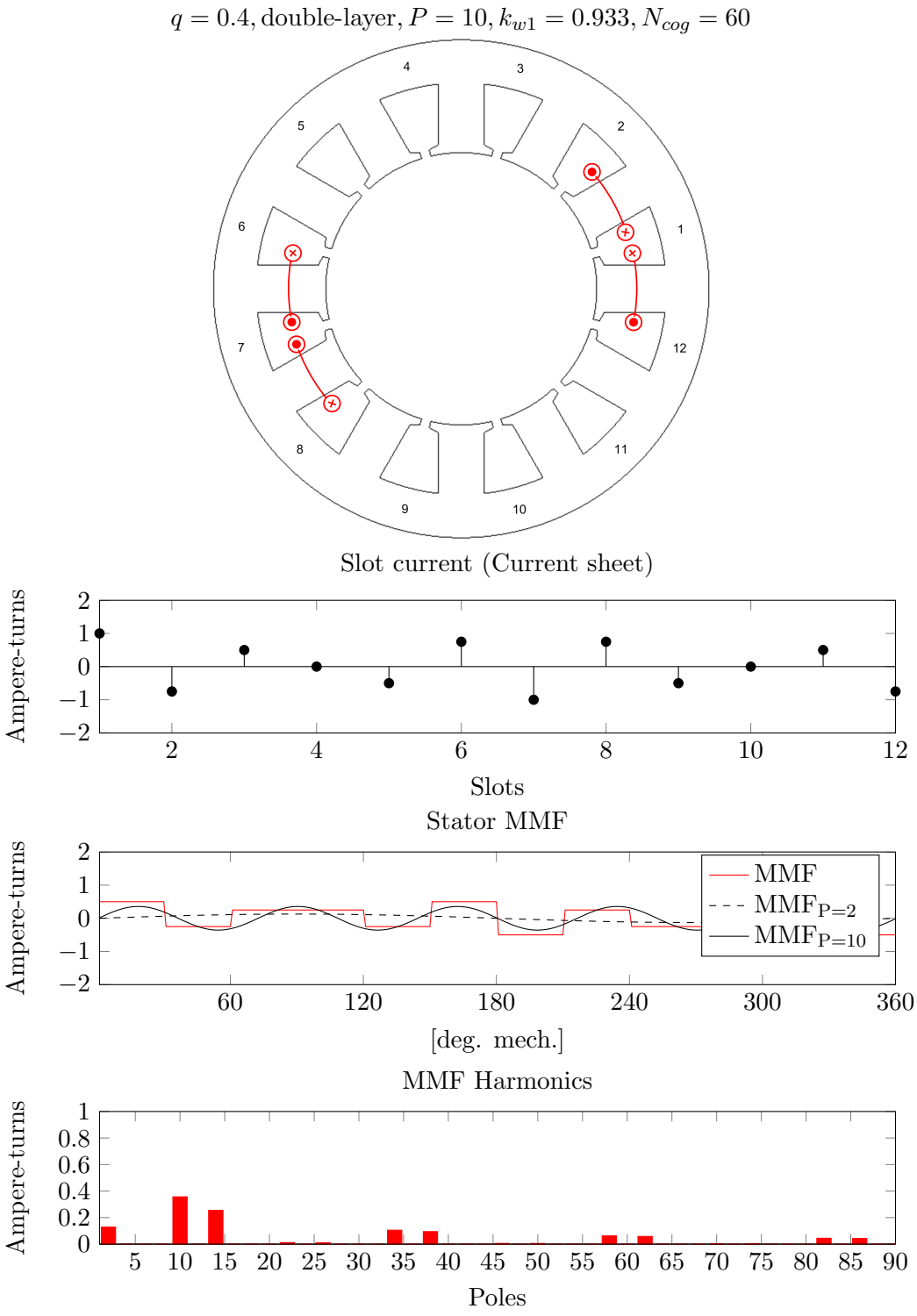

Figure 2.8: Stator MMF produced by 12-slot, 10-pole ($q = 0.4$) **double-layer** winding (waveforms are plotted for a time instant when $i_a = I_{max}$, $i_b = -\frac{1}{2}I_{max}$, $i_c = -\frac{1}{2}I_{max}$

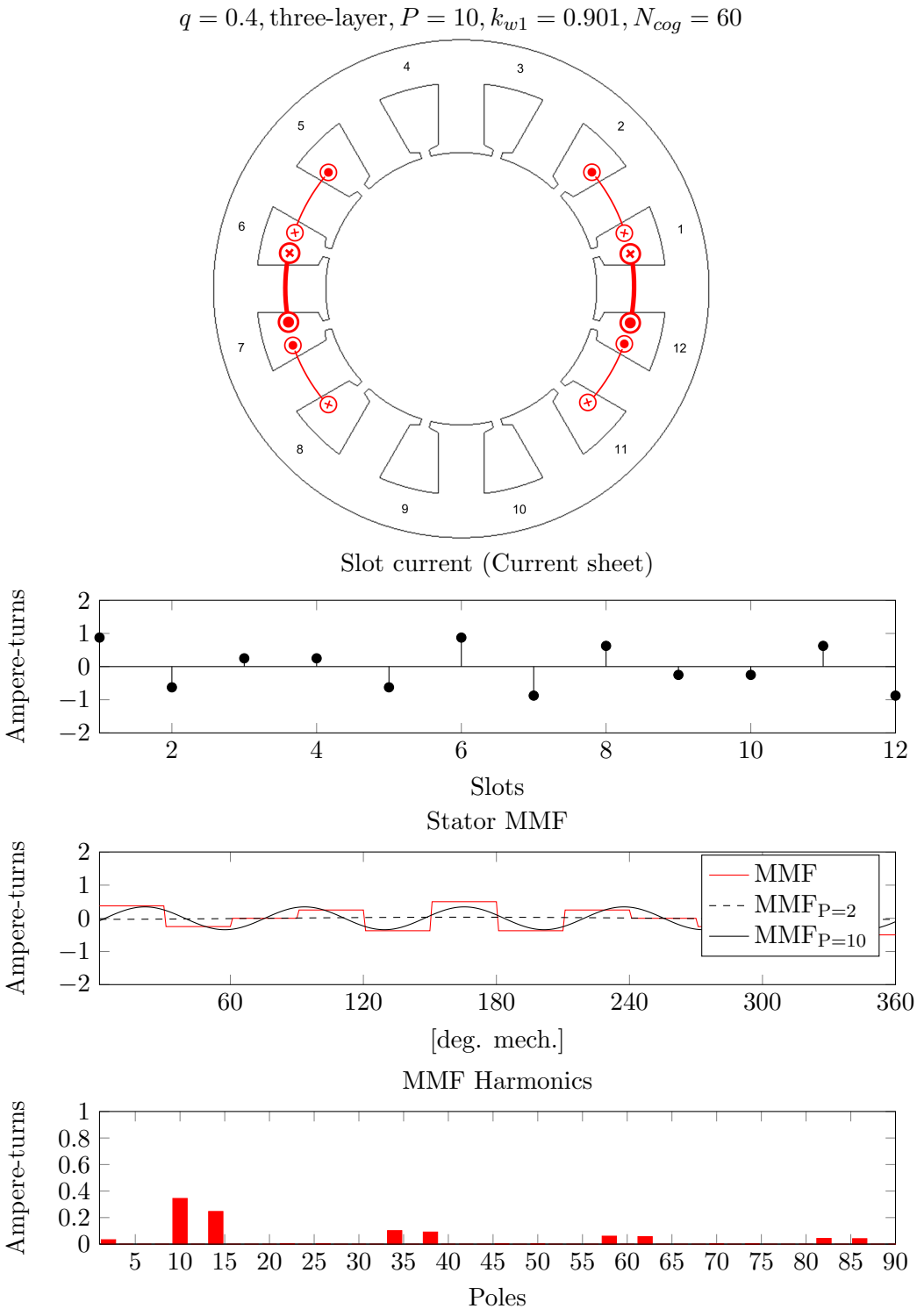

Figure 2.9: Stator MMF produced by 12-slot, 10-pole ($q = 0.4$) **three-layer** winding (waveforms are plotted for a time instant when $i_a = I_{max}$, $i_b = -\frac{1}{2}I_{max}$, $i_c = -\frac{1}{2}I_{max}$

Table 2.4: Number of cogging periods per mechanical revolution, N_{cog}.

Slots	Poles, P												
N_s	2	4	6	8	10	12	14	16	18	20	22	24	26
3	6	-	-	-	-	-	-	-	-	-	-	-	-
6	-	12	-	-	-	-	-	-	-	-	-	-	-
9	-	-	18	72*	10*	36	-	-	-	-	-	-	-
12	-	-	-	24	60*	-	84*	48	-	-	-	-	-
15	-	-	-	-	30	-	210*	240*	-	60	-	-	-
18	-	-	18	-	-	36	126*	144*	-	180*	198*	72*	-
21	-	-	-	-	-	-	42	-	-	-	-	-	-
24	-	24	-	-	-	-	-	48	-	120	264	-	312
27	-	-	-	-	-	-	-	-	54	-	594	216	702
30	-	-	-	-	-	-	-	-	-	60	-	-	390
36	-	-	36	-	-	-	-	-	-	-	-	72	-

* Fractional-slot winding produces unbalanced magnetic pull under normal operation.

such as vibrations and acoustic noise in the selection of slot-pole combinations [91–95]. In radial flux machines, the air-gap field has a significant radial component that results in radial air-gap stresses that are significantly larger than the tangential stresses that produce useful torque. The mode of the spatial distribution of the radial stress waveform is a function of the number of slots and poles. Examples of resultant instantaneous stator tooth forces for several slot-pole combinations, based on [75], are provided in Fig. 2.10. As can be seen from Fig. 2.10, selection of the number of slots and poles has a significant impact on the radial stator stress distribution. Considering the example of Fig. 2.10, machines with 12/10 and 9/6 slot-pole combinations produce resultant stator forces of modes 2 and 3, respectively. A motor with 9/8 slot-pole combination leads to an unbalanced force distribution and is not recommended for integral hp machines. In general, the mechanical structure of the stator is more susceptible to mechanical deformations resulting from stresses with low modes. If not properly mitigated, these deformations can lead to increased vibrations and acoustic noise during normal operation. Topologies that have inherently low radial force modes,

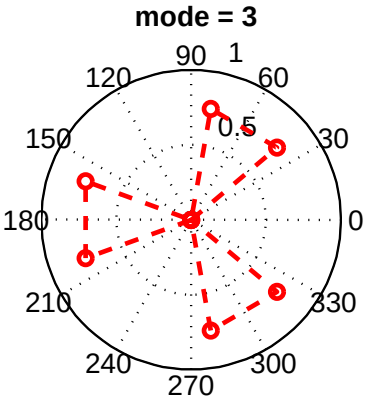

(a) 9-slot 6-pole ($q = 0.5$)

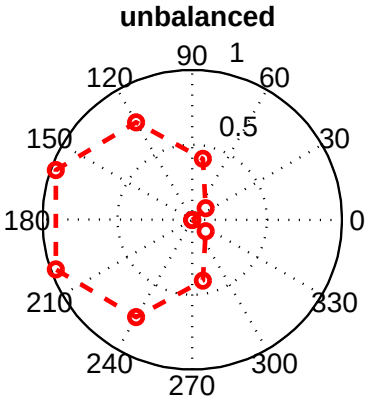

(b) 9-slot 8-pole ($q = 0.375$)

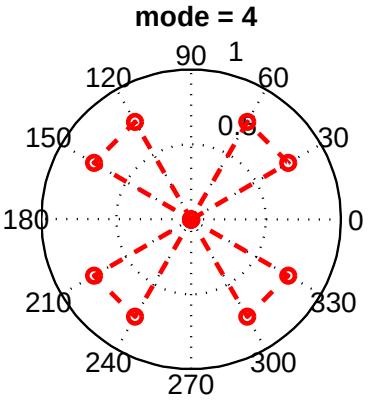

(c) 12-slot 8-pole ($q = 0.5$)

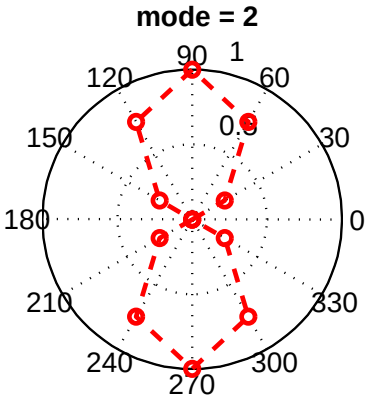

(d) 12-slot 10-pole ($q = 0.4$)

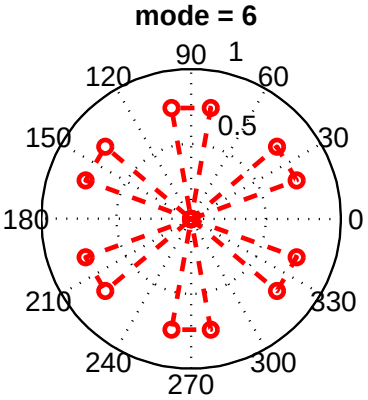

(e) 18-slot 6-pole ($q = 1.0$)

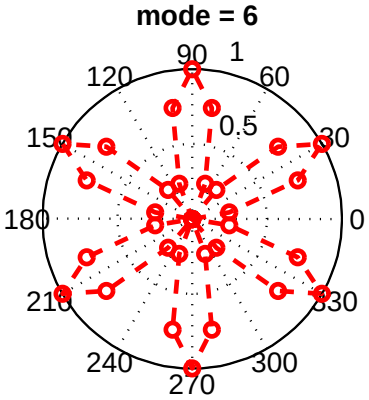

(f) 36-slot 6-pole ($q = 2.0$)

Figure 2.10: Instantaneous resultant stator tooth radial forces for integer-slot and fractional-slot topologies.

such as 12/10, may benefit from stator lamination designs with increased yoke thicknesses, closed stator slots, or other means of increasing stator structural stiffness that will reduce unwanted stator deformations and acoustic noise. It should be mentioned that these changes typically have a negative impact on torque density and cost.

2.2.2 Rotor Topologies

In permanent magnet machines, a wide selection of rotor topologies is available. Two main classes of machines can be identified based on the two basic rotor topologies, namely, surface permanent magnet (SPM) and interior permanent magnet (IPM) machines. Examples of rotor topologies belonging to the class of surface permanent magnet and interior permanent magnet machines are provided in Figs. 2.11 (a) and (b), and (c) through (f), respectively. An example of a generic SPM machine is provided in Figs. 2.11 (a). Torque quality (both cogging and on-load ripple) and emf distortion performance of the generic SPM motor can be improved by properly shaping (chamfering) the surface of the magnet such that it results in an air-gap flux density waveform that approximates a sinusoidal distribution using a topology of Fig. 2.11 (b). A shaped magnet of Fig. 2.11 (b) is in general more expensive since it requires additional material to support increased air-gap, and additional machining required to shape the magnet. Interior permanent magnet rotors are shown in Figs. 2.11 (c) through (f). These topologies offer potential benefits associated with the rotor saliency, an additional reluctance torque component, and improved field-weakening performance. Interior-PM rotors shown in Figs. 2.11 (c) and (d) benefit from simple magnet shapes and are typically used with high energy rare earth magnets. On the other hand, multi-layer and spoke IPM topologies shown in Figs. 2.11 (e) and (f) can take additional advantage of lower-cost alternative magnet materials such as bonded rare-earths and ceramic ferrites. Furthermore, rotor topologies shown in Figs. 2.11 (d), (e), and (f) have an additional design flexibility of providing the means of increasing the air-gap flux density by focusing (concentrating) the flux. It should be mentioned that Fig. 2.11 provides

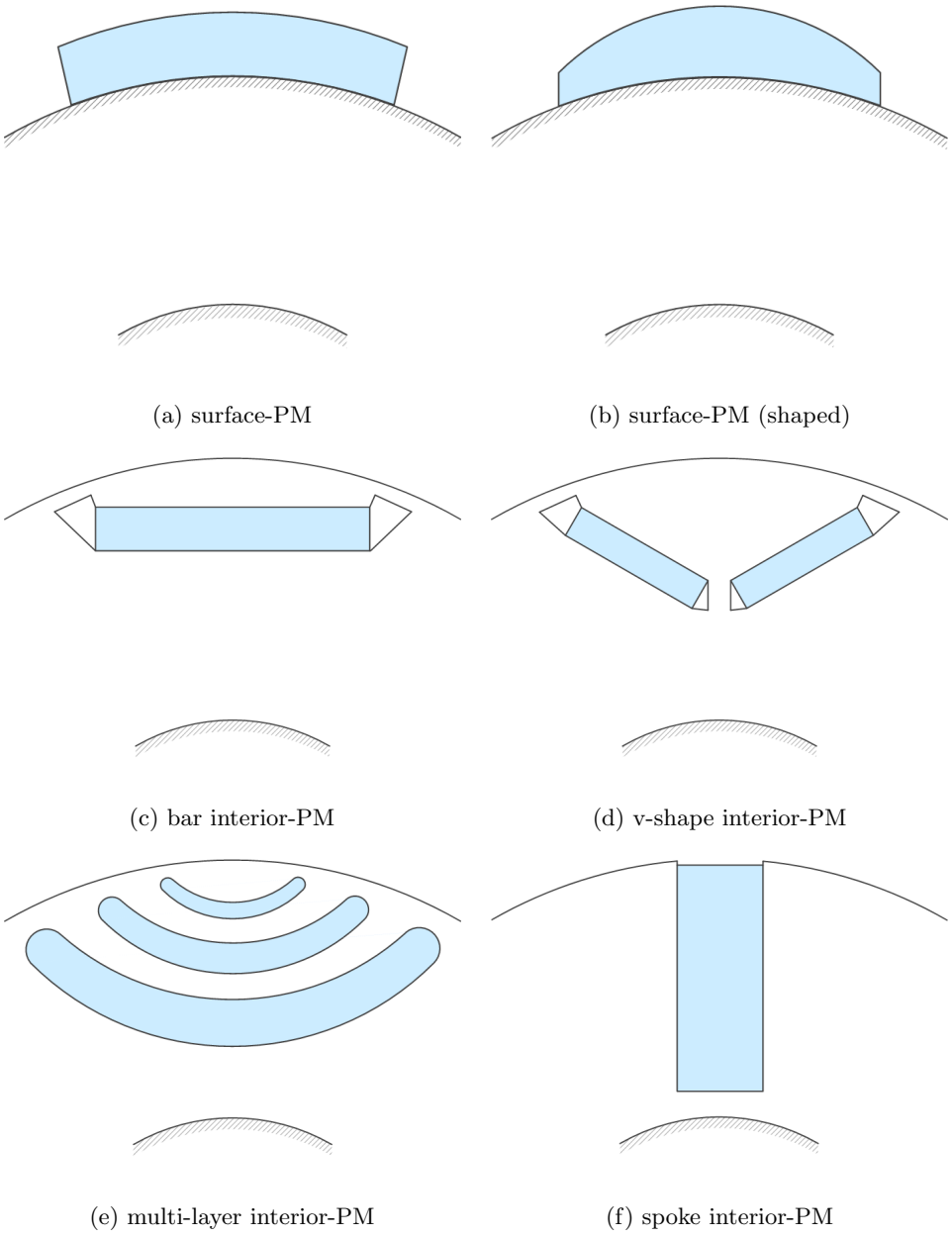

(a) surface-PM (b) surface-PM (shaped)

(c) bar interior-PM (d) v-shape interior-PM

(e) multi-layer interior-PM (f) spoke interior-PM

Figure 2.11: Surface-PM and interior-PM rotor topologies.

only a basic overview of a large number of rotor topologies that are available. Selection of the proper topology depends on the specific target application. For example, SPM motors are predominantly used in servo applications where torque linearity and quality are of high concern. On the hand, various IPM topologies are most commonly found in traction and industrial applications, where high-speed field weakening performance is of importance.

2.2.3 Slot Fill

Maximizing the amount of conductors (copper area) packed into the slot has beneficial effects in terms of minimizing winding ohmic, I^2R, losses and maximizing efficiency. In addition to lowering winding losses, tightly packing conductors into the slot improves thermal conduction between the coil and the core further improving thermal performance.

The slot fill factor, s_f, is defined as the ratio of the total cross-sectional area of the conductors (copper) in the slot, A_{Cu}, to the gross area of the slot, A_{slot}, as follows:

$$s_f = \frac{A_{Cu}}{A_{Slot}} = \frac{n_C \pi d_{Cu}^2}{4 A_{Slot}} \tag{2.22}$$

where, n_C, is the number of conductors in the slot, and d_{Cu}, is the copper conductor diameter. Alternatively, the gross slot fill can be defined as the ratio of the total area of the wire (including wire insulation), A_W, to the gross area of the slot, A_{slot}, as follows:

$$s_{fG} = \frac{A_W}{A_{Slot}} = \frac{n_C \pi d_W^2}{4 A_{Slot}} \tag{2.23}$$

where, d_W, is the diameter of the wire including the insulation film. The former definition (2.23) is the most useful as it is directly related to ohmic losses and conductor current densities. A graphical definition of the variables used in the calculation of the slot fills is provided in Fig. 2.12. Accurate calculation of the slot fill is a tedious task that involves complicated slot geometries and is highly dependent on the winding equipment, lamination design, and insulation system. Establishing theoretical slot fill limits for a given slot-

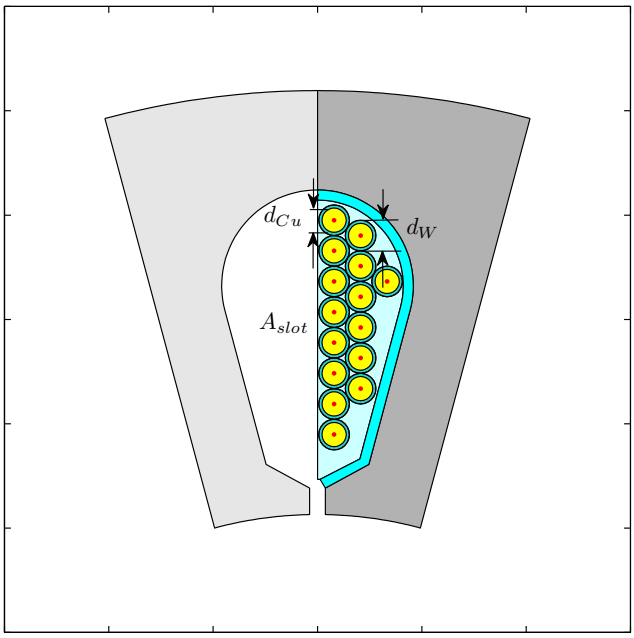

Figure 2.12: Definition of variables used in the calculation of the slot fill.

geometry and wire gauge is an important task in the design of high performance machines. The method used in this dissertation relies on the intuitive optimization approach that is based on the random perturbation of slot position with respect to a circular grid that represents a tightly packed coil. The objective of the random search is to maximize the number of conductors of a given diameter that can be packed in the slot. A pseudo code for the search algorithm is provided below. An example output of the algorithm for several

Algorithm 1 Maximize Number of Conductors in the Slot

initialize circular grid G with circle diameter equal to wire diameter
for $n = 1 \rightarrow$ iterations **do**
  perturb slot position by a small random offset, δ_{xy}, $S_p = S + \delta_{xy}$
  find all complete conductors in the slot, $C = S_p \bigcap G$
  determine number of conductors in the slot, $n_C = \text{size}(C)$
  if $n_C > n_{Cmax}$ **then**
    $n_{Cmax} = n_C$
  end if
end for

common slot topologies is provided in Fig. 2.13. Typical slot fill ranges attainable with random wound coils are 0.35 to 0.5, and 0.3 to 0.45, for single-layer windings and double-layer windings, respectively.

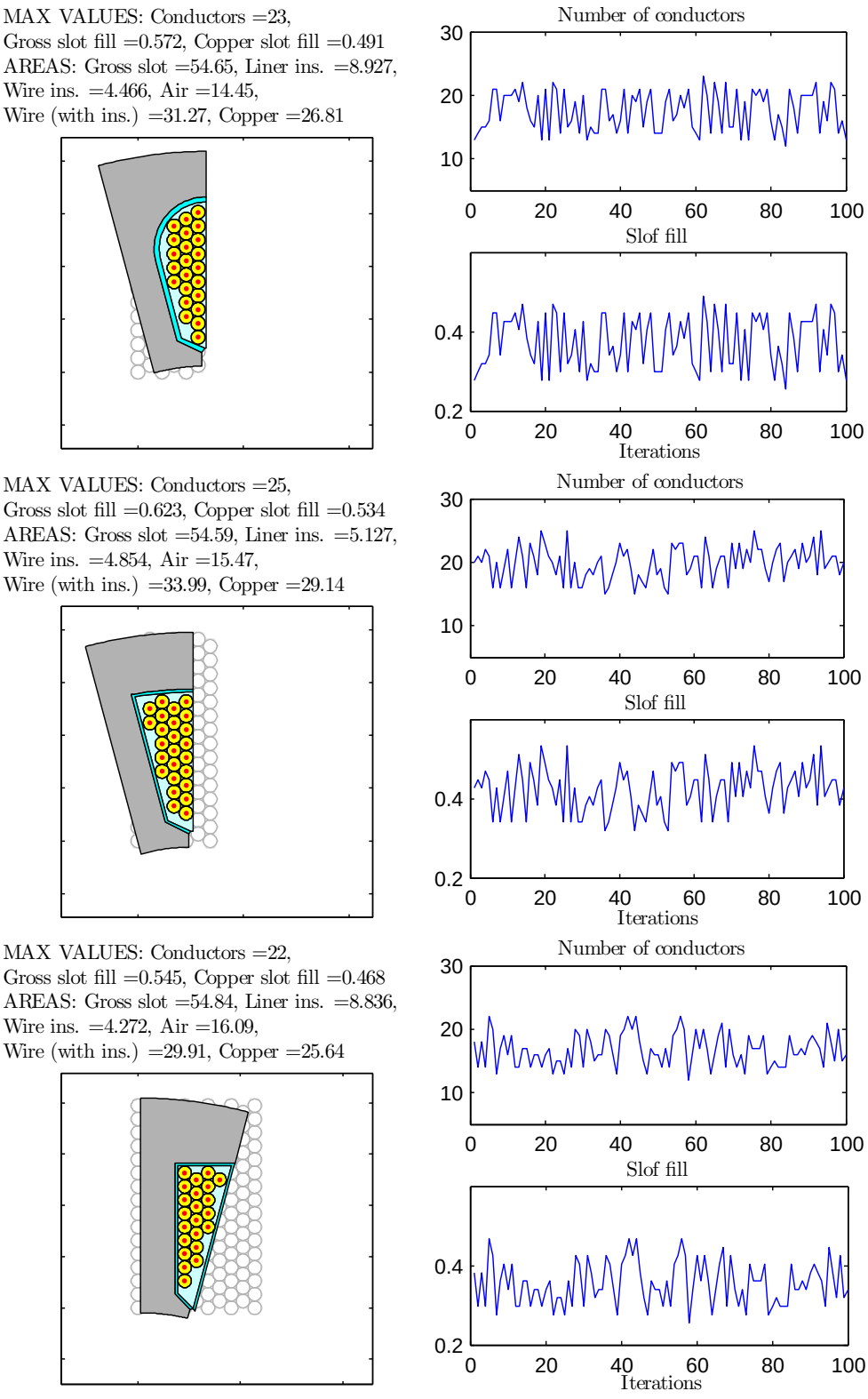

Figure 2.13: Examples of maximum slot fill search for several commonly used slots.

2.3 Machine Losses and Efficiency

Electric machine losses lead to practical performance limitations related to temperature rises of the insulation and permanent magnet systems. Efficiencies attainable in electric machines are mainly limited by the electric (conductor) and magnetic materials used to carry electric currents and magnetic fluxes, respectively. Therefore, understanding and quantifying the main loss mechanisms in such materials is crucial in the design of high performance electric machinery.

2.3.1 Winding Losses

Ohmic losses in the stator winding depend on the winding *rms* current and resistance. Winding *dc* resistance per phase can be calculated using the basic geometric parameters related to the stack length, l_s, mean end winding (end-turn) length, l_{end}, and wire diameter, d_{Cu}, as follows:

$$r_{dc} = \frac{2(l_s + l_{end})N_{ph}}{\sigma A_{Cu} a^2} = \frac{8(l_s + l_{end})N_{ph}}{\sigma \pi d_{Cu}^2 a^2} \tag{2.24}$$

where, N_{ph}, is the number of turns per phase, σ, is the conductivity of the conductor material (typical value for copper at 20^oC is 58MS/m), and a is the number of parallel paths per phase. It should be mentioned that determination of the mean end winding length involves a degree of uncertainty associated with the specifics of the winding manufacturing process. Where possible it should be calibrated with respect to measurements acquired from existing designs. For a temperature rise of ΔT above room temperature, T_o, the winding resistance per phase can be calculated as follows:

$$r_{dc_{hot}} = (1 + \alpha_{Cu}\Delta T) r_{dc_{cold}} \tag{2.25}$$

where, α_{Cu}, is the temperature coefficient of the conductor material (typical value for copper is $0.4041\%/^\circ K$). For a three phase machine, the total armature winding losses can

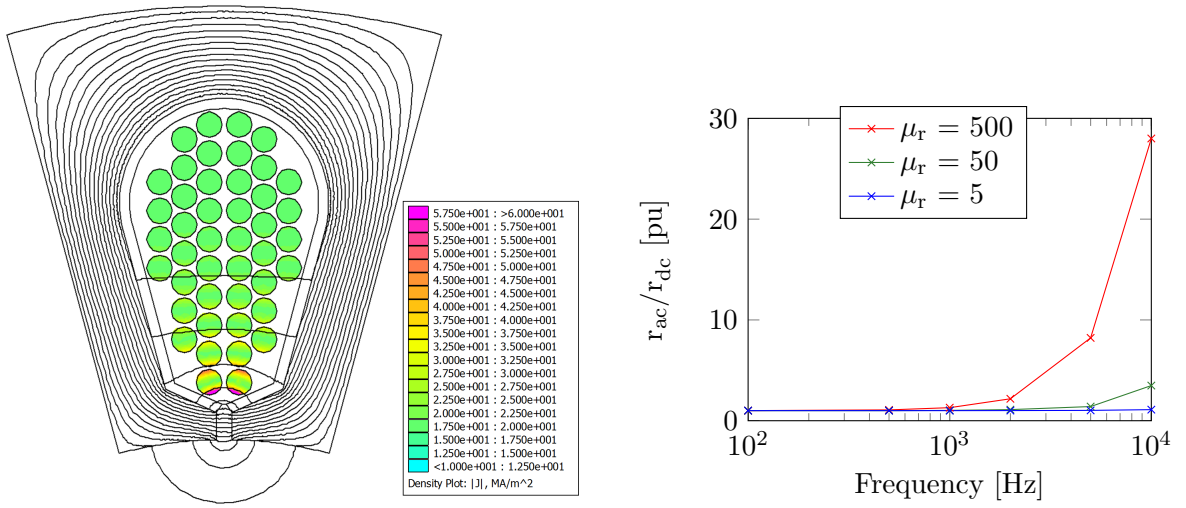

(a) Harmonic FE solution of semi-closed slot (16AWG conductors, supply 1kHz).

(b) Variation of winding *ac* resistance as a function of excitation frequency and core permeability.

Figure 2.14: Winding resistance - high frequency skin and proximity effects.

be calculated using the following:

$$P_{Cu} = 3I_{rms}^2 r_s \tag{2.26}$$

where, r_s, is the winding resistance per phase computed at the correct operating temperature. In addition to the loss in the *dc* component of the resistance, the armature winding will contain frequency dependent losses that are related to the skin and proximity effects of conductors of finite diameter placed in alternating magnetic fields. While leakage fields in the slots of an electric machine are typically small, their frequencies can be significantly high, especially for high speed machines and machines excited with PWM drives. Fig. 2.14 (a) shows the effect of alternating slot leakage on the flux and current density distributions within a commonly used semi-closed slot with 16AWG conductors. Elevated current densities in the vicinity of the slot opening that result from alternating leakage fluxes should be noted. In addition, shown in Fig. 2.14 (b) is the frequency dependent increase of the *ac* resistance, r_{ac}. Results provided in Fig. 2.14 were obtained using a linear harmonic (*ac*) FE solver and are shown for several values of lamination permeability, μ_r. It should be

noted that for the specific example provided in 2.14, the *ac* resistance increases by a factor of 1.3 for 1000Hz, and 28 for 10,000Hz. Considering the example of Fig. 2.14, one should note that high frequency induced ohmic losses are highly dependent on the following:

- slot-opening dimensions,
- conductor diameter and transposition within the slot,
- winding inductance (that provides smoothing of PWM current ripples).

2.3.2 Core Losses

Electromagnetic core losses induced by time-varying fields in laminated electric steels are typically calculated in the post-processing stage of the electromagnetic analysis and are based on the combination of calculated core flux density values and data obtained from loss measurements performed by manufacturers on lamination material samples. Measurements are typically performed at multiple frequencies in the range of 1Hz to 10kHz using an Epstein fixture [96]. Fig. 2.15 shows an example of loss data for electric steel typically used in the construction of industrial electric machines designed to operate in low-to-medium speed range, and shows the variation of core losses with flux density and frequency. Measured specific core loss data (see the example of Fig. 2.15) is fitted to a fixed coefficient Steinmetz expression that is given as follows, [97, 98]:

$$p_{Fe} = k_h f B^{\alpha} + k_e f^2 B^2 + k_a f^{1.5} B^{1.5} \tag{2.27}$$

where, k_e, is the eddy current loss coefficient, k_h, is the hysteresis loss coefficient and, k_a, is an excess loss coefficient used to improve the curve fitting process. The fixed coefficient model provided in (2.27) is limited to a narrow set of frequencies. An improvement to this classical model assumes that the hysteresis power coefficient, α, is equal to 2, the excess loss coefficient, k_a, to be equal to zero, and accounts for the loss coefficients' variation with

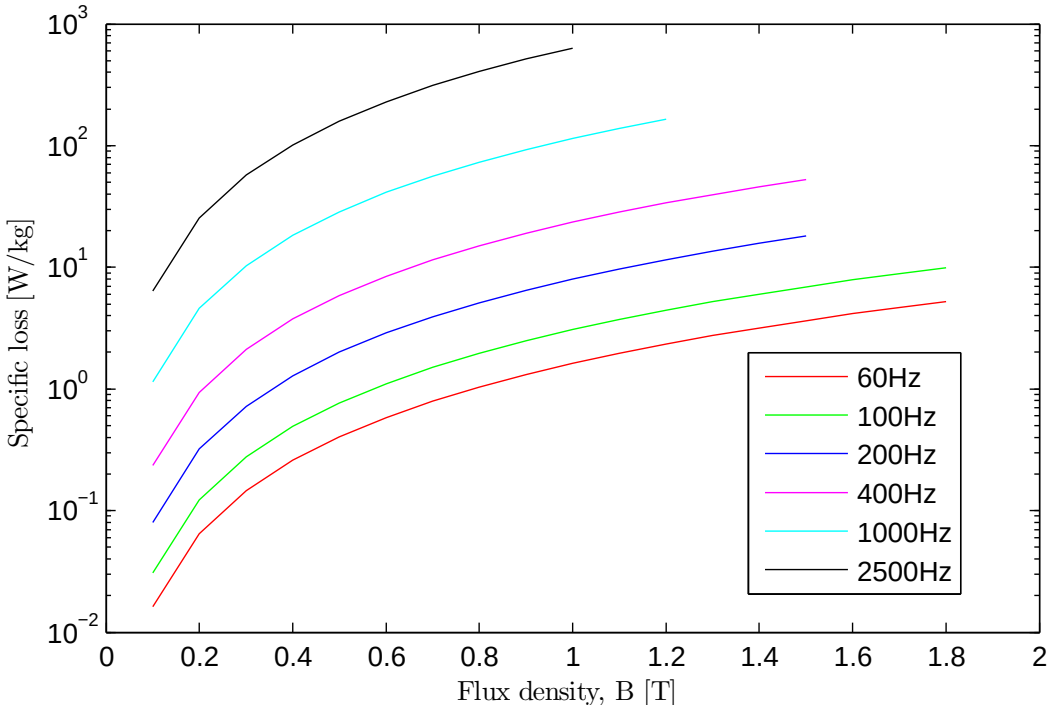

Figure 2.15: Specific core losses for laminated electrical steel M-19, 26-Ga.

both frequency and flux density by expressing these coefficients as $k_e(B, f)$ and $k_h(B, f)$, and thus the loss computation formula takes a general form as proposed in [98]:

$$p_{Fe} = k_h(B, f) f B^2 + k_e(B, f) f^2 B^2. \tag{2.28}$$

Dividing both sides of (2.28) by fB^2 results in the linear equation:

$$\frac{p_{Fe}}{fB^2} = k_h(B, f) + k_e(B, f) f. \tag{2.29}$$

Using (2.29) the variable loss coefficients ($k_e(B, f)$ and $k_h(B, f)$) can be determined from the specific core loss data measured at several frequencies. In this dissertation, the approach outlined in (2.28) and (2.29) is used for the calculation of the stator core losses.

Examples of radial and tangential flux density profiles in the various parts of an electric

machine (shown in Fig. 2.16) are provided in Fig. 2.17. Fig. 2.17 shows pulsating field components in the stator tooth and yoke (back-iron). On the other hand, tooth-yoke junction and tooth-tip regions experience both radial and tangential rotating (distorted elliptic) field components. It should be mentioned that in a typical machine stator teeth and yokes account for the majority of the core losses.

Loss measurements on electric steels used in the laminations of electric machinery are typically performed assuming *ac* pulsating field components. Improvements can be introduced by accounting for *dc* (constant) bias fields and incremental losses in the measurements. In addition, further improvements in the measurements are possible by accounting for the above mentioned rotational field components in the measurement [99, 100].

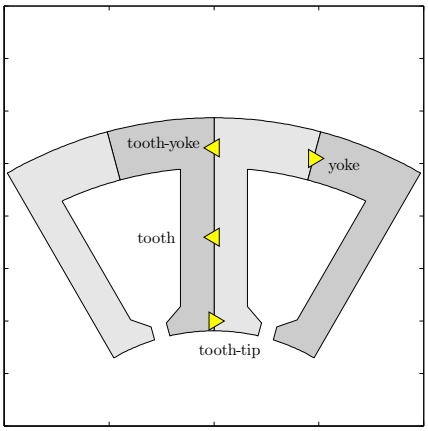

Figure 2.16: Location of stator flux density samples for Fig. 2.17

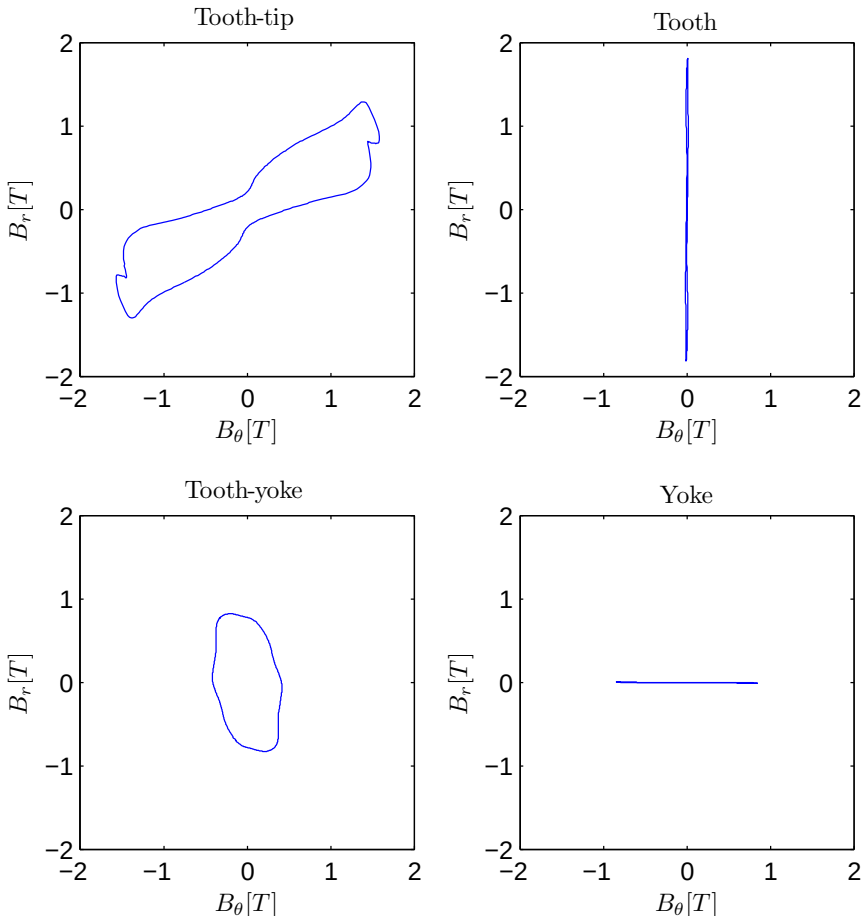

Figure 2.17: Radial and tangential stator core flux densities over a complete electrical cycle.

2.3.3 Solid (Magnet) Losses

Permanent magnet and other solid conductive structural component losses in the rotor are produced by alternating field components that are not synchronized to the rotor rotation. Permanent magnets are solid conductive materials with conductivities in the range of 0.67MS/m for sintered $Nd_2Fe_{14}B$ magnets, 1.18MS/m for sintered Sm_2Co_{17} magnets, and 2MS/m for Sm_1Co_5 magnets [101]. Alternating field components in the rotor structure can be attributed to permeance variation produced by stator lamination slotting (in semi-closed and open slots), space-harmonics produced by armature winding layouts (as shown previously in Figs. 2.4 — 2.9), and time-harmonics produced by either the power supply or a combination of the power supply-motor interaction. The eddy-current loss is the dominant loss component, while magnet hysteresis in the magnet material is typically considered insignificant. Components affecting permanent magnet and rotor losses are summarized below:

- permeance-harmonics due to stator slotting,
- space-harmonics produced by stator/armature winding (especially in fractional-slot machines),
- time-harmonics (PWM supply).

During the machine design process, permanent magnet losses are typically minimized through axial or circumferential magnet segmentation.

2.4 Motor-Drive Operation

A motor-drive system performance can be analyzed using a two axis dq motor model as shown in the phasor diagrams of Fig. 2.18. In Fig. 2.18 the d-axis is assumed to be aligned with the axis of magnetic north pole produced by a permanent magnet. Shown in Fig. 2.18 (a) is a motor operating with no demagnetizing d-axis current, which is typical

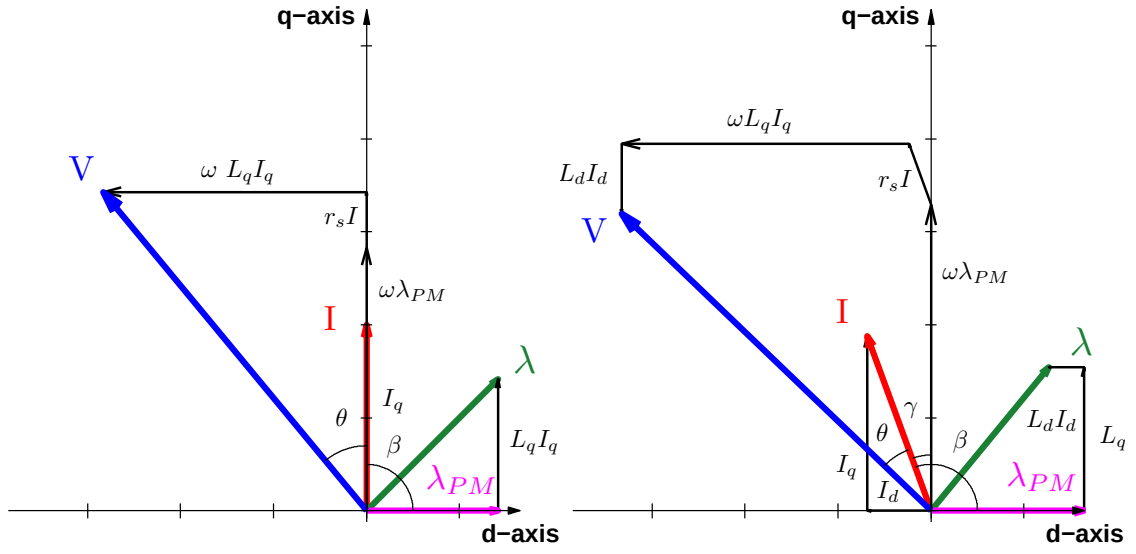

(a) surface-PM (b) interior-PM

Figure 2.18: *dq* phasor diagram of sine-wave current regulated motor-drive system operating in MTPA control.

for maximum-torque-per-amp (MTPA) operation of SPM motors. Shown in Fig. 2.18 (b) is a motor operating with a demagnetizing *d*-axis current component, which is typical for maximum-torque-per-amp (MTPA) operation of IPM motors [102], or field weakening operation of SPM motors.

Assuming no cross-saturation effects (no *dq* coupling effects), the steady-state *dq* flux linkages in the synchronous frame of reference can be written as follows [7]:

$$\lambda_d = \lambda_{PM} + L_dI_d \tag{2.30a}$$

$$\lambda_q = L_qI_q \tag{2.30b}$$

$$\boldsymbol{\lambda} = \lambda_d + j\lambda_q \tag{2.30c}$$

and the resulting terminal voltages can be found by accounting for the resistive voltage

drop as follows:

$$V_d = r_s I_d - \omega L_q I_q \tag{2.31a}$$

$$V_q = r_s I_q + \omega \lambda_{PM} + \omega L_d I_d \tag{2.31b}$$

$$\boldsymbol{V} = V_d + jV_q. \tag{2.31c}$$

Here, the motor current is given as:

$$\boldsymbol{I} = I_d + jI_q. \tag{2.32}$$

The angles shown in Fig. 2.18 are defined as, the torque angle, β, the current advance angle, γ, and the power factor angle, θ, respectively. The average electromagnetic torque can be computed using the following space vector cross product:

$$T_{em} = \frac{3}{2}\frac{P}{2}(\boldsymbol{\lambda} \times \boldsymbol{I}) = \frac{3}{2}\frac{P}{2}(\lambda_d I_q - \lambda_q I_d), \tag{2.33}$$

assuming a linear magnetic circuit and no dq cross-saturation effects implied in (2.30), the torque equation can be further expressed in terms of machine direct and quadrature axes inductances, L_d and L_q, and the permanent magnet flux linking the armature winding, λ_{PM}, as:

$$T_{em} = \frac{3}{2}\frac{P}{2}(\lambda_{PM} I_q + (L_d - L_q) I_d I_q). \tag{2.34}$$

the first term in equation (2.34) is attributed to the alignment torque produced by the interaction of permanent magnet field (flux) and armature field (magnetomotive force), while the last term is produced by the interaction of armature mmf and rotor saliency and is commonly referred to as the reluctance torque. In surface-PM machines, where $L_d \approx L_q$, the reluctance torque component is considered to be negligible, while in interior-PM machines the ratio of $\frac{L_q}{L_d}$ can be designed to maximize reluctance torque production.

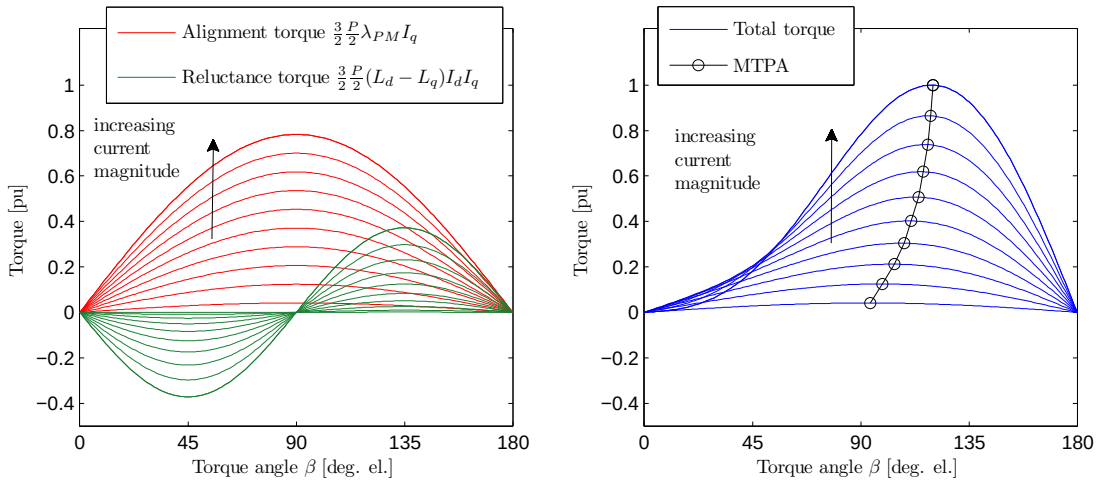

(a) magnet (alignment) and reluctance torque components.

(b) total electromagnetic torque and MTPA trajectory

Figure 2.19: Torque components of an interior-PM motor.

Therefore, interior-PM machines are considered to be a hybrid design between surface-PM and synchronous reluctance motors. Relationships between the electromagnetic torque and torque angle, β, for an interior-PM motor for several values of the current are shown in Fig. 2.19. As can be seen from Fig. 2.19 (a), interior-PM motor has an additional reluctance torque component that can be exploited by advancing the current vector past 90°. Also shown in Fig. 2.19 (b) is the total electromagnetic torque and the MTPA trajectory.

Interior-PM machines offer considerable design flexibility attributed to the selection of λ_{PM}, and $\frac{L_q}{L_d}$ and can be designed to fulfil a wide range of constant torque and constant power requirements. However, it should be noted that while equations (2.30) and (2.34) are useful for analysis of individual flux and torque components, in practical machine analysis their use should be limited. These expressions tend to oversimplify actual machine behavior that is complicated by saturation and dq cross-saturation effects. The expression in (2.33) is recommended when nonlinear effects need to be included in the analysis. Further improvements to the torque expression capturing torque components due to the instantaneous variation of stored magnetic energy can be included in (2.33), as will be discussed in more

detail in Chapter 3.

2.4.1 Drive Voltage and Current Limits

Considering a drive capacity, related to available dc-bus voltage and current rating of an inverter, a motor terminal voltage and current are limited to the following regions:

$$I_{lim} \geq \sqrt{I_d^2 + I_q^2}, \tag{2.35a}$$

$$V_{lim} \geq \sqrt{V_d^2 + V_q^2}, \tag{2.35b}$$

where, the voltage limit, V_{lim}, depends on the specifics of the modulator technology and modulation index limits used in an inverter. The inequalities in (2.35) imply that during normal operation the instantaneous values of the terminal voltages and currents have to remain within the limits imposed by the voltage and current ratings of an inverter supplying the machine. These limitations can be observed in Fig. 2.20, where the the current and voltage limit loci are plotted in the dq-current plane for several surface-PM and interior-PM machine-drive combinations. In a current regulated drive, terminal voltages depend on terminal currents, operating speed and motor parameters (inductances and resistances) as can be observed from (2.31). Therefore, the shape and location of the voltage limited locus in the dq-current plane depends on the specifics of the motor construction as can be observed by comparing Figs. 2.20 (a) and (c). Considering a surface-PM motor, Fig. 2.20 (a), the voltage limit locus at a given speed is mostly circular, while for an interior-PM motor, Fig. 2.20 (c), the voltage limit locus is mostly elliptical. In Fig. 2.20, the point (λ_{PM}/L_d) represents a demagnetizing current required to completely cancel the permanent magnet flux, λ_{PM}. The location of this point in the dq-current plane has a significance when designing motor-drive systems for constant power operation [62]. Examples of motor-drive systems with oversized inverters provided in Figs. 2.20 (b) and (d) can in principle achieve very wide constant power ranges.

In addition to the current and voltage limit loci provided in Fig. 2.20, there are the loci of constant torque operation. Also plotted in Fig. 2.20 are the MTPA trajectories. In Fig. 2.20, the MTPA operating condition represents the point on the constant torque locus that is closest to the origin. It is also possible to operate in the maximum-torque-per-volt (MTPV) region [103] extending the deep field weakening high speed operation of the motor-drive systems of Figs. 2.20 (b) and (d). In theory, the operating speed of an interior-PM motor-drive system can be extended indefinitely. However, in practice high speed operation is limited by core and permanent magnet losses, as well as by the mechanical constraints. Special care should be taken when operating machines at high speeds with high demagnetizing current components. At high speeds, increased losses and consequent thermal stresses along with high demagnetizing currents may lead to irreversible demagnetization of the permanent magnets. It also possible to operate in the maximum efficiency region by instantaneously optimizing the current vector position to minimize copper and core losses. Design of machines considered in this dissertation is concerned with operation in the constant torque region, therefore, MTPA operation is of most interest.

2.4.2 Current Regulation and Issues Related to PWM

High performance permanent magnet motor-drives require nearly instantaneous torque response. This is accomplished by introducing a closed-loop torque controller that regulates motor terminal currents to achieve fast torque response [104]. The rate of the instantaneous current (torque) change is limited by the available dc-bus voltage margin, motor inductance, controller gains, scan time of the control loop, and to a lesser extent by the ability of the mechanical drive-train to withstand fast changing acceleration torques without resonance or failure.

Practical means of ensuring proper operation of a motor-drive system during the design stage are concerned with: 1) winding design (selection of series turns per phase) with respect to the available dc-bus voltage on the motor side, and 2) the selection of the PWM switching

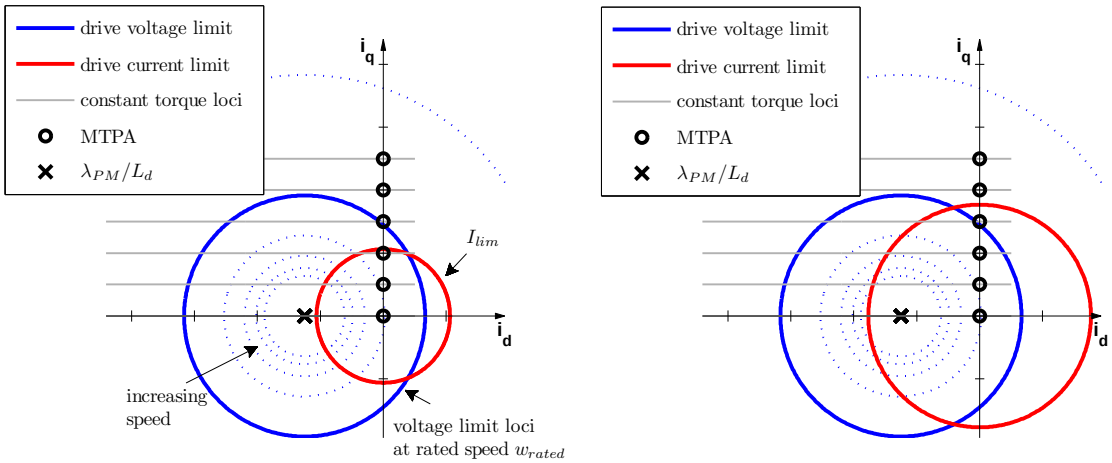

(a) surface-PM

(b) surface-PM with oversized inverter

(c) interior-PM

(d) interior-PM with oversized inverter

Figure 2.20: Voltage and current limited operation of sine-wave current regulated motor-drive system.

frequencies on the drive side to ensure good current waveform quality. Provided in Fig. 2.21 are typical terminal line-to-line voltage and phase current waveform profiles. Also shown in Fig. 2.21 are the loci of voltage space-vectors. Fig. 2.21 shows space-vector PWM (SVPWM) modulated waveforms in the linear modulation region with a typical value of switching frequency, f_{PWM}, set to 4kHz. On the other hand, the example of Fig. 2.22 shows operation of the SVPWM modulated inverter supplying a machine with low synchronous inductance operating at high speed and high modulation index. From Fig. 2.22, significant harmonic distortions in the current waveform should be noted. The elevated current ripple observed in Fig. 2.22 is a result of the reduced number of PWM pulses per fundamental current waveform cycle (or ratio f_{PWM}/f_s). This problem can be further exaggerated in surface-PM motors or motors designed for high speed operation that have inherently low synchronous inductances. The resulting PWM current ripple leads to elevated thermal stresses caused by additional eddy current losses in the laminated stator/rotor cores and permanent magnets. Resistance limited eddy current losses are proportional to the square of the field (flux density) magnitude and excitation frequency such as (f^2B^2) and may lead to significant machine loss increases at high speed if not properly managed.

In summary, in this chapter various aspects related to design of permanent magnet ac machines were discussed. Electric machine sizing equations based on electromagnetic loadings were presented. Design choices and guidelines related to selection of the motor layout (number of slots and poles), winding design and calculation of losses were presented. In addition, practical issues related to design of permanent magnet ac machines for motor-drive operation were discussed. In the next chapter the FEA-based computational method is detailed.

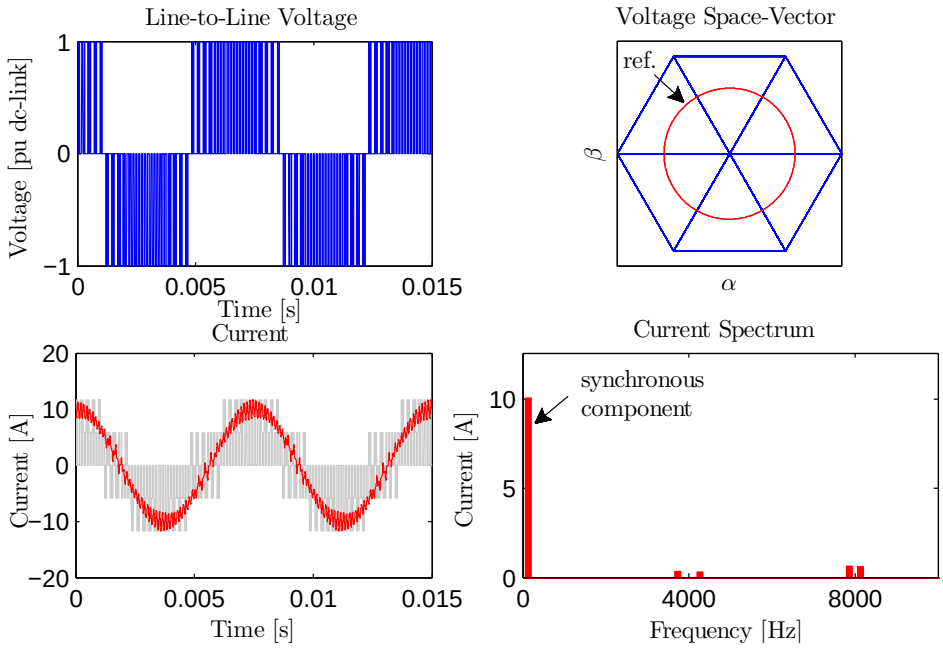

Figure 2.21: PWM line-to-line voltage and phase current profiles for motor-drive system operating in the linear modulation region at moderate speed ($\frac{f_{PWM}}{f_s} = 30$).

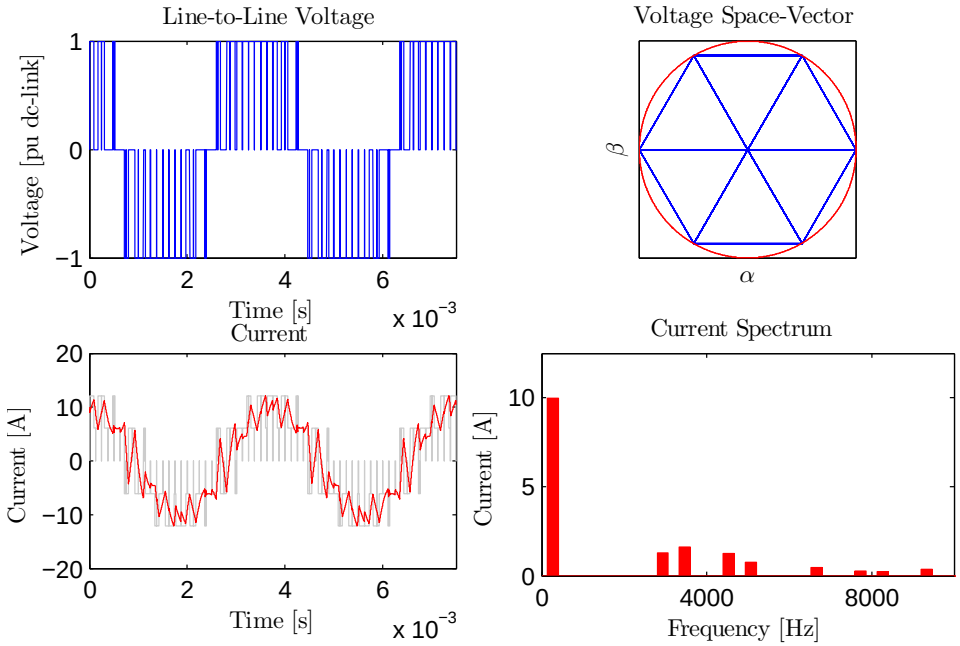

Figure 2.22: PWM line-to-line voltage and phase current profiles for motor-drive system operating the with a high modulation index at high speed ($\frac{f_{PWM}}{f_s} = 15$).

Chapter 3

Computationally-Efficient FEA of Synchronous Machines

3.1 Introduction

In this chapter, a computationally efficient method for finite element analysis of synchronous machines is presented and verified on several example interior permanent magnet machines. Computationally efficient - finite element analysis fully exploits the symmetries of electric and magnetic circuits of sine-wave current regulated synchronous machines and yields substantial savings of computational effort in comparison to full time-stepping finite element models for such machines. Machine performance is evaluated through Fourier analysis of constructed waveforms and a minimum number of magnetostatic solutions. The major steady-state performance indices (average torque, ripple and cogging torque, back emf waveforms, and core losses) are satisfactorily estimated as compared with the results of detailed time-stepping (transient) finite element analysis. Significant reduction of CPU simulation times is achieved (approximately two orders of magnitude) permitting a comprehensive search of large design spaces for machine design optimization purposes.

The machine is assumed to operate at steady-state conditions supplied with a balanced set of three-phase sinusoidal currents. The proposed approach relies on a 2D magnetostatic finite element formulation based on the following two dimensional Poisson's equation in the xy-plane [8, 9]:

$$\frac{\partial}{\partial x}\left(\frac{1}{\mu}\frac{\partial A}{\partial x}\right)+\frac{\partial}{\partial y}\left(\frac{1}{\mu}\frac{\partial A}{\partial y}\right)=-J-J_{PM} \tag{3.1}$$

where, μ, is the permeability, A, is the magnetic vector potential, J, is the conductor current density, and J_{PM}, is the equivalent current density used to model permanent magnet field excitation. It should be emphasized that in this 2D formulation the magnetic vector poten-

tial and the current density have only z-axis components, $A(x, y)$, and, $J(x, y)$, respectively. In this formulation, the magnetic field in the machine is computed at a successive number of rotor positions, in which the model is excited by instantaneous values of a set of sinusoidally time-varying currents. These instantaneous values correspond to a specific value of the load torque and rotor position. The instantaneous values of the rotor position, θ_m, and the phase currents, i_a, i_b, and i_c, are inputs to the model, and the magnetic vector potentials (MVPs), A, are the outputs, which are used in the post-processing stage to generate flux linkages, flux densities, back emfs, and energy/co-energy values. Conventional magnetic circuit periodicity conditions are used to reduce the size of the FE model required to analyze the machine operation under various load conditions. Further computational effort reductions are obtained by recognizing additional electric and magnetic circuit symmetries present in the machine as will be described next.

3.1.1 Electric Circuit Symmetry

For a three-phase synchronous machine operating under symmetrical steady-state load conditions, based on the electric and magnetic circuit symmetries, a single magnetostatic FE solution provides three equidistantly spaced (in time) samples of the average MVPs in the coil sides [32]:

$$A_{a+}(\theta) = A_{a+}(\theta) \tag{3.2a}$$

$$A_{a+}(\theta + 60^\circ) = -A_{b+}(\theta) \tag{3.2b}$$

$$A_{a+}(\theta + 120^\circ) = A_{c+}(\theta) \tag{3.2c}$$

where, A_{a+}, A_{b+}, A_{c+}, are the vector potentials of the coil sides shown in Fig. 3.1. For the example machine with ($q = 0.5$ slots/pole/phase) shown in Fig. 3.1, the flux linking

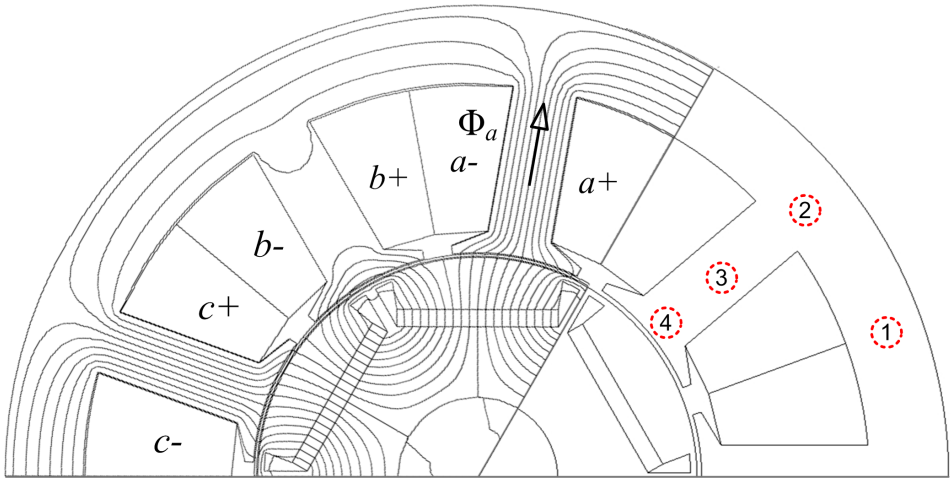

Figure 3.1: Cross-section of the case-study 9-slot, 6-pole motor showing: open-circuit flux distribution, and points used for stator core flux-density estimation.

individual phase coils, Φ, and the total coil flux linkage, λ, can be expressed as follows:

$$\Phi_a(\theta) = l_{Fe}(A_{a+}(\theta) - A_{a-}(\theta)) \tag{3.3a}$$

$$\lambda_a(\theta) = N_{ph}\Phi_a(\theta) \tag{3.3b}$$

where, l_{Fe}, is the effective axial length of the electromagnetic core stack length and, N_{ph}, is the total number of turns per phase connected in series. Alternatively, the symmetry conditions of (3.2) can be applied to the phase flux linkage waveforms directly as follows:

$$\lambda_a(\theta) = \lambda_a(\theta) \tag{3.4a}$$

$$\lambda_b(\theta + 60^\circ) = -\lambda_b(\theta) \tag{3.4b}$$

$$\lambda_c(\theta + 120^\circ) = \lambda_c(\theta). \tag{3.4c}$$

Furthermore, using the half-wave symmetry, the number of points obtained per single solution is doubled to six. Further resolution can be obtained by carrying out additional magnetostatic solutions at equidistant increments of rotor position with corresponding instan-

taneous values of currents over the winding phase-belt. The method can be demonstrated using the example of the fractional-slot tooth wound machine ($q = 0.5$ slots/pole/phase) shown in Fig. 3.1. Shown in Fig. 3.2 is the application of (3.4) to construction of the phase flux linkage waveforms. Additional magnetostatic solutions can be used to improve the resolution of the flux linkage waveform as shown in Fig. 3.2b.

Assuming that a sufficient number of magnetostatic solutions (samples) was carried out to avoid aliasing, the Fourier series of the phase flux linkage waveform can then be expressed as follows:

$$\lambda_a(\theta) = \sum_{n=1}^{n_M} \lambda_n \cos(n\theta + \phi_n). \tag{3.5}$$

Accordingly, the resulting induced voltage waveform can be derived as follows:

$$v_a(\theta) = -\frac{d\lambda_a}{d\theta}\frac{d\theta}{dt} = \omega \sum_{n=1}^{n_M} n\lambda_n \sin(n\theta + \phi_n). \tag{3.6}$$

In the case of a machine operating under load condition, (3.6) would include armature induced voltage drops associated with self and mutual inductances. In the case of a machine operating in an open-circuit mode (zero armature current), (3.6) would become the back emf, e_a, induced by the rotor field excitation (permanent magnets). Similar expressions can be developed for the remaining phases b and c by including the appropriate phase delays. Here, in a 3-phase machine, the relationship between the highest significant harmonic order, n_M, and the number of magnetostatic field solutions, s, is:

$$n_M = 3s - 1. \tag{3.7}$$

Selection of the number of solutions, s, is based on the highest significant harmonic present in the flux linkage waveforms. This is in order to avoid aliasing in the Fourier series of (3.5) and (3.6). A method for selection of the number of solutions will be discussed in more detail in Section 3.4. Shown in Fig. 3.3 is the phase induced voltage waveform at rated-load condition

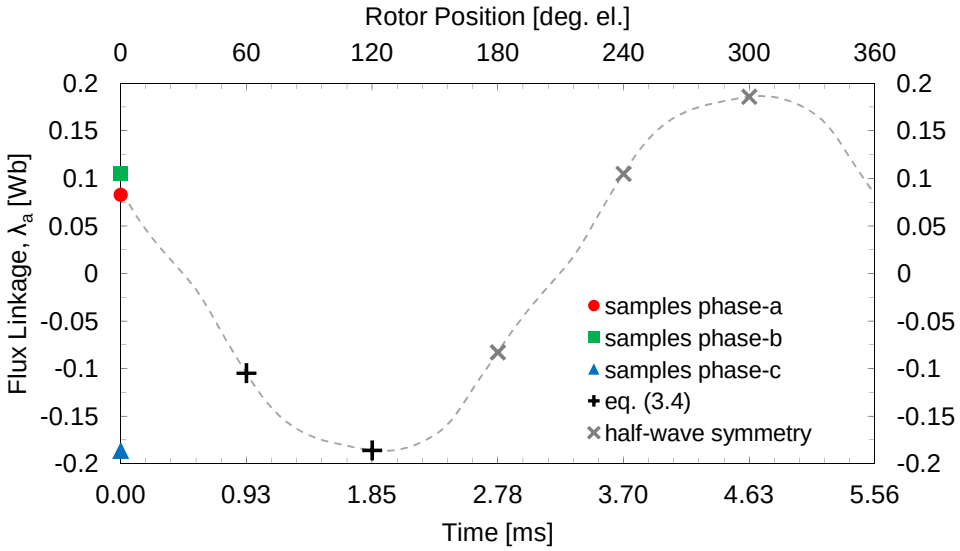

(a) 1 magnetostatic FE solution

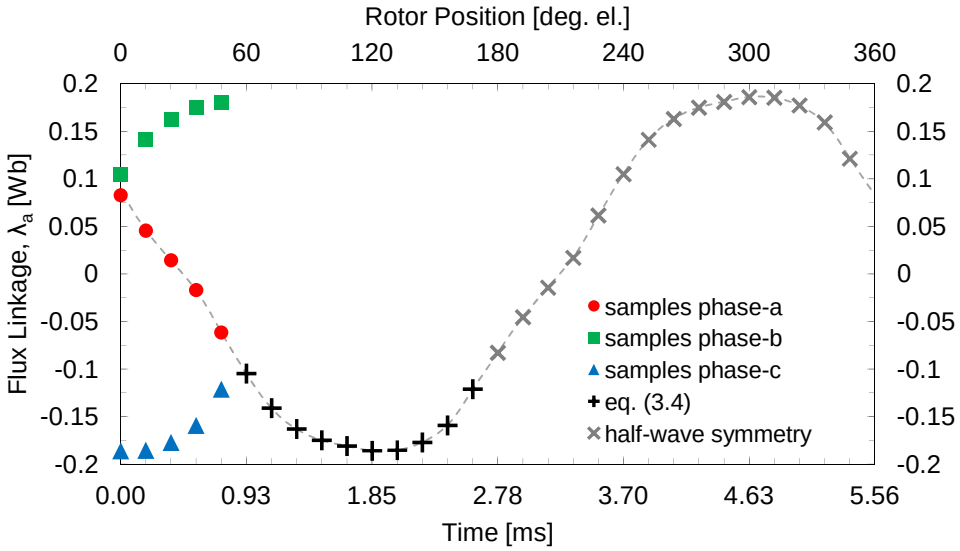

(b) 5 magnetostatic FE solutions

Figure 3.2: Waveform of the rated-load phase flux linkage of the machine shown in Fig. 3.1 obtained using CE-FEA procedure.

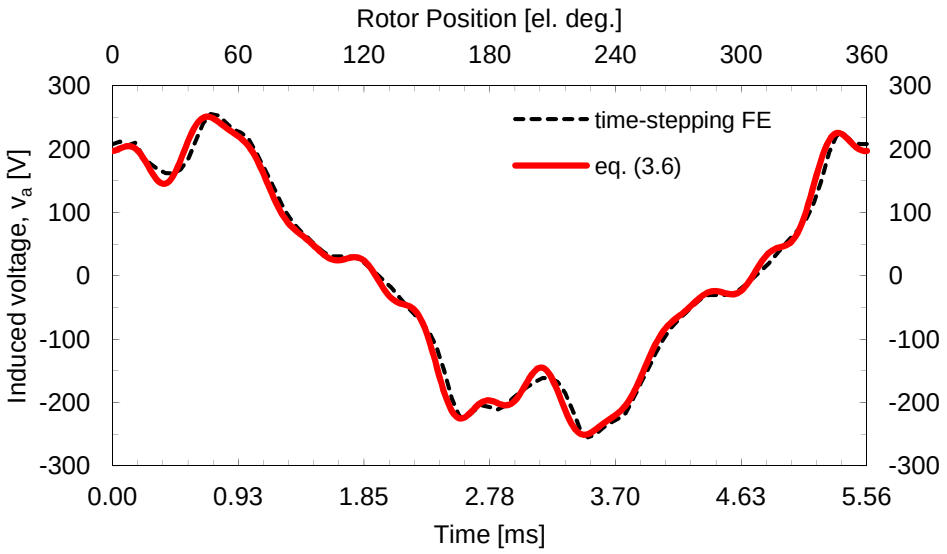

Figure 3.3: Induced phase terminal voltage for the machine shown in Fig. 3.1 operating at rated load. Results obtained using CE-FEA procedure with 5 magnetostatic FE solutions.

obtained using the CE-FEA procedure outlined above with five magnetostatic solutions over $60°e$, and the corresponding comprehensive induced voltage waveform obtained from a time-stepping FE simulation, respectively. Using five magnetostatic field solutions yields a total of 30 sample points of flux linkage over a complete electrical cycle, allowing one to account for harmonic orders up to the 14th harmonic.

It should be noted that this development, which is straightforward for the concentrated winding machine shown in Fig. 3.1, can be extended to other types of motor topologies. Steady-state symmetry of the phase flux linkage waveforms provided in (3.4) is appropriate for any machine with a balanced three-phase winding operating under steady-state condition. Examples of a fractional-slot machine with 12-slots and 10-poles ($q = 0.4$ slots/pole/phase shown in Fig. 3.4) with a double-layer winding and a distributed winding machine with 36-slots and 6-poles and a single-layer winding ($q = 2.0$ slots/pole/phase shown in Fig. 3.6) are shown in Figs. 3.5 and 3.7, respectively.

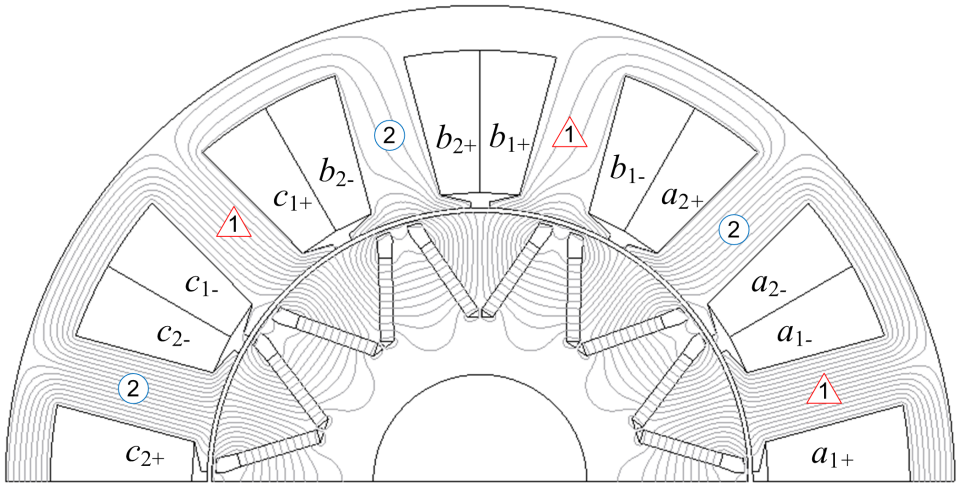

Figure 3.4: Cross-section of the case-study 12-slot, 10-pole motor showing: open-circuit flux distribution, and two types of stator slots.

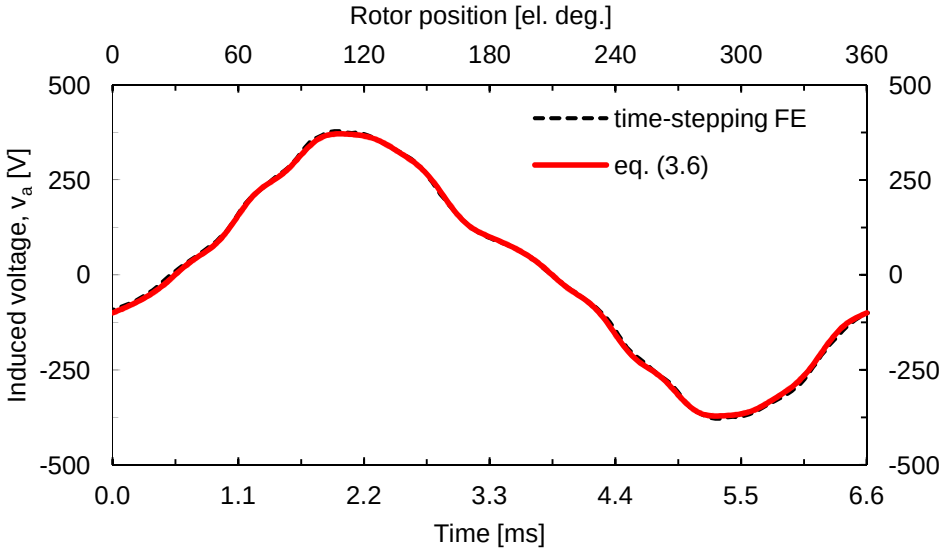

Figure 3.5: Induced phase terminal voltage for the machine shown in Fig. 3.4 operating at rated load. Results obtained using CE-FEA procedure with 5 magnetostatic FE solutions.

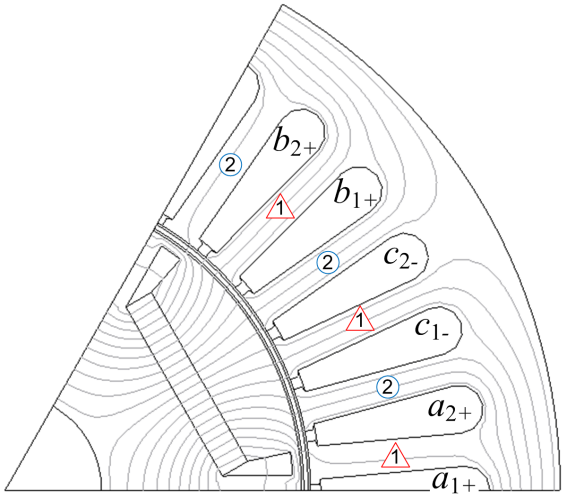

Figure 3.6: Cross-section of the case-study 36-slot, 6-pole motor showing: open-circuit flux distribution, and two types of stator slots.

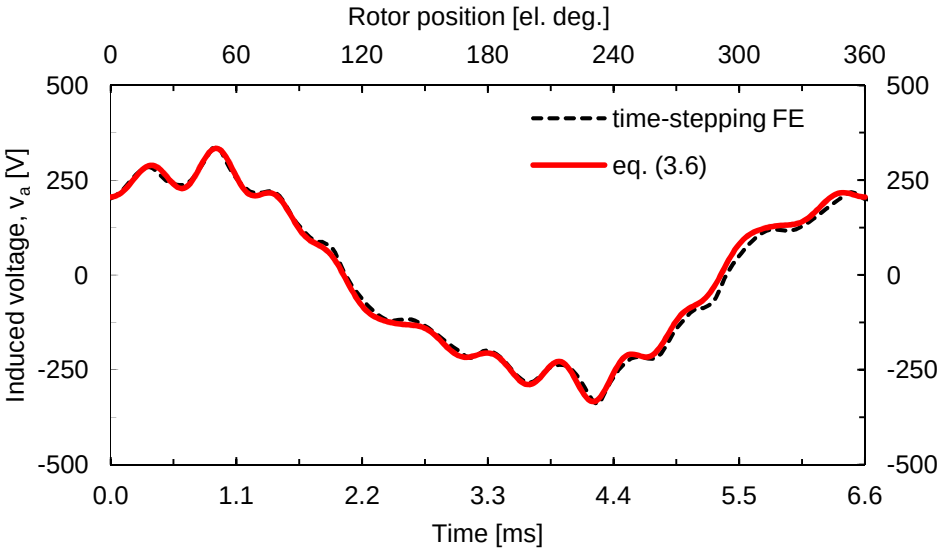

Figure 3.7: Induced phase terminal voltage for the machine shown in Fig. 3.6 operating at rated load. Results obtained using CE-FEA procedure with 5 magnetostatic FE solutions.

3.1.2 Magnetic Circuit Symmetry

Based on the magnetic circuit symmetry, the values of the radial and tangential flux densities at steady-state condition can be estimated as follows [105], [106]:

$$B_{r,t}\left(t+\frac{k\theta_s P}{2\omega}, r, \theta\right) = B_{r,t}\left(t, r, \theta + k\theta_s\right). \tag{3.8}$$

where, k, is the index that depends on the motor topology (number of slots and poles) and specifics of the winding layout, and θ_s, is the slot pitch in mechanical measure. The number of stator slots per machine periodicity span is given by the following:

$$N_{sp} = \frac{N_s}{\gcd(N_s, P)}. \tag{3.9}$$

For machines with a number of stator slots per periodic span, N_{sp}, equal to three, a single magnetostatic solution yields three flux density samples spaced in time by, $\left(\frac{k\theta_s P}{2\omega}\right)$. Assuming the lack of even order harmonics (half-wave symmetry) the number of samples per electrical cycle is doubled to six. For the case-study machine having a 9-slot and 6-pole combination, a single magnetostatic solution yields six samples of elemental flux-densities. For additional points, static FE solutions have to be carried out at equidistant increments of rotor positions over a complete stator slot-pitch. This procedure can be visualized with reference to Fig. 3.8, in which additional samples and half-wave symmetry are used to populate a complete 360°e cycle. Applying the logic used for estimation of the phase flux linkages to the elemental flux densities results in the following Fourier series:

$$B_{r,t}(\theta) = \sum_{h=1}^{n_M} B_n \cos(n\theta + \phi_n). \tag{3.10}$$

Shown in Fig. 3.9 are the profiles of the radial and tangential flux densities at four locations (depicted in the machine cross-section of Fig. 3.1). These locations are at: 1) yoke, 2) tooth-yoke junction, 3) mid tooth, and 4) tooth tip. Good agreement between the values obtained

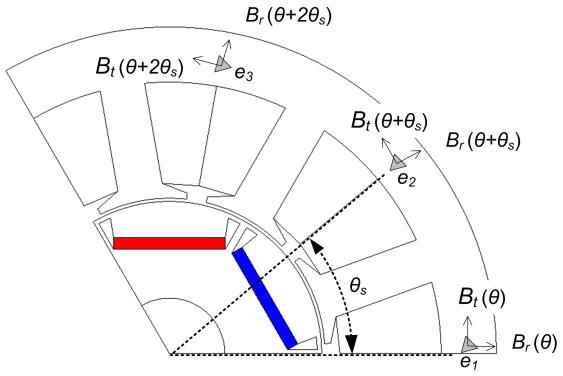

(a) Locations of repeating elements.

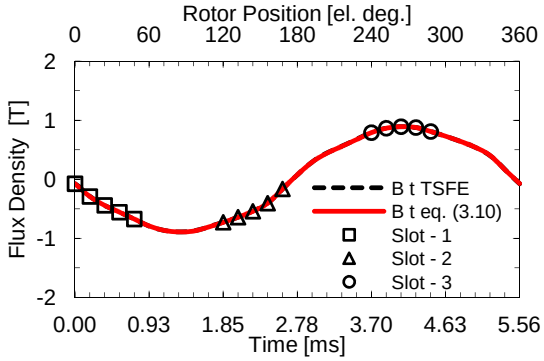

(b) Estimation of stator core flux densities using elements e_1, e_2, and e_3 for five solutions.

Figure 3.8: Cross-section of 9-slot, 6-pole IPM showing the locations of sister elements separated by one slot-pitch, θ_s.

using CE-FEA and a detailed time-stepping FE (TSFE) solution can be observed in Fig. 3.9.

For machines that have more than three slots per periodic span, such as for example in the integer-slot machine with $q = 2.0$ slots/pole/phase or the fractional-slot machine with $q = 0.4$ slots/pole/phase, there are two alternating types of slots that will experience slightly different flux densities. This is in contrast to the previously considered motor with $q = 0.5$ slots/pole/phase with a double-layer winding, where flux densities in consequent slots can be used for waveform reconstruction, since every slot is going to experience the same (albeit time-delayed) flux density. A single magnetostatic solution would yield three flux density samples per slot type. Again, using the half-wave symmetry, the number of points can be extended to six per slot type. Using additional magnetostatic solutions the resolution of the flux density waveform can be improved. Application of expressions (3.9) and (3.10) to estimation of core flux densities in the integer-slot machine with a single-layer winding is provided in Fig. 3.10. In Fig. 3.11 the proposed approach is further validated on a fractional-slot machine that has 12-slots and 10-poles ($q = 0.4$ slots/pole/phase). In all three case-study machines good agreement between the results obtained from the CE-FEA

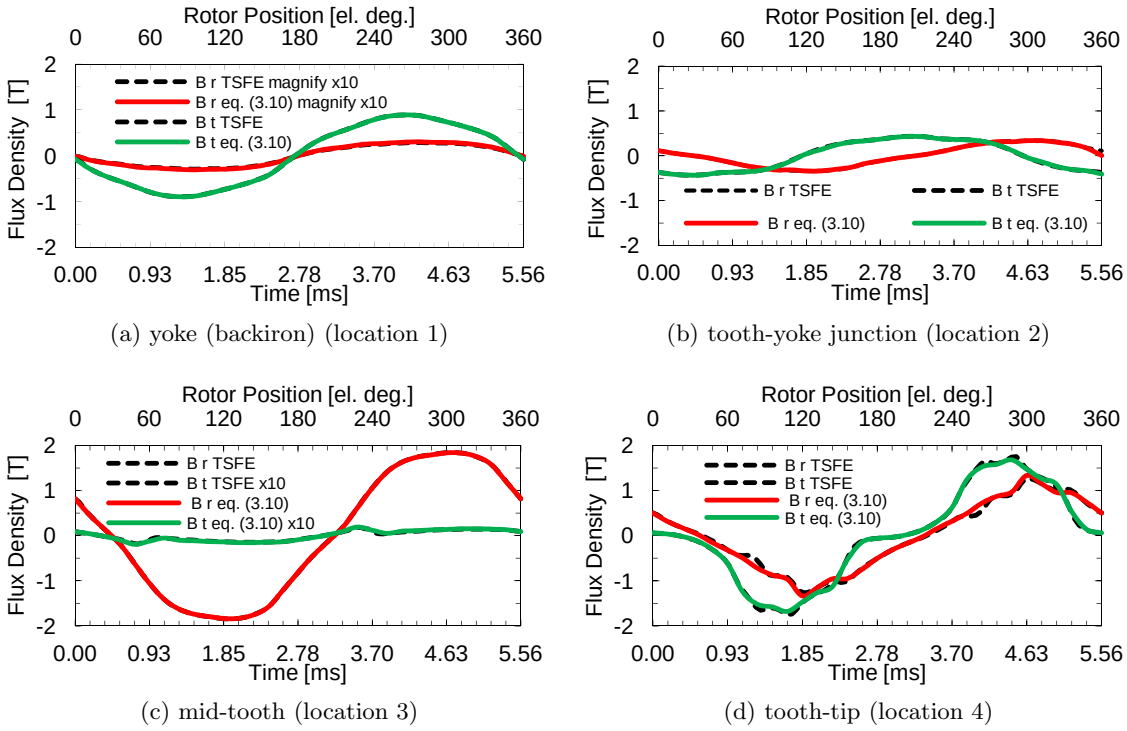

(a) yoke (backiron) (location 1)

(b) tooth-yoke junction (location 2)

(c) mid-tooth (location 3)

(d) tooth-tip (location 4)

Figure 3.9: Waveforms of radial and tangential stator core flux densities at rated-load conditions for 9-slot, 6-pole machine. Results shown for four stator locations identified in Fig. 3.1.

approach , and the significantly more computationally intensive time-stepping FE model was achieved.

Using the radial and tangential components of the core flux densities obtained from (3.10), the specific core losses per unit mass for steady-state conditions can be calculated as follows [98]:

$$p_h = \sum_{n=1}^{n_M} k_h (n f_1) B_n^2 \tag{3.11a}$$

$$p_e = \sum_{n=1}^{n_M} k_e (n f_1)^2 B_n^2 \tag{3.11b}$$

where, the hysteresis and eddy current core loss coefficients, $k_h = k_h(nf_1, B_n)$, and $k_e =$

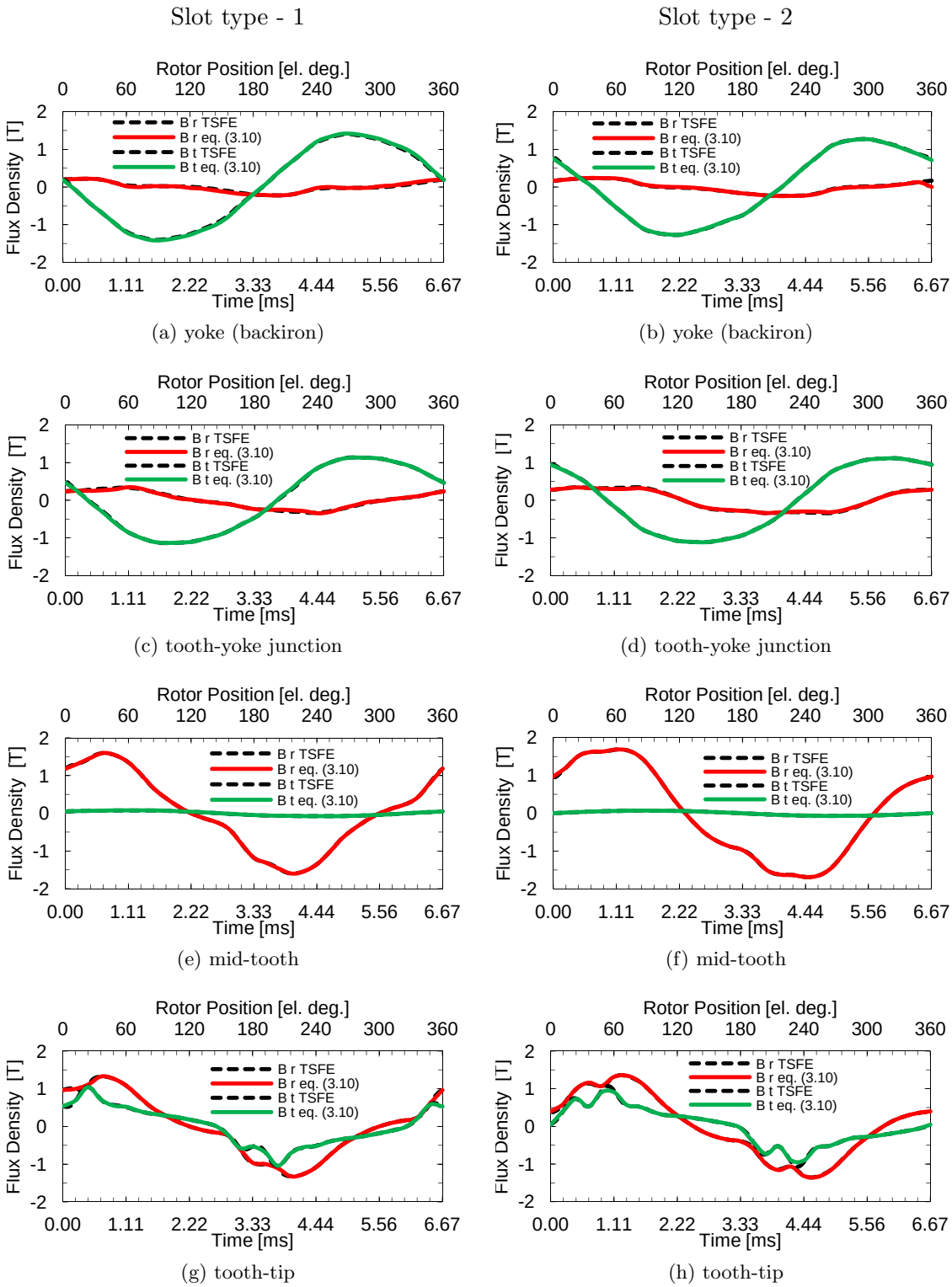

(a) yoke (backiron)

(b) yoke (backiron)

(c) tooth-yoke junction

(d) tooth-yoke junction

(e) mid-tooth

(f) mid-tooth

(g) tooth-tip

(h) tooth-tip

Figure 3.10: Waveforms of radial and tangential stator core flux densities at rated-load conditions for two slot types shown in Fig. 3.6 of the 36-slot, 6-pole machine.

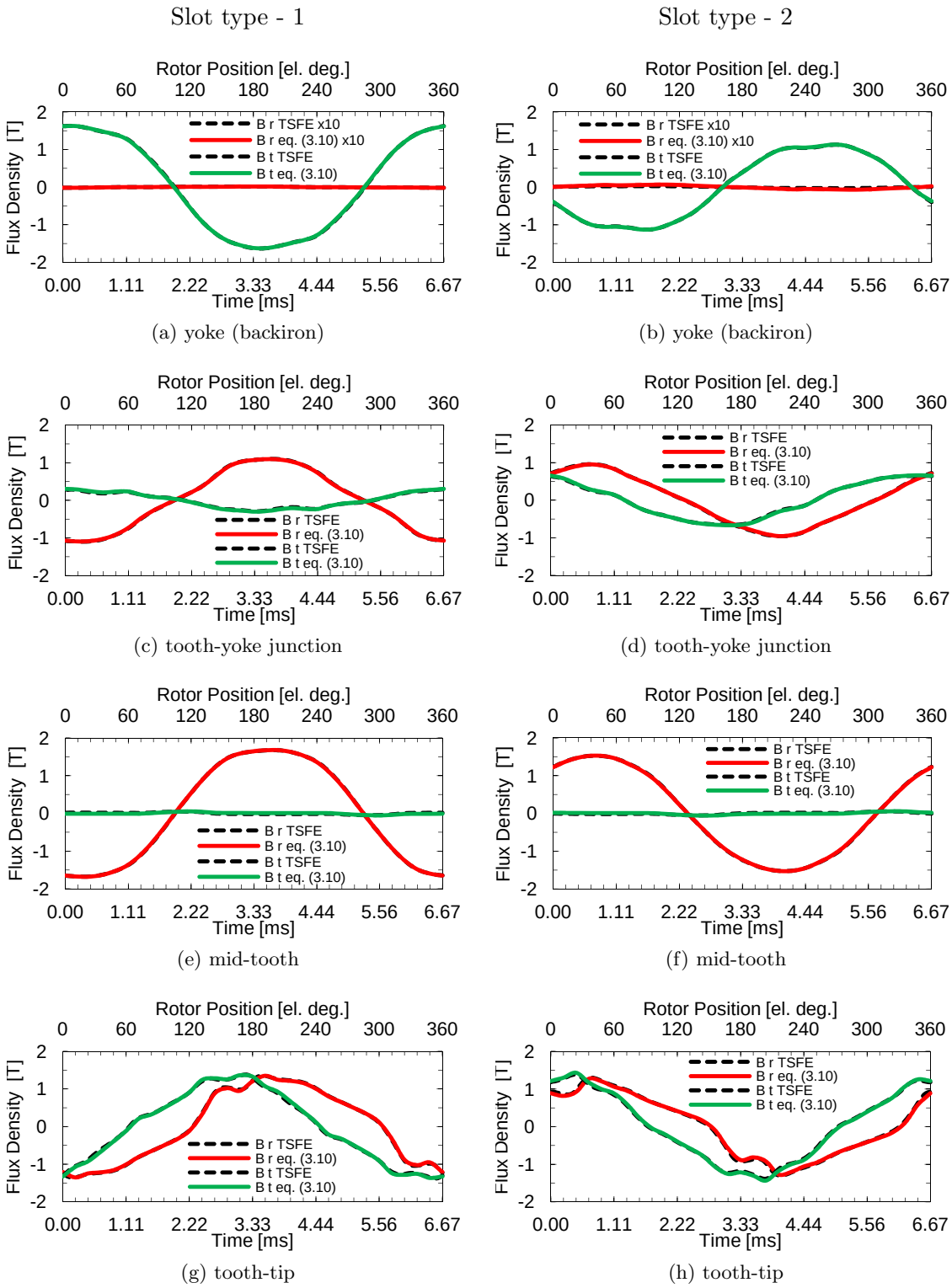

(a) yoke (backiron)

(b) yoke (backiron)

(c) tooth-yoke junction

(d) tooth-yoke junction

(e) mid-tooth

(f) mid-tooth

(g) tooth-tip

(h) tooth-tip

Figure 3.11: Waveforms of radial and tangential stator core flux densities at rated-load conditions for two slot types shown in Fig. 3.4 of the 12-slot, 10-pole machine.

Table 3.1: Calculated and measured core losses. Measured and Calculated using time-stepping FE (TSFE) and CE-FEA with a basic four block subdivision of the magnetic circuit (Fig. 3.1).

Percent of rated torque [%]									
Freq.	50			75			100		
	TSFE	CE-FEA	Meas.	TSFE	CE-FEA	Meas.	TSFE	CE-FEA	Meas.
[Hz]	[W]	[W]	[W]	[W]	[W]	[W]	[W]	[W]	[W]
60	51	57	63	64	69	73	76	78	92
120	74	83	87	97	102	98	113	116	112
180	129	149	161	167	182	184	203	210	194

$k_e(nf_1, B_n)$, are dependent on the harmonic frequency, nf_1, and peak value of harmonic flux density, B_n, as was discussed in detail in Section 2.3.2. A comparison between the results obtained from the two numerical models, CE-FEA and TSFE, is provided in Table 3.1. Table 3.1 also includes the results of experimental measurements that are provided for reference. The difference between the numerical models and the experimental tests can be attributed to manufacturing and measurement uncertainties that are not accounted for in the numerical models. The preferred validation for the CE-FEA is provided by a time-stepping FE of a motor model employing the same materials, geometry and mesh. This approach ensures a fair basis of comparison as it avoids uncertainties and imperfections associated with prototyping or the effects of measurement errors. Satisfactory agreement between the core loss values obtained using the detailed time-stepping FE and the CE-FEA methods is observed, see Table 3.1. In this case, a basic subdivision of the stator magnetic circuit into four sub domains, namely, yoke, tooth-yoke junction, tooth stem, and tooth tip, was employed as shown in Fig. 3.1. Accuracy of the CE-FEA calculation can be increased further by considering a larger number of region discretizations of the magnetic circuit. It should be noted that the CE-FEA based core loss calculation can be implemented on a per element basis with an additional requirement of a repetitive finite element mesh on a slot-pitch basis.

3.2 Torque and Force Production

3.2.1 Electromagnetic Torque

The electromagnetic torque, T_{em}, calculation used in the CE-FEA follows the virtual work principle [24], which is based on the energy stored in the magnetic circuit of the machine, W_{stored}, for every magnetostatic field solution. The Fourier series of the stored energy and its derivative with respect to the mechanical position angle are then constructed as follows:

$$W_{stored}(\theta_m) = \sum_{h=1}^{n_W} W_n \cos(nN_{cog}\theta_m + \phi_n), \tag{3.12}$$

and

$$\frac{dW_{stored}}{d\theta_m} = -N_{cog} \sum_{h=1}^{n_W} nW_n \sin(nN_{cog}\theta_m + \phi_n), \tag{3.13}$$

where, N_{cog}, is the number of cogging periods per mechanical revolution and is given as follows:

$$N_{cog} = \frac{N_s P}{\gcd(N_s, P)} = \text{lcm}(N_s, P) \tag{3.14}$$

In this case, the maximum harmonic order of the estimated stored energy, n_W, is related to the number of solutions, s, such that, $n_W = s/2$. Hence, for satisfactory modeling of the cogging torque a sufficient number of solutions is required in order to accurately capture the variation of energy. Using the expressions developed for the back emf in (3.5), (3.6) and the derivative of the stored energy in (3.13), the electromagnetic torque developed by a three-phase machine can be expressed as follows:

$$\begin{aligned} T_{em}(\theta) &= \frac{P}{2}\left(i_a \frac{d\lambda_a}{d\theta} + i_b \frac{d\lambda_b}{d\theta} + i_c \frac{d\lambda_c}{d\theta}\right) - \frac{dW_{stored}}{d\theta_m} \\ &= \frac{P}{2}\left(i_a(\theta) \sum_{n=1}^{n_M} n\lambda_n \sin(n\theta + \phi_n) + i_b(\theta) \sum_{n=1}^{n_M} n\lambda_n \sin(n(\theta - 120^\circ) + \phi_n)\right. \\ &\left. + i_c(\theta) \sum_{n=1}^{n_M} n\lambda_n \sin(n(\theta - 240^\circ) + \phi_n)\right) + N_{cog} \sum_{h=1}^{n_W} nW_n sin(nN_{cog}\theta_m + \phi_n). \end{aligned} \tag{3.15}$$

Shown in Figs. 3.12 and 3.13 is the electromagnetic torque for the 9-slot, 6-pole machine under various load conditions calculated using (3.15) with five nonlinear magnetostatic field solutions. Simulations are also performed using a substantially more computationally intensive TSFE, which employs Maxwell stress tensor based calculations. Shown in Fig. 3.12 is the variation of stored energy (3.12) with position and the cogging torque under open-circuit conditions. Provided in Fig. 3.13 is the electromagnetic torque for three operating conditions: rated-load, half-load and open-circuit, respectively. The results from Figs. 3.12 and 3.13 show good agreement between the two approaches, the CE-FEA and TSFE methods, under all investigated load conditions.

The estimation of the derivative of the stored magnetic energy in (3.12) is highly dependent on the mesh density and finite element order around the air-gap region and, hence, the recommended air-gap mesh should be fine enough in order to capture the variation of the stored energy (Fig. 3.12) with rotor position, and consequently of the cogging torque component. This is not a limitation of this approach, since such mesh density requirements are even more important for the Maxwell stress tensor torque calculations. The average electromagnetic torque, $T_{em_{\text{avg}}}$, can be estimated from the fundamental components of phase induced voltage and phase current as given below:

$$T_{em_{\text{avg}}} = \frac{P_{em_{\text{avg}}}}{\omega_m} = \frac{3 v_1 i_1}{2\omega_m} \cos\left(\theta_{v1} - \left(\beta - \frac{\pi}{2}\right)\right) \tag{3.16}$$

where, v_1, is the peak value of the fundamental component of the phase induced back emf, θ_{v1}, is the phase angle of the fundamental component of induced back emf, and, i_1, is the peak value of the fundamental component of the phase current. Further verification of the torque expression (3.15) is provided using the examples of an integer-slot machine with 36-slots and 6-poles and a fractional-slot machine with 12-slots and 10-poles. Shown in Figs. 3.14 and 3.15 are the rated torque operation of the two machines shown in Figs. 3.6 and 3.4, respectively. Good agreement with respect to significantly more computationally

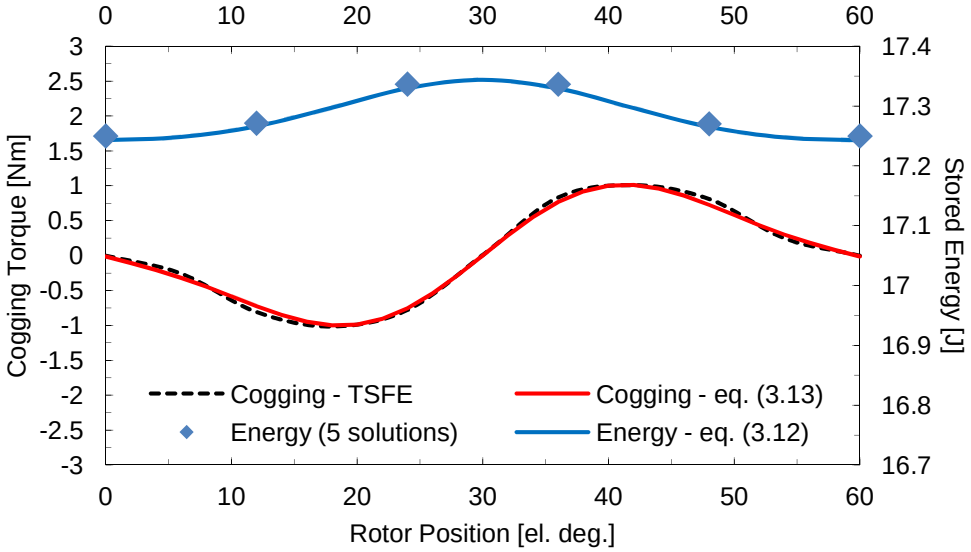

Figure 3.12: Variation of stored energy and cogging torque at open-circuit for 9-slot and 6-pole machine shown in Fig. 3.1.

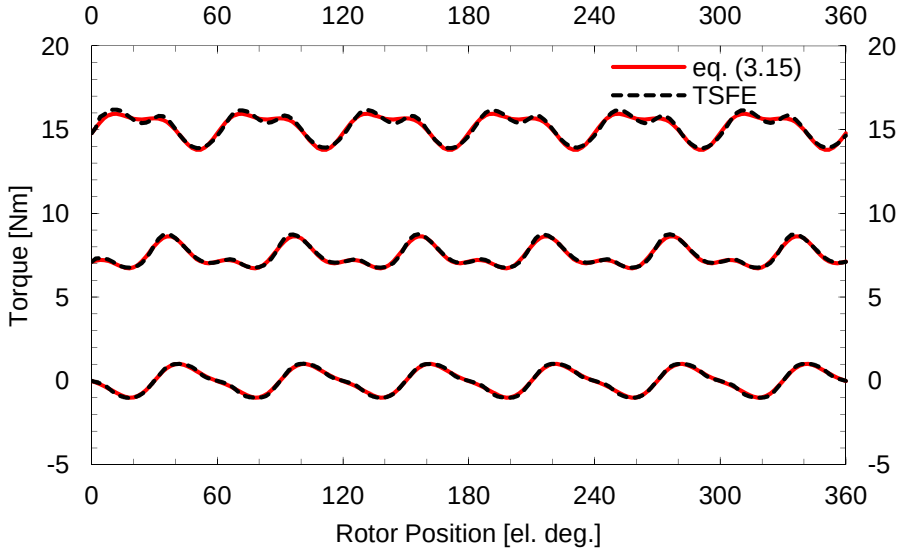

Figure 3.13: Electromagnetic torque: 1) rated-load, 2) half-load, 3) open-circuit, i.e. cogging torque for 9-slot and 6-pole machine shown in Fig. 3.1.

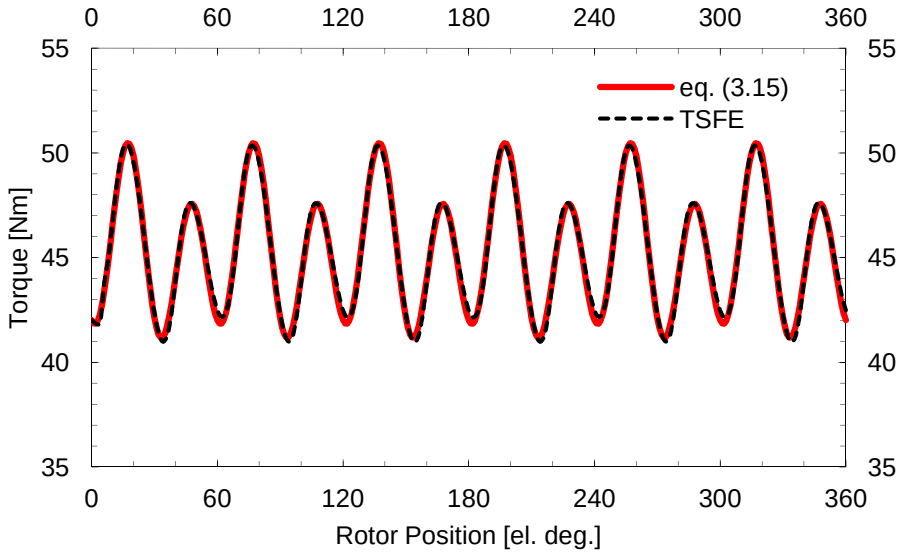

Figure 3.14: Electromagnetic torque at rated-load for 36-slot and 6-pole machine shown in Fig. 3.6.

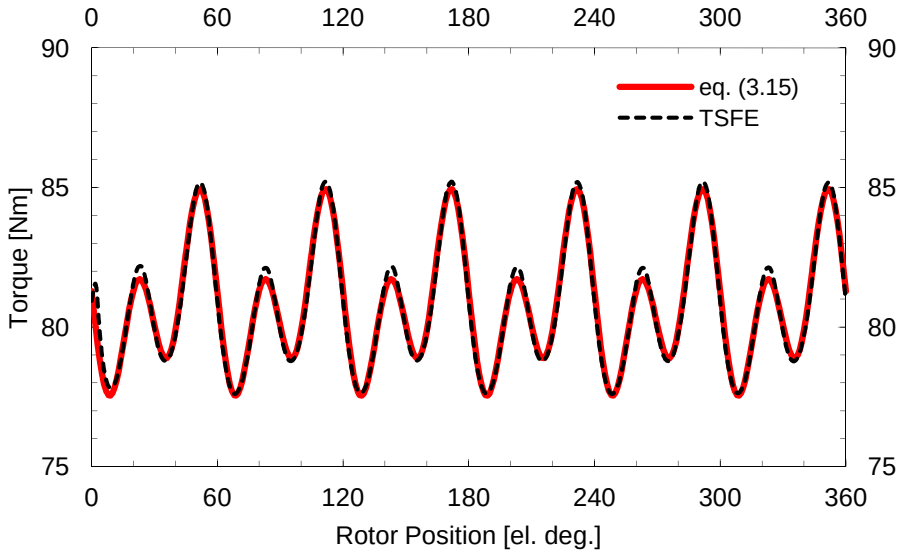

Figure 3.15: Electromagnetic torque at rated-load for 12-slot and 10-pole machine shown in Fig. 3.4.

intensive time-stepping simulations should be noted for all examples considered.

3.2.2 Air-gap Forces

Instantaneous electromagnetically induced stator forces result in core deformations and consequent vibrations that stress mechanical components and may result in unwanted acoustic noise. A fast and accurate method of evaluating air-gap force distribution under steady-state operation introduced in this work relies on the motor electric and magnetic circuit symmetries. Air-gap stresses, the radial component, f_r, and the tangential component, F_t, can be evaluated using a Maxwell stress tensor approach, as follows [107]:

$$f_r(t,\theta) = \frac{B_r(t,\theta)^2 - B_t(t,\theta)^2}{2\mu_o} \tag{3.17}$$

$$f_t(t,\theta) = \frac{B_r(t,\theta)B_n(t,\theta)}{\mu_o} \tag{3.18}$$

where, $B_{r,t}(t,\theta)$, are the radial and tangential flux densities taken at the middle of the air-gap to minimize discretization errors due to the finite element mesh. A procedure for estimating stator flux densities from several magnetostatic solutions has been outlined in the previous sections and is based on the relationship in, (3.10). Depicted in Fig. 3.16 are the radial and tangential flux densities over one electrical cycle for a single air-gap finite element obtained using the CE-FEA and time-stepping FEA models, where good agreement between the two models can be observed. The resultant (lumped) radial and tangential components of the force on the individual stator teeth can be obtained by integrating the stresses over the stator tooth surface as follows:

$$F_r = l_{Fe}\frac{D_{Si}}{2}\int_{-\frac{\theta_T}{2}}^{\frac{\theta_T}{2}} f_r \cos(\gamma) d\gamma \tag{3.19}$$

$$F_t = l_{Fe}\frac{D_{Si}}{2}\int_{-\frac{\theta_T}{2}}^{\frac{\theta_T}{2}} f_t \cos(\gamma) d\gamma \tag{3.20}$$

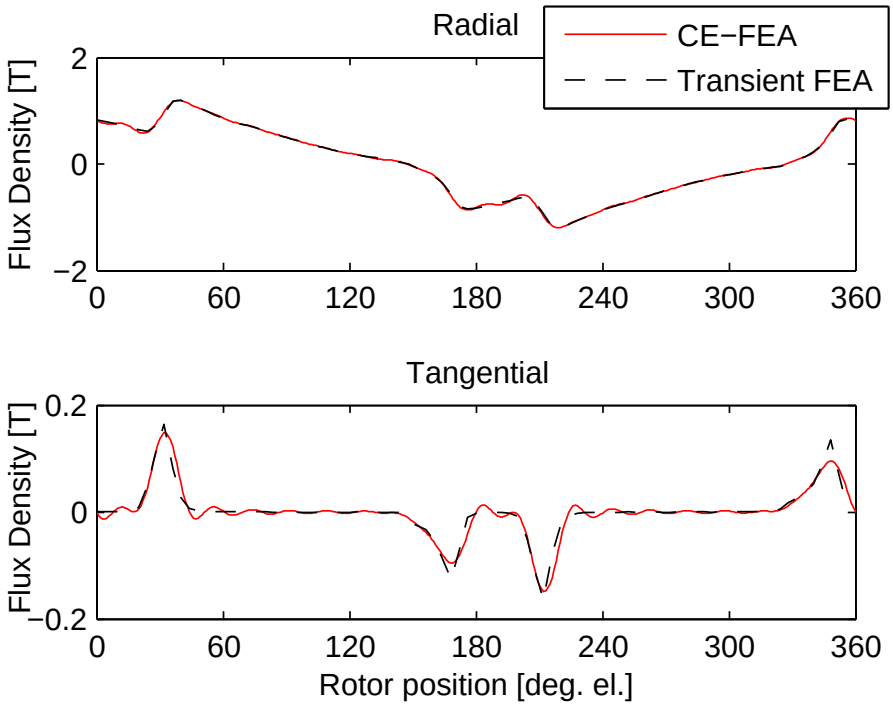

Figure 3.16: Air-gap flux density obtained in one element under the stator tooth using CE-FEA and time-stepping FEA.

where, θ_T is the angular span of the stator tooth in mechanical measure. The resulting radial and tangential stator tooth forces over one electrical cycle are shown in Fig. 3.17. Significant radial component of the tooth force in both open-circuit and rated load conditions should be noted. Rated load distributions of the stator stresses over the air-gap peripheries at a given time instant are shown in Figs. 3.18-3.20. A fractional-slot motor with 12-slots and 10-poles and double-layer winding is included for reference in Fig. 3.20. Shown in Figs. 3.18-3.20 are the distributions of stator teeth forces at a given time instant. Also included in Figs. 3.18-3.20 are the resultant (lumped) stator tooth forces. Comparing integer-slot and two fractional-slot motors, reduction of waveform symmetry and consequent reduction of the order of force distribution should be noticed. This is most noticeable in the 12-slot, 10-pole motor (Fig. 3.20) where the force distribution is of mode-2 order, potentially

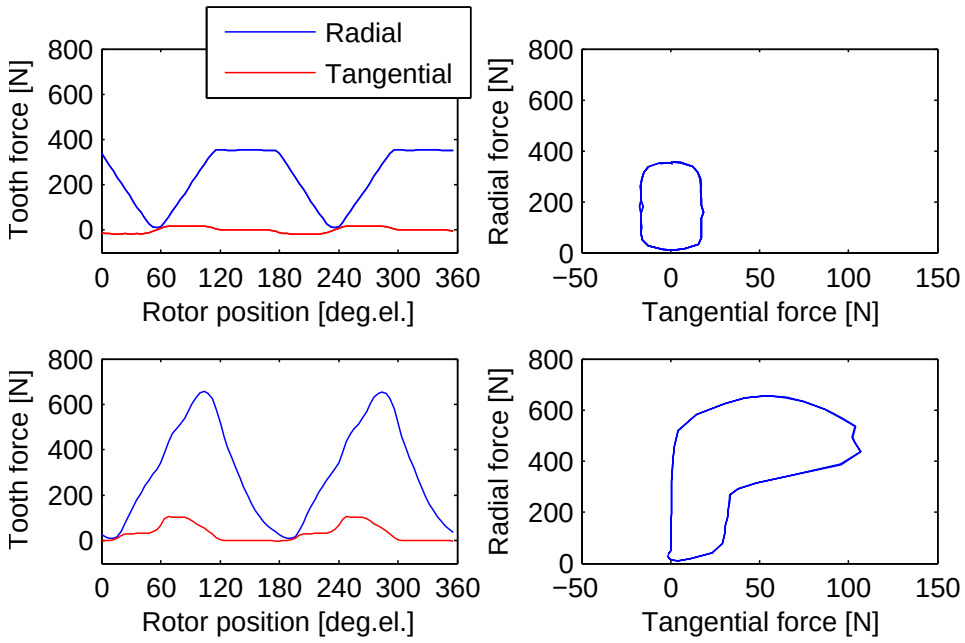

Figure 3.17: Stator tooth forces for one electrical cycle for fractional-slot motor (9-slot, 6-pole, q=0.5) operating at: **top** - open-circuit, **bottom** - rated load.

causing large stator core deflections which may lead to increased acoustic noise under normal (non-resonant) operation. For most topologies, the fundamental mode of the stator force distribution is related to the motor symmetry and the greatest common divisor of the number of slots, N_s, and the number of poles, P, as $\gcd(N_s, P)$. It has been pointed out in [94], that stator force distribution of low order modes (1 and 2) result in high stator core deformations leading to increased acoustic noise.

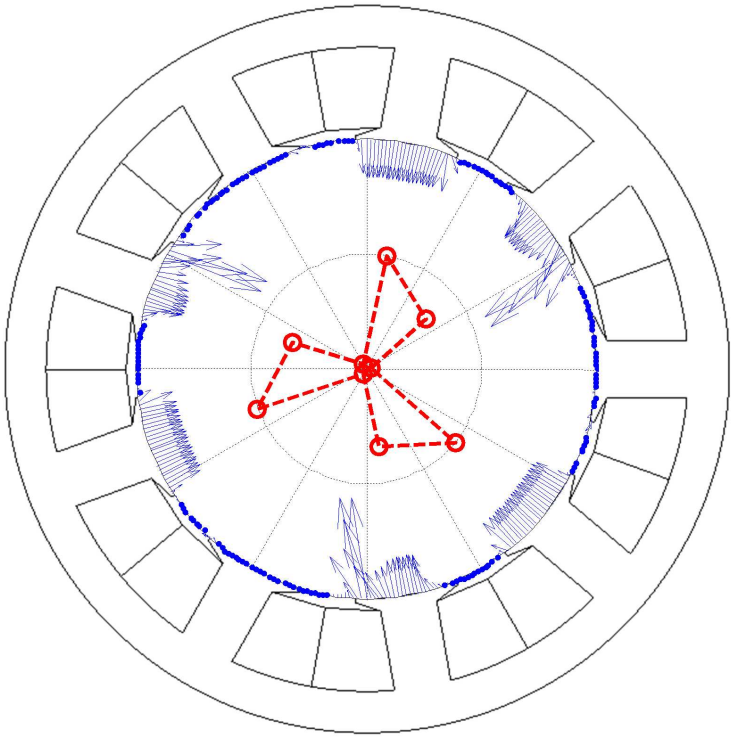

(a) Distributed stator forces at a given time instant. Also shown are the resultant stator forces.

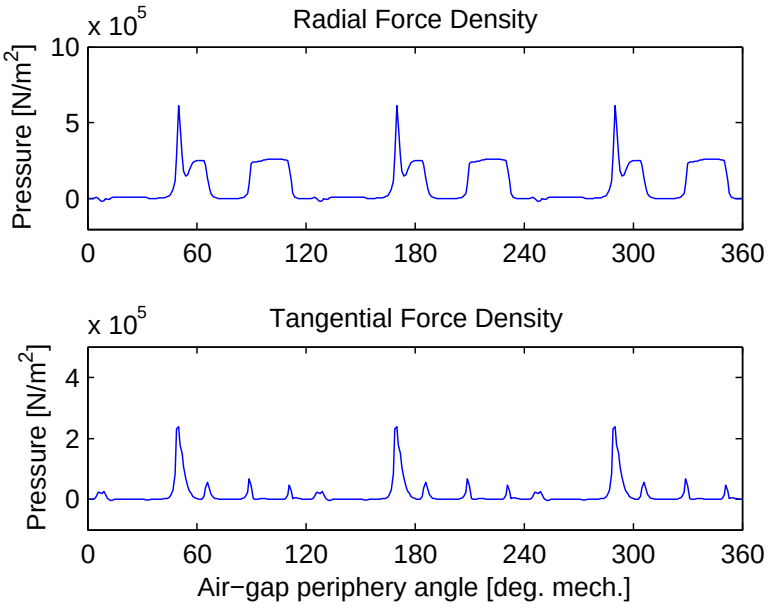

(b) Air-gap stresses at rated-load conditions at a given time instant.

Figure 3.18: Air-gap stresses and resultant stator forces at rated-load conditions for a given time instant (9-slot, 6-pole motor, q=0.5).

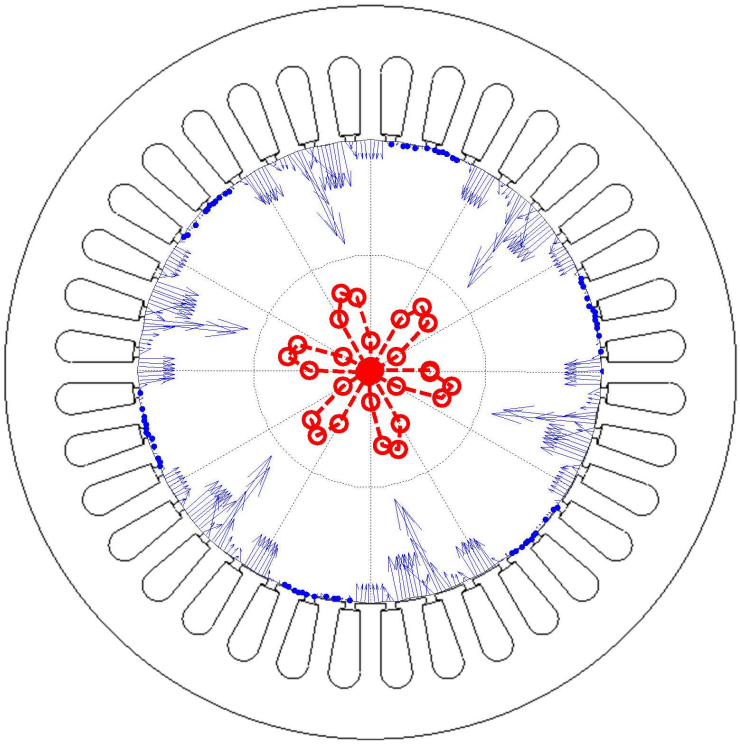

(a) Distributed stator forces at a given time instant. Also shown are the resultant stator forces.

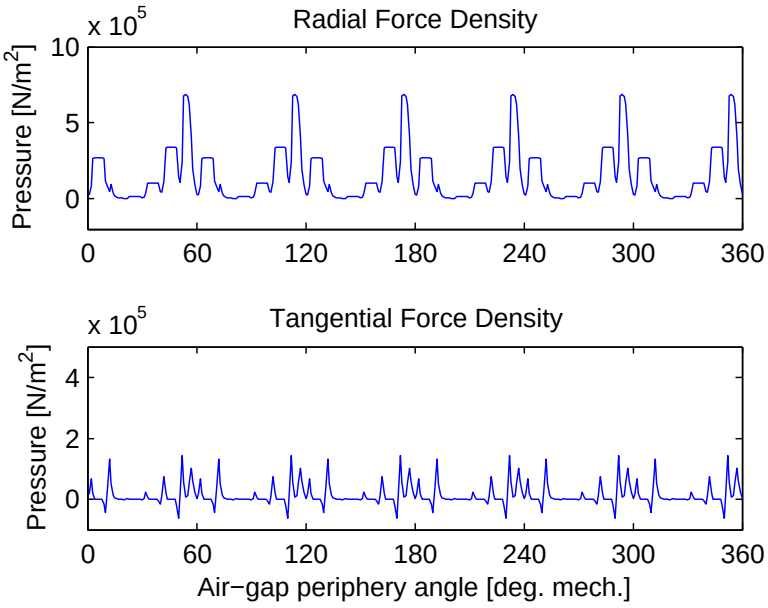

(b) Air-gap stresses at rated-load conditions at a given time instant.

Figure 3.19: Air-gap stresses and resultant stator forces at rated-load conditions for a given time instant(36-slot, 6-pole motor, q=2).

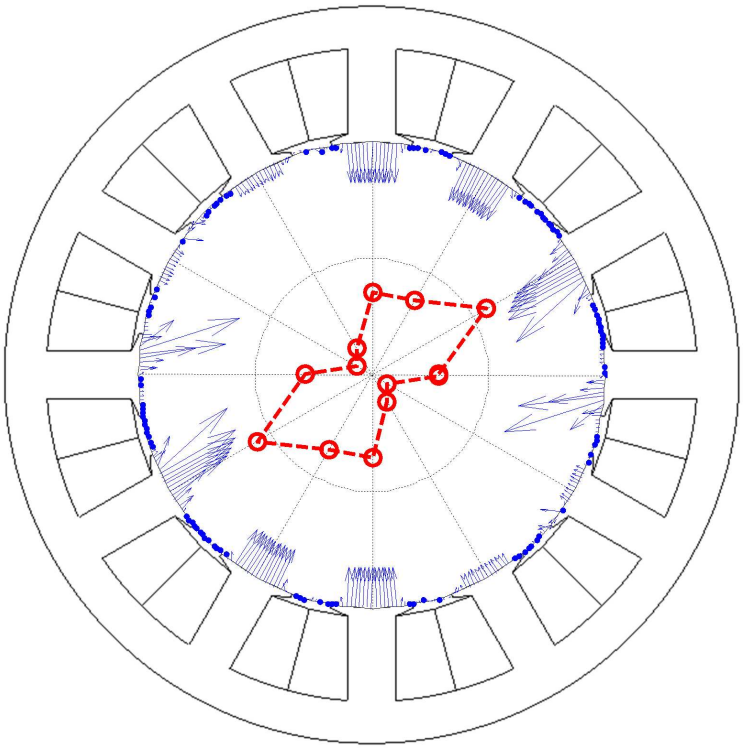

(a) Distributed stator forces at a given time instant. Also shown are the resultant stator forces.

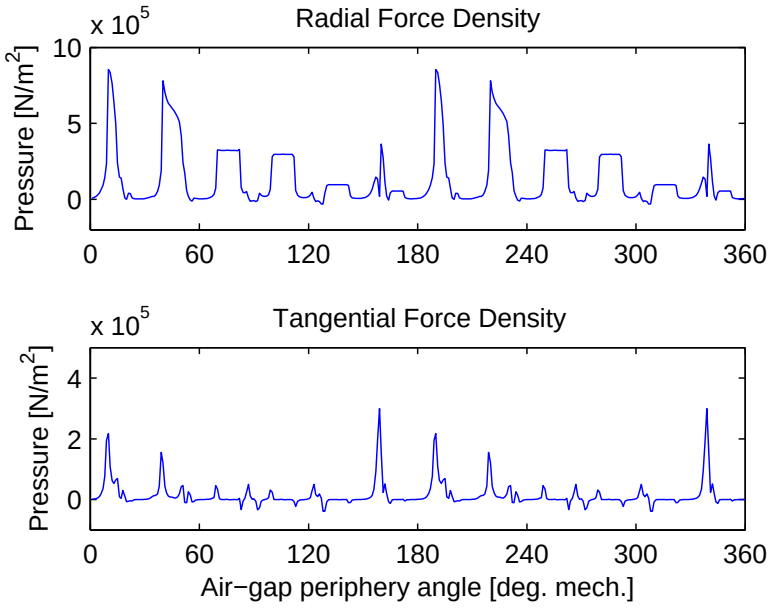

(b) Air-gap stresses at rated-load conditions at a given time instant.

Figure 3.20: Air-gap stresses and resultant stator forces at rated-load conditions for a given time instant(12-slot, 10-pole motor, q=0.4).

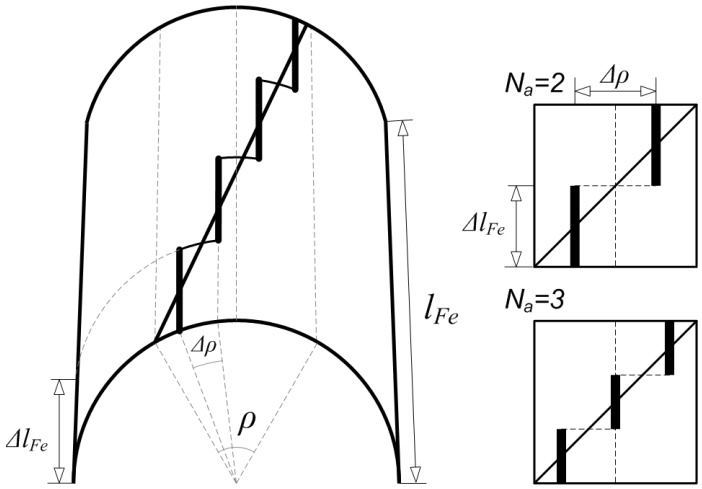

Figure 3.21: Representation of the stator and/or rotor skew.

3.3 Modeling of Skew

Flux linkages, induced voltages and energy/co-energy used in the torque calculations can be rapidly evaluated from several magnetostatic FEA solutions as described in [74], [32]. Application of the torque expression in (3.15) allows one to partially separate the torque ripple components due to flux linkage (induced voltage) harmonics and stored energy variation. It should be mentioned that an alternative to (3.15) includes evaluation of derivatives of phase currents and co-energy and results in the identical torque waveform for a sine-wave regulated motor. Several approaches that provide the means to include stator and/or rotor skew in 2-D FEA have been proposed [108], [109]. Here, the induced voltages and torques for the skewed machines are calculated using a single CE-FEA evaluation. A non-skewed machine is simulated at a given load condition and the waveforms of phase flux-linkages, voltages and the total stored magnetic energy/co-energy are post-processed to account for the skew. The process results in effectively averaging the flux-linkages, induced voltages and energies of the non-skewed motor over a rotor rotation that corresponds to the skew angle. In this process the waveforms of flux-linkage and energy required for torque calculation are

phase shifted and averaged over a rotational angle equal to the skew angle (Fig. 3.21), as provided in (3.21) and (3.22) below:

$$\lambda_a = \frac{1}{\rho}\int_{-\frac{\rho}{2}}^{\frac{\rho}{2}} \lambda_a(\theta+\gamma)d\gamma \tag{3.21}$$

$$W = \frac{1}{\rho}\int_{-\frac{\rho}{2}}^{\frac{\rho}{2}} W(\theta+\gamma)d\gamma \tag{3.22}$$

where, ρ, is the skew angle in electrical radians. This assumes that all axial parts of the skewed machine are operating in an identical magnetic state (core saturation and PM operating point) which implies only a phase difference between differential flux-linkages and energies corresponding to different axial positions. This process can also be accomplished by application of harmonic skew factors to the individual harmonics of the flux-linkage, induced voltage and energy waveforms. The classical harmonic skew factor is provided in (3.23), below:

$$k_{sn} = \frac{\sin(\frac{n\rho}{2})}{\frac{n\rho}{2}} \tag{3.23}$$

Application of the harmonic skew factors to the Fourier series of the flux-linkage and induced voltage waveforms that are readily available from CE-FEA is given in (3.24) and (3.25):

$$\lambda_a = \sum_{n=1}^{3s-1} k_{sn}\lambda_n \cos(n\theta+\phi_n) \tag{3.24}$$

$$v_a = \omega\sum_{n=1}^{3s-1} nk_{sn}\lambda_n \sin(n\theta+\phi_n) \tag{3.25}$$

where, s, is the number of magnetostatic FEA solutions used in the construction of the waveforms.

The method at hand is verified on two interior-PM sine-wave regulated motors: 1) an integer-slot motor with $q = 2$ slots/pole/phase (36-slot, 6-pole) and 2) a fractional-slot motor with $q = 0.5$ slots/pole/phase (9-slot, 6-pole), shown in Figs. 3.22 and 3.23,

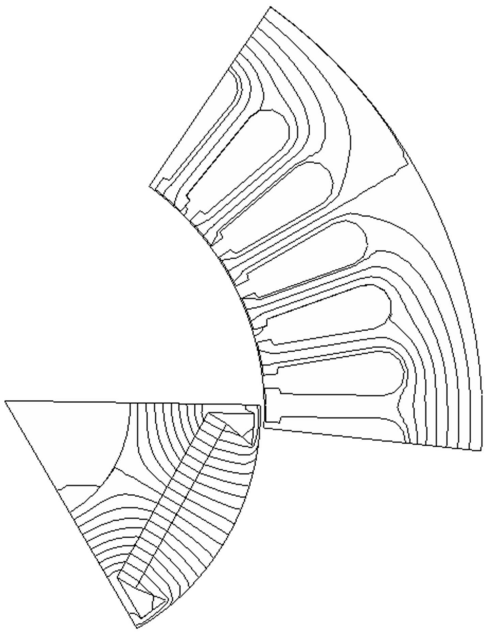

Figure 3.22: Cross-section and open-circuit flux distribution of the integer-slot motor, (36-slot, 6-pole, $q = 2$).

respectively. Good agreement between the simplified approach outlined above and the significantly more computationally intensive multi-slice 2-D transient (time-stepping) FEA method is observed in Figs. 3.24 and 3.25. Also provided in Fig. 3.24b and 3.25b are the experimental measurements of the open-circuit back emfs performed on the motors with step-skewed rotors further verifying the two models. Dependencies of the torque ripple and average torque on the skew angle for the two machines are provided in Fig. 3.26. It should be noted that results provided in Fig. 3.26 require only a single CE-FEA evaluation. Expected improvement for the torque ripple performance for a skew corresponding to one slot-pitch is observed for the integer-slot machine. Computational times required for evaluation of the skewed motor models are compared in Table 3.2. Significant reduction of simulation times is achieved.

In permanent magnet motors, the skew can be used to mitigate unwanted torque ripple. In addition, the skew improves waveform quality of the induced voltage at the terminals of

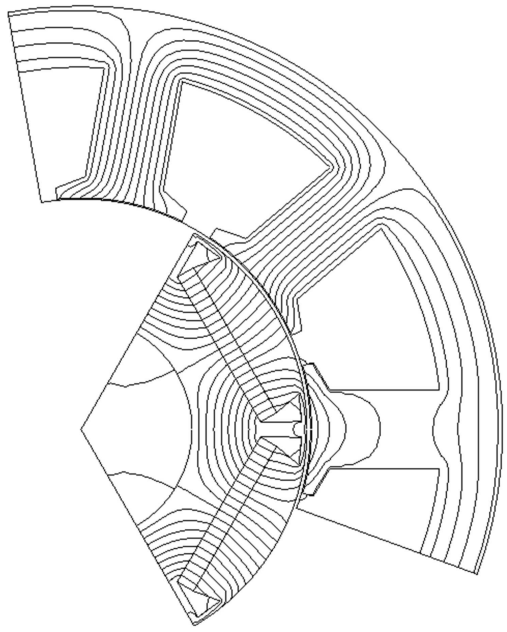

Figure 3.23: Cross-section and open-circuit flux distribution of the fractional-slot motor, (9-slot, 6-pole, $q = 0.5$).

the machine by minimizing the harmonic content as can be seen from Figs. 3.24 and 3.25. This has additional benefits of:

- improving motor-drive integration by reducing the controller effort to regulate a sinusoidal current,
- reducing the peak of the induced voltage at the terminals of the loaded motor (Figs. 3.24c and 3.24d) allowing for higher dc-bus voltage margin for current regulator operation.

Assuming that the stator core is a rigid body allows one to consider the effects of skew

Table 3.2: Simulation times for estimation of skewed motor performance with CE-FEA and transient (time-stepping) FEA. Both models utilize identical FEA mesh and 2^{nd} order elements.

	CE-FEA (7-static)	Transient FEA
Integer-slot (36-slot, 6-pole)	21 sec	1080 sec (540 sec/slice)
Fractional-slot (9-slot, 6-pole)	26 sec	1340 sec (670 sec/slice)

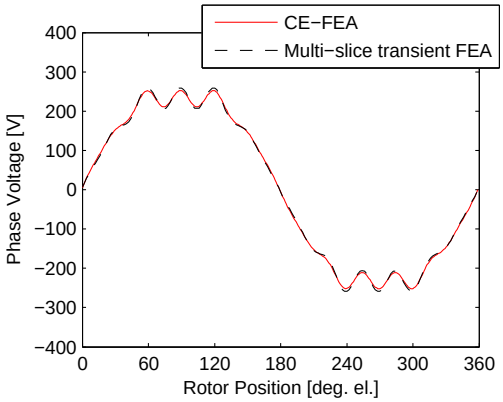

(a) Non-skewed

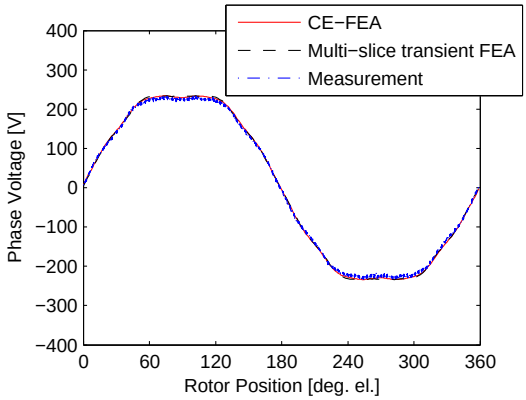

(b) Skewed (30° el.)

Open-circuit phase emf.

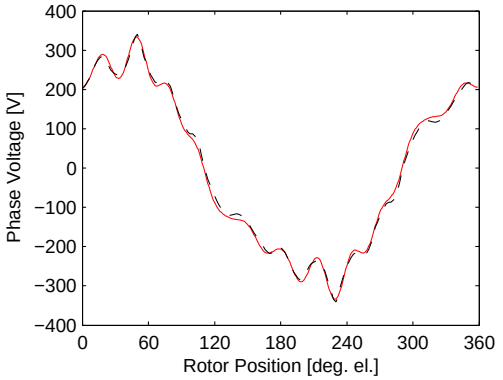

(c) Non-skewed

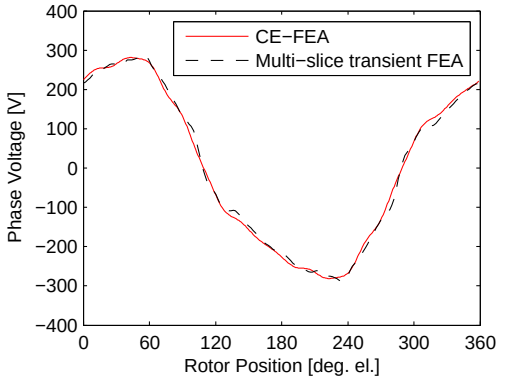

(d) Skewed (30° el.)

Rated-load induced phase voltage (magnet emf and armature).

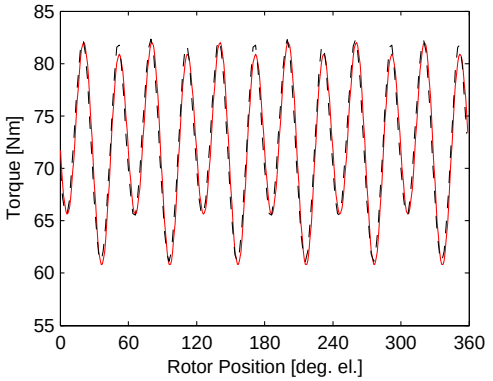

(e) Non-skewed

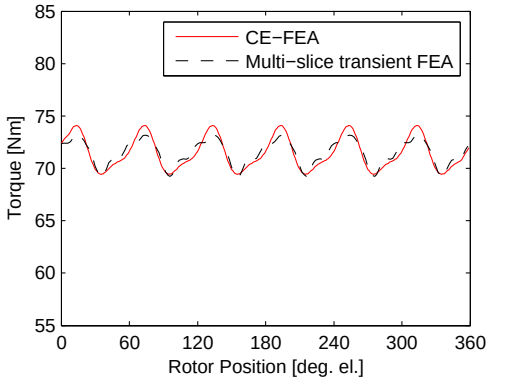

(f) Skewed (30° el.)

Electromagnetic torque at rated-load.

Figure 3.24: **Integer-slot** machine (36-slot, 6-pole, $q = 2$). 2-D CE-FEA calculations are performed with 7 static solutions. Skewed 2-D transient FEA is performed with 2 staggered/sliced machines. Measurement is performed on the motor with two section step-skewed rotor.

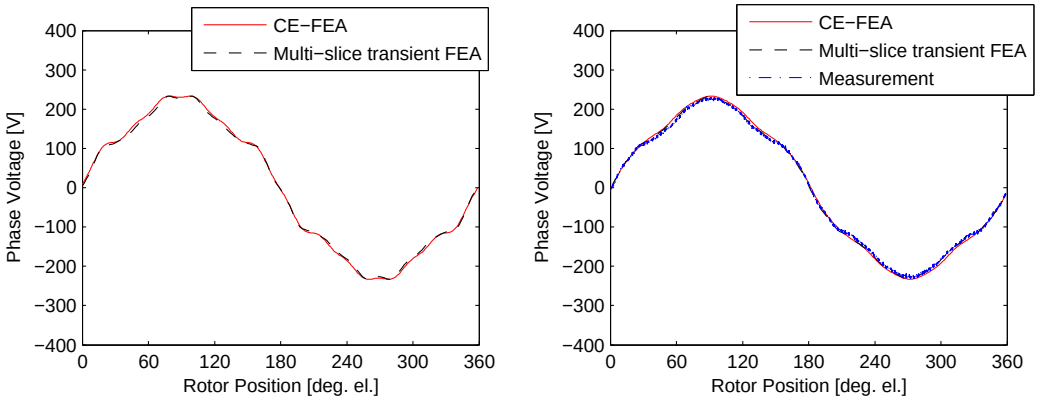

(a) Non-skewed (b) Skewed (30° el.)

Open-circuit phase emf.

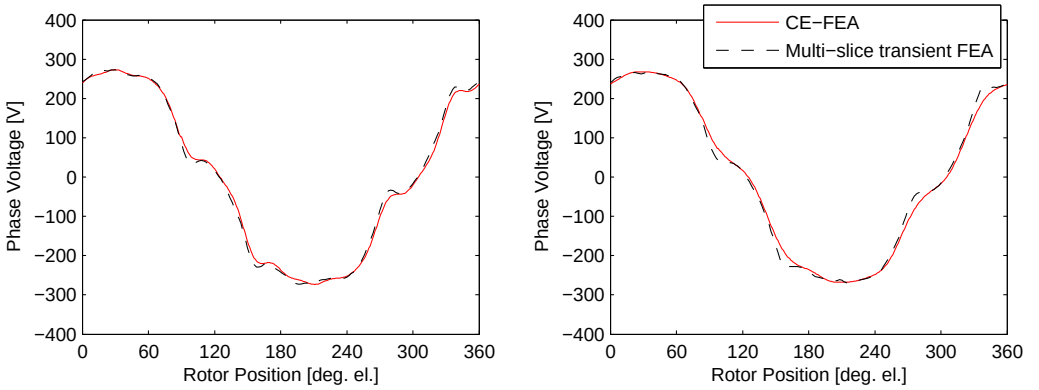

(c) Non-skewed (d) Skewed (30° el.)

Rated-load induced phase voltage (magnet emf and armature).

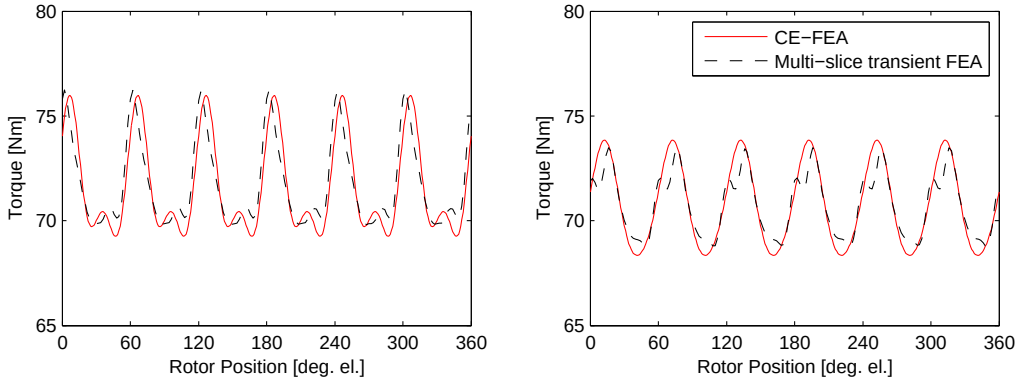

(e) Non-skewed (f) Skewed (30° el.)

Electromagnetic torque at rated-load.

Figure 3.25: **Fractional-slot** machine (9-slot, 6-pole, $q = 0.5$). 2-D CE-FEA calculations are performed with 7 static solutions. Skewed 2-D transient FEA is performed with 2 staggered/sliced machines. Measurement is performed on the motor with two section step-skewed rotor.

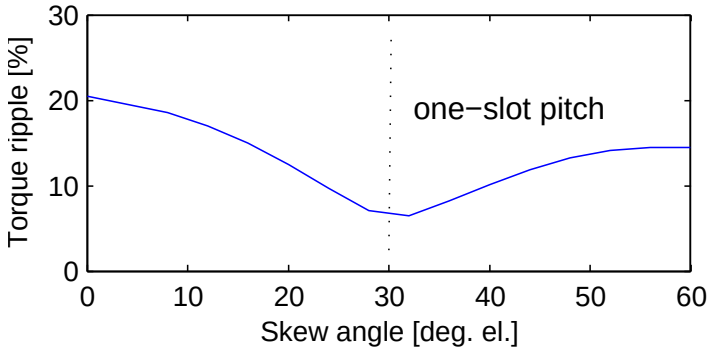

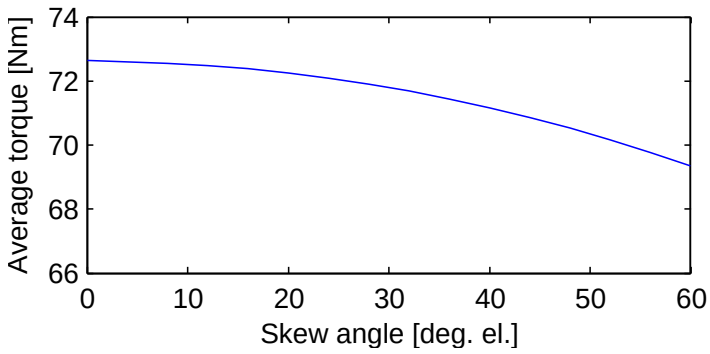

(a) Integer-slot motor

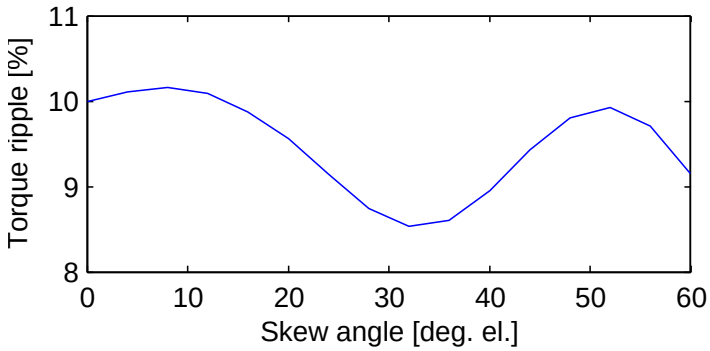

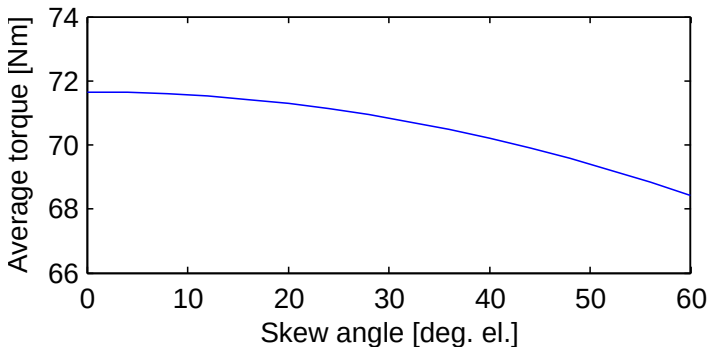

(b) Fractional-slot motor

Figure 3.26: Torque ripple and average torque as a function of skew angle for two case-study motors. Results obtained using CE-FEA and procedure (one CE-FEA evaluation is required).

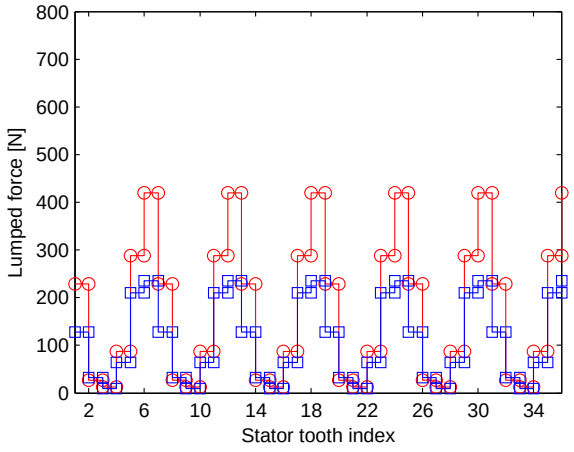

(a) Integer-slot (q=2).

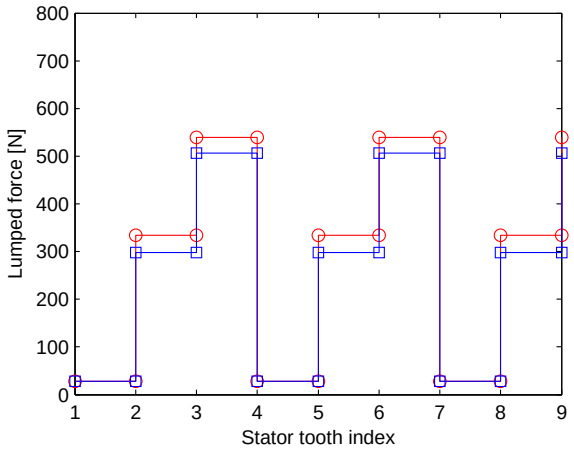

(b) Fractional-slot (q=0.5).

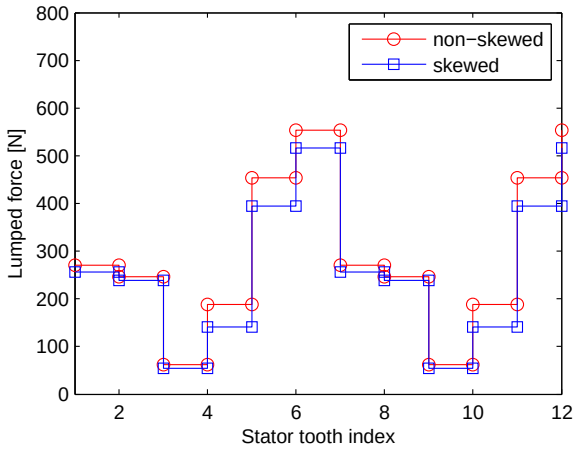

(c) Fractional-slot (q=0.4).

Figure 3.27: Resultant (lumped) stator tooth forces at a given time instant. Also included are the results for the motors with 30° el. step-skewed rotors.

by adding the air-gap stresses along the axial length of the motor core. This assumption effectively states that the forces experienced by the laminations at both ends of the core stack are additive and can be averaged over the skew angle. Effects of skew on the developed stator forces are shown in Fig. 3.27. From Fig. 3.27a, a noticeable reduction of the developed peak tooth force is observed for the integer-slot motor with a skew of one slot-pitch. On the other hand, both fractional-slot concentrated winding motors (Figs. 3.27a and b) have only a marginal reduction in the peak of the developed force. It should be noted that for fractional-slot topologies increasing the skew may have a beneficial effect of reducing the developed tooth forces. However, it will also result in significant reduction of the average torque as can be seen in Fig. 3.26.

3.4 Practical Implementation

3.4.1 Constant Torque and Field Weakening Operation

In the design of interior PM machines constant torque and field weakening operation needs to be considered. In the constant torque mode of operation the maximum torque per amp (MTPA) operating condition has to be identified for every operating condition. This typically requires additional costly model evaluations. In this work, to reduce the number of the required model evaluations two methods are used. The first method relies on FE-based calculation of fundamental phase flux flinkages and the average electromagnetic torque from (3.5) and (3.16), and the assumption of the simplified dq-model given below.

$$\lambda_d = \lambda_{PM} + L_d I_d \tag{3.26a}$$

$$\lambda_q = L_q I_q \tag{3.26b}$$

The procedure is detailed below:

1. Perform one *reduced* CE-FEA evaluation of the motor with q-axis current only. Deter-

mine permanent magnet flux linking the stator, λ_{PM}, and q-axis apparent inductance, L_q, using the following:

$$\lambda_{PM} = \lambda_d, \tag{3.27}$$

$$L_q = \frac{\lambda_q}{I_q}. \tag{3.28}$$

2. Perform an additional *reduced* CE-FEA evaluation of the motor with the current phasor advanced by an arbitrary advance angle. Determine the d-axis inductance using the values of permanent magnet flux linkage, λ_{PM}, obtained in step (1) by the following relationship:

$$L_d \approx \frac{\lambda_d - \lambda_{PM}}{I_d}. \tag{3.29}$$

3. The average electromagnetic torque for a fixed current magnitude as a function of the torque (advance) angles can be estimated using equation (3.30):

$$\begin{aligned} T_{em} &= \frac{3}{2}\frac{P}{2}\left(\lambda_{PM} I_q + (L_d - L_q) I_d I_q\right) \\ &= \frac{3}{2}\frac{P}{2}\left(\lambda_{PM} I_m \cos(\gamma) - \frac{1}{2}(L_d - L_q) I_m^2 \sin(2\gamma)\right). \end{aligned} \tag{3.30}$$

The procedure described above assumes that changes in the core saturation pattern resulting from the current phasor advance are minimal. Furthermore, it assumes no cross-axis mutual coupling (λ_{dq}) effect. On the other hand, if the advance angle is selected to be too small (resulting in the small value of the d-axis current) errors in calculation of the apparent d-axis inductance ($\frac{\lambda_d - \lambda_{PM}}{i_d}$) can be significant. Therefore, it is recommended to select the advance angle to be in the range of 15° to 30° electrical to avoid errors. This method provides additional information about the motor in the form of the saturated dq-parameters. For more accurate estimation of saturated dq-parameters a "frozen" permeability method [15–18] can also be used.

An alternative procedure relies on the sampling of the torque characteristic by advancing the current phasor and using curve fitting techniques to approximate the MTPA operating

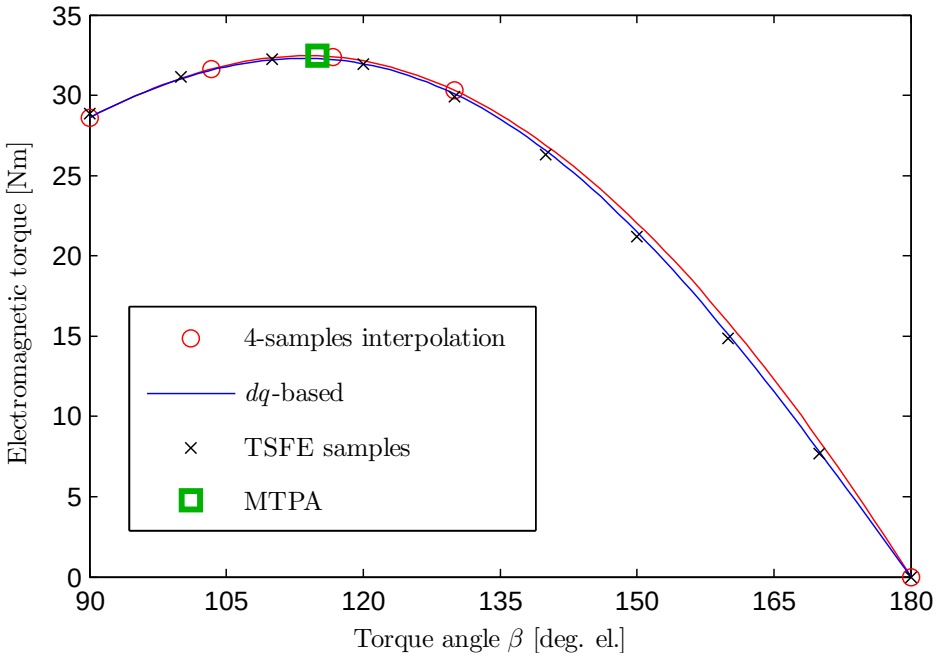

Figure 3.28: Determination of the maximum torque per amp (MTPA) operating condition.

condition. This method requires additional *reduced* CE-FEA evaluations. Reasonable estimation of the MTPA operating condition is possible with 4 CE-FEA evaluations and an additional zero average torque point at 180° advance angle (corresponding to only negative d-axis current). Application of both methods to estimation of the MTPA operating condition is demonstrated in the Fig. 3.28. In Fig. 3.28, both methods are validated with respect to time-stepping FE simulations. In addition provided in Fig. 3.29 is the evolution of the fundamental component of the motor terminal voltage as a function of the torque angle. Fig. 3.30 demonstrates that in some machines the instantaneous peak voltages can be significantly higher than the fundamental component resulting in potential problems associated with motor current regulation at high speeds stemming from inverter dc-bus voltage limitations.

In this work both methods were implemented to facilitate determination of the optimum motor operating conditions and saturated motor parameters. A combination of two

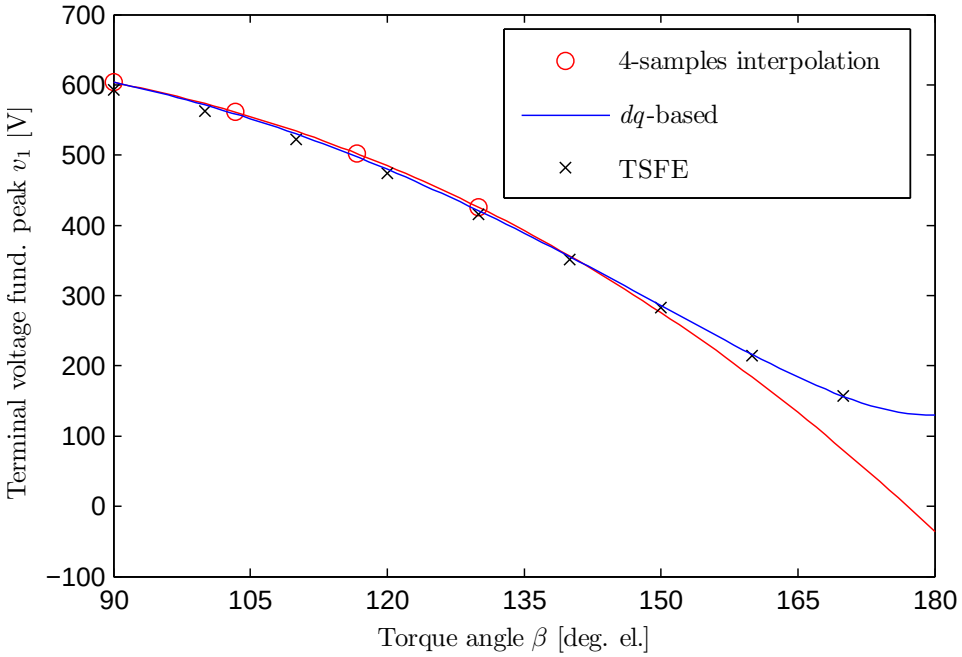

Figure 3.29: Fundamental component of terminal line voltage as a function of torque (advance) angle β.

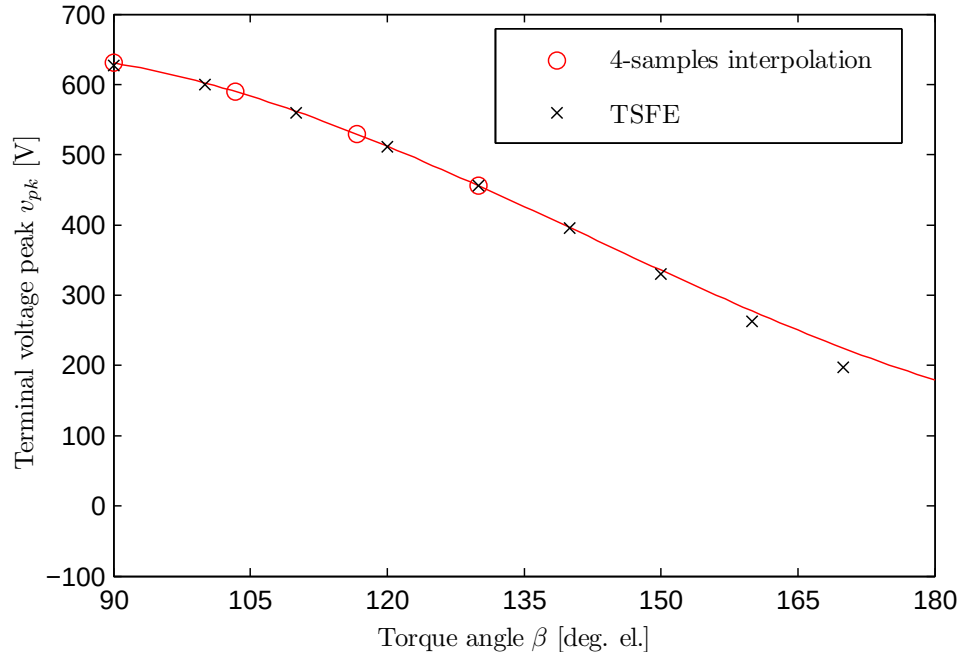

Figure 3.30: Peak of the total (including all harmonics) line voltage as a function of torque (advance) angle β.

approaches allows one to rapidly estimate machine performance and relevant parameters.

3.4.2 Discussion on Possible Aliasing Effects

In the CE-FEA, Fourier analysis is used for the construction of the magnetic vector potentials, flux linkages, back emfs, and energy waveforms. Since the Fourier analysis is applied to a finite set of samples, aliasing of higher order harmonics is possible, with the error depending on the magnitudes of the harmonics that are cut-off (truncated) from the Fourier series. Such errors in the flux linkages will be further amplified in the back emf and induced voltage due to the differentiation process and will therefore also affect the torque estimation. This places a constraint on the minimum number of magnetostatic FE solutions, s, which depends mainly on the magnitude and order of the highest harmonic present in the waveform. In other words, if a small number of solutions is performed resulting in a number of samples insufficient for capturing higher order harmonics (which may have significant magnitudes), aliasing will occur leading to errors. Aliasing errors will be further amplified in the derivative process associated with calculation of the induced voltage in (3.6). The magnitude of the aliasing error is highly dependent on the machine design parameters and operating point conditions. For some fractional slot concentrated winding machines, such as the one used here for demonstration, the error may be more significant due to the fact that the on-load flux linkage and induced back emf waveforms (Fig. 3.3) have a rich harmonic content, which is dependent on the current amplitude and the torque angle. The frequency spectrum of the phase induced back emf waveform under rated-load condition (Fig. 3.31) shows that in the example motor the harmonics higher than the 13th order are negligible. Hence, by applying (3.7) one can choose the number of solutions, $s = 5$, in order to avoid aliasing. The effect of aliasing on the estimation of the fundamental component of the induced back emf and on the average torque calculation in (3.16) is illustrated in Fig. 3.32, showing that, in this case, a further increase (beyond $s = 5$) in the number of static solutions will not provide additional accuracy in the estimation of the average torque.

On the other hand, it is expected that in cases of distributed winding machines, and especially those with short-pitched windings, and/or machines with well-shaped (sinusoidal) rotor mmf waveforms as few as one FE solution may be required in order to obtain an accurate estimate of the average torque. This is due to the fact that such machines have low harmonic content and, hence, an insignificant error due to aliasing. Here, it should be noted that when the ripple torque needs to be considered with high precision in the overall torque production, one could increase the number of solutions in order to provide sufficient harmonic resolution of the stored energy and hence of the cogging torque component. This is further verified with additional results presented in Figs. 3.33 through 3.35. Shown in Figs. 3.33 *a* and *b* are the flux density and flux distributions corresponding to the machine operating at 120° and 170° torque angles, respectively. As expected under the deep field weakening operating condition, corresponding to 170° torque angle (Fig. 3.33b), significant reduction of resulting flux densities due to high armature mmf demagnetization is observed. This results in a significant reduction of the fundamental induced voltage component, as can be observed from Fig. 3.34. Shown in Fig. 3.34 are the induced voltages for the machine operating under 120° and 170° torque angles, respectively. Also shown in Fig. 3.35 are the developed torque profiles, corresponding to the two operating conditions, estimated using CE-FEA and TSFE, respectively. Again, from Figs. 3.34 and 3.35, good agreement between the CE-FEA employing 5 magnetostatic solutions and detailed TSFE simulations for a wide range of operating conditions should be noted.

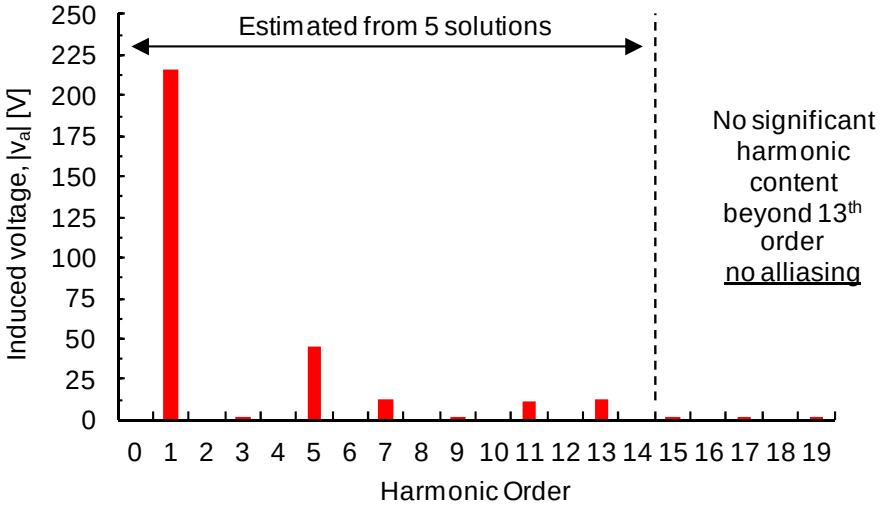

Figure 3.31: Harmonic analysis of the induced phase terminal voltage for the machine shown in Fig. 3.1 operating at rated load.

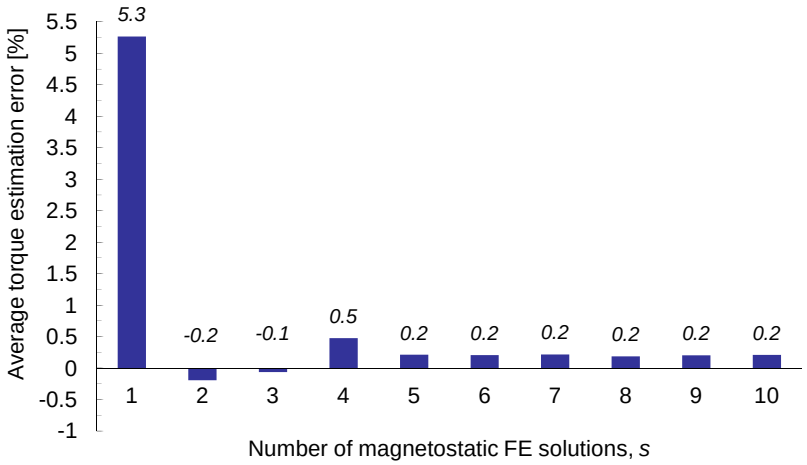

Figure 3.32: Error of the average torque computed with CE-FEA and with a TSFE simulation.

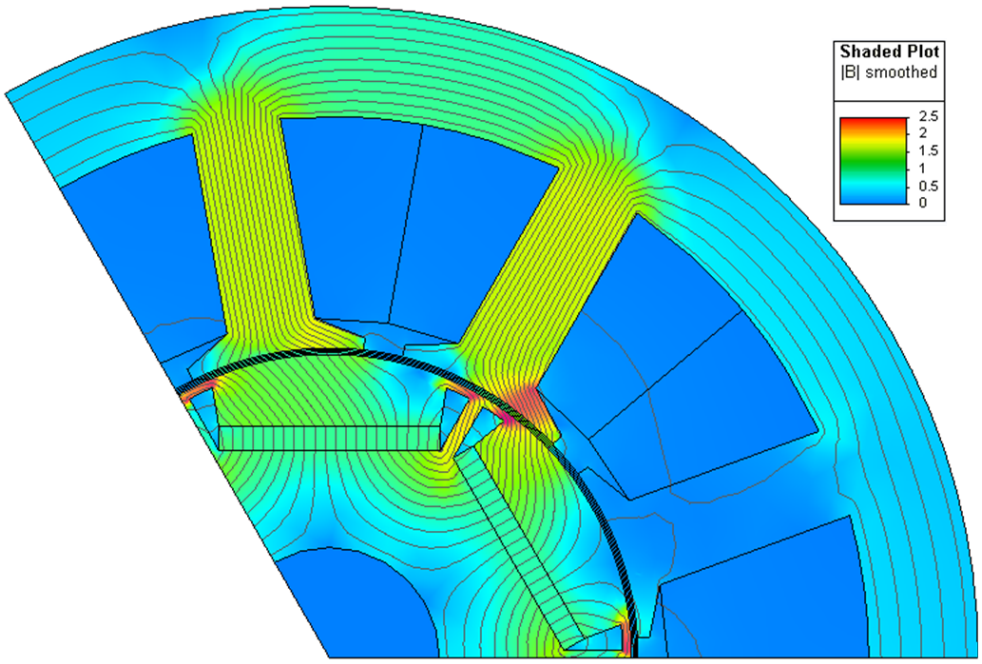

(a) Rated-load, MTPA, torque angle 120°

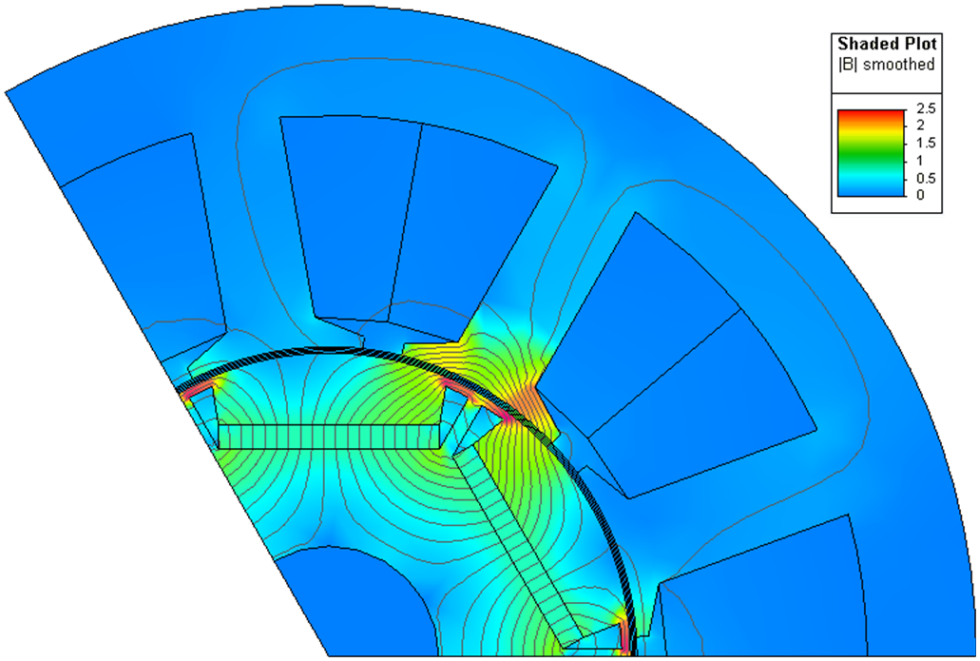

(b) Field weakening, torque angle 170°

Figure 3.33: Flux density distributions for: a) maximum torque per amp condition (120° torque angle), and b) flux weakening operation (170° torque angle).

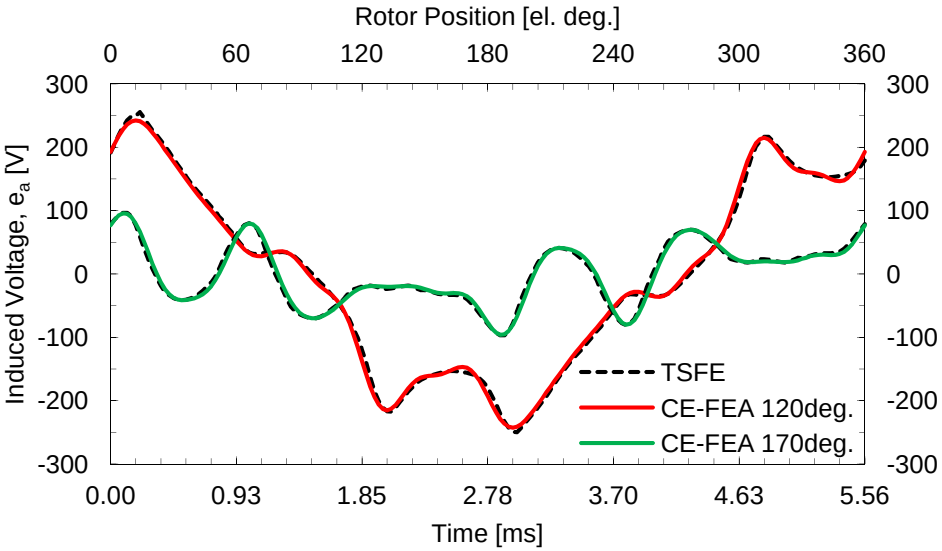

Figure 3.34: Induced voltage profiles corresponding to maximum torque per amp condition (120° torque angle), and flux weakening operation (170° torque angle).

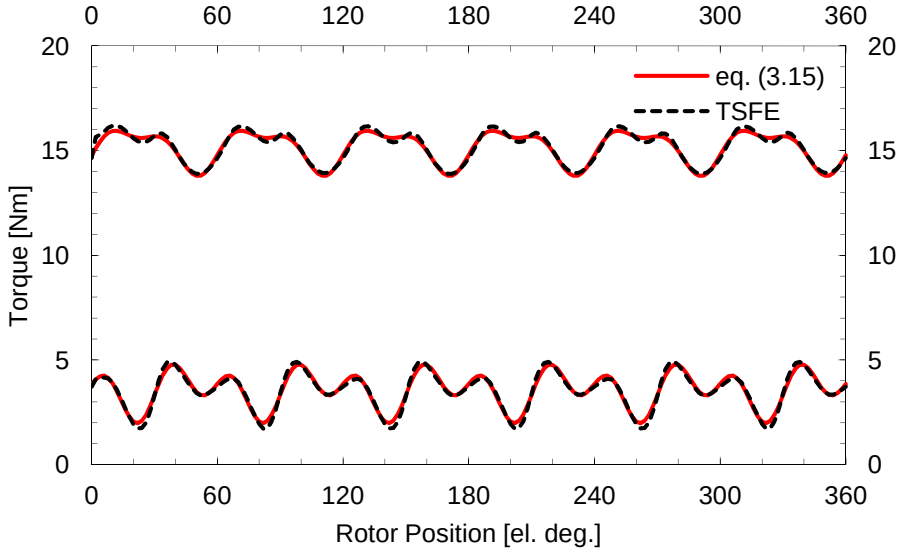

Figure 3.35: Developed torque profiles corresponding to maximum torque per amp condition (120° torque angle), and flux weakening operation (170° torque angle).

3.4.3 Discussion on Mesh Density and Finite Elemental Order

Effects of mesh density on the performance parameters and execution time are presented in Table 3.3. Results presented in Table 3.3 are compared to a detailed time-stepping FE model employing a fine mesh and second order elements. As can be seen from Table 3.3, the best accuracy in estimation of the average torque, torque ripple, and induced voltage are obtained with second order elements. It should be noted that an FEA based solely on first order elements may be sufficient for estimation of the average torque. Hence, a CE-FEA based on first order elements may be used in the search for an optimum operating condition (maximum torque per amp) or field weakening capability evaluation. On the other hand, a more detailed and computationally intensive CE-FEA based on second order finite elements can be used for detailed analysis that includes accurate cogging torque and torque ripple calculation. Also, provided in Table 3.3 are computational times averaged over several simulations on a Intel-Xenon E5520 2.27GHz workstation with 4GB-RAM.

Table 3.3: Effects of Mesh Density and Finite Element Order on CE-FEA Estimation Accuracy and Computational Time.

Mesh Density/Order	Error Torque [%]		Error Voltage [%]		Computational Time [s]
	Avg.	Ripple	Fund. e_1	THD	
Coarse (2787 el.) 1st order	0.18	13.68	2.20	4.12	5.7
Fine (4262 el.) 1st order	0.17	10.72	0.55	3.67	7.6
Coarse (2787 el.) 2nd order	0.15	2.45	0.25	1.70	9.8

3.5 CE-FEA in Motor-Drive System Simulations

Detailed co-simulation of the motor-drive system that accounts for space-harmonics and saturation of the electromagnetic core is a time consuming task that typically requires a coupled simulation of the drive power circuit and FE-based motor model. An alternative approach relies on creating a look-up-table (LUT) based motor model that can be used in a power circuit simulation without the computational burden associated with FE-based model. The LUT model capturing a wide operating range can be constructed offline using the FE-based solver. Example of the complex relationships between the operating condition and motor harmonic flux linkages is demonstrated in Figs 3.36. Shown in Fig. 3.36a is the variation of the magnitude of the fundamental phase flux linkage with respect to the terminal dq currents. The fundamental component of the phase flux linkage can be reduced to zero when sufficiently large demagnetizing d-axis current is injected in to the winding. This current is referred to as characteristic current of the machine. The relationships between higher order flux harmonics and excitation currents are more difficult to interpret, as can be seen from Figs. 3.36b and c for the 5th and 7th flux linkage harmonics.

The modeling approach described in this chapter can be extended to simulations that include motor-drive-controller interactions. Effects of complex electromagnetic phenomena related to position dependent flux variations and core saturation can be efficiently simulated using CE-FEA in combination with a LUT-based machine model. The CE-FEA method is used to construct flux linkage LUTs that capture nonlinear relationships between instantaneous stator armature currents, rotor position and

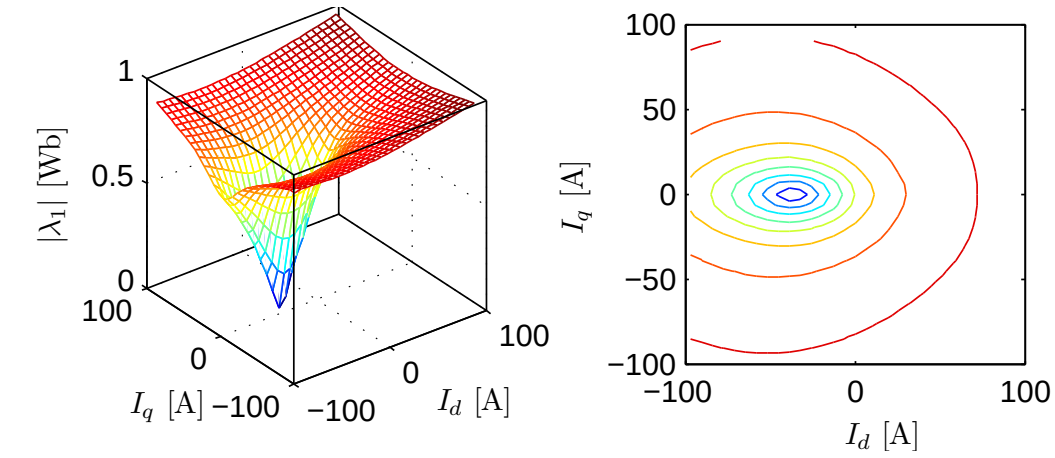

(a) Fundamental harmonic

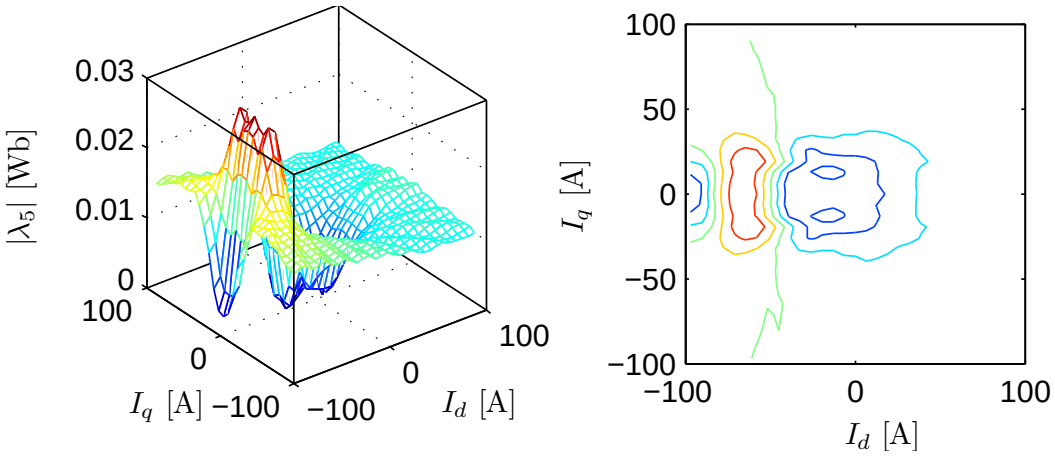

(b) 5th harmonic

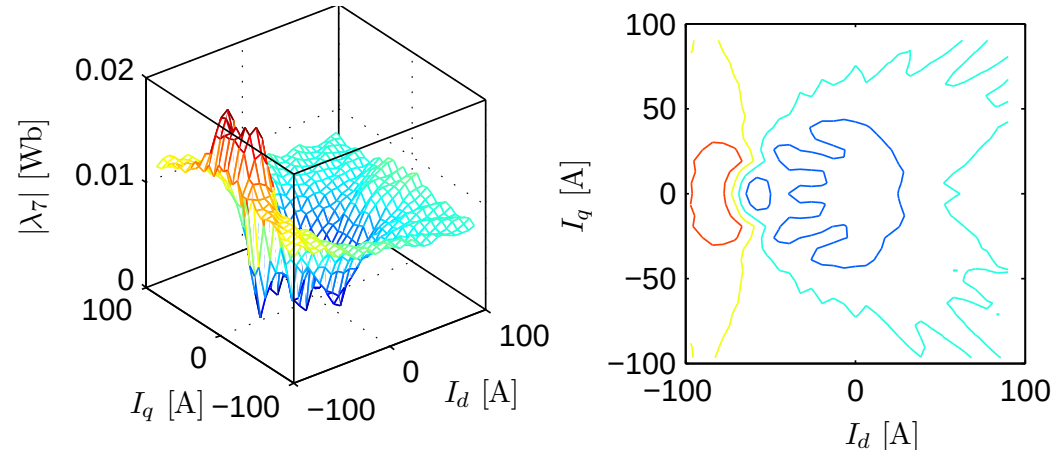

(c) 7th harmonic

Figure 3.36: Variation of the phase flux linkage harmonic magnitudes with operating condition.

flux linkages as follows:

$$\lambda_d = \lambda_d(i_d, i_q, \theta) \tag{3.31a}$$

$$\lambda_q = \lambda_q(i_d, i_q, \theta). \tag{3.31b}$$

Similarly, to capture the effects of variation of stored energy on torque ripple an LUT of the stored energy for various load conditions can be constructed from the simulations used in construction of (3.31) as:

$$W_{stored} = W_{stored}(i_d, i_q, \theta). \tag{3.32}$$

Shown in Figs. 3.37 and 3.38 are the dq flux linkages at several rotor positions obtained by performing 900 (30×30) CE-FEA evaluations of the 36-slot motor operating at various load conditions. Variation of d-axis flux linkage with rotor position can be observed by comparing Figs. 3.37a and 3.37b. This variation is caused by a combination of the space harmonics related to winding layout and position dependent variation of core saturation. Also, examining Figs. 3.37 and 3.38 cross-axis saturation between the d and q-axes should be noted. The LUT-based motor model uses phase flux linkages as state variables and is shown in the block diagram of Fig. 3.39. Current-flux relationships ($i - \lambda$) are provided below:

$$i_d = i_d(\lambda_d, \lambda_q, \theta) \tag{3.33a}$$

$$i_q = i_q(\lambda_d, \lambda_q, \theta). \tag{3.33b}$$

which are obtained directly from LUTs of Figs. 3.37 and 3.38 as shown for one specific rotor position in Fig. 3.40.

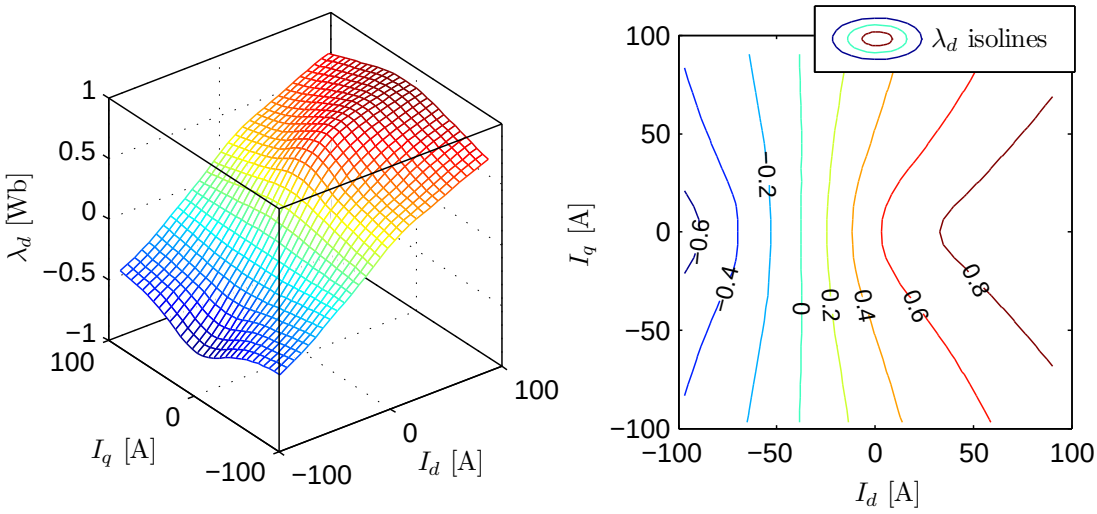

(a) d-axis flux linkage ($\theta = 0°$)

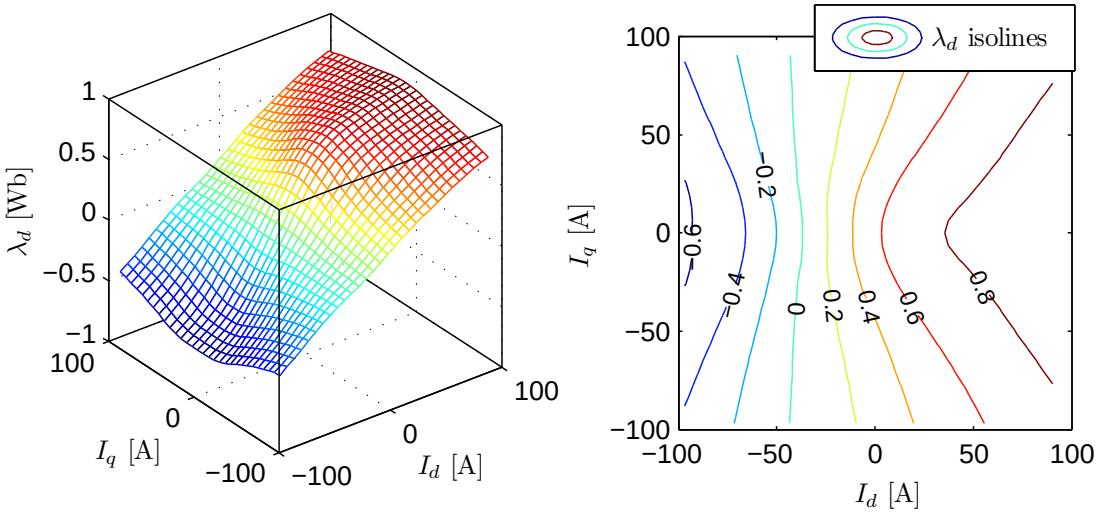

(b) d-axis flux linkage ($\theta = 30°$)

Figure 3.37: d-axis flux linkage as a function of dq currents and rotor position.

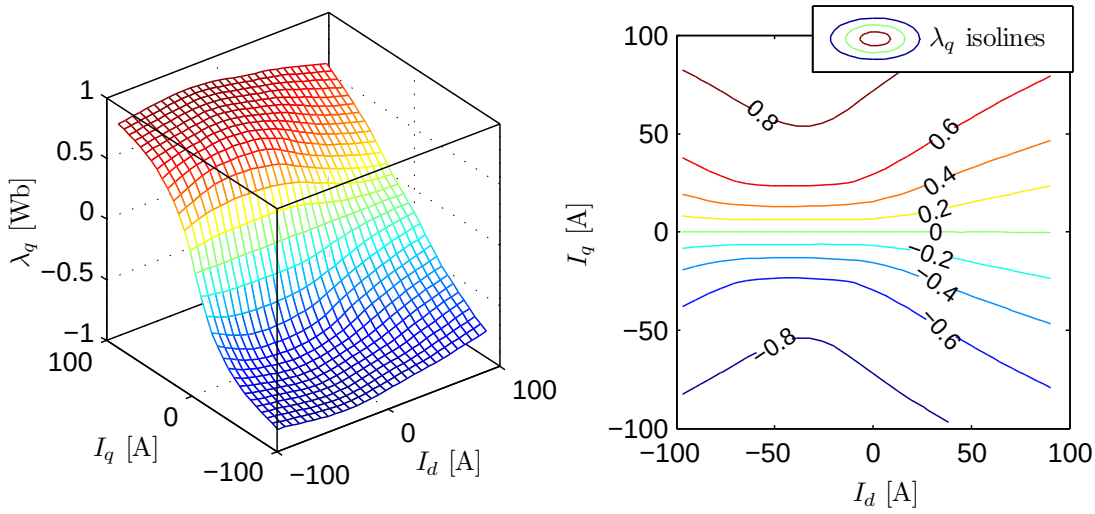

(a) q-axis flux linkage ($\theta = 0°$)

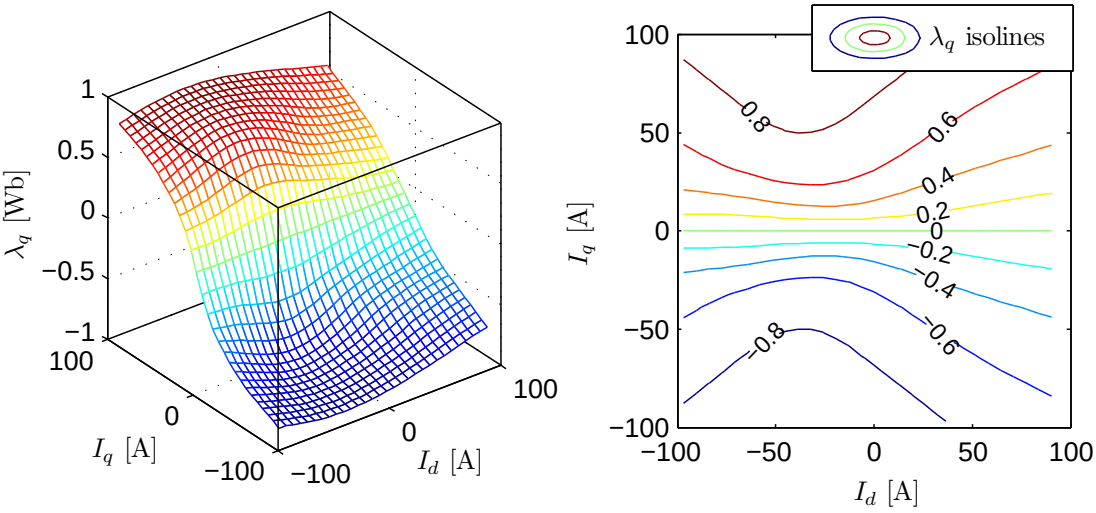

(b) q-axis flux linkage ($\theta = 30°$)

Figure 3.38: q-axis flux linkage as a function of dq currents and rotor position.

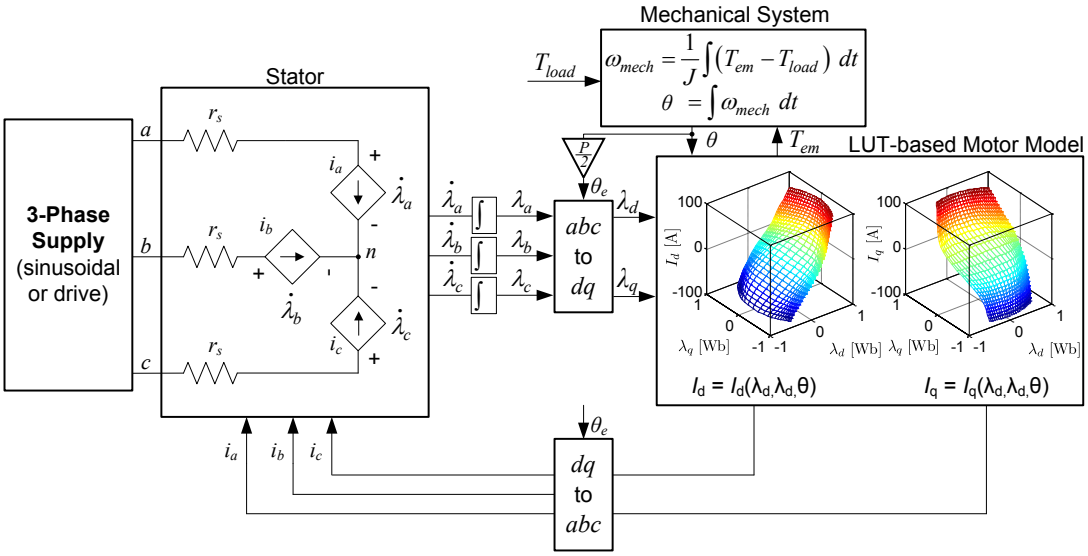

Figure 3.39: Block diagram of the motor-drive LUT-based model.

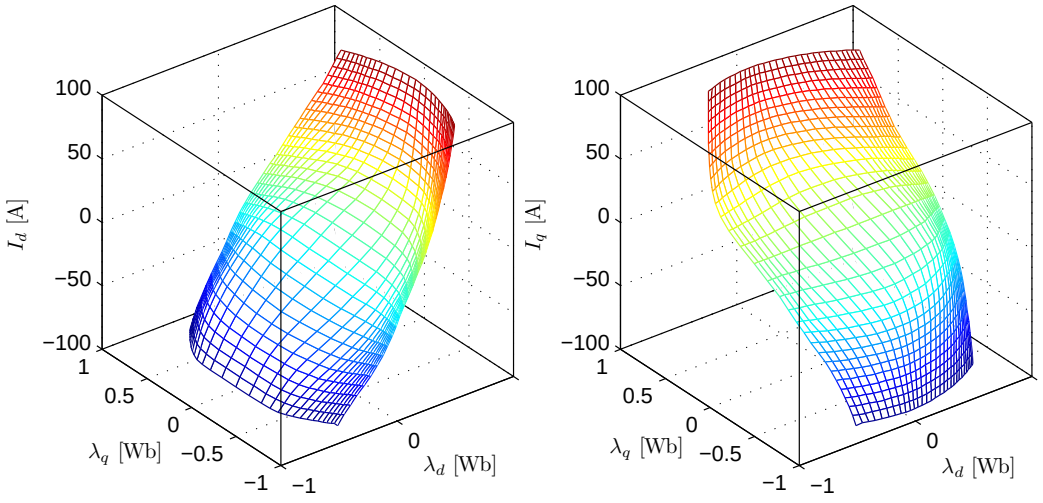

(a) d-axis current ($\theta = 0°$) (b) q-axis current ($\theta = 0°$)

Figure 3.40: Inverse relationships between dq flux linkages and motor currents.

Example application of the LUT-based model in the time-stepping simulation of the current regulated motor-drive system is shown in the block diagram of Fig. 3.41. A synchronous current regulator is used to control motor currents and provides gate signals to the power circuit model of the inverter, which is coupled to the LUT-based model of the IPM motor. The model is implemented in a Matlab-Simulink environment. The current and voltage profiles of the motor-drive steady-state operation with PWM supply are shown in Fig. 3.42. Dynamic simulation of the performance of the motor-drive system is shown in Fig. 3.43. This type of simulation performed with conventional direct coupling between the FE solver and the circuit/system solver is time consuming, especially when switching ripples are considered. In comparison to conventional circuit coupled FE simulations the proposed method results in significant reduction of simulation time and decouples the FE modeling from the circuit and system simulation while preserving the fidelity of the FE-based model. The LUT-based model properly accounts for machine nonidealities related to saturation and space harmonics typically not considered in simplified dq-based machine modeling used in system level simulations.

In summary, this chapter presented the computational method that allows one to rapidly estimate major steady-state performance parameters of synchronous electric machines. A method for calculation of phase flux linkages, induced voltage waveforms, stator core losses, developed electromagnetic torque, air-gap forces, and saturated equivalent circuit parameters (inductances and permanent magnet flux linkage) was presented. The method of stator core flux density calculations was extended and generalized to account for effects of different stator winding layouts. A technique for including three dimensional effects of stator and (or) rotor skew was provided. In addition, application of the method to high fidelity system level simulations was presented. The method exploits electromagnetic and electric circuit symmetries of the electric machine and relies on a reduced set of FEA simulations to extract samples of electromagnetic field and electric circuit quantities that are used to construct Fourier series. The number of required simulations has to be selected to such that

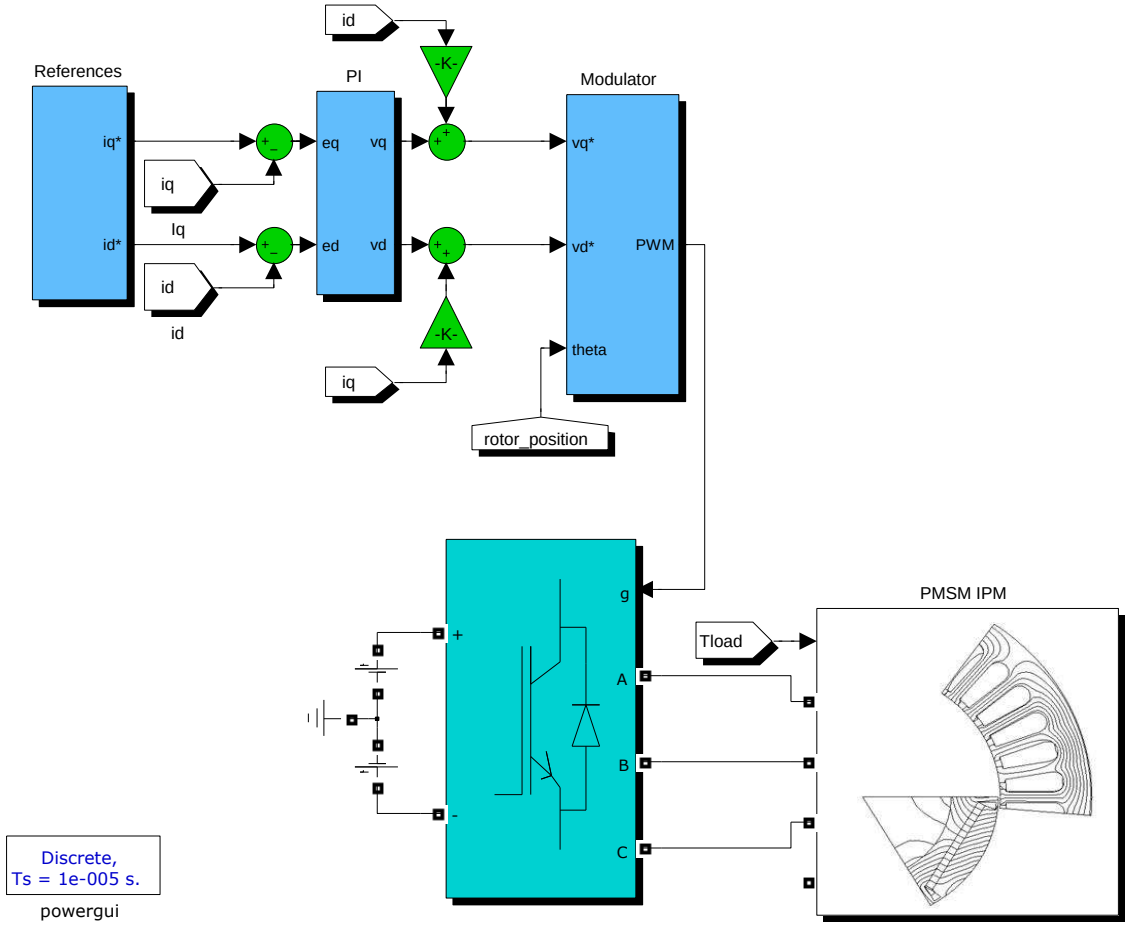

Figure 3.41: Block diagram of the Simulink motor-drive simulation model. Also shown is the synchronous current regulator used to regulate motor current.

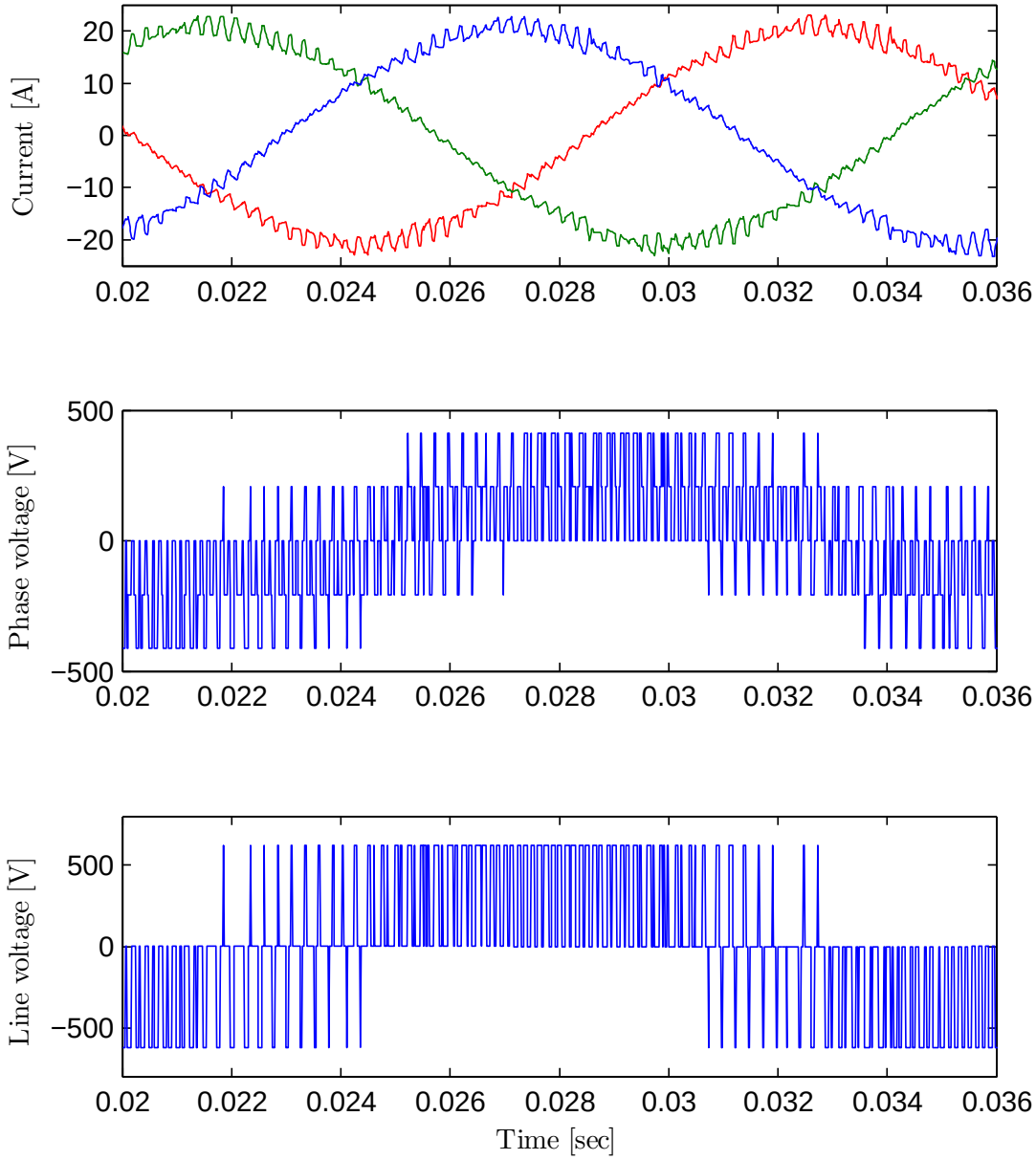

Figure 3.42: Simulated current, phase and line voltage waveforms of 36-slot 6-pole IPM synchronous motor operated with a 4 kHz current regulated SVPWM drive using LUT-based motor model.

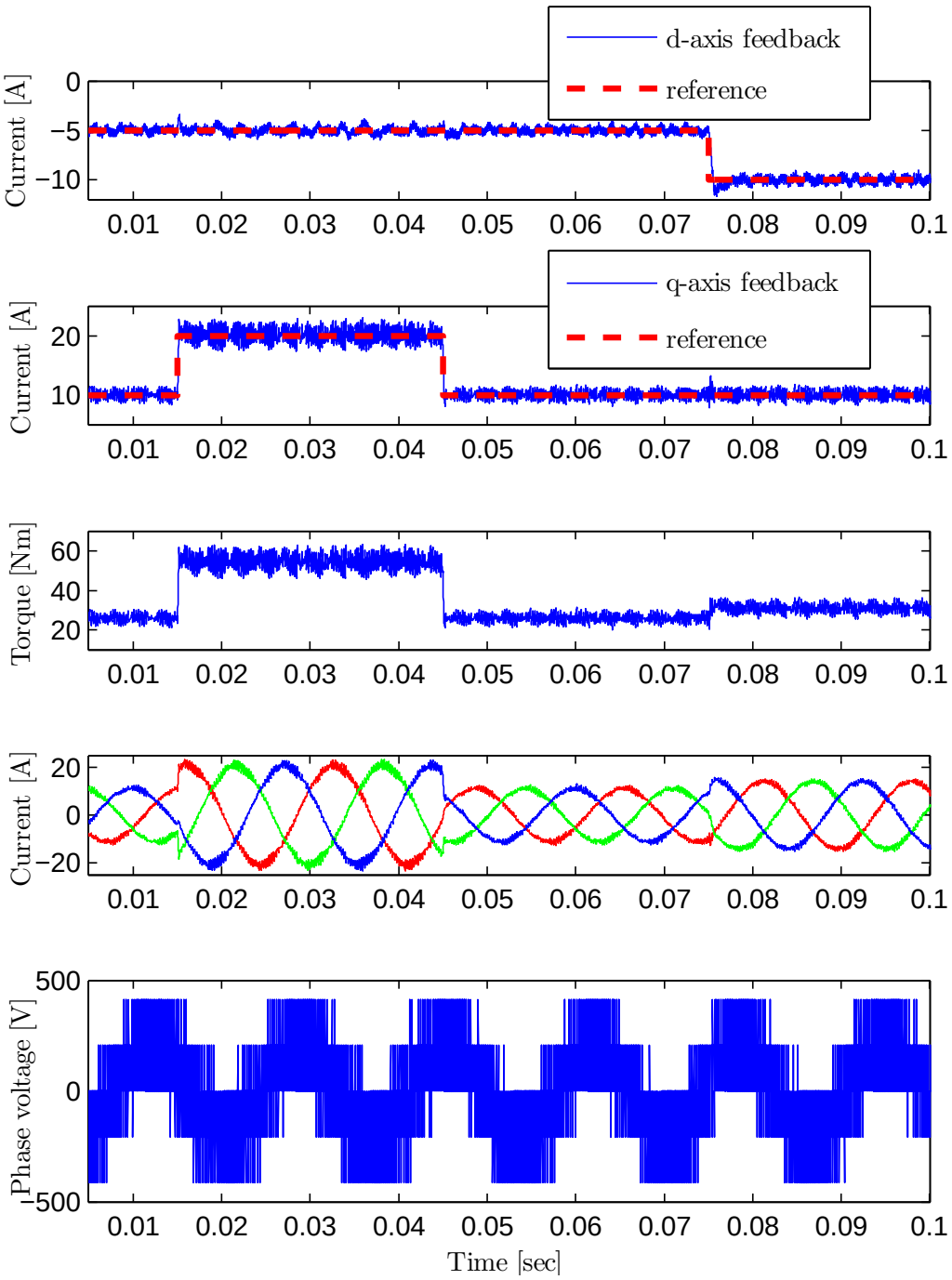

Figure 3.43: Simulated dynamic performance of the 36-slot 6-pole IPM synchronous machine using LUT-based motor model.

one avoids (or minimizes) aliasing effects. The number of FEA solutions varies from 1 to 3 static solutions for average torque extraction, and 5 to 9 static solutions for complete machine analysis that includes waveforms/profiles of the electromagnetic torque, terminal flux linkages, induced terminal voltages, stator core flux densities and core losses. In comparison to the well-established time-stepping (transient) FEA method, the developed analysis technique results in one-to-two orders of magnitude of reduction in simulation time. The time-stepping analysis may require anywhere between 60 to 720 solutions per electrical cycle to estimate terminal voltages which require a noise sensitive differentiation of winding flux linkages. The method was demonstrated on several fractional-slot and integer-slot motor topologies and validated with respect to experimental measurements and significantly more computationally intensive simulation using time-stepping finite element models. The method was implemented using scripting facilities available within two commercially available FEA packages, namely, ANSYS Maxwell [110] and Infolytica MagNet [111]. Application of the method to the problem of electric machine optimization will be demonstrated in the next chapter.

Chapter 4

Design Optimization and Synthesis

4.1 Introduction

In this chapter, an automated design tool that couples the CE-FEA computational method and the Differential Evolution (DE) optimizer [112] is presented. The method is demonstrated on two comprehensive, large-scale design optimization studies that involve evaluation of thousands of candidate designs. The first design study shows the application of the automated tool to the optimization of the existing design. This study demonstrates the possibility of torque-dense and torque ripple free design of the interior-PM motor with three slots per pole pair. The second design study shows the application of the method to the systematic motor topology comparison where four high-power motor topologies are compared based on the optimal Pareto sets. The following four case-study machines are optimized and compared based on optimal Pareto sets: fractional-slot embedded surface-PM (SPM), fractional-slot interior-PM (IPM), integer-slot embedded SPM, and integer-slot IPM. In both examples, a large number of stator and rotor variables are used to automatically optimize the average torque, efficiency, the cogging and the ripple torques. Two additional examples demonstrating the application of the automated procedure to design and prototyping of two industrial motors is provided. In the first example, the method is applied to the design of a 15kW (20hp) motor for a hermetic compressor application. In the second example, the method is applied to the design of a 22kW (30hp) general purpose motor.

The block diagram of the proposed model-based design optimization is shown in Fig.4.1. In this figure, a DE algorithm is used to dynamically update and improve the candidate

design population, and the CE-FEA is used to extract the objectives (average and ripple torques, core losses, saturated inductances, etc.). It should be noted that for the case-study IPM machine parameters, such as the average electromagnetic and shaft torques, torque ripples, and efficiency, are extracted at a single load point from several magnetostatic field solutions. These solutions take several seconds to execute using a typical PC-based workstation. The CE-FEA is applicable to steady-state analysis of sine-wave energized current-regulated synchronous machines. In the CE-FEA a static nonlinear finite element solver is utilized and significant computational savings are obtained by utilizing additional symmetries of the magnetic circuit (beyond odd/even periodicity conditions) and electric circuits. The machine is analyzed/evaluated at several rotor positions with corresponding sequentially-sampled phase current excitations based on the sinusoidal current waveform. Outputs such as the magnetic vector potentials, phase flux-linkages, and stator core flux-densities are reconstructed using the waveform symmetry conditions that stem from the magnetic and electric circuit symmetries. Corresponding Fourier series of the reconstructed quantities are obtained paying special attention to possible aliasing effects. As a result, using the CE-FEA, performance parameters such as the back-emf waveforms, average torque, profiles of cogging torque and torque ripples, as well as stator core losses can be extracted from a minimum number of magnetostatic FE solutions. This leads to a significant reduction of execution times when compared to the laborious TSFE approaches, while preserving the main benefits of FE solvers, i.e., accuracy of geometric shape and magnetic saturation representations. For example, to evaluate a candidate motor at a single operating condition CE-FEA requires as few as 3 magnetostatic solutions (3 rotor positions) for *average* torque, and 6 solutions (6 rotor positions) for *detailed* analysis that includes terminal voltage, torque ripple and accurate core loss calculation.

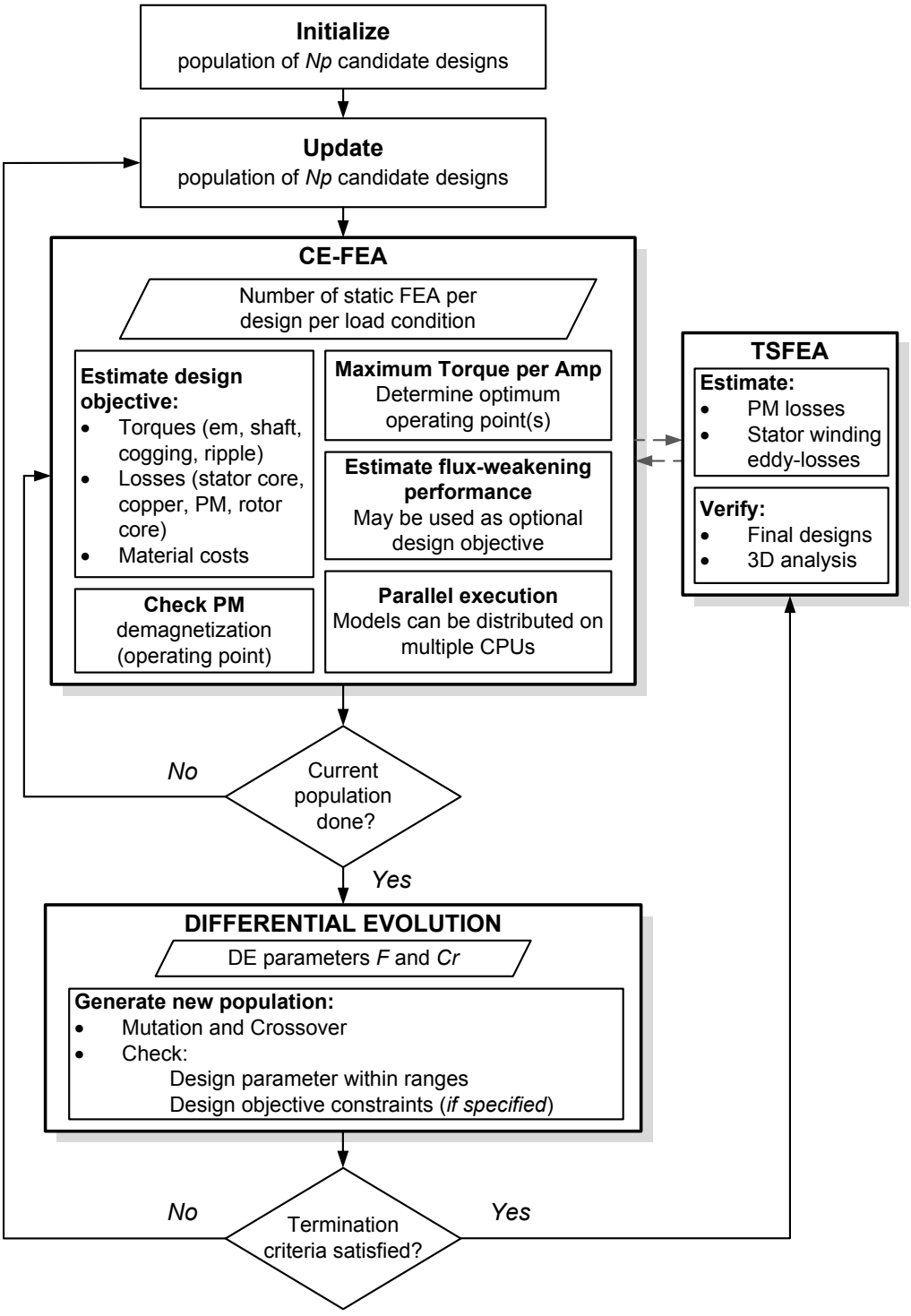

Figure 4.1: Block diagram for model-based design optimization procedure employing Computationally Efficient-FEA (CE-FEA) and Differential Evolution (DE) optimizer.

4.2 Overview of the Differential Evolution (DE) Algorithm

The differential evolution algorithm belongs to the wide-class of meta-heuristic optimizers that attempts to find a global minimum/maximum by iteratively improving a population of candidate designs until the stopping (convergence) criteria are satisfied [112]. The differential part of the DE algorithm implies that unlike other derivative-free population based evolutionary algorithms (Genetic Algorithms, Particle Swarms, Simulated Annealing, etc.) DE utilizes a weighted difference between candidate designs to facilitate the improvement of future generations. The DE approach has been shown to outperform most population based evolutionary algorithms on a number of bench mark test functions [71, 112–114].

In DE the population, $\mathbf{P}_g$, and individual population members, $\mathbf{x}_{g,k}$, of which it is composed are defined as follows:

$$\mathbf{P}_g = [\mathbf{x}_{g,1}, \mathbf{x}_{g,2}, ..., \mathbf{x}_{g,k}],\ g = 0,\ 1,\ 2,\ ...,\ G_{max},\ k = 0,\ 1,\ 2,\ ...,N_p \tag{4.1}$$

$$\mathbf{x}_{g,k} = [x_1, x_2, ..., x_i],\ i = 0,\ 1,\ 2,\ ...,\ p \tag{4.2}$$

where, G_{max}, is the maximum number of generations, Np, is the number of members in a generation and, p, is the number of design parameters (variables) that describes an individual member of the population. The initial population, $\mathbf{P}_0$, is randomly initialized using predefined lower and upper parameter boundaries (variable ranges), b_{Li} and b_{Ui}, respectively. For the first generation, random initialization of individual parameters, x_i, within a bounded parameter space is performed using the following:

$$x_i = b_{Li} + rand(0,1)(b_{Ui} - b_{Li}). \tag{4.3}$$

where, $rand(0,1)$, is a randomly generated number. A similar approach is used during

mutation to ensure that design parameters, x_i, remain within the feasible region specified by b_{Li} and b_{Ui}.

In DE's most basic form, the parameters, u_i, of the new trial member, $\mathbf{u}$, are updated based on mutation and crossover ideas given in the following:

$$u_i = \begin{cases} x_{r0} + F(x_{r1} - x_{r2}) & \text{if } (rand(0,1)) \leq C_r, \\ x_i, \end{cases} \tag{4.4}$$

where, x_i, is the parameter of the current population member, and $x_{r0} + F(x_{r1} - x_{r2})$, is the mutation operation applied to the parameters of the three randomly selected current population members,$\mathbf{x}_{g,r0}$, $\mathbf{x}_{g,r1}$, and $\mathbf{x}_{g,r2}$, with F being a positive real difference scale factor. The mutation operation is carried out only if the following crossover condition is satisfied, $rand(0,1) \leq C_r$, where, C_r, is a predefined crossover probability. Once the trial member, $\mathbf{u}$, is created its objective function, $f(\mathbf{u})$, is evaluated and compared to the objective function of the present member, $f(\mathbf{x})$. The trial vector, $\mathbf{u}$, is allowed to enter the population only if it outperforms the present member, $\mathbf{x}$.

The number of members in the generation (population size), Np, difference scale factor, F, and crossover probability, Cr, are selected heuristically [112]. Whereas, the number of design parameters, p, depends on the specifics of the optimization problem. The number of members in the generation (population size), Np, is normally selected to be at least ten times greater than the number of design variables, p. The difference scale factor, F, and the crossover probability, Cr, are selected in the range (0,1). The implementation of the DE algorithm is summarized in a pseudo code provided on next page.

There are two approaches to multi-objective optimization. The straightforward approach is based on a weighted sum of objectives that transforms a multi-objective problem into a simple single-objective case, as given in (4.5):

$$f_1 = \sum_{n=1}^{N} w_n f_n(\mathbf{x}) \tag{4.5}$$

Algorithm 2 DE crossover, mutation and selection (single-objective)

initialize a random generation, $\boldsymbol{P_0} = [\mathbf{x}_{0,1}, \mathbf{x}_{0,2}, ..., \mathbf{x}_{0,k}]$
for every parameter, x_i, of members $\mathbf{x}_{0,k} = [x_1, x_2, ..., x_i]$ **do**

$$x_i = rand(0,1)(b_{Ui} - b_{Li}) + b_{Li}$$

end for
while stopping (convergence) criteria are not satisfied
(or number of max., G_{max}, iterations not reached) **do**
  for every population member, $\mathbf{x}_{g,k}$, in current generation, P_g **do**
    choose random members, $\mathbf{x}_{g,r0}$, $\mathbf{x}_{g,r1}$, $\mathbf{x}_{g,r2}$
    generate a *trial* member, $\mathbf{u}$, by performing *crossover* and *mutation* on every design parameter, x_i, of $\mathbf{x} = [x_1, x_2, ..., x_i]$

$$u_i = \begin{cases} x_{r0} + F(x_{r1} - x_{r2}) & \text{if } (rand(0,1)) \leq C_r, \\ x_i \end{cases}$$

    select *trial* member (if it outperforms the existing member)

$$\mathbf{x}_{g+1,k} = \begin{cases} \mathbf{u} & \text{if } (f(\mathbf{u}) \leq f(\mathbf{x}_{g,k})), \\ \mathbf{x}_{g,k} \end{cases}$$

  end for
end while

However, in this approach a choice of weights, w_n, may have a significant impact on the optimality of the final design. Moreover, the dual nature of some objectives (conflicting/non-conflicting) may lead to problems with proper weight assignment. For a given set of weights, this approach leads to a single optimal design that either maximizes or minimizes the objective function given in (4.5). The second approach to multi-objective optimization problems, used in this work, is based on the Pareto-dominance selection criteria. This approach typically results in the family of the best-compromise designs that provide the designer with a clear view of various trade-offs between a number of Pareto-optimal designs. Pareto-dominance selection criteria can be incorporated into the DE using several approaches outlined in [112] and [115].

In electric machine design, in addition to optimizing certain objectives it is also useful to define inequality constraints. For examples, to avoid permanent magnet demagnetization it is useful to define a constraint that would limit demagnetization to a safe limit. In DE formulation this is best accomplished by the inequality constraint handling method proposed by Lampinen in [112]. In the method proposed in [112], inequality constraint handling is built into the design selection step as follows:

Select the trial vector, $\mathbf{u}$, if:

- trial member, $\mathbf{u}$, satisfies all constraints and has better or equal objective function (or dominates using the Pareto criterion), $f(\mathbf{u}) \leq f(\mathbf{x}_{g,k})$, than current member, $\mathbf{x}_{g,k}$, or
- trial member, $\mathbf{u}$, satisfies all constraints while current member, $\mathbf{x}_{g,k}$, does not, or
- trial member, $\mathbf{u}$, and current member, $\mathbf{x}_{g,k}$, both violate the constraints, but $\mathbf{u}$ is closer to the feasible region.

Alternatively, constraints can be applied in the post-processing stage by screening through generations and eliminating designs that do not meet certain performance constraints. However, this approach may lead to additional unnecessary objective function evaluations in the infeasible region of the design space.

4.3 Case Study - I:

Optimization of a 5.6kW IPM Motor (9-slot, 6-pole)

In this section, an optimization study of an IPM motor (9-slot, 6-pole) with fractional-slot ($q = 0.5$ slots/pole/phase) is discussed. The parametric motor model showing the design variables used to optimize the motor performance is provided in Fig. 4.2. The multi-objective definition of the PM ac machine optimization problem can be summarized as follows:

- *minimize* torque ripple and total losses (core and copper), meanwhile
- *maximize* the torque production per unit volume at rated load.

One way to achieve this is by considering two objectives given by the following:

$$\begin{aligned} &minimize: f_1 = T_{em(pk-pk)}, \\ &maximize: f_2 = \frac{T_{em}}{\sqrt{P_{Cu} + P_{Fe}}}, \end{aligned} \tag{4.6}$$

where, f_1, corresponds to the peak-to-peak torque ripple, and f_2, corresponds to a so-called "goodness" factor, which is a measure of average torque production with respect to total losses. The outside diameter and axial length are fixed during the optimization. In this case, the axial length is then scaled to achieve the desired output ratings of different optimized machine designs. The axial length is then scaled to achieve the desired output ratings of 15Nm at 3600r/min, which corresponds to the power output rating of 5.6kW (7.5hp). Current density and slot fill are fixed at $7\text{A}_{rms}/\text{mm}^2$ and 0.3, respectively. The rare-earth magnet remanence and relative permeability are equal to 1.14 T and 1.1, respectively. Every candidate design for these IPM machines is evaluated at an MTPA condition. The permanent magnet material and steel (M43-26Ga) used in the core construction are fixed. A purely sinusoidal current regulated sine-wave drive is assumed to be energizing such

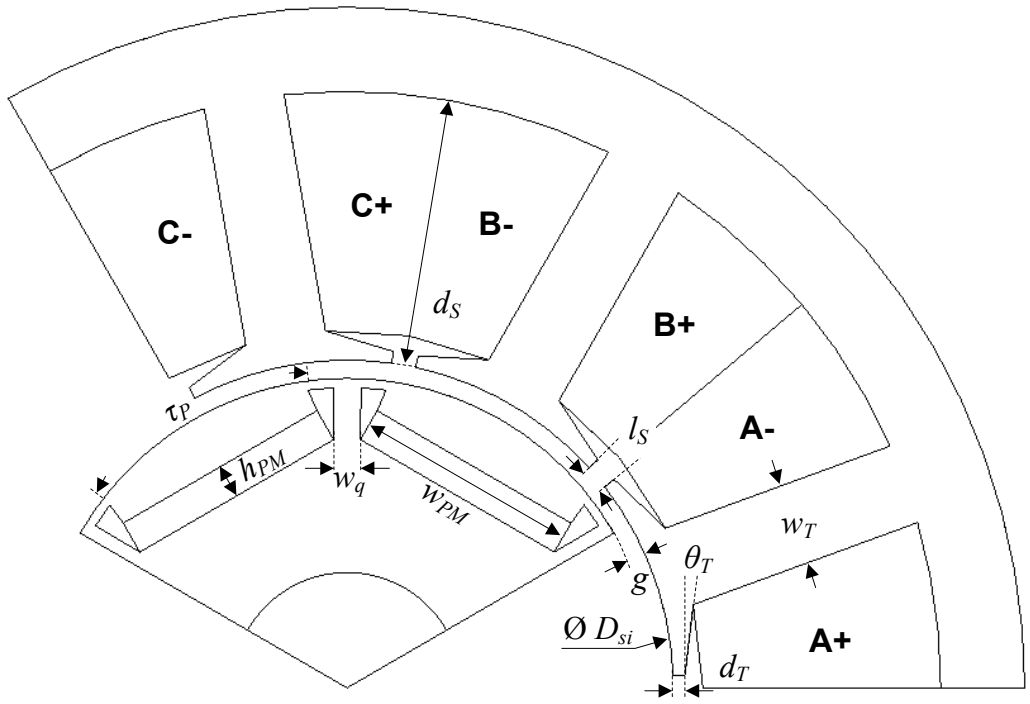

Figure 4.2: Cross-section of the 9-slot 6-pole IPM machine with 11 independent geometric variables used in multi-objective optimization.

machines. A total of eleven geometric variables (7-stator and 4-rotor) are varied during optimization. The resulting parameter vector is given in, below:

$$\mathbf{x} = [D_{Si}, g, w_T, l_S, d_S, d_T, \theta_T, w_{PM}, h_{PM}, \tau_P, w_q,] \tag{4.7}$$

where, the variable definitions are specified in Fig. 4.2 and Table 4.1.

The machine has been optimized following the procedure outlined in Sections 4.2, with design parameter limits set to the values provided in Table 4.1. The population size of a single generation was set to 100, and the DE algorithm was executed for 100 generations. These settings resulted in the total of 10,000 candidate design evaluations. In the CE-FEA, 6 magnetostatic FE solutions are used to perform a detailed evaluation of every candidate motor operating at MTPA load condition. Additional search for MTPA operating

Table 4.1: Optimization parameters: limits and values corresponding to machine of Fig. 4.5. Values are per unit of pole-pitch arc length and the unit for angle is deg. mech.

Optimized Parameters 7-stator, 4-rotor		Fractional-slot (9-slot, 6-pole)					
		Limits		Machine			
		Lower	Upper	M-1	M-2	M-3	Typ.
Stator	D_{si}	1.940	2.156	1.941	1.941	1.965	1.979
	g	0.027	0.069	0.028	0.040	0.062	0.034
	w_T	0.213	0.355	0.266	0.266	0.253	0.284
	l_s	0.062	0.275	0.072	0.070	0.084	0.156
	d_s	0.550	0.824	0.801	0.820	0.815	0.742
	d_T	0.029	0.048	0.028	0.036	0.036	0.038
	θ_T	7.50	30.00	9.02	8.83	12.42	18.75
Rotor	w_{PM}	0.550	0.687	0.661	0.683	0.686	0.687
	h_{PM}	0.055	0.103	0.099	0.102	0.103	0.079
	τ_P	0.548	0.940	0.641	0.627	0.600	0.778
	w_q	0.027	0.096	0.092	0.091	0.072	0.062

Table 4.2: Number of magnetostatic solutions and computational time required for evaluation of a single candidate design at MTPA.

CE-FEA	Solutions	Mesh density/Order	Computational Time [s]
Reduced	3	2384 el. / 1st	2.2
Detailed	6	2384 el. / 2nd	10.1
TOTAL	$4 \times Reduced + 1 \times Detailed$		18.9

condition is performed on every candidate design requiring 4 additional *reduced* CE-FEA evaluations with 3 static solutions each. *Reduced* CE-FEA with 3 static solutions per torque (advance) angle allows one to rapidly estimate the average torque while ignoring the torque ripple and bypassing costly post-processing associated with flux density computations that require additional computational effort. The total simulation time required for evaluation of 10,000 candidate designs on single core of PC-based workstation is approximately 52 hours. Detailed breakdown of model simulation times is provided in Table 4.2.

Shown in Fig. 4.3 is the evolution of the Pareto front over the course of optimization with 100 generations. Also provided are the number of non-dominated solutions in the Pareto-optimal set after every generation. Figs. 4.3a through 4.3d show how the DE

algorithm is working to iteratively improve the population. Also, comparing the Pareto fronts after 50th and the final 100th generations, Figs. 4.3c and 4.3d, one should note that the DE algorithm appears to converge to the location of the optimal Pareto set after 50th generation. After the 50th generation, the DE improves the resolution on the Pareto-optimal front by locating additional non-dominated designs see Fig. 4.3d. Shown in Fig. 4.4 are the values of the design objectives specified above for all 10,000 candidate designs, as well as the objective function values corresponding to the final Pareto-optimal designs.

The average shaft torque that accounts for core losses is plotted in Fig. 4.4 to provide a familiar basis of comparison of average and ripple torque production. From Fig. 4.4 it should be observed that a large variation between the torque ripple and the average torque production occurs from values as low as 0.4% to 32%, with the shaft torque varying from 6 Nm to 21 Nm. Three Pareto-optimal machines are selected from the Pareto-optimal set:

- M-1, has the highest shaft torque (specific torque),
- M-2, is a compromise between high torque and low ripple, and
- M-3 posses the low torque ripple.

Cross-sections corresponding to machines M-1, M-2, and M-3 are shown in Fig. 4.5. Also shown in Fig. 4.5d is a typical non-optimal design used for reference. Values of design variables corresponding to all machines are provided in Table 4.1. Shown in Figs. 4.6a and 4.6b, are the torque profiles corresponding to the four machines operating at rated-load (MTPA), and open-circuit (cogging torque) conditions, respectively. A significant reduction of both on-load and open-circuit ripple (cogging) is observed for the optimized designs. For machines M-1 and M-2 a significant increase in the average torque production is observed. More specifically, a 37% increase of the average torque is observed for machine M-1. From the results shown in Fig. 4.6b, one observes a significant reduction of the cogging torque in the case of the optimized machines. The cogging torque is reduced by as much 90% in the case of the optimized machine M-3. It should be noted that results provided in Fig.

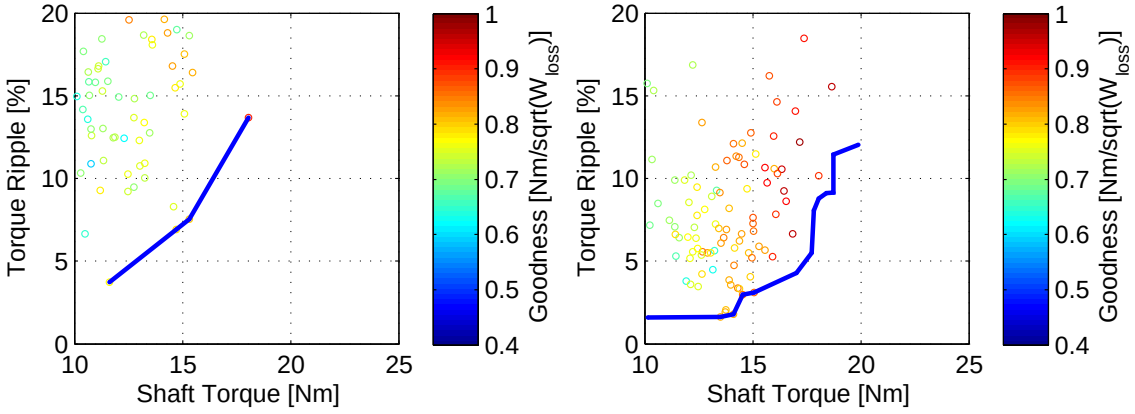

(a) Generation P_1 (4 non-dominated solutions)

(b) Generation P_{10} (13 non-dominated solutions)

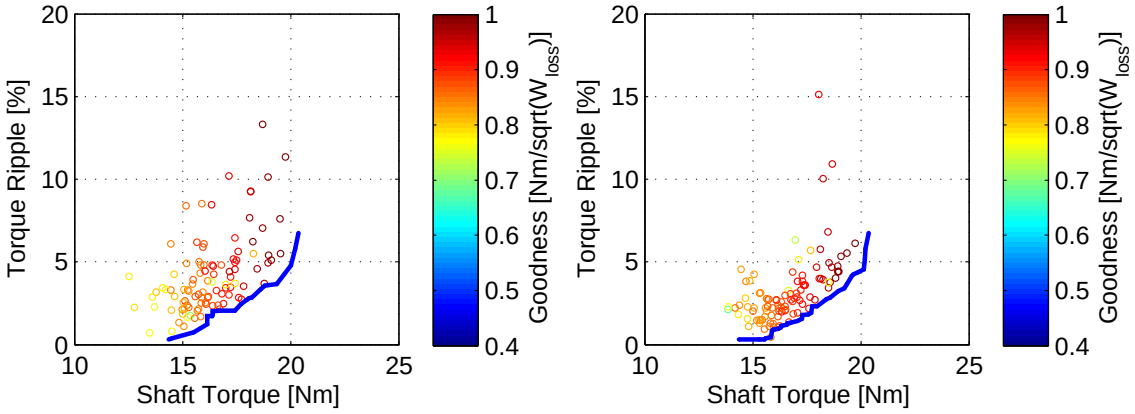

(c) Generation P_{50} (20 non-dominated solutions)

(d) Generation P_{100} (34 non-dominated solutions)

Figure 4.3: Evolution of the Pareto front over the course of optimization after 1^{st}, 10^{th}, 50^{th}, and 100^{th} generation.

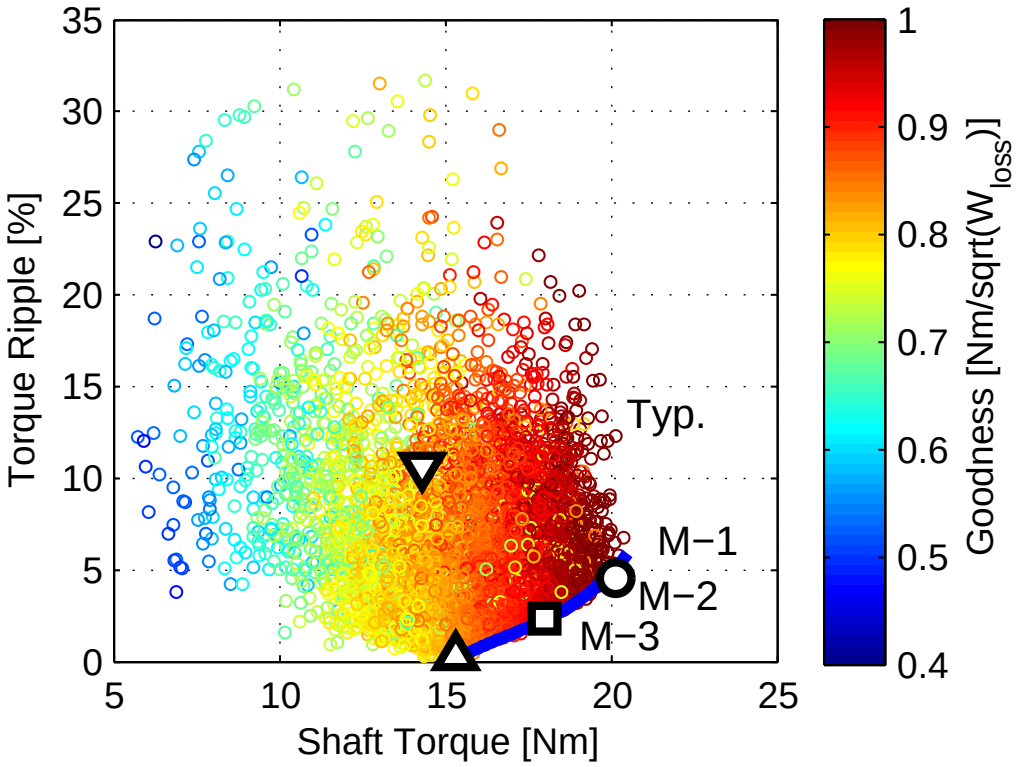

Figure 4.4: Pareto-optimal set for design objectives. Three optimal machines M-1, M-2 M-3, and the conventional machine are labeled. Shaft torque corresponds to the output torque after the core losses.

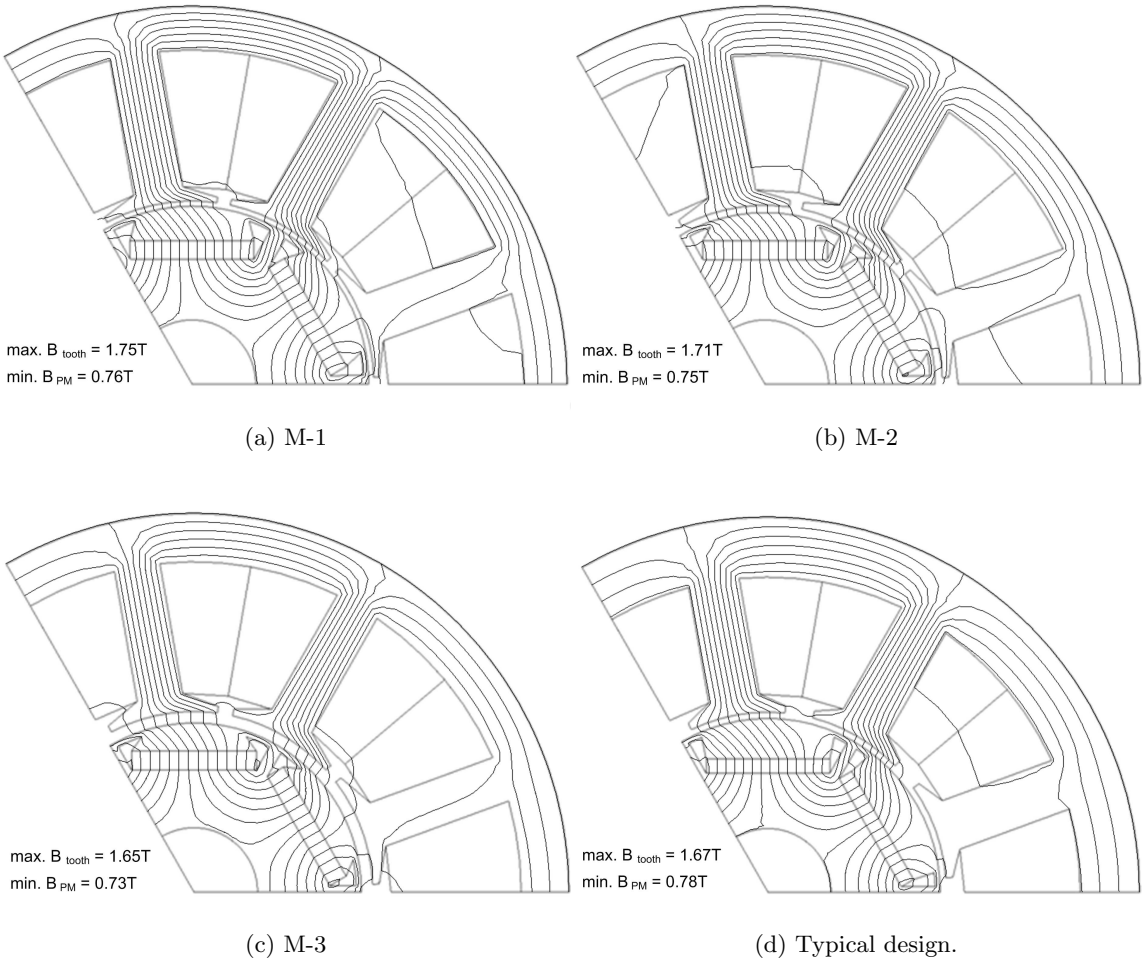

(a) M-1

(b) M-2

(c) M-3

(d) Typical design.

Figure 4.5: Cross-sections of optimized machines corresponding to Fig. 4.4 and Table 4.1. Also shown are the flux plots for the rated-load conditions and the maximum flux density in mid-tooth and minimum flux density in the permanent magnet indicating demagnetization proximity.

4.6 were verified with a detailed FEA that employs the Maxwell stress tensor and second order finite elements for the calculation of the electromagnetic torque. The open-circuit and rated-load induced voltages for the four machines are provided in Fig. 4.7, with their corresponding harmonics breakdowns given in Fig. 4.8 and Table 4.3.

Design Scaling to 5.6kW (7.5hp, 15Nm, 3600r/min)

Here, the three optimized machines (M-1, M-2, M-3) and the typical non-optimal (conventional) machine were scaled to achieve the desired 5.6kW (7.5hp) output rating. The axial length, l_{Fe}, is used to achieve this. Given in Table 4.4 are the corresponding axial lengths in per unit (pu) of the pole-pitch arc length for the four machines. Also, reported in Table 4.4 are the permanent magnet and total machine masses per unitized to the non-optimal machine of typical proportions. As expected, machine, M-1, having the highest specific torque (Fig. 4.6a), results in the shortest and lightest machine that utilizes the least permanent magnet material for the given rating. More specifically, for machine M-1 the mass of permanent magnet material is reduced by 7% while the total machine mass and length are reduced by 25% and 23%, respectively. This is while the rated-load torque ripple and open-circuit cogging torque are reduced by 54% and 79%, respectively. In the case of applications demanding higher torque production quality, further reductions of the torque ripple can be achieved with machines M-2 and M-3. Shown in Fig. 4.9 are the separations of loss components for the four machines. Here, it should be observed that machine M-2 results in the lowest overall loss and hence the highest efficiency of 94%. An almost equal split between copper and core losses for machine M-2 should also be noted, which is another indication of the "optimality" of the design from a loss point of view. Overall, machine M-2 offers the best balance between the output torque quality, efficiency, material and manufacturing costs.

Discussion

The optimization results presented in this work show several design trends that may seem

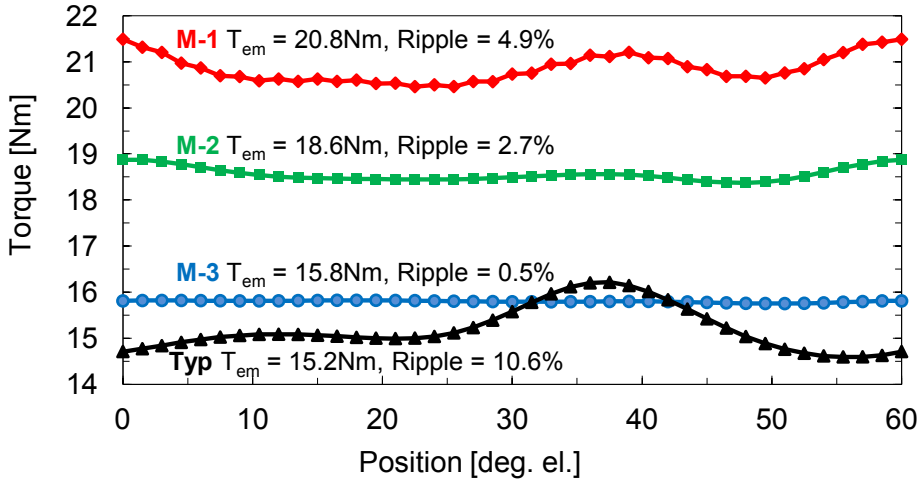

(a) Torque at rated-load conditions

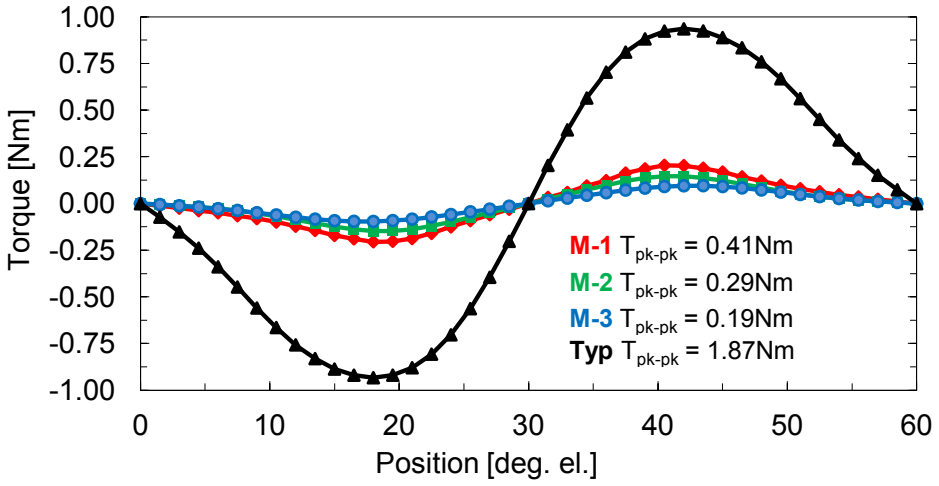

(b) Cogging torque

Figure 4.6: Electromagnetic torque for machines of Fig.4.5 (red: M-1, green: M-2, blue: M-3, black: Typ.) supplied by a current regulated sine-wave drive (purely sinusoidal currents are assumed). Torque profiles are verified/obtained using detailed FEA with Maxwell stress tensor and 2nd order elements.

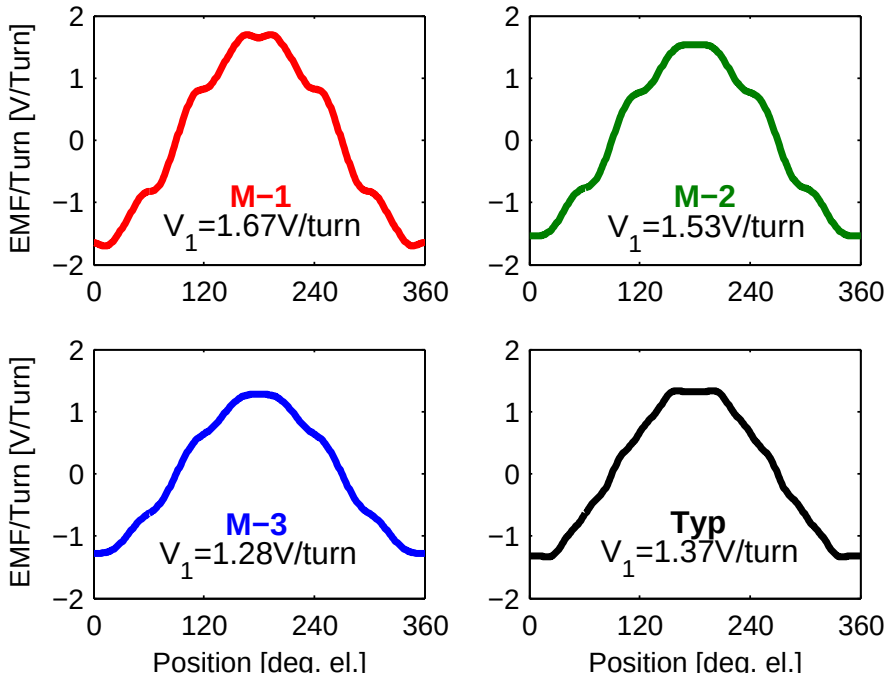

(a) Open-circuit

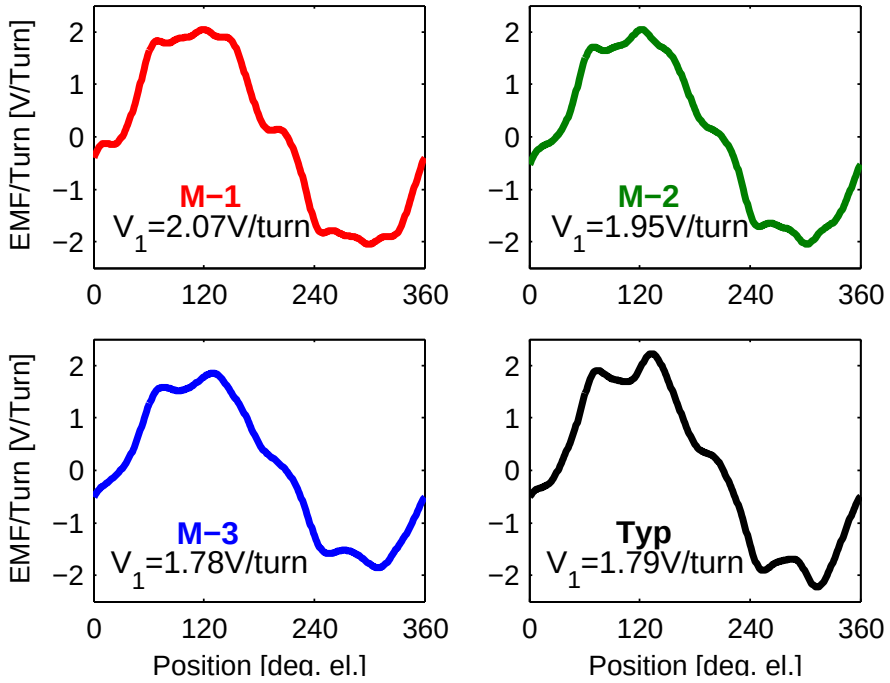

(b) Rated-load (MTPA)

Figure 4.7: Induced phase voltages at open-circuit and rated-load for machines in Fig.4.5 (red: M-1, green: M-2, blue: M-3, black: Typ.). Also shown are the peak values of the fundamental components.

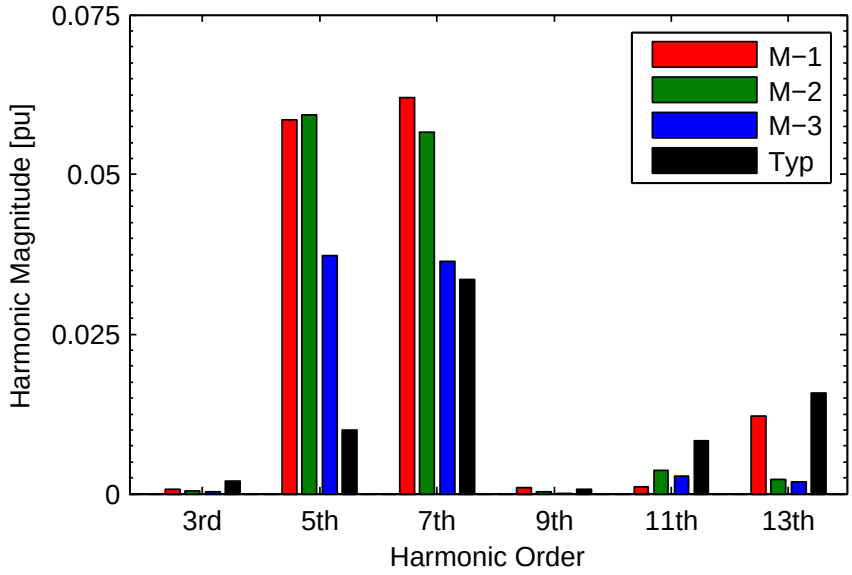

(a) Open-circuit

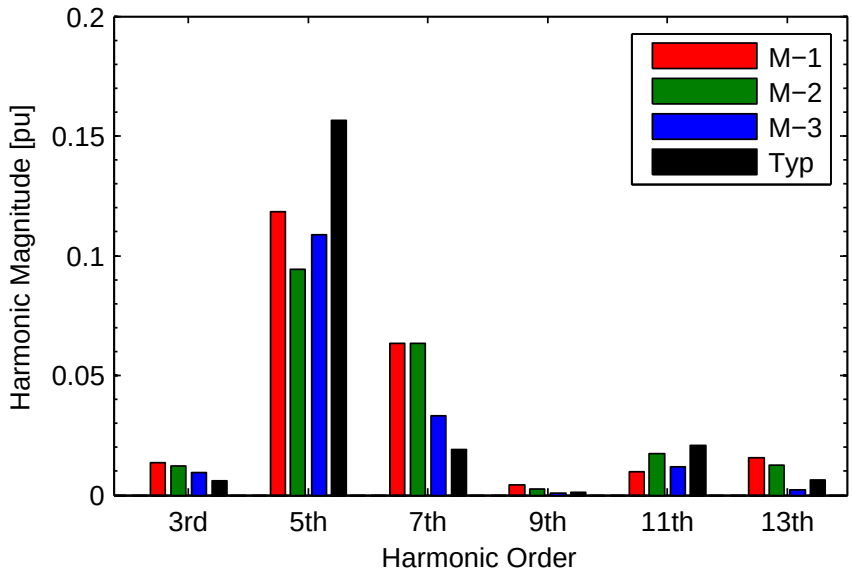

(b) Rated-load (MTPA)

Figure 4.8: Harmonic analysis of induced phase voltages shown in Fig. 4.7. Fundamental component is not shown for clarity.

Table 4.3: Harmonic analysis of induced voltages shown in Fig.4.7.

	Motors	Harmonic order				
		1st	5th	7th	11th	13th
Open circuit [V/turn]	M-1	1.67	0.098	0.10	0.002	0.020
	M-2	1.53	0.091	0.87	0.005	0.002
	M-3	1.28	0.048	0.047	0.003	0.002
	Typ.	1.37	0.014	0.046	0.012	0.022
Rated-load (MTPA) [V/turn]	M-1	2.07	0.245	0.131	0.020	0.032
	M-2	1.95	0.185	0.124	0.034	0.024
	M-3	1.78	0.194	0.059	0.021	0.004
	Typ.	1.79	0.316	0.038	0.042	0.013

Table 4.4: Axial length and masses for 5.6kW (7.5hp) rating. Per unit length is defined with respect to the pole-pitch arc length, and mass values are per unitized to typical design (Fig.4.5d)

	M-1	M-2	M-3	Typ.
Axial length [pu]	2.08	2.33	2.73	2.85
PM mass [pu]	0.93	1.05	1.25	1.00
Total mass [pu]	0.75	0.81	0.92	1.00

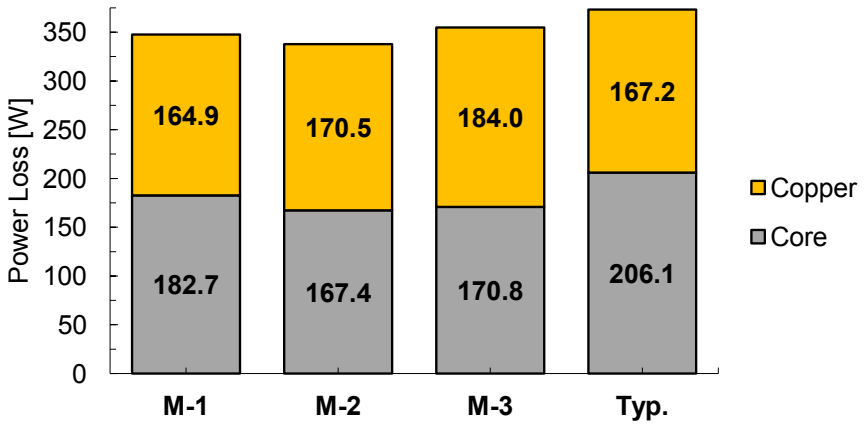

Figure 4.9: Separation of loss components: core loss (hysteresis and eddy), copper winding loss for machines in Fig.4.5.

unconventional. First, the optimized machines have a significant reduction, of up to an order of magnitude, of both rated-load and open-circuit (cogging) torque ripples, see Fig. 4.6. This is while the induced voltage waveforms at both open-circuit and rated-load conditions are rich in their harmonic content, as can be observed from Figs. 4.7 and 4.8. In the optimized machines, the reduction in the torque ripple is achieved through a combination of design variables, namely, air-gap height, slot opening and tooth-tip shape (tip depth and tip angle), and the pole arc length. In the optimized machines, these parameters result in a balance between the torque ripple produced by the back-emf harmonics and the torque ripple resulting from the position-dependent variation of the stored magnetic energy (cogging). Also, considering harmonics of the back-emf waveforms provided in Fig. 4.8a, one should note that optimized (low torque ripple) machines tend to have balanced 5^{th} and 7^{th} harmonics. It should be noted that significant reduction of torque ripple levels in the optimized machines eliminates the need for stator and/or rotor skewing. Ripple-free operation of non-skewed optimized machines can be achieved with a well tuned sine-wave current regulated drive, capable of regulating/eliminating higher order current harmonics (5th and 7th) that may result from the back-emf harmonics.

Second, the three optimized machines tend to have lower pole-arc coverage (0.62 average) resulting in higher permanent magnet flux concentration/focusing. As can be seen from Fig. 4.7, this results in an increase of the fundamental component of the induced voltage of the optimized machines. For example, for machine M-1, operating under open-circuit conditions, the induced voltage is increased by 22% in comparison to the machine that has a conventional pole-arc coverage of 0.78.

4.4 Case Study - II: Concept Comparison of a 20MW Machine

In this study, application of the multi-objective design method for selection and comparison of different electromagnetic design concepts is presented. Four motor topologies are systematically compared based on Pareto optimal sets. In the four machines shown in Fig. 4.10, two stator cores: 1) fractional-slot with $q = 0.5$, and 2) integer-slot with $q = 2$, and two rotor topologies: 1) SPM (embedded) with radial magnetization, and 2) generic IPM with single layer and uniform/parallel magnetization, are considered. In the fractional-slot topologies the semi-closed slot opening was preferred to enable the generalization of results to a wide range of designs and ratings. For the larger machines the magnetic equivalent of the tooth tip shown in Figs. 4.10a and 4.10b can be realized for example by using a magnetic wedge. In the design of the machines, the outside diameter, conductor current density, frequency and number of poles, are assumed to be constant and are summarized in Table 4.5. The outer diameter of the machine has been fixed to a value of 3 meters, while the slot fills corresponding to the integer-slot and the fractional-slot topologies are equal to 35% and 40%, respectively. The rare-earth magnet remanence and relative permeability are equal to 1.14 T and 1.1, respectively. The steel assumed for the construction of both stator and rotor cores is M19-26Ga. The stator and rotor geometric design parameters and corresponding ranges used in the design process are summarized in Table 4.6. It should be noted that in the case of the fractional-slot surface-PM and interior-PM machines (Figs. 4.10a and 4.10b), *seven* and *eight* parameters are used for optimization, respectively, whereas in the case of the integer- slot SPM and IPM machines (Figs. 4.10c and 4.10d), *six* and *seven* parameters are used, respectively.

An additional search of an optimum operating point (MTPA) was performed for every IPM candidate machine design. The four topologies shown in Fig. 4.10 were evaluated with 5,000 candidate designs each, resulting in a total of 20,000 candidate machine design

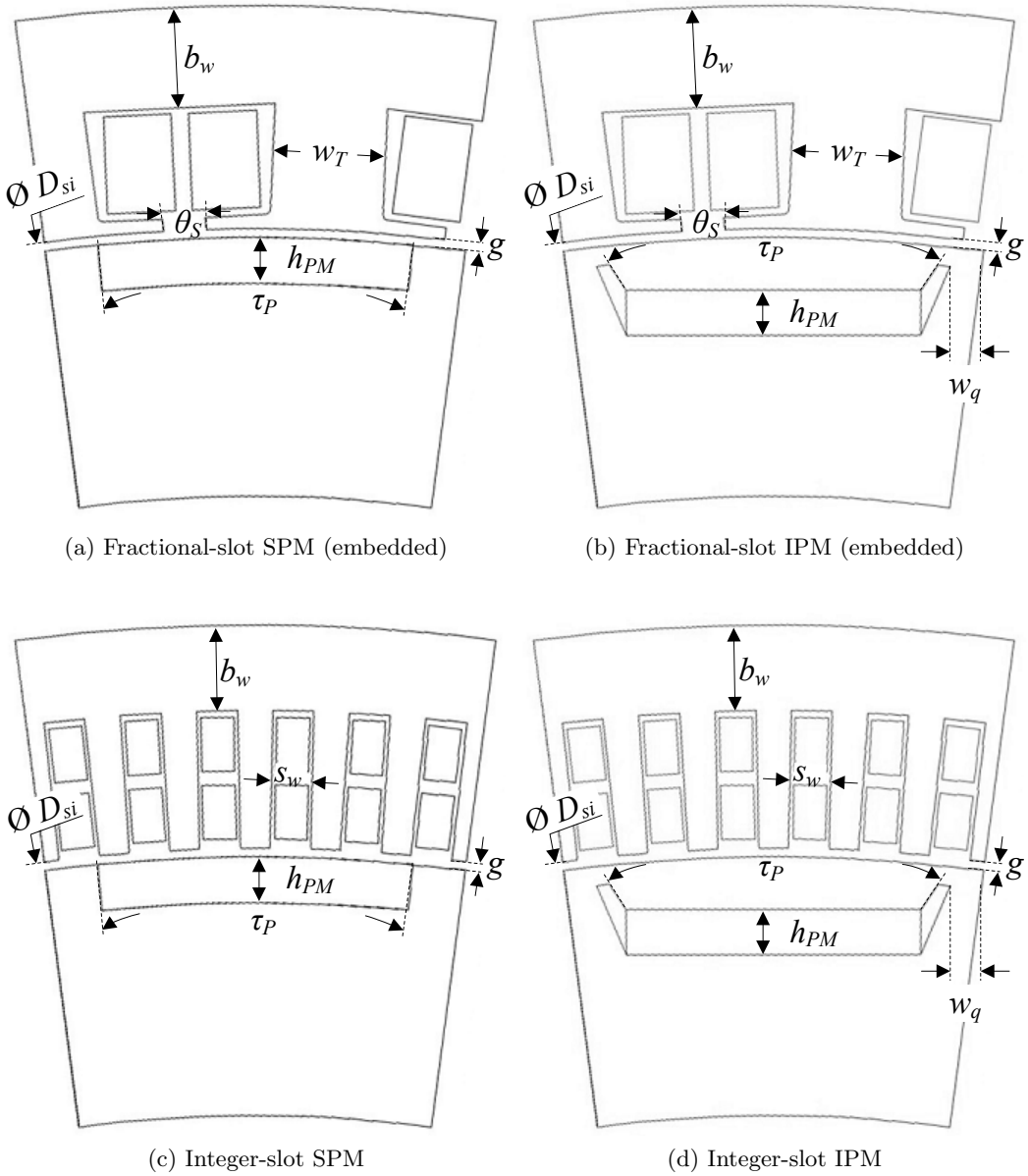

(a) Fractional-slot SPM (embedded)

(b) Fractional-slot IPM (embedded)

(c) Integer-slot SPM

(d) Integer-slot IPM

Figure 4.10: Cross-sections of four case-study machines, showing machine geometries. Due to the even periodicity two poles of fractional slot machines are modeled (a and b), due to the odd periodicity only a single pole of integer slot machines is modeled (c and d).

Table 4.5: Fixed Design Parameters for the Case Study-2 of Fig.4.10

	Fractional-slot	Integer-slot
Number of slots	36	144
Number of poles	24	24
Rated frequency [Hz]	30	30
Stator outer diameter, D_{so} [mm]	3000	3000
Current density $[A_{rms}/mm^2]$	4.05	4.65

Table 4.6: Independent Design Variables and Limits for the Case Study-2 of Fig.4.10

	Fractional-slot		Integer-slot	
	min	*max*	*min*	*max*
Stator inner diameter, D_{si} [mm]	2500	2650	2500	2650
Air-gap height, g [mm]	4	10	4	10
Tooth width, w_T [mm]	50	125	N/A	N/A
Slot width, w_S [mm]	N/A	N/A	15	45
Back iron width, w_B [mm]	110	150	25	100
Slot opening, θ_S [deg. mech.]	0.5	4	N/A	N/A
	SPM		IPM	
Pole arc angle, τ_P [deg. el.]	110	170	110	150
PM height, h_{PM} [mm]	15	60	15	50
q-axis bridge, w_q [mm]	60	70	N/A	N/A

Table 4.7: Number of magnetostatic solutions and computational time required for evaluation of a single candidate design (including MTPA search for IPMs).

Fractional-slot SPM			
CE-FEA	Solutions	Mesh density/Order	Computational Time [s]
Detailed	7	2991 el. / 2nd	15.7
TOTAL	$1 \times Detailed$		15.7
Fractional-slot IPM			
Reduced	3	2588 el. / 1st	2.5
Detailed	7	2588 el. / 2nd	16.1
TOTAL	$4 \times Reduced + 1 \times Detailed$		26.1
Integer-slot SPM			
Detailed	9	1963 el. / 2nd	19.5
TOTAL	$1 \times Detailed$		19.5
Integer-slot IPM			
Reduced	3	1852 el. / 1st	2.1
Detailed	9	1852 el. / 2nd	20.2
TOTAL	$4 \times Reduced + 1 \times Detailed$		28.6

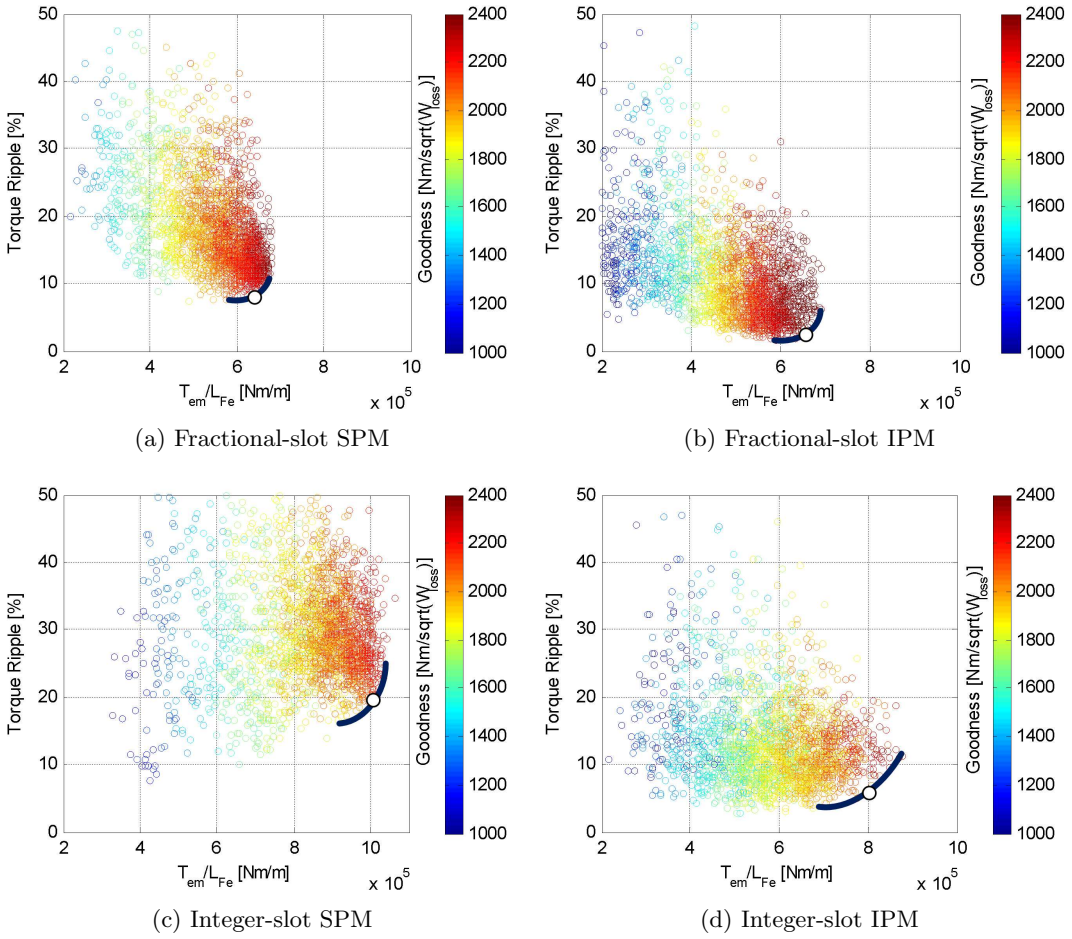

(a) Fractional-slot SPM

(b) Fractional-slot IPM

(c) Integer-slot SPM

(d) Integer-slot IPM

Figure 4.11: Design objectives showing: design objectives of all candidate designs, Pareto-optimal sets after 50 generations and the selected optimal machines.

evaluations. The total simulation time on a typical PC workstation utilizing a single core was equal to a very reasonable 124 hours. Detailed breakdown of model simulation times is provided in Table 4.7. It should be noted that further reduction of the simulation time is achievable by evaluating CE-FEA candidate design models in parallel on multiple cores.

Optimization Results

Optimization results of the four machine topologies (Fig. 4.10) are shown in Fig. 4.11. Shown in Fig. 4.11 are the objective function values, i.e. the electromagnetic torque per unit

axial length and the torque ripple at rated-load, subject to parameter constraints provided in Table 4.6. As mentioned before, the outside stator diameter is fixed to 3 meters, hence, here the specific torque is defined as the torque per unit axial length of the machine. The objective functions corresponding to all the candidate designs (20, 000) are shown in Figs. 4.11. Also, shown in Fig. 4.11 are the Pareto-optimal sets corresponding to every machine topology of Fig. 4.10.

Depicted in Fig. 4.12 are the evolutions of the design parameters for the fractional-slot embedded surface-PM machine during the course of optimization. From Fig. 4.12, it should be noted that in the multi-objective optimization that results in the distributed Pareto-optimal sets, such as the ones shown in Fig. 4.11, the design parameters are not guaranteed to converge to constant values. This is in contrast to single-objective optimization studies where all design parameters are guaranteed to converge to constant optimal values corresponding to a single optimal machine design. As can be seen from Fig. 4.12, design variables converge to a bounded region of parameter values that corresponds to designs in the Pareto-optimal set.

As can be observed from the results of Fig. 4.11, the two objectives considered in the optimization study are conflicting. This means that the choice of an optimal machine design involves evaluating trade-offs between the designs in the Pareto-optimal set. From Fig. 4.11 a large variability of the specific torque, torque ripple, and "goodness" factor should be noted. Comparing integer-slot and fractional-slot machines one should notice a significant increase of the specific torque for the machines with integer-slot stators. This can be explained by the fact that the fractional-slot topology used in this work has a low fundamental winding factor of 0.866. Also, as expected, fractional-slot machine designs have lower torque ripple values when compared to the integer-slot machines. On the other hand, comparison of the "goodness" factor of the fractional and integer-slot machines may be affected by several factors not fully accounted for in the current analysis. More specifically, fractional-slot winding machine designs may result in increased eddy current losses in the

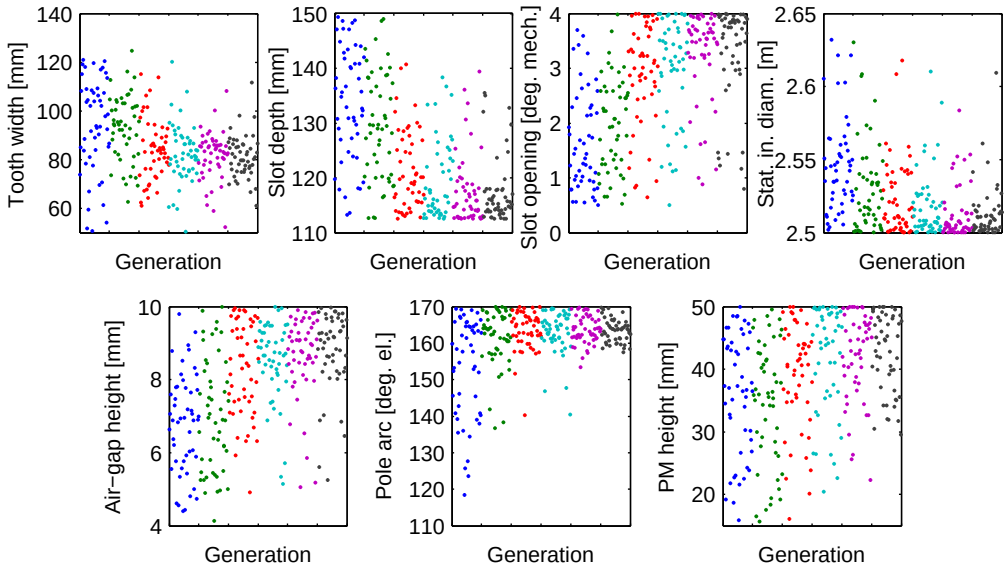

Figure 4.12: Evolution of design parameters of fractional-slot embedded surface-PM motor during the fifty generations (only 1^{st}-blue, 10^{th}-green, 20^{th}-red, 30^{th}-cyan, 40^{th}-purple, 50^{th}-black, generations are plotted). Every point represents a candidate design parameter in the corresponding generation. Variables are not expected to converge to constant values in a multi-objective optimization.

permanent magnets and in the stator windings due to the high harmonic content of the armature mmf. Another factor that may affect the comparison of the loss performance of the two winding topologies is the active axial length, which affects the ratio of end winding losses to the total machine losses.

Four optimal designs corresponding to every motor topology are selected from the four optimal sets shown in Fig. 4.11. Namely, these designs are fractional-slot SPM (F-SPM), fractional-slot IPM (F-IPM), integer-slot SPM (I-SPM) and integer-slot IPM (I-IPM).

The designs are selected based on the best compromise between the specific torque and the torque ripple corresponding to every Pareto-set in Fig. 4.11. The cross-sections corresponding to the four optimal designs and the corresponding parameters are provided in Fig. 4.13 and Table 4.8. From Figs. 4.13b and 4.13d, one should note that the non-magnetic space at the end of the magnets was not geometrically correlated as a dependent variable of the magnet arc or length facing the air-gap. It was expected that the optimization algorithm would push the magnet to the maximum allowable dimensions to a configuration that has no space at the end of the magnet as shown in Fig. 4.10b and 4.10d.

Depicted in Figs. 4.14a and 4.14b, are the torque profiles corresponding to the four machines operating at rated-load (MTPA), and open-circuit (cogging torque) conditions, respectively. As mentioned previously, a significant increase of the specific torque is observed for the integer-slot machines (I-SPM and I-IPM). On the other hand, a significant improvement of the torque ripple is achieved with fractional-slot designs (F-SPM and F-IPM). Ripple-free operation of the optimized F-IPM machine, at both rated-load and open-circuit conditions, should be noted. In the F-IPM machine the need for stator and/or rotor skewing is practically eliminated. The torque profiles shown in Fig. 4.14 were verified with a detailed FEA that employs the Maxwell stress tensor and second order finite elements.

Design to Achieve Desired Rating of 20MW at 150 r/min

In this section, four optimized machines (F-SPM, F-IPM, I-SPM, I-IPM) were scaled

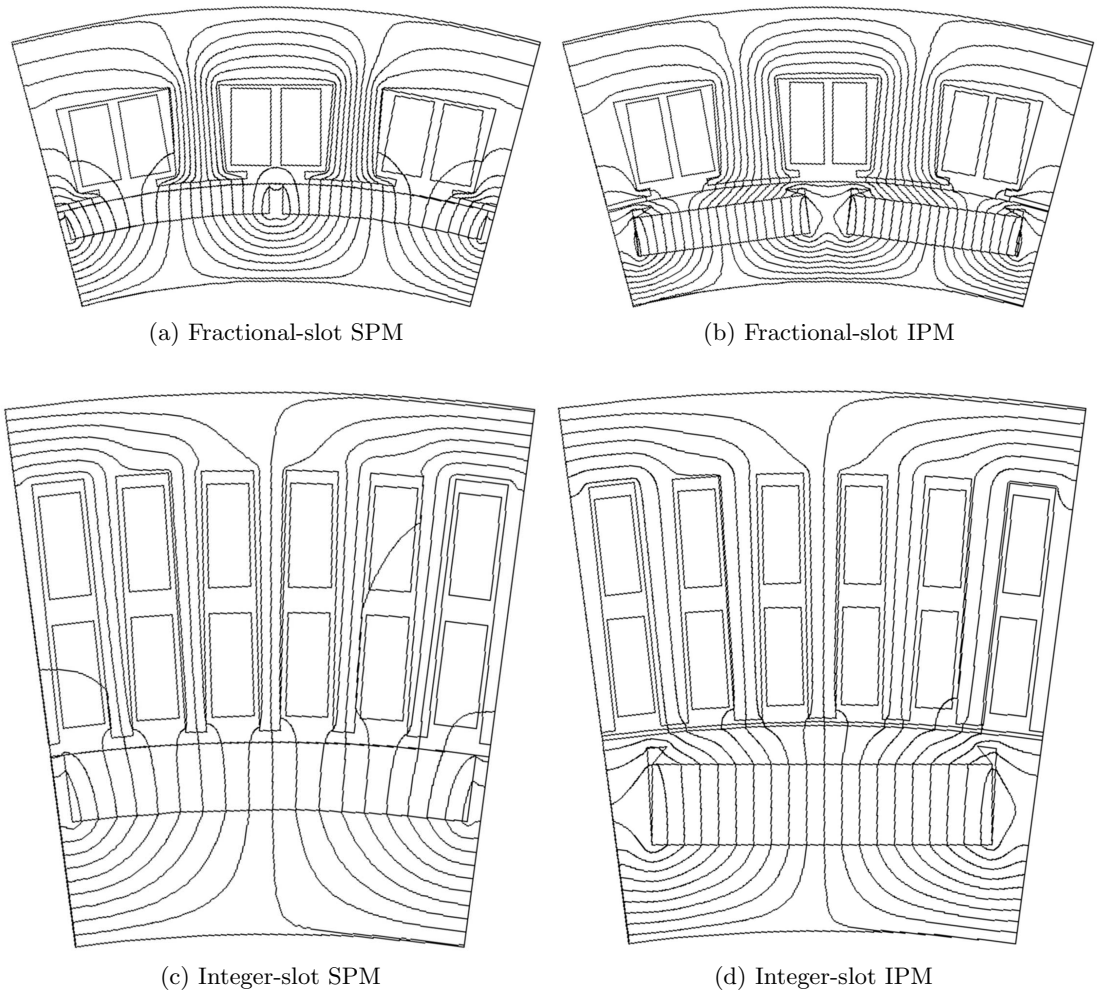

(a) Fractional-slot SPM

(b) Fractional-slot IPM

(c) Integer-slot SPM

(d) Integer-slot IPM

Figure 4.13: Cross-sections of four optimal machines, showing machine geometries and open circuit flux distributions. Due to the even periodicity two poles of fractional slot machines are modeled (a and b), due to the odd periodicity only a single pole of integer slot machines is modeled (c and d). The combination of a and b has different scale with the combination of c and d.

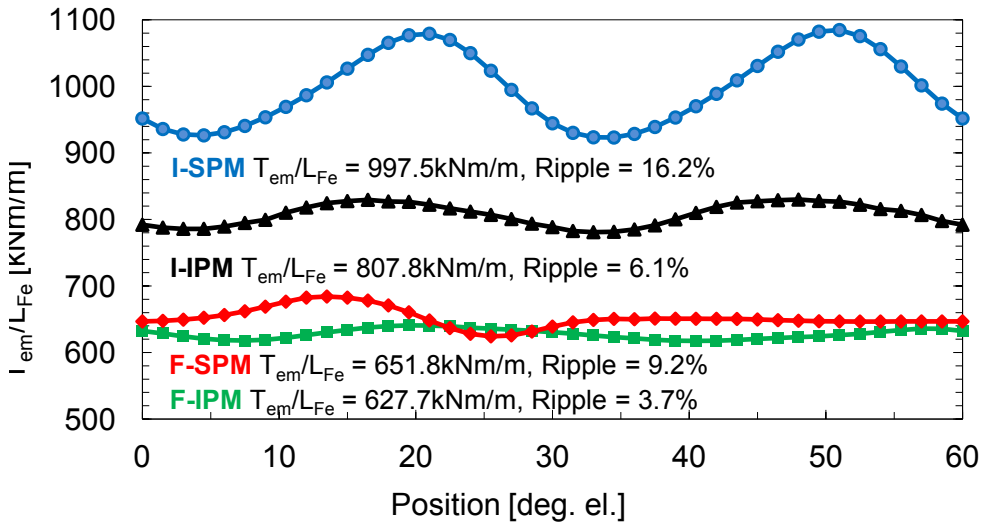

(a) Torque at rated-load conditions

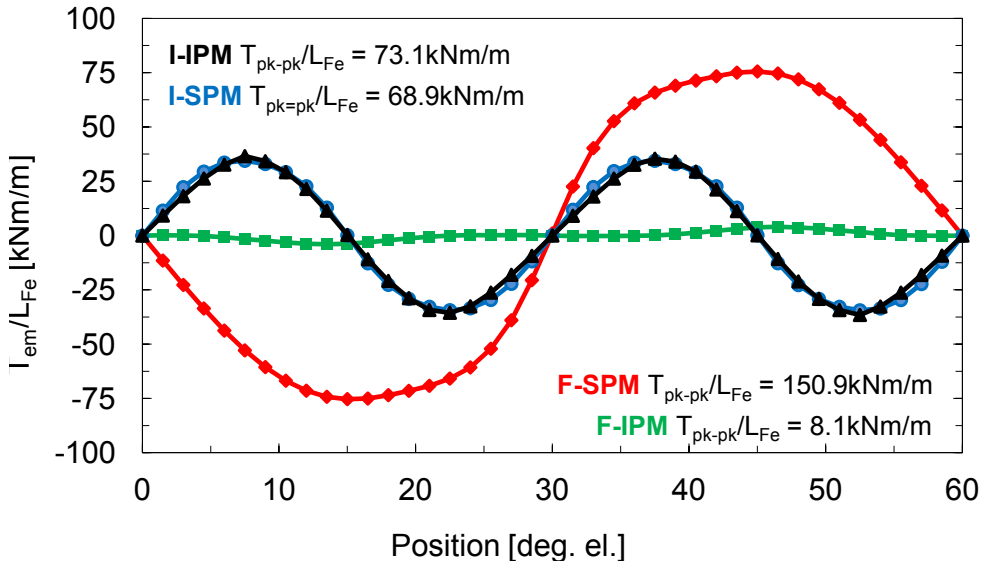

(b) Torque at open-circuit conditions

Figure 4.14: Electromagnetic torque for machines of Fig.4.13 (red: F-SPM, green: F-IPM, blue: I-SPM, black: I-IPM.) supplied by a current regulated sine-wave drive (purely sinusoidal currents are assumed). Torque profiles are verified/obtained using detailed FEA with Maxwell stress tensor and 2^{nd} order elements.

Table 4.8: Optimal Design Parameters Corresponding to Machines Shown in Fig.4.13

	F-SPM	F-IPM	I-SPM	I-IPM
Stator inner diameter, D_{si} [mm]	2500	2505	2501	2515
Air-gap height, g [mm]	9.0	7.1	8.8	5.6
Tooth width, w_T [mm]	76.6	96.7	N/A	N/A
Slot width, w_S [mm]	N/A	N/A	38.9	34.3
Back iron width, w_B [mm]	113.0	113.1	57.5	61.0
Slot opening, θ_S [deg. mech.]	4.0	3.85	N/A	N/A
Axial length, l_{Fe} [mm]	1953	2028	1276	1576
Pole arc angle, τ_P [deg. el.]	165.9	110.1	169.3	128.1
PM height, h_{PM} [mm]	49.7	56.4	50.5	59.7
PM height, h_w [mm]	N/A	251.2	N/A	252.5
q-axis bridge, w_q [mm]	N/A	68.9	N/A	65.2

Table 4.9: PM mass and total active machine mass.Per unit PM mass of I-SPM optimal design with PM mass of 3,440kg. Per unit total mass of I-SPM optimal design with total active mass of 63,467kg.

	F-SPM	F-IPM	I-SPM	I-IPM
PM mass [pu]	1.49	1.58	1.00	1.24
Total mass [pu]	1.57	1.64	1.00	1.25

axially to achieve the desired 20MW output rating. The corresponding axial lengths for the four machines are provided in Table 4.8. Also, depicted in Table 4.9 are the permanent magnet and total machine masses corresponding to the four optimal designs. As expected, the I-SPM machine (Fig. 4.13c), having the highest specific torque (Fig. 4.14a), results in the shortest and lightest machine that utilizes the least permanent magnet material for the given rating. The permanent magnet mass and the total active material mass (magnet, copper and iron) of the I-SPM design are 3,440 kg and 63,467 kg, respectively.

Discussion

The optimized machines presented in this example aim at improving torque production quality while minimizing active machine mass and losses. These objectives are oftentimes conflicting as can be observed from Fig. 4.11. In other words, selecting a design with high specific torque usually results in a machine with high torque ripple. In addition, selecting a

design with high specific torque may result in a machine having a significantly shorter axial length, hence, increasing the proportion of end winding losses in the overall total machine loss and potentially reducing the efficiency. In addition, machines with high specific torque result in smaller machines with less surface area to dissipate the losses, hence potentially requiring more sophisticated thermal management.

As shown in this example, accurate comparison of different machine topologies should be performed on the basis of comparing their respective Pareto-optimal sets. In this approach the variability of design objectives due to design parameters is eliminated allowing one to compare only optimal machines corresponding to every topology (number of slots/poles, magnet arrangement, etc.). For example, considering the case of the fractional-slot with surface-PM (Fig. 4.11a) and interior-PM (Fig. 4.11b) arrangements, there exists a large number of sub-optimal designs that result in similar design objectives. However, comparing the Pareto-optimal sets, it is clear that the interior-PM design outperforms the surface-PM design in terms of both the specific torque and torque ripple performance.

4.5 Case Study - III: Design Synthesis of a 13.5kW Motor for Compressor Application

In this section, design of an IPM motor for a piston type compressor used in a heat pump water heater application is described. In this application the IPM motor is designed to replace an existing induction motor to improve the overall system efficiency. The motor outside diameter, axial length and inner rotor (shaft) diameter are fixed by the existing compressor housing geometry. Hermetic application requires a motor to have sufficient electromagnetic saliency to operate with a current regulated drive in a sensorless (encoder-less) mode. A commercial drive employs a high frequency injection method to estimate the rotor (PM) position at low speed [116]. In this work, two prototype motors were designed

and tested.

The design optimization and synthesis method described earlier in this chapter was used to design three competing motor topologies based on optimal Pareto sets. Two fractional-slot tooth wound topologies having $q = 0.5$ slots/pole/phase, one with 12-slots and 8-poles and the other with 9-slots and 6-poles, and a third integer-slot topology with $q = 2$ slots/pole/phase, with 36-slots and 6-poles were considered. Parametric motor geometries showing the dimensions used in optimization are provided in Fig. 4.15. Design specifications, objectives, and constraints are provided below.

Design Specifications

- Motor type: permanent magnet ac (sine-wave current regulated)
- Rotor type: IPM (flat-bar)
- Materials:
  - stator/rotor steel: M19-26Ga,
  - permanent magnet

Type	NdFeB (VACODYM 677HR)
Energy product, BH_{max}	270 kJ/m^3
Remanence, B_{rem}	1.18 T
Normal coercivity, H_{cB}	915 kA/m
Intrinsic coercivity, H_{cJ}	2465 kA/m
Temperature coefficient, $\alpha_{B_{rem}}$	-0.085 %/°C
Temperature coefficient, $\alpha_{H_{cJ}}$	-0.55 %/°C

- Stator diameter, D_{So}: 190 mm
- Shaft diameter, D_{Ro}: 63.5 mm
- Rated power: 13.5 kW (18hp)
- Rated speed: 1800 r/min

Design Objectives

Two objectives were selected based on the target performance and cost.

Multi-objective definition:

1. maximize rated-load efficiency. η_{rated}:

$$f_1 = \max(\eta_{rated}),$$

2. minimize permanent magnet mass, m_{PM}:

$$f_2 = \min(m_{PM}).$$

Design Constraints

1. ensure safe permanent magnet operation by limiting demagnetization at rated output load and steady-state rated-load PM temperature to:

$$\min(B_{PM}) \geq 0.2 \text{ T}$$

where, $\min(B_{PM})$, is the lowest value of flux density in the direction of PM magnetization in the bulk permanent magnet material.

2. limit rated-load torque ripple to be less than 10% of the rated average torque:

$$\frac{\max(T_{em}) - \min(T_{em})}{\text{avg}(T_{em})} \leq 10\%$$

where, T_{em}, is the electromagnetic torque.

3. limit the saliency ratio, $\xi = L_q/L_d$, to be greater than 1.4 to ensure low speed sensorless operation, that is:

$$\xi = L_q/L_d \geq 1.4$$

where, ξ is the saliency ratio, and L_d and L_q, are the direct and quadrature axes inductances, respectively.

4. limit maximum axial stack length, l_{stk}, to 133 mm:

$$l_{stk} \leq 133 \text{ mm}$$

where, l_{stk}, is the total axial lamination stack length that is related to the effective stack length, l_{Fe}, through the stacking factor, f_{stk}, as $l_{Fe} = f_{stk} l_{stk}$.

A multi-objective design optimization considering a total of 22,500 candidate designs has been performed. The optimization results are provided in Figs 4.16 and 4.17. Shown in Fig. 4.16 are the design objectives corresponding to all 22,500 candidate designs of the aforementioned three motor topologies. Fig. 4.17 shows the design objectives corresponding to motors that satisfy design constraints. Also shown in Fig. 4.17 are the selected best-compromise designs that provide a balance between rated efficiency and material costs.

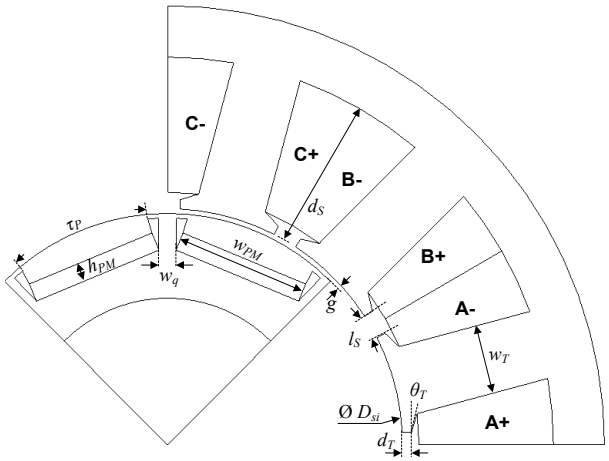

(a) 12-slot 8-pole fractional-slot IPM

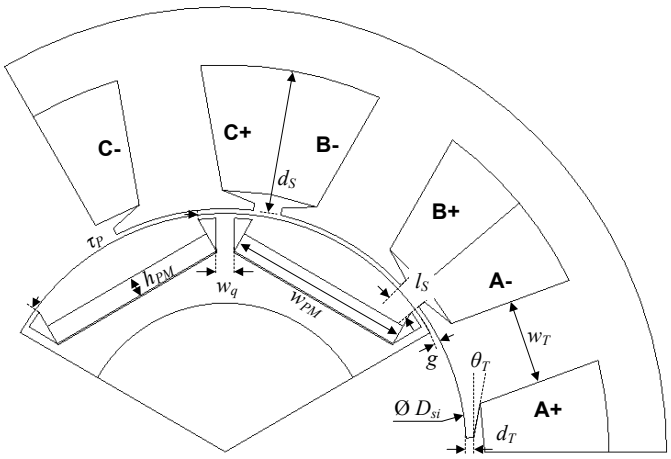

(b) 9-slot 6-pole fractional-slot IPM

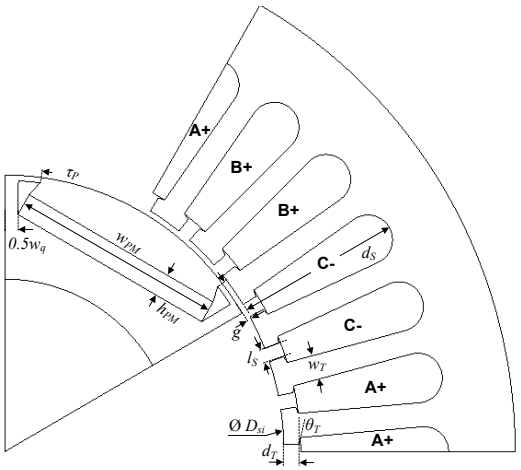

(c) 36-slot 6-pole integer-slot IPM

Figure 4.15: Cross-sections of three case-study machines, showing design variables. Due to the even periodicity two poles of fractional-slot machines are modeled (a and b), due to the odd periodicity a single pole of integer-slot machine is modeled (d).

Comparing efficiency values attainable with two fractional-slot motors one should note that the 6-pole motor has a slight advantage over the 8-pole motor. This can be explained by the increase of the core losses caused by the increased power supply synchronous frequency in the 8-pole motor. Comparing efficiency values of the two fractional-slot machines to the integer-slot motor, the difference between the efficiency values can be explained by the lengthier end winding conductor connections and the consequent additional losses in the integer-slot motor. The cross-sections of the optimized machines and relevant performance criteria are provided in Fig. 4.18, and Table 4.10.

Table 4.10: Performance Parameters of the Machines Shown in Fig.4.18

	12-slot, 8-pole (q=0.5)	9-slot, 6-pole (q=0.5)	36-slot, 6-pole (q=2)
Estimated efficiency [%]	95.2	95.6	93.8
PM mass [kg]	0.909	0.912	0.892
Torque ripple [%]	9.7	9.6	28.9(5.5 skewed)
Stack length [mm]	131.2	133.0	126.1
Saliency L_q/L_d	1.72	1.80	2.02

Considering the results of Fig. 4.16, one should note that the 6-pole fractional-slot motor delivers higher efficiency at rated operating conditions. The efficiency of the 12-slot, 8-pole motor is reduced due to an increase in the core losses at rated speed, when compared to the 9-slot, 6-pole motor case.

Based on the results of the optimization study two motors were prototyped and tested. In order to minimize prototyping costs, the two 6-pole motors were built, one with an integer-slot stator and one with a fractional-slot stator. A common rotor based on the optimal design of a 9-slot motor was used for both machines to further minimize prototyping costs. Two stators are shown in Figs. 4.19a and 4.19b. The common rotor is shown in Fig. 4.19c. The rotor assembly was step skewed to minimize torque ripple and back emf harmonics of the integer-slot motor as discussed in Chapter 3. The skew equivalent of one slot-pitch of the integer-slot motor was approximated using a staggered skew with two sections. One of the assembled motors is shown in Fig. 4.19d. Fig. 4.20 shows the

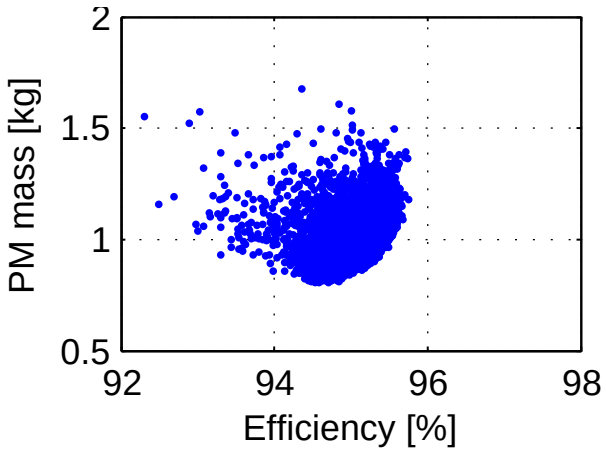

(a) 12-slot 8-pole fractional-slot IPM

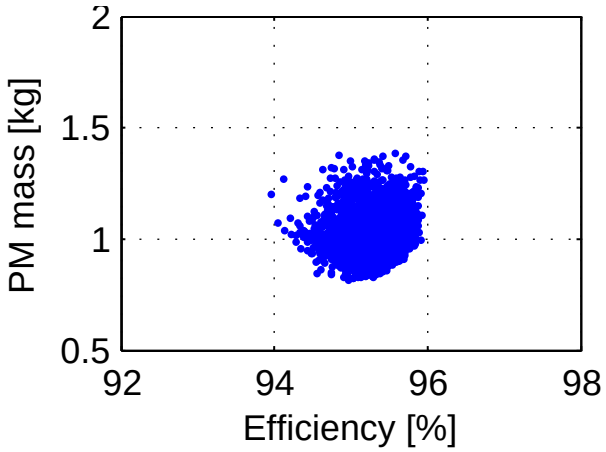

(b) 9-slot 6-pole fractional-slot IPM

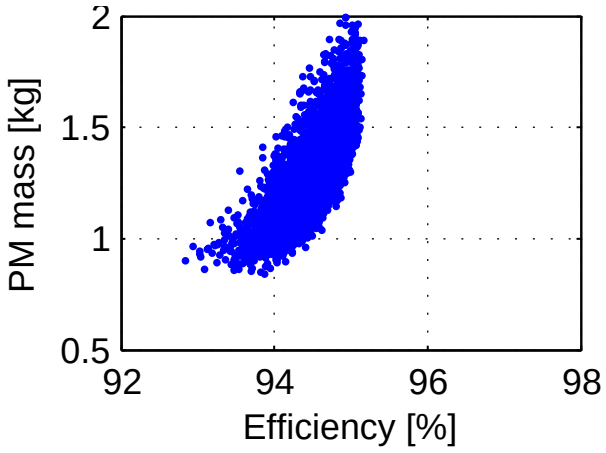

(c) 36-slot 6-pole integer-slot IPM

Figure 4.16: Design objectives corresponding to all 22,500 candidate designs evaluated during optimization.

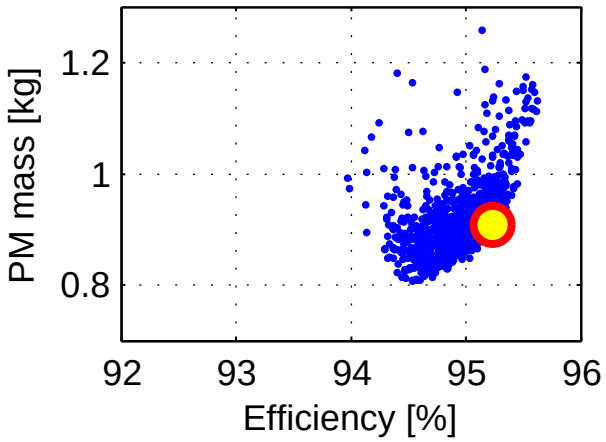

(a) 12-slot 8-pole fractional-slot IPM

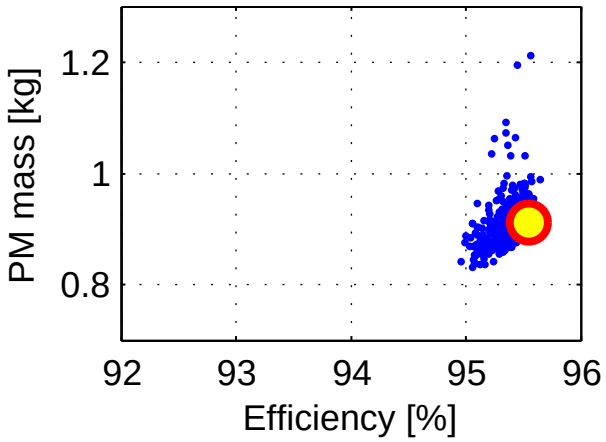

(b) 9-slot 6-pole fractional-slot IPM

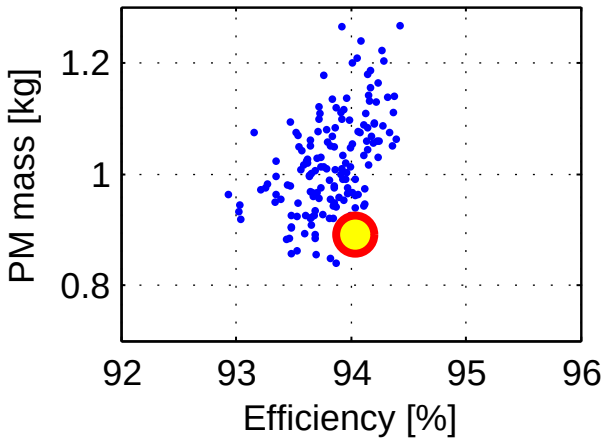

(c) 36-slot 6-pole integer-slot IPM

Figure 4.17: Design objectives corresponding only to motors satisfying the design constraints. Also shown are the selected best compromise designs corresponding to every topology.

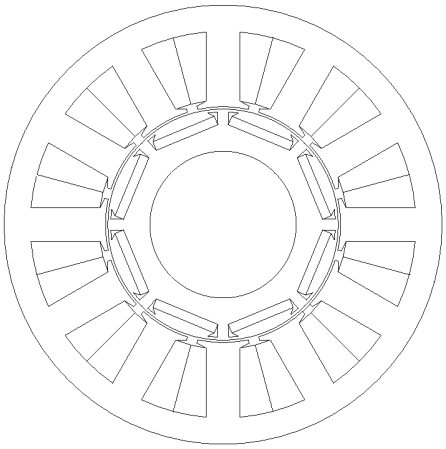

(a) 12-slot 8-pole fractional-slot IPM

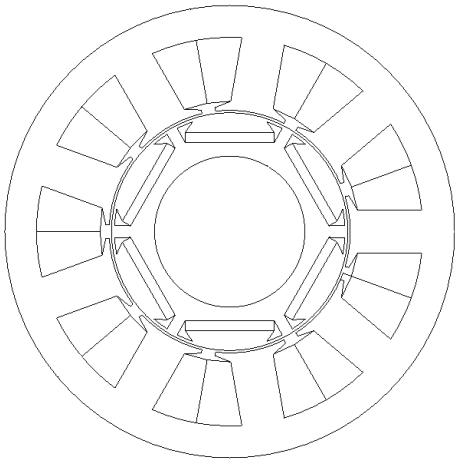

(b) 9-slot 6-pole fractional-slot IPM

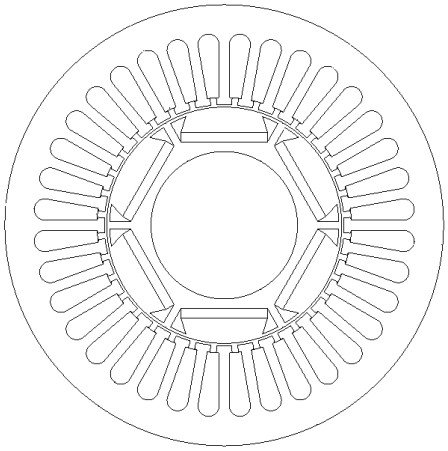

(c) 36-slot 6-pole integer-slot IPM

Figure 4.18: Cross-sections of optimized motors.

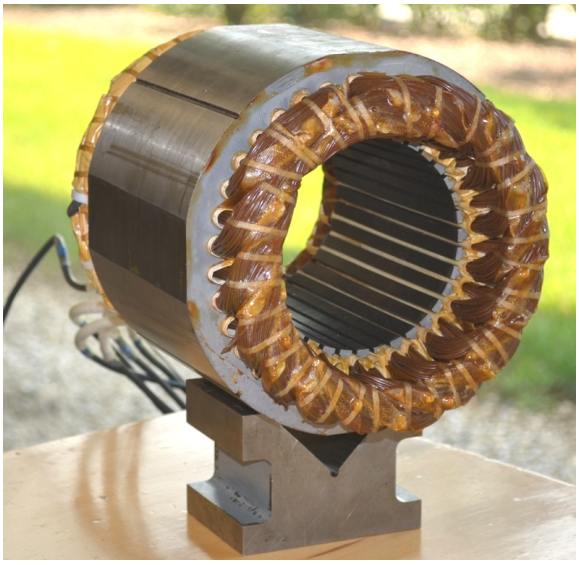

(a) 36-slot 6-pole fractional-slot stator.

(b) 9-slot 6-pole fractional-slot stator.

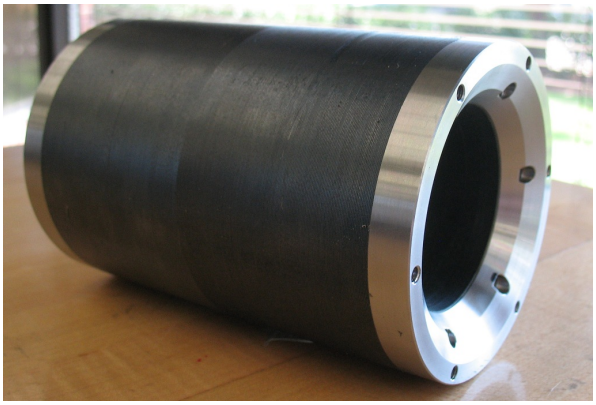

(c) Common 6-pole IPM rotor with step skew.

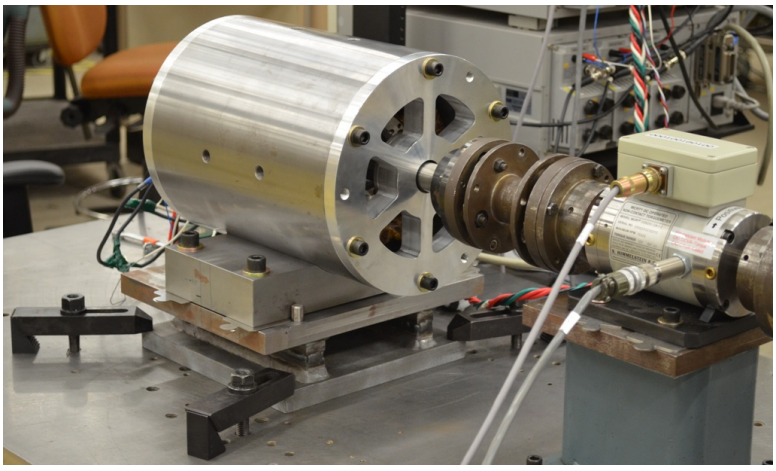

(d) Assembled motor.

Figure 4.19: Prototyped 13.5kW IPM motors.

Figure 4.20: Dynamometer setup used for testing.

dynamometer test set-up for one of the two motors.

Open-circuit Testing

Open-circuit tests were performed to validate the designs. Shown in Fig. 4.21 and Fig. 4.22 are the open-circuit back emf waveforms of the integer-slot and fractional-slot motors. Also, provided in Tables 4.11 and 4.12 are the peak values of the fundamental components of the line-to-neutral and line-to-line open-circuit emfs. Good agreement between the predicted values and measurements was observed.

Losses at open-circuit conditions were measured in two steps to segregate friction and windage losses from open-circuit electromagnetically induced core losses. First, friction and windage losses were measured in the operating speed range with a demagnetized rotor. Results are provided in Fig. 4.23a. Second, the motor open-circuit losses were measured with the magnetized rotor. Results are provided in Fig. 4.23b and Fig. 4.23c. The difference between the open-circuit losses and friction and windage losses, shown in Fig. 4.23, is an estimate of the open-circuit core losses induced by the rotating field established by the permanent magnets. Also provided in Fig. 4.23 are the predicted values of the open-circuit losses. Tests were performed on a small dynamometer with a torque transducer that allows for measurements of low friction, windage and core-loss-induced braking torques. Good agreement between measurement and FEA predicted open-circuit losses should be noted in these results.

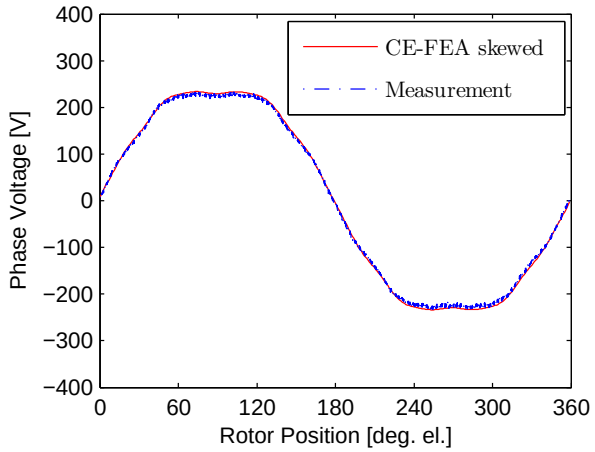

(a) Phase (line-to-neutral) emf.

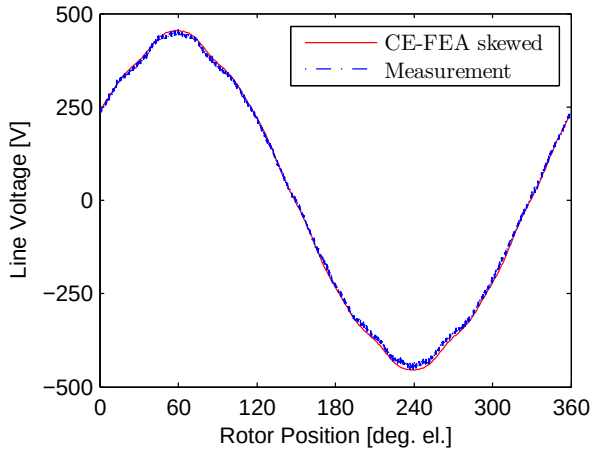

(b) Line (line-to-line) emf.

Figure 4.21: Measured and simulated open-circuit back emf waveforms for 36-slot 6-pole motor operating at 1800 r/min.

Table 4.11: Open-circuit emf values of 36-slot 6-pole motor.

	CE-FEA skewed	Measurement
Phase (line-to-neutral) e_{pk} [V]	233.7	233.3
Phase (line-to-neutral) e_1 [V]	255.8	249.8
Line (line-to-line) e_{pk} [V]	454.1	457.0
Line (line-to-line) e_1 [V]	443.4	436.1

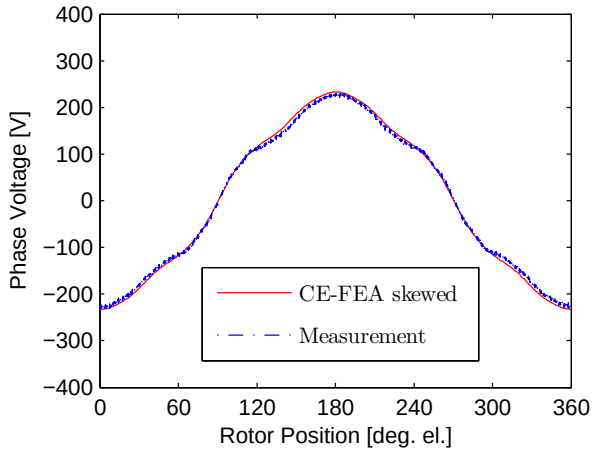

(a) Phase (line-to-neutral) emf.

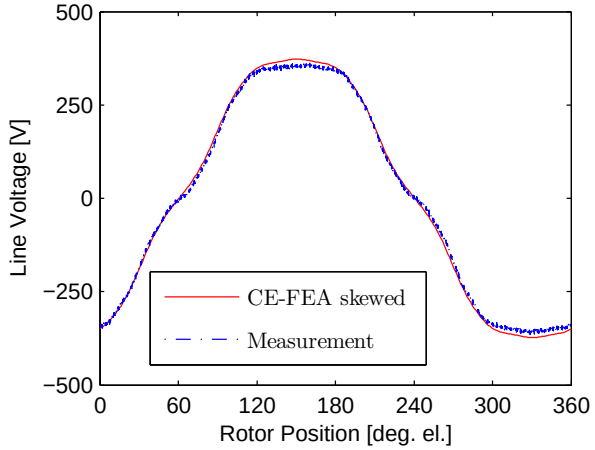

(b) Line (line-to-line) emf.

Figure 4.22: Measured and simulated open-circuit back emf waveforms for 9-slot 6-pole motor operating at 1800 r/min.

Table 4.12: Open-circuit emf values of 9-slot 6-pole motor.

	CE-FEA skewed	Measurement
Phase (line-to-neutral) e_{pk} [V]	232.9	229.8
Phase (line-to-neutral) e_1 [V]	223.6	214.0
Line (line-to-line) e_{pk} [V]	373.1	362.3
Line (line-to-line) e_1 [V]	387.3	371.5

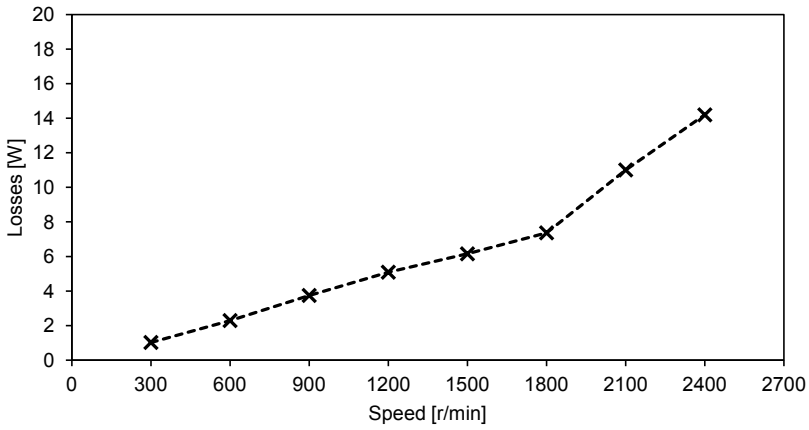

(a) Friction and windage loss measurements with demagnetized rotor.

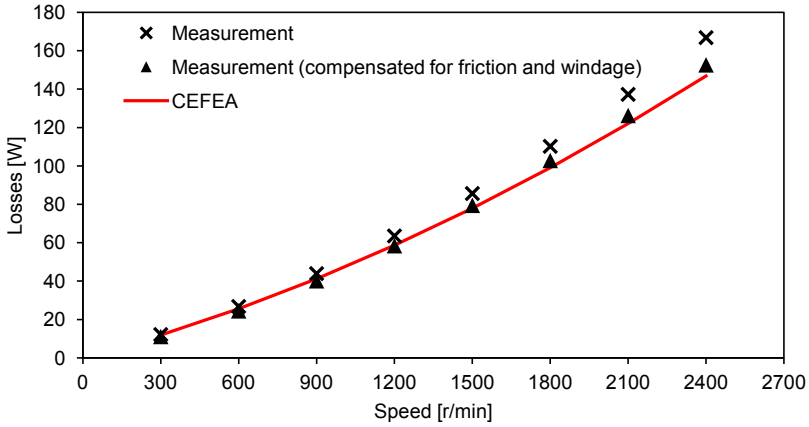

(b) 36-slot 6-pole open-circuit losses.

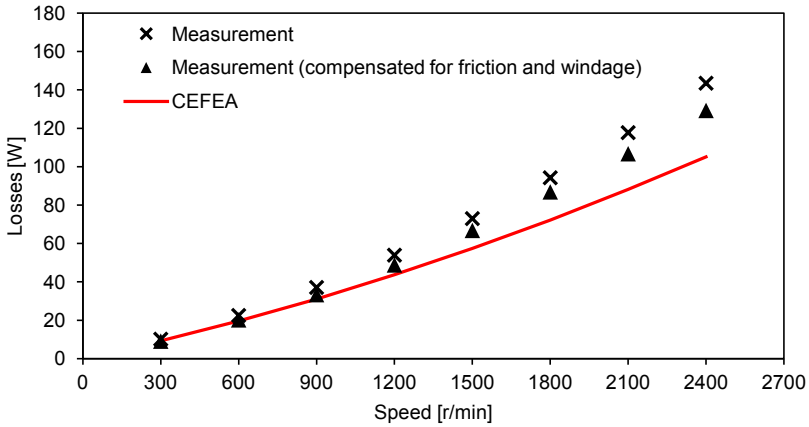

(c) 9-slot 6-pole open-circuit losses.

Figure 4.23: Measured and simulated open-circuit losses.

Equivalent Circuit Parameters

Winding resistances and inductance were measured at room temperature. Results are provided in Table 4.13. Variation of dq inductances with the magnitude of the load current (q-axis) is shown in Fig. 4.24. Measured inductance values provided in Fig. 4.24 were estimated using the drive firmware algorithm. Also shown in Fig. 4.24 are the values of apparent inductances predicted by the FEA software using the procedure outlined in Chapter 3. Reasonable correlation between the measurements and predicted values should be noted.

Load Testing

Load testing was performed to validate the performance of both motors in a wide range of torque-speed operating conditions. The motors were supplied by a commercially available general purpose ac drive (Yaskawa A1000). Load testing was performed on a dynamometer with an induction machine load that was regulated by an ac drive (ABB ACS800). Efficiency measurements were performed using torque and speed measurements obtained using an in-line torque transducer and motor terminal current and voltage measurements. In addition, overall motor-drive system efficiency was measured using a second set of terminal current and voltage measurements at the input of the drive. Two Yokogawa power analyzers (WT1800 and PZ4000), one for motor efficiency measurements and one for drive efficiency measurements were used to process the data. The experimental setup showing the instrumentation used for efficiency measurements is shown in Fig. 4.20. In the final application, the optimized motor is to be housed inside of a compressor with compressed fluid passing through the motor assembly providing additional cooling. To avoid insulation system damage due to excessive temperature rise during dynamometer testing, the motor was cooled with additional external fans and the temperature was monitored using thermocouples embedded into the stator winding. Provided in Fig. 4.25 are the waveforms of phase currents for the integer-slot and fractional-slot motors operating at the rated load

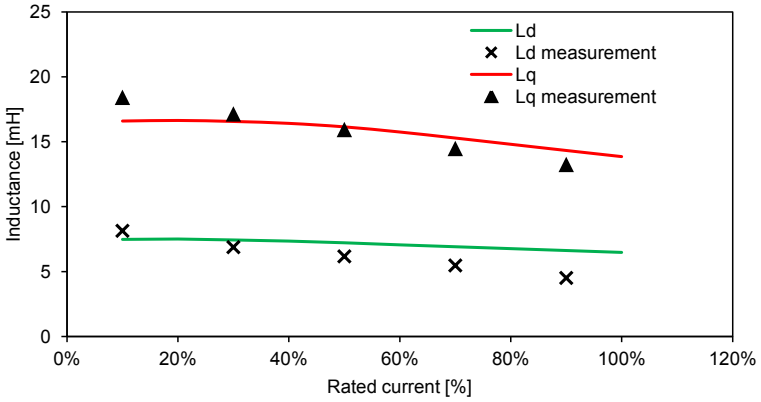

(a) 36-slot 6-pole motor.

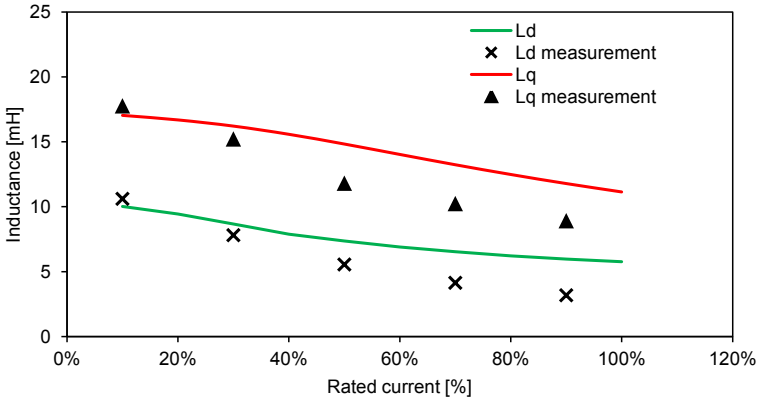

(b) 9-slot 6-pole motor.

Figure 4.24: Measured and simulated dq inductances.

Table 4.13: Motor equivalent parameters and terminal quantities at 20°C.

	36-slot 6-pole	9-slot 6-pole
Phase resistance r_s [Ω]	0.27	0.20
Permanent flux linkage λ_{PM} [mWb]	441.7	378.4
Rated line voltage V_s [V_{rms}]	460	460
Rated current I_s [A_{rms}]	24.1	28.0
Rated MTPA torque angle β [deg. el.]	123° (γ=33°)	119° (γ=29°)

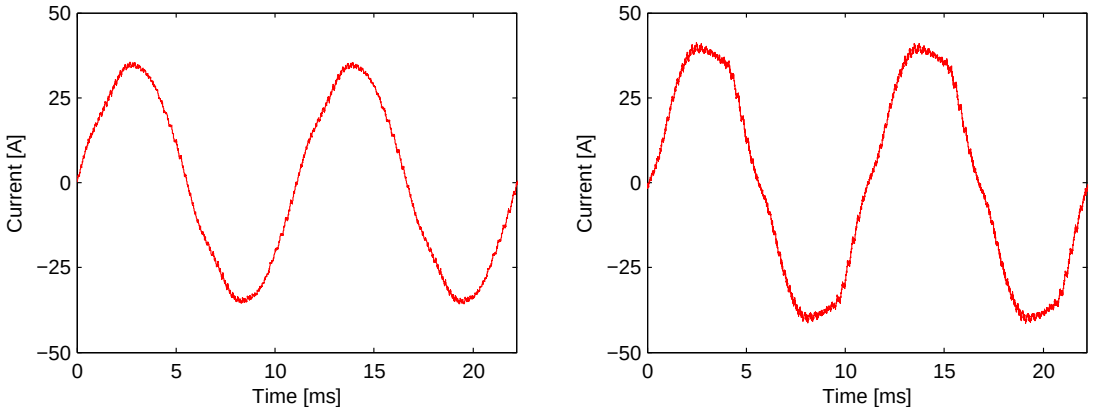

(a) 36-slot 6-pole motor.

(b) 9-slot 6-pole motor.

Figure 4.25: Measured terminal currents at rated load conditions (1800 r/min, 70 Nm).

conditions. Motor, drive and system efficiencies for the two motors obtained from experimental measurements performed at various torque-speed operating conditions are shown in Figs. 4.26 and 4.27, respectively. Comparing Figs. 4.26 and 4.27 one should notice a slight efficiency advantage for the integer-slot design. This can be explained by the fact that the motor end winding resistance of the integer-slot motor was overestimated during the design stage. Furthermore, comparing terminal current profiles of the two machines shown in Fig. 4.25, one should notice a slight increase of the current waveform distortion in the fractional-slot motor leading to additional core losses not accounted for during the design optimization/synthesis stage. This distortion can be partially attributed to increased distortion in the back emf waveform of the fractional-slot motor as evidenced in the waveforms of Fig. 4.22.

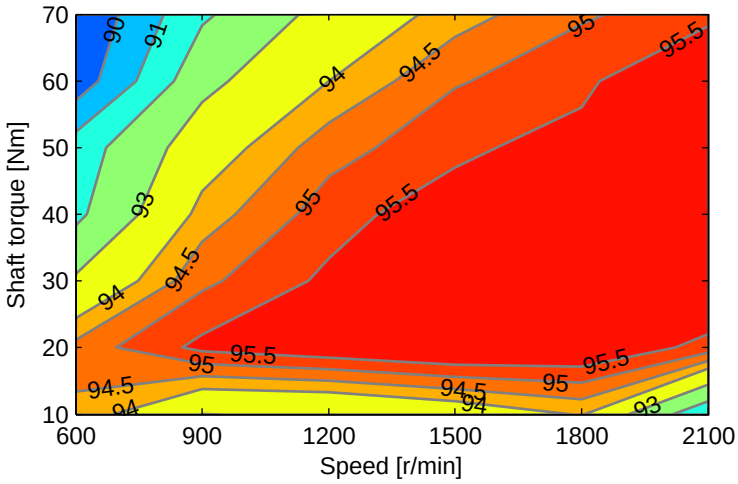

(a) Motor efficiency.

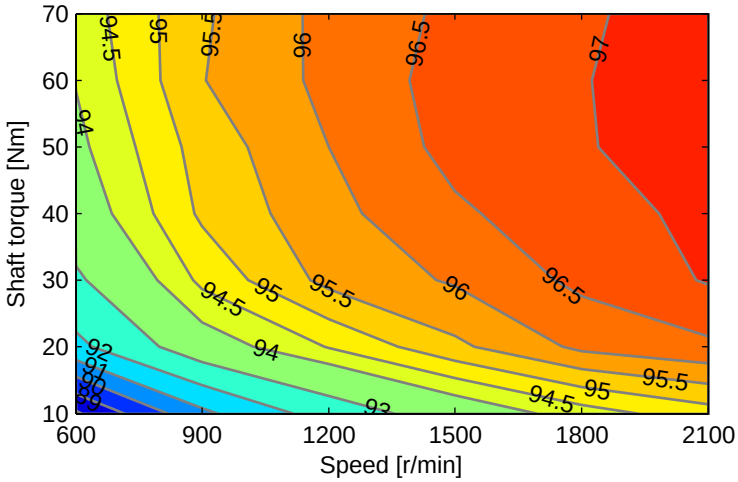

(b) Drive efficiency.

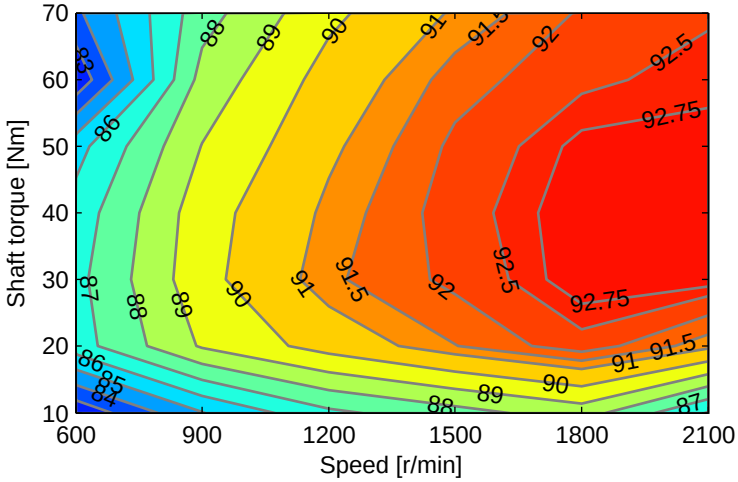

(c) System efficiency.

Figure 4.26: Measured motor, drive and system efficiencies for 36-slot 6-pole motor.

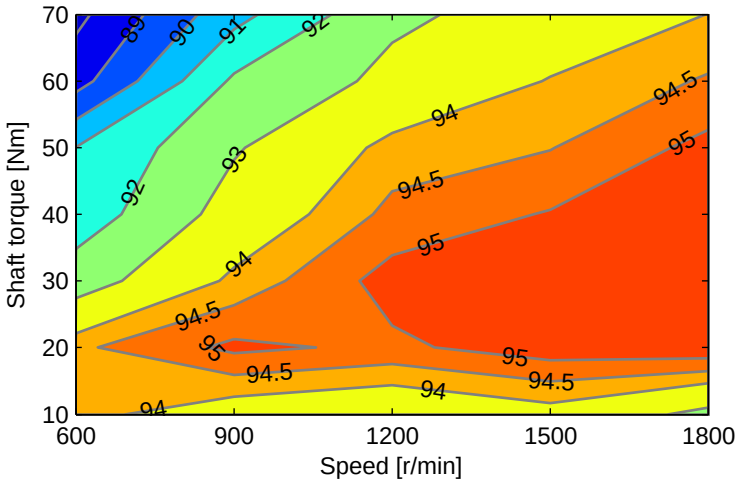

(a) Motor efficiency.

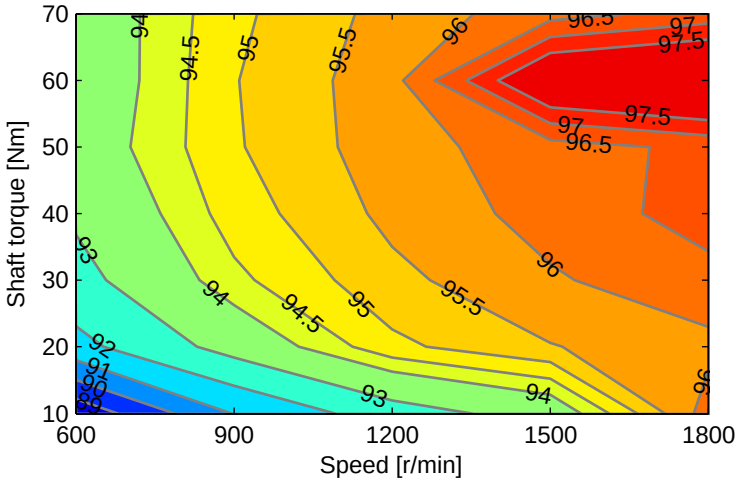

(b) Drive efficiency.

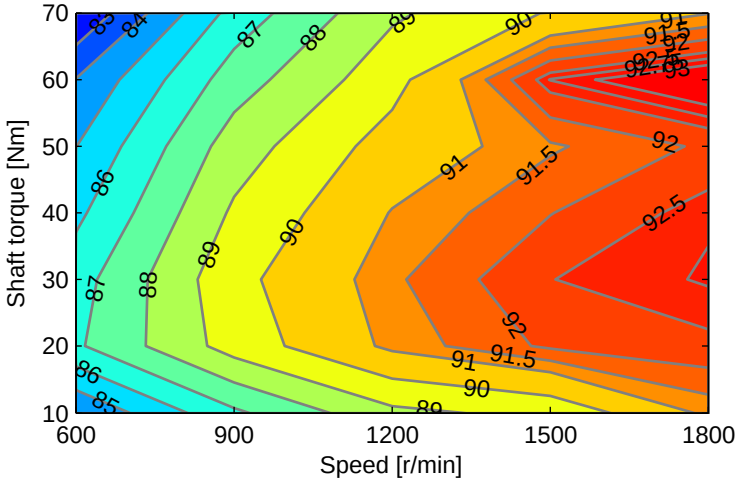

(c) System efficiency.

Figure 4.27: Measured motor, drive and system efficiencies for 9-slot 6-pole motor.

4.6 Case Study - IV: Design of a 22kW Motor for General Purpose Application

In this section, an optimization of an IPM motor for a general purpose high efficiency application is described. In this application the IPM motor was designed to replace an existing induction motor to improve the overall system efficiency. The motor outside diameter and inner rotor (shaft) diameter are fixed by the existing NEMA totally enclosed fan cooled (TEFC) induction motor housing. An open-slot stator configuration was used to facilitate and simplify the stator winding manufacturing. The original IPM motor had a flat bar-type magnet rotor layout similar to the one shown in Fig. 2.11c. An alternative motor design that employed a V-shaped magnet layout was used in the optimization to reduce material costs and increase rated-load efficiency of the existing design. The magnets were segmented to reduce eddy current losses induced by the armature mmf harmonics typical of motors with fractional-slot q=0.4 slots/pole/phase construction. Detailed analysis of the armature mmf harmonics was presented in Chapter 2, namely in Fig. 2.8. In this work, one prototype motor was designed and tested.

The design optimization method was used to optimize an existing fractional-slot IPM motor configuration with 12-slots stator and 10-pole rotor ($q = 0.4$), and a double-layer winding. Parametric motor geometry showing the geometric variables used in the optimization is provided in Fig. 4.28. A total of 9 stator and rotor geometric variables have been used in the optimization.

Stator (4 variables):

- stator inner diam., D_{Si}, air-gap, g, tooth width, w_T, slot depth, d_S.

Rotor (5 variables):

- PM width, w_{PM}, PM thickness, h_{PM}, PM depth, d_{PM},pole-arc angle, τ_P, q-axis bridge, w_q.

In this optimization, the thickness of the slot wedge, t_{wedge}, and its position with respect

to the air gap, d_{wedge}, were fixed. In addition, the radial PM bridge width, w_{rad}, PM webs, w_{Fe1}, and, w_{Fe2}, and the depth of the q-axis bridge, d_q, were assumed fixed.

Permanent magnet and lamination material properties are given in Table 4.14. Both the permanent magnets and stator winding are assumed to operate at 100° C.

Design specifications

Design specifications, objectives, and constraints are provided below.

- Stator slot and rotor pole combination: 12-slot/10-pole
- Rotor type: V-shape (segmented magnets) (Fig. 4.28)
- Winding: double-layer/fractional-slot tooth-wound type
- Rating: 22kW (30hp), 1800r/min
- Stator OD: 317.5 mm (12.5")
- Current density: 2.25A$_{rms}$/mm^2, target slot fill: 0.44

Design objectives

In this optimization study, potential improvements of the original design in terms of cost and efficiency were investigated. These improvements can be summarized in two objectives:

1. Minimize material costs, with a cost function weighted as follows:

$$\min(207m_{PM} + 8m_{Cu} + m_{Fe})$$

Table 4.14: Material data 22kW IPM motor.

Stator and rotor cores: M19-26Ga
PM: NdFeB (35SH), 270 kJ/m^3, H$_{cB}$=-876 kA/m, B$_{rem}$=1.17 T
PM demag.: $\alpha_{B_{rem}}$=-0.10 %/°C, $\alpha_{H_{cJ}}$=-0.55 %/°C
Slot wedge: $\mu_R = 4.5$
Material temperature: Copper 100°C, PMs 100°C
PM (@ 100°C): H$_{cB}$=-805.9 kA/m, B$_{rem}$=1.08 T
Copper (@ 100°C): ρ_{Cu}=2.25897 $\times 10^{-8}$ Ωm

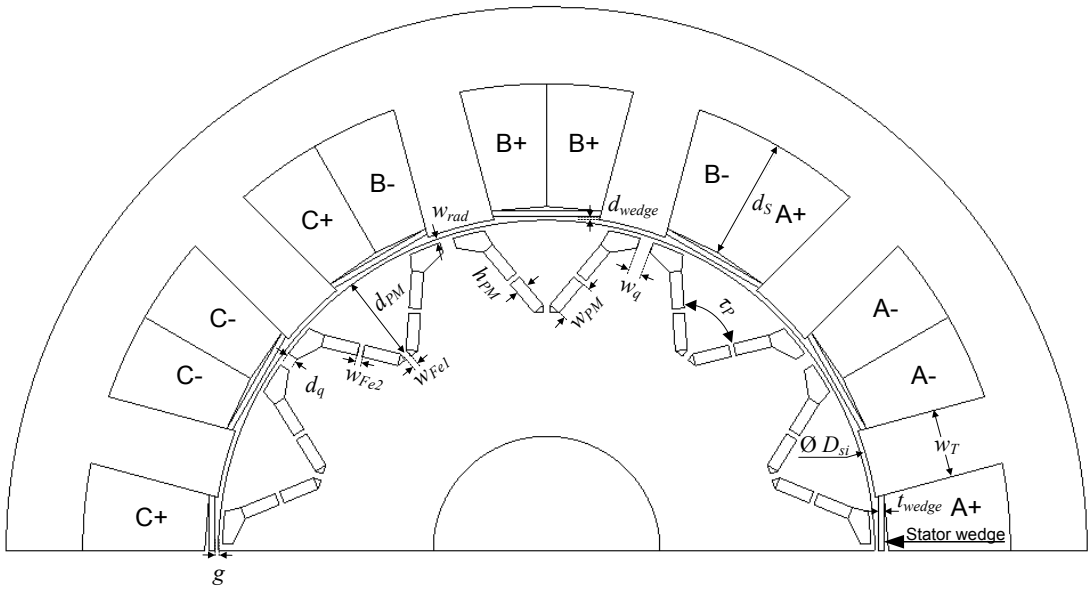

Figure 4.28: Parametric cross-section of the 22kW IPM motor showing design variables. Due to odd periodicity five-poles of the fractional-slot machine are modeled.

where, m_{PM}, m_{Cu} and m_{Fe} are masses of permanent magnets, stator winding, and stator and rotor laminated cores, respectively.

2. Minimize stator winding and core losses:

$$\min(P_{Cu} + P_{Fe})$$

where, P_{Cu} and P_{Fe}, are the *dc* stator winding losses, and stator core losses, respectively.

Design constraints

Three performance constraints ensuring acceptable torque quality, sinusoidal induced terminal voltage and safe operation of permanent magnets to prevent demagnetization under load were enforced by the following:

1. Limit the rated-load torque ripple:

$$\frac{\max(T_{em}) - \min(T_{em})}{\text{avg}(T_{em})} < 5\%$$

where, T_{em}, is the electromagnetic torque.

2. Ensure near sinusoidal induced voltage waveform:

$$\frac{\sqrt{v_5^2 + v_7^2}}{v_1} < 3\%$$

where, v_1, v_5 and v_7 are the magnitudes of the fundamental, fifth and seventh harmonics of the induced voltage waveform at the terminals of the machine.

3. Avoid local PM demagnetization based on the estimated minimum flux density in the PM by stipulating that:

$$\min(B_{PM}) > 0.3B_{rem}$$

where, $\min(B_{PM})$, is the lowest value of flux density in the direction of PM magnetization in the bulk permanent magnet material, and B_{rem}, is the permanent magnet remanent flux density at room temperature.

A multi-objective optimization using the DE algorithm was carried using the settings provided in Table 4.15. The objective functions, cost and losses, corresponding to all the motors evaluated during optimization are shown in Figs. 4.29a and 4.29b. In Fig. 4.29a, a total of 3,000 candidate designs were evaluated during the optimization search. A large variability of the objectives in the design space can be observed. Shown in Fig. 4.29b are the design objectives corresponding to 338 machines satisfying the design constraints, which are a subset of the 3,000 candidate designs of Fig. 4.29a evaluated during the optimization search. Fig. 4.29b also includes the Pareto-optimal set of designs. Also shown in Fig. 4.29b are the objectives corresponding to the original design, three selected optimized designs, and the Pareto-optimal set. The objectives corresponding to the original design are plotted for reference. The predicted performance parameters of the optimized machines are summarized in Table 4.16. The optimized machines have reduced cost and magnet masses. Considering the three optimal motors, M-1, M-2 and M-3, the case M-2 offers the best compromise between material costs and efficiency. Accordingly, the resulting prototyped motor M-2 is shown in Fig. 4.30.

The winding design consists of the selection of the number of stator turns and parallel paths. The number of series turns per phase was selected based on the terminal voltage

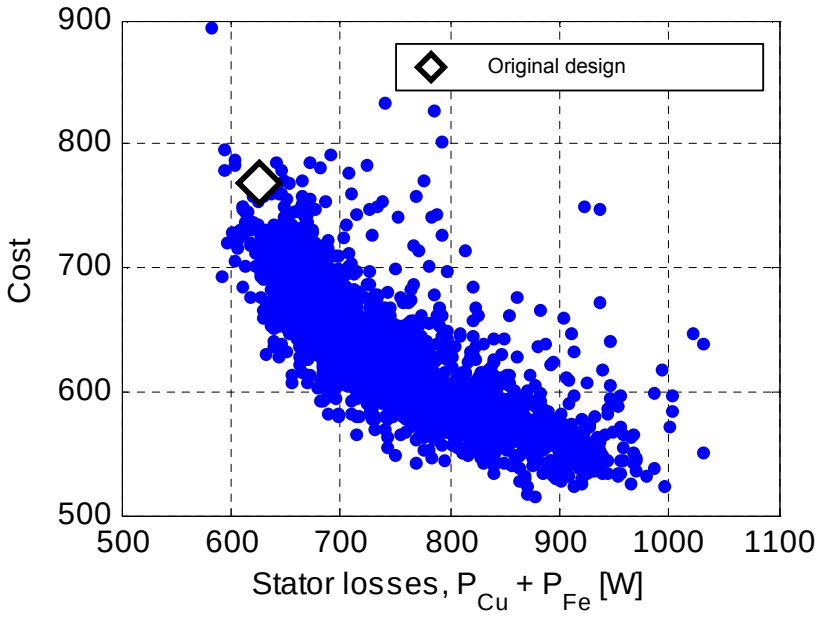

(a) 3,000 candidate designs evaluated in the optimization search.

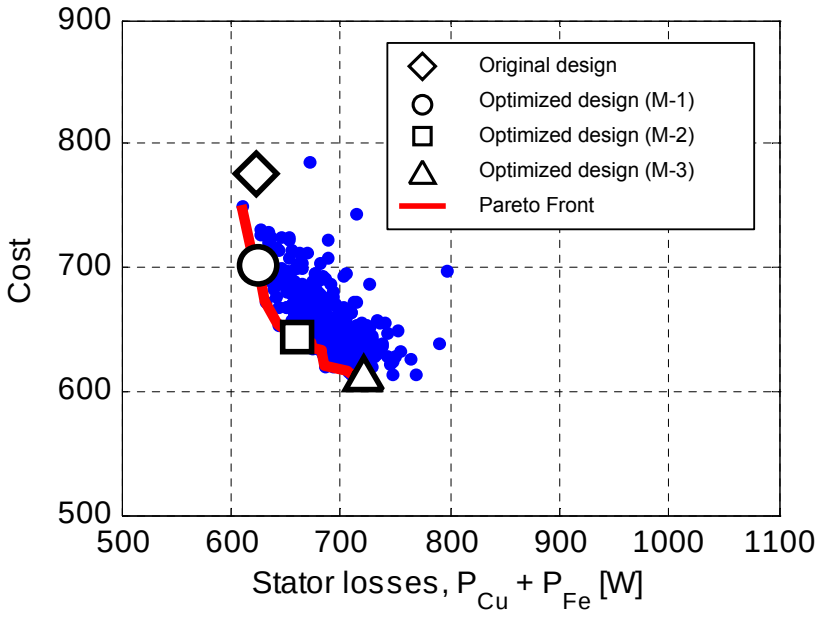

(b) 338 candidate designs satisfying the design constraints.

Figure 4.29: Design objectives showing: design objectives of all candidate designs, Pareto-optimal set after 60 generations and the selected optimal machines.

Table 4.15: Optimization settings (22kW IPM).

Model:	Static nonlinear CE-FEA
Algorithm:	DE/local-to-best/1, $C_R = 1.0$, F = 0.85
Setup:	Population size, $N_P = 50$, Generations $N_G = 60$
Candidate designs:	3,000

Table 4.16: Machine costs and performance (22kW IPM).

Masses	Original	M-1	M-2	M-3
Cost ($w_{PM} = 207, w_{Cu} = 8, w_{Fe} = 1$)	770.4	727.7	675.6	624.4
PM mass, m_{PM} [kg]	3.1	2.4	2.2	2.0
Total active mass, m_{motor} [kg]	79.4	114.3	99.8	93.1
Rotor inertia, J_{rotor} [kg m^2]	0.16	0.22	0.14	0.13
Losses and Efficiency				
Copper Losses [W]	189.1	228.7	219.5	211.9
Steel Stator [W]	451.3	462.9	520.3	581.8
Steel Rotor (post-optimization) [W]	164.1	161.9	129.7	134.5
PM (2-D Eddy) (post-optimization) [W]	141.8	62.1	61.2	66.3
Total Losses [W]	946.3	915.7	930.8	994.5
Efficiency [%]	96.1	96.3	96.2	95.9

at rated-load condition. In this process contributions due to: 1) back emf (induced by the PMs), and 2) the induced voltage due to the armature current, are both included. Proper operation of the ac drive current regulator is ensured by providing for a reasonable margin between the dc-link voltage and the terminal voltage of the machine.

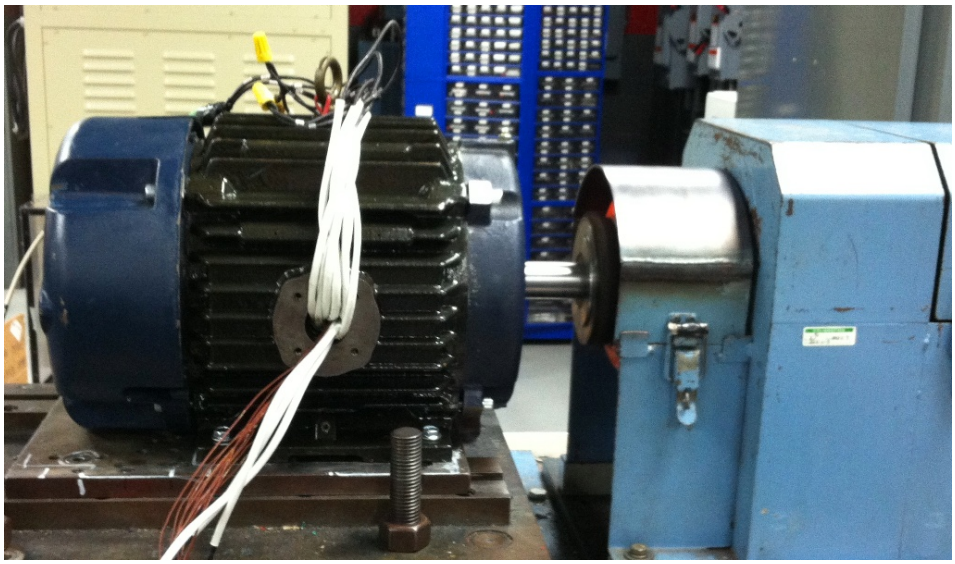

(a) Assembled motor (M-2).

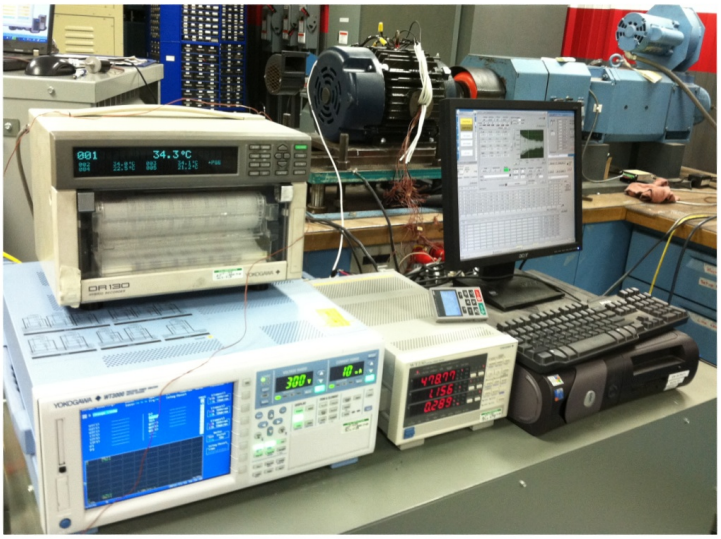

(b) Dynamometer testing.

Figure 4.30: Prototyped 22kW IPM motor and experimental setup.

Open-circuit Testing

The open-circuit tests were performed to validate the design. Shown in Fig. 4.31 are the FEA predicted and measured open-circuit back emf waveforms. Also, provided in Table 4.17 are the total and fundamental peak values of the open-circuit emf. The measured open-circuit emf of the prototyped motor was found to be reduced by 15% less than the FEA predicted value. The difference was attributed to the discrepancies between the FEA model and the prototyped motor. Three major sources of differences were identified as follows:

- rotor lamination clearances for magnet insertion were not accounted for in the initial FEA model,
- stack length of the prototyped motor was found to be reduced by 5% less than the initial FEA model,
- magnets used in prototype construction had 4% lower magnet remanence than the nominal datasheet values used in the initial FEA model.

The reduction of the open-circuit emf resulted in the derating of the prototyped motor power in order to maintain acceptable thermal performance and efficiency. The FEA model was modified to match the prototyped motor. The results obtained from the modified FEA model are shown in Fig. 4.32.

Losses at open-circuit conditions were measured with a magnetized rotor. Results are provided in Fig. 4.33. Also, included in Fig. 4.33 are the predicted open-circuit losses. Satisfactory agreement between measurements and open-circuit losses predicted by FEA should be noted.

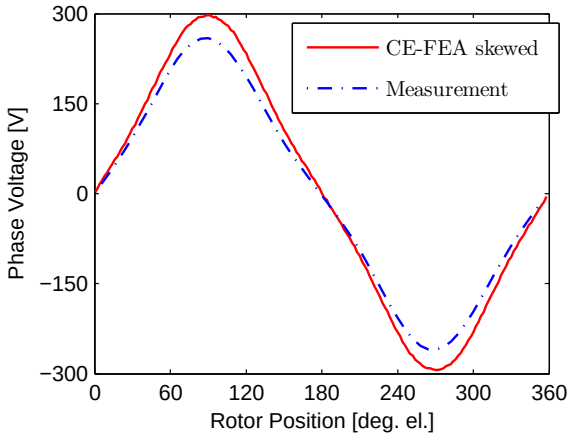

(a) Phase (line-to-neutral) emf.

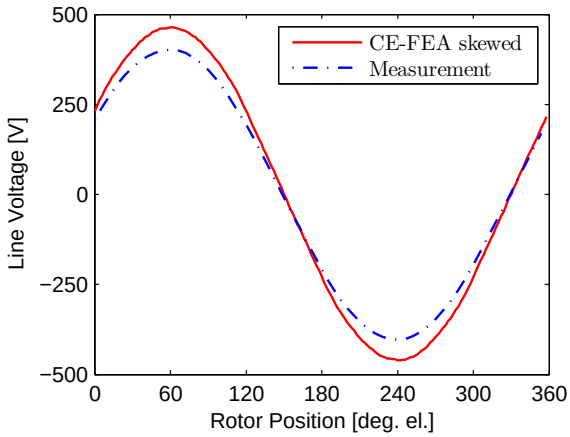

(b) Line (line-to-line) emf.

Figure 4.31: Measured and simulated (initial FEA model) open-circuit back emf waveforms 22kW motor operating at 1800 r/min.

Table 4.17: Open-circuit emf values of 22kW motor.

	CE-FEA skewed	Measurement
Phase (line-to-neutral) e_{pk} [V]	296.2	259.1
Phase (line-to-neutral) e_1 [V]	246.4	209.9
Line (line-to-line) e_{pk} [V]	463.8	402.3
Line (line-to-line) e_1 [V]	426.8	364.1

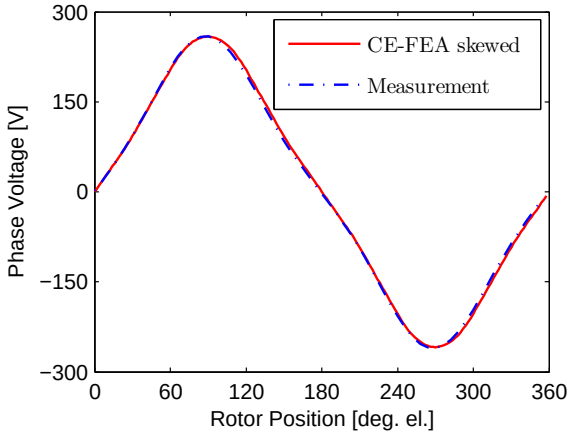

(a) Phase (line-to-neutral) emf.

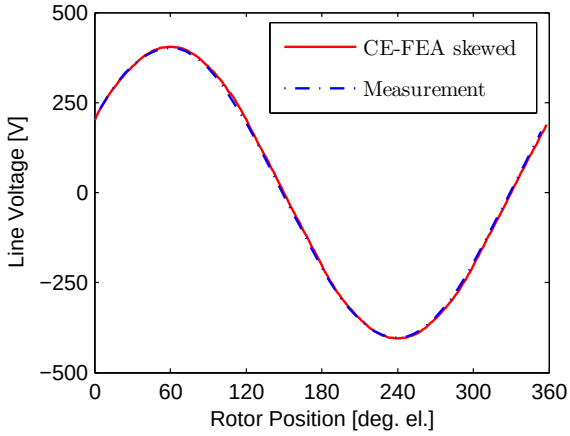

(b) Line (line-to-line) emf.

Figure 4.32: Measured and simulated (updated FEA model) open-circuit back emf waveforms 22kW motor operating at 1800 r/min.

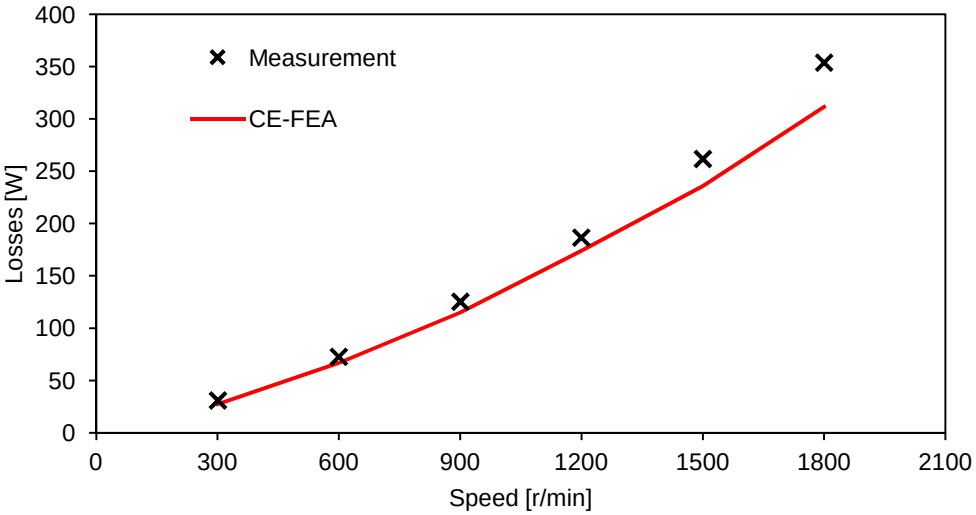

Figure 4.33: Measured and simulated open-circuit losses (22kW motor).

Table 4.18: Motor equivalent parameters and terminal quantities at 20°C.

	FEA (updated)	Measurement
Phase resistance r_s [mΩ]	27	30
Permanent flux linkage λ_{PM} [mWb]	435.7 (372.2)	371.2
Direct-axis inductance (open-circuit) L_d [mH]	2.8	2.5
Quadrature-axis inductance (open-circuit) L_q [mH]	3.5	3.4
Saliency ratio (open-circuit) L_q/L_d [mH]	1.28	1.38
Rated line voltage V_s [V_{rms}]	460	460
Rated current I_s [A_{rms}]	45.7	45.8
Rated MTPA torque angle β [deg. el.]	121° (γ=31°)	n/a

Equivalent Circuit Parameters

Winding resistances and inductance for the prototyped motor were measured at room temperature. The results are provided in Table 4.18. The measured inductance values are provided in Table 4.18 for reference. Also given in Table 4.18 are the values of the apparent inductances predicted by FEA using the procedure outlined in Chapter 3. Reasonable agreement between the inductance measurements and predicted values should be noted.

Separation of Losses

Shown in Figs. 4.34a and 4.34b is the separation of losses at 1800 r/min at open-circuit and rated-load (current) conditions obtained using the updated FEA model. Significant stator and rotor core losses should be noted. The increase of core and magnet eddy current losses from open-circuit conditions to rated-load can be attributed to significant armature mmf harmonics of the fractional-slot stator winding used in this prototype. These simulations were performed assuming an ideal sinusoidal armature current supply. This implies that losses induced by the PWM current ripples were neglected in the FEA computations.

Thermal Performance

The thermal measurements were performed on the prototyped motor. The temperature rises of the critical motor components, namely, the insulation system were measured to be within allowable temperature ranges, thus verifying the analysis performed during the

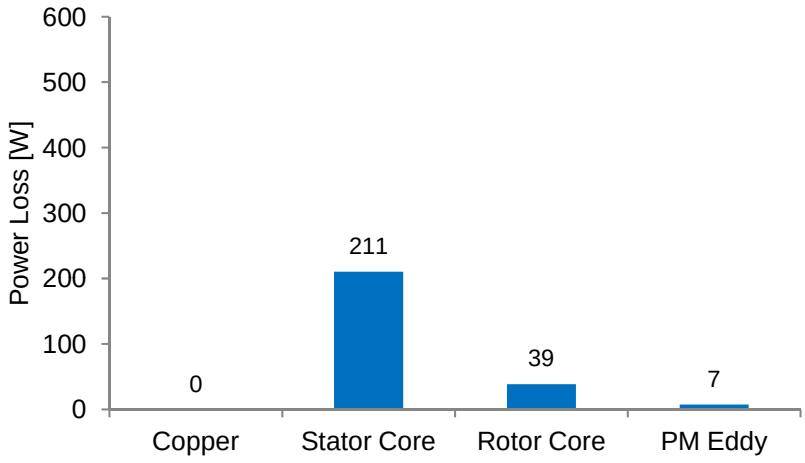

(a) Open-circuit.

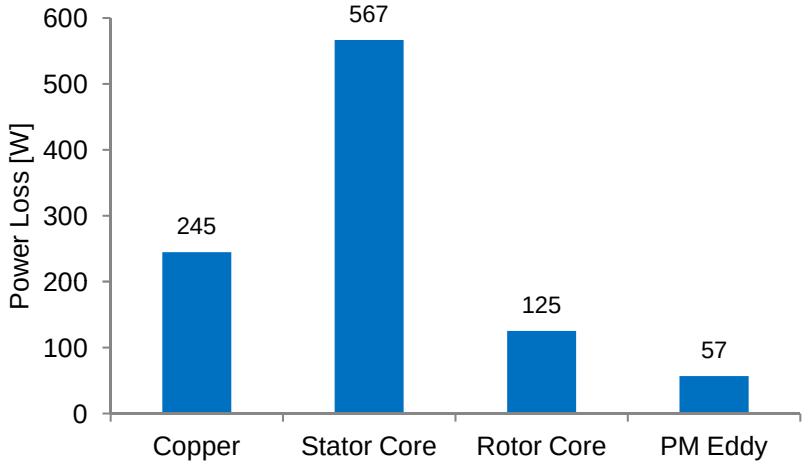

(b) Rated-load (1800 r/min, 120 Nm).

Figure 4.34: Simulated losses separated by major motor component (22kW IPM).

design and optimization stage. At rated load and speed, the winding temperature increases to 120°C under normal ambient temperatures. The corresponding stabilized temperature measurements are summarized in Fig. 4.35. Provided in Fig. 4.35 are the temperature measurements in several locations in the slot and coil. Also shown is the separation of losses in different stator components obtained from FEA. Fig. 4.35a shows the temperature distribution of the motor operating at 1800 r/min and rated-torque. In addition, the temperature measurements corresponding to the motor operating at 900 r/min and rated-torque are summarized in Fig. 4.35b.

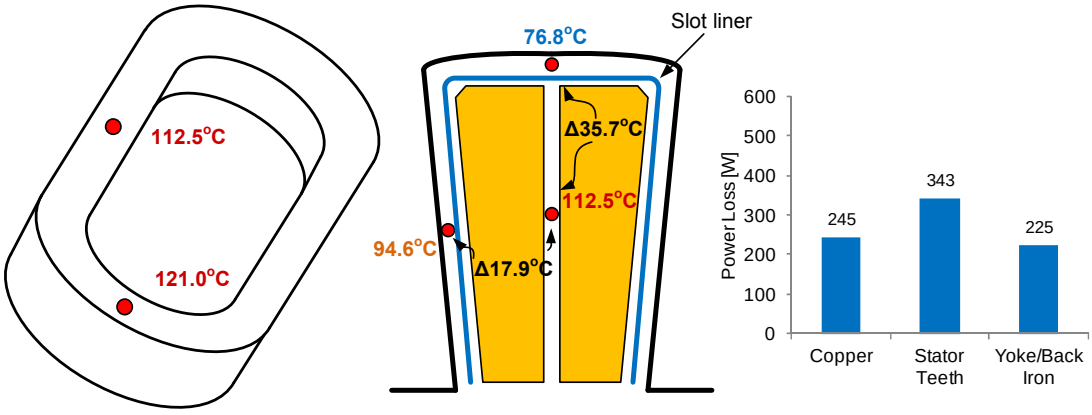

(a) Rated conditions at 1800 r/min.

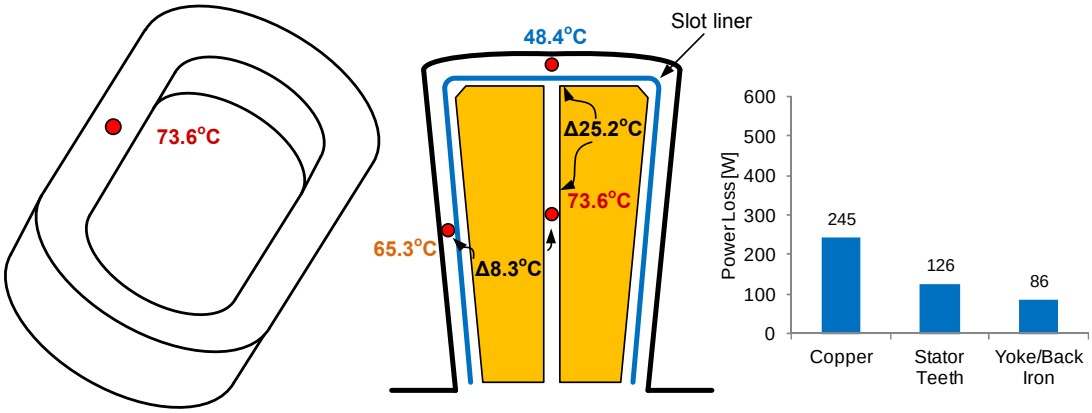

(b) Rated conditions at 900 r/min.

Figure 4.35: Measured stabilized temperature distributions. Also shown is the separation of losses for various stator components obtained using FEA.

In summary, this chapter presented a multi-objective model-based design optimization method that relies on an efficient nonlinear FEA model for calculation of motor performance, and uses differential evolution to search large multi-dimensional design spaces. The method was demonstrated on four case-study motor designs. In the first case-study, application of the method to design optimization of an existing motor was presented. This example demonstrated the conflicting nature of two common design objectives, and possibility of significant performance improvements obtained using the developed automated design tool. In the second example, application of the design tool to a motor topology selection process was demonstrated. This example demonstrated a method for quantitatively comparing different motor technologies optimized with respect to the same objectives and constraints. In the last two examples, application of the automated design tool to design optimization and synthesis of two industrial motors was demonstrated. Three prototype motors were built and tested to validate the analysis. Based on the contents of this chapter and the previous three chapters, the main conclusions are given in the following concluding Chapter 5.

Chapter 5

Conclusions

5.1 Summary and Conclusion

In this dissertation, a large-scale model-based design optimization and synthesis method for electric machines was presented. The computational method outlined in this work provides a frame-work for accurate and rapid analysis of steady-state performance of synchronous electric machines with special focus on permanent magnet sine-wave current regulated permanent magnet machines. A nonlinear electromagnetic FE-based model was used to rapidly calculate a comprehensive set of performance parameters that include torque ripple profiles and cogging torques, induced voltages, as well as stator losses and electric machine efficiency. The method for calculation of stator core flux densities was generalized and extended to include fractional and integer-slot winding layouts. In addition, the method includes means for rapid estimation of distributed stator forces and effects of stator and/or rotor skew on the performance of the machine. The method employs Fourier analysis based on the results provided by a minimum number of magnetostatic FEA solutions and achieves a good balance between speed and precision, which makes it well suited for optimization studies that involve thousands of candidate design evaluations.

A population-based design optimization and synthesis method that uses a well-established differential evolution optimizer has been presented. The effectiveness of the method was demonstrated on examples of several comprehensive large-scale FEA-based multi-objective design optimization studies of PM ac machines. For the first case-study of a fractional-slot IPM motor, a total of eleven stator and rotor independent design variables have been simultaneously optimized to satisfy multiple design criteria. A total of 10,000 candidate

designs have been evaluated during the search, this included the search for the maximum torque per ampere condition for every candidate design. In the second case study, design of an integral MW direct-drive machine was considered. Four competing motor topologies were optimized. The topologies considered in this example were: 1) fractional-slot embedded SPM, 2) fractional-slot IPM, 3) integer-slot embedded SPM, 4) and integer-slot IPM, respectively. A total of 20,000 candidate machine designs have been evaluated using a modest pc-based computing setup. The Pareto-optimal design sets derived through a DE algorithm were used as a basis for quantitatively analyzing the trade-offs specific to the multi-objective optimization. Comparison on the basis of Pareto-optimal design sets, provides a method of evaluating and comparing different motor technologies (number of slots and poles, and various rotor layouts) designed to meet identical design requirements and constraints. The first case-study has showed that an optimal design with high efficiency and virtually zero torque ripple can be achieved even for a fractional-slot IPM topology with three slots per pole pair. In the second case-study, different machine topologies were systematically compared in terms of specific torque output, torque ripple and cost, leading to an optimal design selection. Two additional case-studies demonstrating the application of the developed method to design synthesis and optimization of industrial motors were presented. In the first example, an IPM motor for hermetic compressor application was designed and prototyped. In the second example, an IPM motor for general purpose high efficiency application was optimized and prototyped.

Application of electromagnetic FEA-based solvers allows for accurate estimation of intricate performance parameters, such as, cogging torque and torque ripple, core losses, and terminal conditions. However, to date the computational burden associated with FE-based models has limited their use in large-scale multi-dimensional design synthesis and optimization tools. The design method presented in this dissertation relies on the efficient FE modeling approach that reduces computational times by up to two orders of magnitude when compared to the conventional time-stepping FE analysis. This allows one to tackle large-

scale multi-dimensional electric machine design problems using modest pc-based computing facilities, while taking full advantage of the high fidelity of the FE-based electromagnetic solvers. The presented case studies demonstrate that the developed FEA-based approach practically eliminates the need for using less accurate analytical and lumped parameter equivalent circuit models for electric machine design optimization.

5.2 Recommendations for Future Work

In this work, methods for optimal design of electric machines have been investigated. A fast method for electromagnetic analysis has been developed and coupled to a population-based DE optimizer. In the current implementation the method is capable of rapidly estimating stator losses that include *dc* ohmic losses in the winding and core losses in stator laminations. Further improvements can be introduced by accounting for rotor losses in the core laminations and permanent magnets. This will be especially useful for fractional-slot machines that may have significant rotor losses due to increased armature mmf harmonics. High frequency losses due to pulse width modulated supplies can have significant effect on both core losses and permanent magnet losses. In future work, a method for calculation of high frequency components of stator winding ohmic losses, lamination and permanent magnet losses should be developed to further improve loss and efficiency calculation methods. These additional loss components can be included in the design optimization process in the future. In the optimization studies presented in this work, thermal performance of candidate design was not implicitly considered during optimization. The present method can be extended to include a thermal model of the machine to ensure safe operation of the insulation and permanent magnet systems during the design stage thus eliminating any unsuitable candidate designs during the search and optimization process.

BIBLIOGRAPHY

[1] A. S. Langsdorf, *Theory of Alternating-Current Machinery*. McGraw-Hill, 1937.

[2] M. Liwschitz-Garik and C. C. Whipple, *Theory of Alternating-Current Machinery*. New York, Van Nostrand, 1946.

[3] M. G. Say, *Alternating Current Machines*. Wiley, 1976.

[4] A. V. Ivanov-Smolensky, *Electrical Machines*. MIR Publishers, 1982.

[5] J. Pyrhonen, T. Jokinen, and V. Hrabovcova, *Design of Rotating Electrical Machines*. John Wiley and Sons, 2009.

[6] A. E. Fitzgerald, C. Kingsley, and S. D. Umans, *Electric Machinery*. McGraw Hill 6th Edition, 2003.

[7] J. R. Hendershot and T. J. E. Miller, *Design of Brushless Permanent-Magnet Machines*. Motor Design Books LLC. 2nd Edition, 2010.

[8] P. Silvester and M. Chari, "Finite element solution of saturable magnetic field problems," *IEEE Transactions on Power Apparatus and Systems*, vol. PAS-89, pp. 1642 –1651, September 1970.

[9] M. V. K. Chari and P. Silvester, "Analysis of turboalternator magnetic fields by finite elements," *IEEE Transactions on Power Apparatus and Systems*, vol. PAS-90, pp. 454 –464, March 1971.

[10] N. A. Demerdash, H. B. Hamilton, and G. W. Brown, "Simulation for design purposes of magnetic fields in turbogenerators with symmetrical and asymmetrical rotors part I-model development and solution technique," *IEEE Transactions on Power Apparatus and Systems*, vol. PAS-91, pp. 1985 –1992, September 1972.

[11] N. A. Demerdash and H. B. Hamilton, "Simulation for design purposes of magnetic fields in turbogenerators with asymmetrical and symmetrical rotors part II - model calibration and applications," *IEEE Transactions on Power Apparatus and Systems*, vol. PAS-91, pp. 1992 –1999, September 1972.

[12] N. A. Demerdash and H. B. Hamilton, "A simplified approach to determination of saturated synchronous reactances of large turbogenerators under load," *IEEE Transactions on Power Apparatus and Systems*, vol. 95, pp. 560–569, March 1976.

[13] T. W. Nehl, F. A. Fouad, and N. A. Demerdash, "Determination of saturated values of rotating machinery incremental and apparent inductances by an energy perturbation method," *IEEE Transactions on Power Apparatus and Systems*, vol. PAS-101, pp. 4441 –4451, December 1982.

[14] T. W. Nehl, N. A. Demerdash, T. M. Hijazi, and T. L. McHale, "Automatic formulation of models for simulation of the dynamic performance of electronically commutated dc machines," *IEEE Transactions on Power Apparatus and Systems*, vol. PAS-104, pp. 2214 –2222, August 1985.

[15] D. M. Ionel, M. J. Balchin, J. F. Eastham, and E. Demeter, "Finite element analysis of brushless dc motors for flux weakening operation," *IEEE Transactions on Magnetics*, vol. 32, pp. 5040 –5042, September 1996.

[16] D. M. Ionel, J. F. Eastham, E. Demeter, M. J. Balchin, D. Stoia, and C. Apetrei, "Different rotor configurations for bldc motors operating in flux weakening mode," in *Proc. ICEM'96 Conference, Vigo, Spain*, vol. II, pp. 331 – 336, September 1996.

[17] N. Bianchi and S. Bolognani, "Magnetic models of saturated interior permanent magnet motors based on finite element analysis," in *Industry Applications Conference, 1998. Thirty-Third IAS Annual Meeting. The 1998 IEEE*, vol. 1, pp. 27 –34 vol.1, October 1998.

[18] D. Zarko, *A Systematic Approach to Optimized Design of Permanent Magnet Motors with Reduced Torque Pulsations*. PhD thesis, University of Wisconsin Madison, Madison, USA, 2004.

[19] N. A. Demerdash, T. M. Hijazi, and A. A. Arkadan, "Computation of winding inductances of permanent magnet brushless dc motors with damper windings by energy perturbation," *IEEE Transactions on Energy Conversion*, vol. 3, pp. 705 –713, September 1988.

[20] N. A. Demerdash and T. W. Nehl, "Electric machinery parameters and torques by current and energy perturbations from field computations. i. theory and formulation," *IEEE Transactions on Energy Conversion*, vol. 14, pp. 1507 –1513, December 1999.

[21] N. Demerdash and T. Nehl, "Electric machinery parameters and torques by current and energy perturbations from field computations. ii. applications and results," *IEEE Transactions on Energy Conversion*, vol. 14, no. 4, pp. 1514–1522, 1999.

[22] N. A. Demerdash and T. W. Nehl, "Dynamic modeling of brushless dc motors for aerospace actuation," *IEEE Transactions on Aerospace and Electronic Systems*, vol. AES-16, pp. 811–821, November 1980.

[23] T. M. Hijazi and N. A. Demerdash, "Computer-aided modeling and experimental verification of the performance of power conditioner operated permanent magnet brushless dc motors including rotor damping effects," *IEEE Transactions on Energy Conversion*, vol. 3, pp. 714 –721, September 1988.

[24] R. Wang and N. Demerdash, "Computation of load performance and other parameters of extra high speed modified lundell alternators from 3d-fe magnetic field solutions," *IEEE Transactions Energy Conversion*, vol. 7, pp. 342–352, June 1992.

[25] J. Bangura and N. Demerdash, "Simulation of inverter-fed induction motor drives with pulse-width modulation by a time-stepping coupled finite element-flux linkage-based state space model," *IEEE Transactions on Energy Conversion*, vol. 14, no. 3, pp. 518–525, 1999.

[26] L. Alberti, N. Bianchi, M. Morandin, and J. Gyselinck, "Finite-element analysis of electrical machines for sensorless drives with signal injection," in *Energy Conversion Congress and Exposition (ECCE), 2012 IEEE*, pp. 861 –868, September 2012.

[27] N. Bianchi and L. Alberti, "Mmf harmonics effect on the embedded fe analytical computation of pm motors," *IEEE Transactions on Industry Applications*, vol. 46, pp. 812 –820, March-April 2010.

[28] D. A. Staton, R. P. Deodhar, W. L. Soong, and T. J. E. Miller, "Torque prediction using the flux-mmf diagram in ac, dc, and reluctance motors," *IEEE Transactions on Industry Applications*, vol. 32, pp. 180 –188, January-February 1996.

[29] R. P. Deodhar, D. A. Staton, T. M. Jahns, and T. J. E. Miller, "Prediction of cogging torque using the flux-mmf diagram technique," *IEEE Transactions on Industry Applications*, vol. 32, pp. 569 –576, May-June 1996.

[30] D. M. Ionel, M. Popescu, M. I. McGilp, T. J. E. Miller, and S. J. Dellinger, "Assessment of torque components in brushless permanent-magnet machines through numerical analysis of the electromagnetic field," *IEEE Transactions on Industry Applications*, vol. 41, pp. 1149 – 1158, September-October 2005.

[31] T. J. E. Miller, M. Popescu, C. Cossar, M. I. McGilp, M. Olaru, A. Davies, J. Sturgess, and A. Sitzia, "Embedded finite-element solver for computation of brushless permanent-magnet motors," *IEEE Transactions on Industry Applications*, vol. 44, pp. 1124 –1133, July-August 2008.

[32] D. M. Ionel and M. Popescu, "Finite-element surrogate model for electric machines with revolving field - application to ipm motors," *IEEE Transactions on Industry Applications*, vol. 46, pp. 2424 –2433, November-December 2010.

[33] C. Schlensok, M. H. Gracia, and K. Hameyer, "Combined numerical and analytical method for geometry optimization of a pm motor," *IEEE Transactions on Magnetics*, vol. 42, pp. 1211 –1214, April 2006.

[34] W. Zhu, B. Fahimi, and S. Pekarek, "A field reconstruction method for optimal excitation of permanent magnet synchronous machines," *IEEE Transactions on Energy Conversion*, vol. 21, pp. 305 – 313, June 2006.

[35] J. Gyselinck, P. Dular, W. Legros, and D. Grenier, "Hybrid magnetic equivalent circuit finite element modeling of transormer fed electrical machines," *COMPEL The International Journal for Computation and Mathematics in Electrical Engineering*, vol. 22, no. 3, pp. 643–658, 2003.

[36] S. M. Saunders, "Digital computers as an aid in electric-machine design," *American Institute of Electrical Engineers, Part I: Communication and Electronics, Transactions of the*, vol. 73, pp. 189 –192, May 1954.

[37] C. G. Veinott, "Induction machinery design being revolutionized by the digital computer," *Power Apparatus and Systems, Part III. Transactions of the American Institute of Electrical Engineers*, vol. 75, pp. 1509 –1517, January 1956.

[38] B. J. Chalmers and B. J. Bennington, "Digital-computer program for design synthesis of large squirrel-cage induction motors," *Electrical Engineers, Proceedings of the Institution of*, vol. 114, pp. 261 –268, February 1967.

[39] N. Demerdash and T. Nehl, "An evaluation of the methods of finite elements and finite differences in the solution of nonlinear electromagnetic fields in electrical machines," *IEEE Transactions on Power Apparatus and Systems*, vol. PAS-98, no. 1, pp. 74–87, 1979.

[40] T. Nakata and N. Takahashi, "New design method of permanent magnets by using the finite element method," *IEEE Transactions on Magnetics*, vol. 19, pp. 2494 – 2497, November 1983.

[41] K. Preis, C. Magele, and O. Biro, "Fem and evolution strategies in the optimal design of electromagnetic devices," *IEEE Transactions on Magnetics*, vol. 26, pp. 2181–2183, September 1990.

[42] O. Mohammed and W. Jones, "A dynamic programming-finite element procedure for the design of nonlinear magnetic devices," *IEEE Transactions on Magnetics*, vol. 26, pp. 666 –669, March 1990.

[43] G. F. Uler, O. A. Mohammed, and C.-S. Koh, "Utilizing genetic algorithms for the optimal design of electromagnetic devices," *IEEE Transactions on Magnetics*, vol. 30, pp. 4296 –4298, November 1994.

[44] V. Cingoski, K. Kaneda, H. Yamashita, and N. Kowata, "Inverse shape optimization using dynamically adjustable genetic algorithms [electric machine design]," *IEEE Transactions on Energy Conversion*, vol. 14, pp. 661 –666, September 1999.

[45] F. Deng, "Commutation-caused eddy-current losses in permanent-magnet brushless dc motors," *IEEE Transactions Magnetics*, vol. 33, pp. 4310–4318, September 1997.

[46] F. Deng and T. W. Nehl, "Analytical modeling of eddy-current losses caused by pulse-width-modulation switching in permanent-magnet brushless direct-current motors," *IEEE Transactions Magnetics*, vol. 34, pp. 3728–3736, September 1998.

[47] Z. Q. Zhu, K. Ng, N. Schofield, and D. Howe, "Analytical prediction of rotor eddy current loss in brushless machines equipped with surface-mounted permanent magnets. i. magnetostatic field model," in *Electrical Machines and Systems, 2001. ICEMS 2001. Proceedings of the Fifth International Conference on*, vol. 2, pp. 806–809, August 2001.

[48] Z. Q. Zhu, K. Ng, N. Schofield, and D. Howe, "Analytical prediction of rotor eddy current loss in brushless machines equipped with surface-mounted permanent magnets. ii. accounting for eddy current reaction field," in *Electrical Machines and Systems, 2001. ICEMS 2001. Proceedings of the Fifth International Conference on*, vol. 2, pp. 810–813, August 2001.

[49] D. Zarko, D. Ban, and T. A. Lipo, "Analytical calculation of magnetic field distribution in the slotted air gap of a surface permanent-magnet motor using complex relative air-gap permeance," *IEEE Transactions Magnetics*, vol. 42, pp. 1828–1837, July 2006.

[50] B. L. J. Gysen, K. J. Meessen, J. J. H. Paulides, and E. A. Lomonova, "General formulation of the electromagnetic field distribution in machines and devices using fourier analysis," *IEEE Transactions Magnetics*, vol. 46, pp. 39–52, January 2010.

[51] Y. Duan, R. G. Harley, and T. G. Habetler, "A useful multi-objective optimization design method for pm motors considering nonlinear material properties," in *Energy Conversion Congress and Exposition, 2009. ECCE 2009. IEEE*, pp. 187–193, September 2010.

[52] V. Ostovic, *Dynamics of Saturated Electric Machines.* New York, Springer-Verlag, 1989.

[53] K. Hameyer and R. Hanitsch, "Numerical optimization of the electromagnetic field by stochastic search and MEC-model," *IEEE Transactions on Magnetics*, vol. 30, pp. 3431 –3434, September 1994.

[54] E. C. Lovelace, T. M. Jahns, and J. H. Lang, "Impact of saturation and inverter cost on interior pm synchronous machine drive optimization," *IEEE Transactions on Industry Applications*, vol. 36, pp. 723 –729, May-June 2000.

[55] K.-C. Kim, J. Lee, H. J. Kim, and D.-H. Koo, "Multiobjective optimal design for interior permanent magnet synchronous motor," *IEEE Transactions on Magnetics*, vol. 45, pp. 1780 –1783, March 2009.

[56] B. N. Cassimere, S. D. Sudhoff, and D. H. Sudhoff, "Analytical design model for surface-mounted permanent-magnet synchronous machines," *IEEE Transactions on Energy Conversion*, vol. 24, pp. 347–357, June 2009.

[57] B. N. Cassimere and S. D. Sudhoff, "Population-based design of surface-mounted permanent-magnet synchronous machines," *IEEE Transactions on Energy Conversion*, vol. 24, pp. 338–346, June 2009.

[58] J. Baek, M. M. Rahimian, and H. A. Toliyat, "Optimal design of pm assisted synchronous reluctance generators using lumped parameter model and differential evolution strategy," in *Energy Conversion Congress and Exposition, 2009. ECCE 2009. IEEE*, pp. 2453 –2459, September 2009.

[59] N. Bianchi and S. Bolognani, "Design optimisation of electric motors by genetic algorithms," *IEE Proceedings - Electric Power Applications*, vol. 145, pp. 475–483, September 1998.

[60] M. A. Alhamadi and N. A. O. Demerdash, "Optimization of the skew angle of rotor poles in permanent magnet machines based on the inverse problem method," *IEEE Transactions on Energy Conversion*, vol. 14, pp. 1496–1501, December 1999.

[61] W. Ouyang, D. Zarko, and T. A. Lipo, "Permanent magnet machine design practice and optimization," in *Industry Applications Conference, 2006. 41st IAS Annual Meeting. Conference Record of the 2006 IEEE*, vol. 4, pp. 1905 –1911, Oct. 2006.

[62] R. F. Schiferl and T. A. Lipo, "Power capability of salient pole permanent magnet synchronous motors in variable speed drive applications," *IEEE Transactions on Industry Applications*, vol. 26, pp. 115 –123, Januare-February 1990.

[63] M. Beniakar, E. Tsampouris, C. Patsios, and A. Kladas, "Evolutionary optimization of permanent magnet machine design for traction applications," in *Electromagnetic Field Computation (CEFC), 2010 14th Biennial IEEE Conference on*, p. 1, May 2010.

[64] A. A. Arkadan, M. N. ElBsat, and M. A. Mneimneh, "Particle swarm design optimization of ala rotor synrm for traction applications," *IEEE Transactions on Magnetics*, vol. 45, pp. 956 –959, March 2009.

[65] S. Giurgea, D. Fodorean, G. Cirricione, A. Miraoui, and M. Cirrincione, "Multimodel optimization based on the response surface of the reduced FEM simulation model with application to a PMSM," *IEEE Transactions on Magnetics*, vol. 46, pp. 812–820, September 2008.

[66] I. P. Brown and R. D. Lorenz, "Induction machine design methodology for self-sensing: balancing saliencies and power conversion properties," *IEEE Transactions on Industry Applications*, vol. 47, pp. 79 –87, January-February 2011.

[67] G. Pellegrino and F. Cupertino, "FEA-based multi-objective optimization of IPM motor design including rotor losses," in *Energy Conversion Congress and Exposition (ECCE), 2010 IEEE*, pp. 3659–3666, September 2010.

[68] F. Parasiliti, M. Villani, S. Lucidi, and F. Rinaldi, "Finite-element-based multiobjective design optimization procedure of interior permanent magnet synchronous motors for wide constant-power region operation," *IEEE Transactions on Industrial Electronics*, vol. 59, pp. 2503 –2514, June 2012.

[69] W. Jiang, T. M. Jahns, T. A. Lipo, W. Taylor, and Y. Suziki, "Machine design optimization based on finite element analysis in a high-throughput computing environment," in *Energy Conversion Congress and Exposition (ECCE), 2012 IEEE*, pp. 869–876, September 2012.

[70] Y. Duan and D. M. Ionel, "A review of recent developments in electrical machine design optimization methods with a permanent magnet synchronous motor benchmark study," in *Energy Conversion Congress and Exposition (ECCE), 2011 IEEE*, pp. 3694–3701, September 2011.

[71] Y. Duan and D. M. Ionel, "Non-linear scaling rules for brushless pm synchronous machines based on optimal design studies for a wide range of power ratings," in *Energy Conversion Congress and Exposition (ECCE), 2012 IEEE*, pp. 2334–2341, September 2012.

[72] G. Y. Sizov, D. M. Ionel, and N. A. O. Demerdash, "Modeling and design optimization of PM AC machines using computationally efficient - finite element analysis," in *Energy Conversion Congress and Exposition (ECCE), 2010 IEEE*, pp. 578–585, September 2010.

[73] G. Y. Sizov, D. M. Ionel, and N. A. O. Demerdash, "A review of efficient FE modeling techniques with applications to PM AC machines," in *Power and Energy Society General Meeting, 2011 IEEE*, pp. 1–6, July 2011.

[74] G. Y. Sizov, D. M. Ionel, and N. A. O. Demerdash, "Modeling and parametric design of permanent-magnet AC machines using computationally efficient finite-element analysis," *IEEE Transactions on Industrial Electronics*, vol. 59, pp. 2403–2413, June 2012.

[75] G. Y. Sizov, P. Zhang, D. M. Ionel, N. A. O. Demerdash, I. P. Brown, and M. G. Solveson, "Modeling and analysis of effects of skew on torque ripple and stator tooth forces in permanent magnet AC machines," in *Energy Conversion Congress and Exposition (ECCE), 2012 IEEE*, pp. 3055–3061, September 2012.

[76] G. Y. Sizov, D. M. Ionel, and N. A. O. Demerdash, "Multi-objective optimization of PM AC machines using computationally efficient - FEA and differential evolution," in *Electric Machines Drives Conference (IEMDC), 2011 IEEE International*, pp. 1528–1533, May 2011.

[77] G. Y. Sizov, P. Zhang, D. M. Ionel, N. A. O. Demerdash, and M. Rosu, "Automated bi-objective design optimization of multi-MW direct-drive PM machines using CE-FEA and differential evolution," in *Energy Conversion Congress and Exposition (ECCE), 2011 IEEE*, pp. 3672–3678, September 2011.

[78] G. Y. Sizov, P. Zhang, D. M. Ionel, N. A. O. Demerdash, and M. Rosu, "Automated multi-objective design optimization of PM AC machines using computationally efficient - FEA and differential evolution," *IEEE Transactions on Industrial Applications*, vol. accepted for publication, 2012.

[79] I. P. Brown, G. Sizov, M. W. Critchley, J. Yin, S. B. Memory, S. W. Elbel, C. D. Bowers, M. Petersen, and P. S. Hrnjak, "Design and evaluation of interior permanent magnet compressor motors for commercial transcritical CO2 (R-744) heat pump

water heaters," in *Energy Conversion Congress and Exposition (ECCE), 2012 IEEE*, pp. 2790–2797, September 2012.

[80] N. Demerdash, "Design and analysis of electric motors in adjustable speed drives." Course Notes, 2005.

[81] M. M. Liwschitz, "Distribution factors and pitch factors of the harmonics of a fractional-slot winding," *American Institute of Electrical Engineers, Transactions of the*, vol. 62, no. 10, pp. 664–666, 1943.

[82] F. Magnussen and C. Sadarangani, "Winding factors and joule losses of permanent magnet machines with concentrated windings," in *Electric Machines and Drives Conference, 2003. IEMDC'03. IEEE International*, vol. 1, pp. 333–339 vol.1, 2003.

[83] P. Salminen, *Fractional Slot Permanent Magnet Synchronous Motors for Low Speed Applications*. PhD thesis, Lappeenranta University of Technology, Lappeenranta, Finland, December 2004.

[84] N. Bianchi and M. Dai Pre, "Use of the star of slots in designing fractional-slot single-layer synchronous motors," *Electric Power Applications, IEE Proceedings* -, vol. 153, no. 3, pp. 459–466, 2006.

[85] L. Alberti, "Koil v1.1.0." `http://www.koil.sourceforge.net`, December 2012.

[86] S. Meier, "Emetor." `http://www.emetor.com`, December 2012.

[87] K. Ito, K. Naka, N. Masatsugu, and K. Manabu, "Electric machine." US Patent No.: 7,605,514 B2, 2009.

[88] M. V. Cistelecan, F. J. T. E. Ferreira, and M. Popescu, "Three phase tooth-concentrated multiple-layer fractional windings with low space harmonic content," in *Energy Conversion Congress and Exposition (ECCE), 2010 IEEE*, pp. 1399–1405, 2010.

[89] L. Alberti, M. Barcaro, and N. Bianchi, "Design of a low torque ripple fractional-slot interior permanent magnet motor," in *Energy Conversion Congress and Exposition (ECCE), 2012 IEEE*, pp. 509–516, 2012.

[90] P. B. Reddy, A. M. EL-Refaie, and K.-K. Huh, "Effect of number of layers on performance of fractional-slot concentrated-windings interior permanent magnet machines," in *Power Electronics and ECCE Asia (ICPE ECCE), 2011 IEEE 8th International Conference on*, pp. 1921–1928, 2011.

[91] F. Magnussen and H. Lendenmann, "Parasitic effects in pm machines with concentrated windings," *IEEE Transactions Industry Applications*, vol. 43, pp. 1223–1232, September-October 2007.

[92] J. F. Gieras, C. Wang, C. S. L. Joseph, and N. Ertugrul, "Analytical prediction of noise of magnetic origin produced by permanent magnet brushless motors," in *Electric Machines Drives Conference, 2007. IEMDC '07. IEEE International*, pp. 148–152, 2007.

[93] G. Dajaku and D. Gerling, "Magnetic radial force density of the pm machine with 12-teeth/10-poles winding topology," in *Electric Machines and Drives Conference, 2009. IEMDC '09. IEEE International*, pp. 1715–1720, 2009.

[94] M. Islam, R. Islam, and T. Sebastian, "Noise and vibration characteristics of permanent magnet synchronous motors using electromagnetic and structural analyses," in *Energy Conversion Congress and Exposition (ECCE), 2011 IEEE*, pp. 3399–3405, 2011.

[95] T. Sun, J.-M. Kim, G.-H. Lee, J.-P. Hong, and M.-R. Choi, "Effect of pole and slot combination on noise and vibration in permanent magnet synchronous motor," *IEEE Transactions Magnetics*, vol. 47, pp. 1038–1041, May 2011.

[96] A348/A348M-05(2011), "Standard test method for alternating current magnetic properties of materials using the wattmeter-ammeter-voltmeter method, 100 to 10 000 hz and 25cm epstein frame," 2011.

[97] G. Bertotti, "General properties of power losses in soft ferromagnetic materials," *IEEE Transactions Magnetics*, vol. 24, pp. 621–630, January 1988.

[98] D. M. Ionel, M. Popescu, M. I. McGilp, T. J. E. Miller, S. J. Dellinger, and R. J. Heideman, "Computation of core losses in electrical machines using improved models for laminated steel," *IEEE Transactions Industry Applications*, vol. 43, pp. 1554–1564, November-December 2007.

[99] J. Lavers and P. Biringer, "Prediction of core losses for high flux densities and distorted flux waveforms," *IEEE Transactions Magnetics*, vol. 12, no. 6, pp. 1053–1055, 1976.

[100] N. Alatawneh and P. Pillay, "Design of a novel test fixture to measure rotational core losses in machine laminations," *IEEE Transactions Industry Applications*, vol. 48, pp. 1467–1477, September-October 2012.

[101] P. Campbell, *Permanent Magnet Materials and Their Application*. Cambridge University Press, 1994.

[102] T. M. Jahns, G. B. Kliman, and T. W. Neumann, "Interior permanent-magnet synchronous motors for adjustable-speed drives," *IEEE Transactions Industry Applications*, vol. IA-22, pp. 738–747, July 1986.

[103] S. Morimoto, Y. Takeda, T. Hirasa, and K. Taniguchi, "Expansion of operating limits for permanent magnet motor by current vector control considering inverter capacity," *IEEE Transactions Industry Applications*, vol. 26, pp. 866–871, September-October 1990.

[104] T. Rowan and R. Kerkman, "A new synchronous current regulator and an analysis of current-regulated pwm inverters," *IEEE Transactions Industry Applications*, vol. IA-22, no. 4, pp. 678–690, 1986.

[105] F. Fouad, T. Nehl, and N. Demerdash, "Magnetic field modeling of permanent magnet type electronically operated synchronous machines using finite elements," *IEEE Transactions Power Apparatus and Systemsn*, vol. PAS-100, pp. 4125–4135, September 1981.

[106] D. Ionel and M. Popescu, "Ultrafast finite-element analysis of brushless pm machines based on space-time transformations," *IEEE Transactions Industry Applications*, vol. 47, pp. 744–753, March-April 2011.

[107] S. Salon, *Finite Element Analysis of Electrical Machines*. Boston, MA: Kluwer, 1995.

[108] M. A. Alhamadi and N. A. Demerdash, "Modeling of effects of skewing of rotor mounted permanent magnets on the performance of brushless dc motors," *Energy Conversion, IEEE Transactions on*, vol. 6, pp. 721 –729, December 1991.

[109] S. Williamson, T. J. Flack, and A. F. Volschenk, "Representation of skew in time-stepped two-dimensional finite-element models of electrical machines," *IEEE Transactions Industry Applications*, vol. 31, pp. 1009 –1015, September-October 1995.

[110] ANSYS, "Maxwell 2d/3d." `http://www.ansys.com`, Version 15.

[111] Infolytica, "Magnet 2d." `http://www.infolytica.com/`, Version 7.

[112] K. V. Price, R. M. Storn, and J. A. Lampinen, *Differential Evolution-A Practical Approach to Global Optimization*. Springer-Verlag Berlin Heidelberg, 2005.

[113] R. Storn and K. Price, "Differential evolution a simple and efficient heuristic for global optimization over continuous spaces," *Journal of Global Optimization*, vol. 11, no. 4, pp. 341–359, 1997.

[114] S. Das and P. Suganthan, "Differential evolution: A survey of the state-of-the-art," *IEEE Transactions Evolutionary Computation*, vol. 15, no. 1, pp. 4–31, 2011.

[115] K. Deb, *Multi-objective optimization using evolutionary algorithms*. New York, J. Wiley and Sons, Ed, 2001.

[116] J. Kang, "Sensorless control of permanent magneg motors," *Control Engineering*, vol. 57, April 2010.